



Synthesis of Nanoparticles and Nanostructured Materials by Self-Assembly

Miriam Varón Izquierdo

Tesi doctoral

Estudis de Doctorat en Química

Director: Víctor F. Puntes

**Departament de Química
Facultat de Ciències**

Abril 2012

Synthesis of Nanoparticles and Nanostructured Materials by Self-Assembly

Memòria presentada per aspirar al Grau de Doctor
per Miriam Varón Izquierdo

Bellaterra, Abril de 2012



El Dr. Victor F. Punes, responsable del grup Inorganic Nanoparticles a l'Institut Català de Nanotecnologia i professor associat del Departament de Química de la Facultat de Ciències de la Universitat Autònoma de Barcelona,

Certifica:

Que el treball descrit en aquesta memòria titulada “**Synthesis of Nanoparticles and Nanostructured Materials by Self-Assembly**” presentada per Miriam Varón Izquierdo per optar al grau de Doctor, ha estat realitzada sota la meua direcció i recull, sota el meu punt de vista, els requisits exigits per a la consecució del citat títol.

Perquè quedi constància, signo el present certificat

Dr. Víctor F. Punes

Bellaterra, 11 d'Abril de 2012

*La ciència serà sempre una cerca, mai un descobriment real.
Es un viatge, mai una arribada.*

Karl R. Popper

Contents

Acknowledgements	vii
Structure of the Thesis	ix
Objectives	xi
I. Introduction	1
1.1 Nanostructured Materials. A Bottom-up Approach	1
1.2 Nanoparticles as Building Blocks	2
1.3 Inorganic Nanoparticles	3
1.3.1 Colloidal Stability of Nanoparticles	5
1.3.2 Synthetic Processes of Inorganic Nanoparticles	6
1.4 Magnetic Characteristics of Nanoparticles	8
1.4.1 Magnetic Properties of Solids	8
1.4.2 Magnetic Nanoparticles	11
1.4.3 Magnetic Anisotropy	11
1.4.4 Superparamagnetism	12
1.4.5 Exchange Bias: FM-AFM Coupled Systems	13
1.4.6 Inter-particle Interactions: Dipolar Interactions	13
1.5 Self-Assembly Process	15
1.6 References	17
II. Synthesis of Metallic and Bimetallic Nanoparticles	21
2.1 Synthesis of Co Nanoparticles	22
2.1.1 Experimental	23

2.1.1.1 Chemicals	23
2.1.1.2 Synthesis of ϵ -Co Nanoparticles	23
2.1.2 Results and Discussion	24
2.1.2.1 Structural Characterization	24
2.1.2.2 Size-Dependent Properties	27
2.1.2.3 Magnetic Characterization	28
2.1.3 Summary	29
2.2 Formation of Core/Shell Co/CoO and Hollow CoO Nanoparticles	30
2.2.1 Exposure to Open-Air Conditions:	
Core/Shell Co/CoO Nanoparticles	30
2.2.1.1 Experimental	30
<i>Formation of Core/Shell Co/CoO Nanoparticles</i>	30
2.2.1.2 Results and Discussion	30
2.2.2 Exposure to Water/Air Interface Conditions:	
Hollow CoO Nanoparticles	32
2.2.2.1 Experimental	33
<i>Formation of Hollow CoO Nanoparticles</i>	33
<i>Recovery Process of Hollow CoO Nanoparticles</i>	34
2.2.2.2 Results and Discussion	34
<i>Structural Characterization</i>	33
<i>Magnetic Characterization</i>	38
<i>Formation Mechanism: Kirkendall Effect</i>	41
2.2.3 Summary	42
2.3 Synthesis of Pt and PtCo Nanoparticles	42
2.3.1 Synthesis of Pt and PtCo Nanoparticles Assisted by Metal Traces	42
2.3.1.1 Experimental	43
2.3.1.2 Results and Discussion	44
2.3.1.3 Summary	50
2.3.2 Synthesis of Pt and PtCo Nanoparticles by Using Competing Reducers	50
2.3.2.1 Experimental	51
<i>Chemicals</i>	51
<i>Synthesis</i>	51
<i>Increasing Co Content</i>	51

<i>Increasing Hydride Content</i>	52
<i>Increasing HDD Content</i>	52
2.3.2.2 Results and Discussion	52
<i>Increasing Co Content</i>	52
<i>Increasing Hydride Content</i>	56
<i>Increasing HDD Content</i>	57
2.3.2.3 Summary	60
2.4 Synthesis of Bimetallic Pt/Au Heterostructures	60
2.4.1 Experimental	61
2.4.1.1 Chemicals	61
2.4.1.2 Synthesis of Pt Nanocrystals	61
2.4.1.3 Synthesis of Pt/Au Heterodimers at Room Temperature	61
2.4.2 Results and Discussion	62
2.4.2.1 The Reaction Time	62
2.4.2.2 Structural Characterization	63
2.4.2.3 Role of Pt Nanocrystals	65
2.4.3 Summary	67
2.5 Synthesis of Extremely Long Rod Shaped Au Nanocrystals	67
2.5.1 Experimental	68
2.5.1.1 Chemicals	68
2.5.1.2 Synthesis of CTAB Stabilized Pt Seed Nanoparticles	68
2.5.1.3 Synthesis of CTAB Stabilized Au Seed Nanoparticles	69
2.5.1.4 Synthesis of Au Rods Using Pt Seed Nanoparticles	69
2.5.1.5 Synthesis of Au Rods Using Au Seed Nanoparticles	69
2.5.2 Results and Discussion	69
2.5.2.1 Structural Characterization	69
2.5.2.2 Effect of Pt ²⁺ and Pt Seeds in the Synthesis	72
2.5.2.3 Effect of Different Amount of Pt Seeds in the Synthesis	73
2.5.3 Summary	74
2.6 Conclusions	75
2.7 References	76

III. Study of the Self-Assembly Process of Magnetic and Noble Metal Nanoparticles	89
3.1 Self-Assembly of Metal Nanoparticles onto TEM Carbon Substrates	90
3.1.1 Spherical Nanoparticles	90
3.1.1.1 Au Nanoparticles	90
3.1.1.2 Co Nanoparticles	91
3.1.2 Non-Spherical Nanoparticles	92
3.1.2.1 Pt Nanoparticles	92
3.1.2.2 Rod Shaped Au Nanoparticles	93
3.1.3 Summary	95
3.2 Self-assembly of Co Nanoparticles at Compatible Substrates:	
Graphite	96
3.2.1 Experimental	97
3.2.1.1 Co Nanoparticles	97
3.2.1.2 Deposition of Co Nanoparticles onto Graphite	97
3.2.2 Results and Discussion	98
3.2.2.1 Structural Characterization	99
3.2.2.2 Magnetic Characterization	101
3.2.2.3 Effect of Increasing Particle Size	103
3.2.2.4 Effect of Applied Magnetic Fields.....	105
3.2.2.5 Formation Mechanism	106
3.2.3 Summary	108
3.3 Self-Assembly of Co Nanoparticles at Non-Compatible Substrates:	
Silicon Wafers	109
3.3.1 Experimental	110
3.3.1.1 Substrates	110
3.3.1.2 Deposition of Co Nanoparticles onto Silicon Wafers	110
3.3.2 Results and Discussion	111
3.3.3 Summary	114
3.4 Conclusions	114
3.5 References	115

IV. Electron Holography and Lorentz Microscopy of Self-Assembled Cobalt Nanoparticles Structures	121
4.1 Basis of Lorentz Microscopy and Electron Holography	123
4.1.1 Off-Axis Electron Holography	125
4.1.1.1 Imaging Theory	126
4.1.1.2 Hologram Reconstruction	127
4.1.2 Magnetic and Mean Inner Potential Contributions to the Phase	129
4.1.3 Measurement of Magnetic Fields	130
4.1.3.1 Separation of Phase Information	130
4.1.3.2 Visualization of the Magnetic Contribution to the Phase	131
4.2 Electron Holography of Chain-Like Self-Assembled Structures	132
4.2.1 Experimental	132
4.2.1.1 Sample Preparation	132
4.2.1.2 Data Acquisition	132
4.2.2 Results and Discussion	132
4.2.3 Summary	138
4.3 Electron Holography of Self-Assembled Co Structures with Increasing Temperature	138
4.3.1 Experimental	138
4.3.1.1 Sample Preparation	138
4.3.1.2 Data Acquisition	138
4.3.2 Results and Discussion	139
4.3.2.1 Region 1	140
4.3.2.2 Region 2	144
4.3.3 Summary	146
4.4 Lorentz Microscopy and Electron Holography of Wire-Like Co Self-Assembled Structures	146
4.4.1 Experimental	146
4.4.1.1 Sample Preparation	146
4.4.1.2 Data Acquisition Lorentz Microscopy	146
4.4.1.3 Data Acquisition Electron Holography	146

4.4.2 Results and Discussion	147
4.4.2.1 Electron Holography	147
4.4.2.2 Lorentz Microscopy	149
4.3.3 Summary	150
4.5 Conclusions	150
4.6 References	151
V. General Conclusions	157
VI. Appendix: Instrumentation	161
A.1 Synthesis of Co Nanoparticles	161
A.2 Formation of Core/Shell Co/CoO and Hollow CoO Nanoparticles	161
A.3 Synthesis of Pt and PtCo Nanoparticles	162
A.3.1 Synthesis of Pt and PtCo Nanoparticles Assisted by Metal Traces	162
A.3.2 Synthesis of Pt and PtCo Nanoparticles by Using Competing Reducers	163
A.4 Synthesis of Bimetallic Au/Pt Heterostructures	163
A.5 Synthesis of Extremely Long Rod Shaped Au Nanocrystals	164
A.6 Self-Assembly of Co Nanoparticles at Compatible Substrates: Graphite	165
A.7 Self-Assembly of Co Nanoparticles at Non-Compatible Substrates: Silicon Wafers ..	165
A.8 References	165
List of Abbreviations	167
List of Publications	169

Acknowledgments

The work presented here is the result of collaboration with a number of people. First of all, I want to thank my supervisor, Dr. Victor F. Puntes, for giving me the opportunity to work in the Inorganic Nanoparticles Group and introduce me to the Nanotechnology. I am very grateful for his guidance and multiple advices during the last years which allowed me to be trained as a researcher.

Thanks to all the members of the Inorganic Nanoparticles Group for make this experience more enriching with their discussions and, not less important, for the funny moments. In particular, I would like to thank both Stephanie Lim and Isaac Ojea for their help and collaboration in the present work.

Thanks to Dr. Lluís Balcells and Dr. Benjamin Martínez, from the Institut de Ciència de Materials de Barcelona, for their collaboration and for the magnetic measurements of my particles. And thanks to Dr. Jordi Arbiol, from the Institut de Ciència de Materials de Barcelona, for the numerous and valuable TEM measurements and analyses of the nanoparticles.

I want to express my gratitude to Dr. Cathrine Frandsen for her advice and guidance during my two stays at DTU and for welcoming me so nicely. I also want to thank Prof. Rafal E. Dunin-Borkowski and Dr. Takeshi Kasama from the Center of Electron Nanoscopy for introducing me to the electron holography and for their productive discussions concerning to the results presented in this thesis.

Tanks to the Spanish MICINN for the financial support though the scholarship BES-2007-17164 associated to the research project MAT2006-13572-C02-02.

Gracias a mi familia y amigos, especialmente a mis padres, por darme siempre su apoyo. Gracias Juanjo por haber estado y estar siempre ahí. Espero poder seguir compartiendo muchas cosas contigo.

Structure of the Thesis

This thesis has been divided into the following chapters:

- **Chapter zero** exposes the objectives of the dissertation.
- **Chapter one** presents the basic concepts and the theoretical background for a better understanding of the presented work. Some physical and chemical phenomena related to the research presented in this thesis will be briefly introduced.
- **Chapter two** is focused in the description of the synthetic processes of different metallic and bimetallic nanoparticles and their characterization.
- **Chapter three** shows the self-assembly process of different nanoparticles. In particular two main works have been carried out studying of the self-assembly process of magnetic Co nanoparticles at different substrates.
- **Chapter five** resumes the general conclusions of the thesis.
- **Chapter six**, formed by the appendix, compiles the description of the instrumentation techniques used in each section of the previous chapters.

Finally, at the end of the thesis can be found the list of the abbreviations used along the text and the list of publications generated from this work, as well the manuscripts that are in preparation.

Every chapter in this dissertation includes conclusions and also the references cited along the chapter.

Objectives

The aim of this work is to acquire basic knowledge and technology for the preparation of nanoparticles (NPs) and nanostructured composite magnetic materials, including self-assembly (SA) processes (controlled aggregation) of NPs. This goal includes activities going from the optimization of basic properties and growing conditions up to the control of NPs SA processes on top of technological substrates, useful for the fabrication composite magnetic materials, with controlled properties, for the development of technological devices.

On one hand, we face topics related with metallic NP size and shape control. The goal is to determine the most relevant parameters controlling the growth process of NPs by the proper selection of synthetic conditions such as surfactants, reducing agents, time and temperature. To achieve this goal, it is fundamental the development of experimental protocols and theoretical knowledge for the preparation and the analysis of the NPs. In this context, different kind of metallic and bimetallic NPs have been studied (Co, Co-Pt, Pt-Au, Au). First, Co magnetic NPs of different size have been synthesized (**Section 2.1**) and their oxidation processes have been also studied (**Section 2.2**), generating Co oxide hollow particles. We also used these Co particles as reaction assistant in the synthesis of Pt and PtCo NPs (**Section 2.3**). We continued with the synthesis of bimetallic Pt/Au heterostructures (**Section 2.4**). And, finally, Au long rods are synthesized by using Pt NPs as reaction catalyst (**Section 2.5**).

On the other hand, we deal about problems related to NPs SA and the study of all the forces that take place in the process, which depends on different parameters such as the composition of the NPs and their size and shape among others. SA processes may yield the organization of building blocks into a crystalline material with orientational and translational symmetry. The macroscopic properties of such nanocrystalline superlattices are determined not only by the individual properties of the building blocks but also by the interactions between them. Thus, the studies of the interactions that intervene in these processes allow the study of the nature of

the NPs beyond of their structural characterization, and allow feedback the synthetic processes and improve the design of desired NP. This part of the work mainly studies the interactions between the NPs and also the interaction with the substrates (**Section 3.1**). Moreover, NPs SA process into ordered structures on top of technological substrates (**Section 3.2** and **Section 3.3**) is very interesting not only by the particular properties that such ordered nanostructures may exhibit but also due to their potential applications as a procedure to prepare templates for the fabrication of other nanostructures in combination with etching and/or growing techniques. This fabrication procedure, based on the SA of nanoscopic units, called bottom-up approximation, is radically different from the traditional top-down procedures, which usually requires expensive etching and lithographic techniques. These studies have been mainly carried out with magnetic NPs because present very interesting properties for forming part of magnetoelectronic devices.

Additionally, the study of the influence of the magnetic properties in the SA process, and the study of the inter-particle interactions inside the self-assembled structures, at the nanometric level, is fundamental for the full understanding of the SA process. Thanks to two productive stays realized in the Prof. Catherine Frandsen group at the physics department of the Technical University of Denmark (DTU) and collaborating with the Center for Electron Nanoscopy (CEN), it has been studied different self-assembled structures, formed by Co NPs, by Lorentz microscopy and electron holography, which allow the study of electrical and magnetic fields of the materials (**Chapter 4**). Thanks to electron holography we have been able to directly image dipolar ferromagnetic-like patterns (superferromagnetism) in the structures with nanometer resolution, demonstrating the formation of ordered regions and vortex states (**Section 4.2**). Moreover, we have studied the magnetic changes in self-assembled structures with increasing temperature (**Section 4.3**). Finally, self-assembled wire-like Co structures have been also studied by both above mentioned techniques (**Section 4.4**). The observed structures indicate collective effects among the whole NPs forming the structures.

Chapter 1

Introduction

1.1 Nanostructured Materials. A Bottom-up Approach

A nanostructured material is defined as a solid material formed by units (or building blocks) that have dimensions at the nanometer scale. Fundamentally, two different approaches have been followed to reach the nanometer-world. Engineers adopted a top-down strategy, i.e. by starting from well-established structures and principles in the macro-world they ventured into the nm-range via successive cycles of miniaturization. On the other hand, chemists naturally adopted a bottom-up strategy as they progressed from synthesizing simple compounds consisting of just a few atoms to long macromolecules.

The bottom-up approach makes use of chemical or physical forces operating at the nanoscale to assemble basic units into larger structures. The inspiration of bottom-up approach comes from biological systems, where nature has employed self-organization of essential building blocks such as amino acids, monosaccharides or lipids, in order to create a wide range of complex structures needed by life.¹ In that way, researchers try to mimic this ability of nature. The main advantages of the bottom-up technique is that a wide variety of preparation methods are available, thus allowing a good control onto scale dimension, while they are not as expensive as top-down approaches. Nevertheless, the preparation of self-assembled systems of complexities comparable to those found in nature still remains a challenge.

Similarly to atoms or molecules, NPs can be used as the building blocks of condensed matter. Assembling NPs into solids opens up the possibility of fabricating new solid-state materials and devices with novel or enhanced physical and chemical properties. Moreover, interactions between proximal NPs can give rise to new collective phenomena. Thus, by choosing an

appropriate nanoparticulate building block it is possible to tailor the properties of the final material.²

1.2 Nanoparticles as Building Blocks

NPs constitute the basic building blocks for nanotechnology and therefore are considered for numerous applications in energy,³ biomedicine,⁴ electronics,⁵ environment,⁶ new materials⁷ and consumer goods,⁸ among others. These NPs need to be synthesized, passivated (control their chemical reactivity), stabilized against particle aggregation, and functionalized to achieve specific performance goals. A huge variety of NPs are available considering their wide chemical nature (semiconductor, noble metal, magnetic, alloy and oxide), morphology, medium in which they are present, their state of dispersion and the nature of surface modifications, fact that makes this a rich field for scientific investigations.

One of the growing interests in NPs research is their use as building blocks for constructing electronic, optoelectronic and magnetic devices.⁹ If a precise control of the NPs size, shape and surface coating is possible, their chemical and physical properties can be manipulated as desired, and consequently these NPs can be used as the building blocks for assembling new nano-scale devices in a similar manner to assembling “Lego” blocks. For most practical applications, the NPs have to be organized into a specific structure (in one, two or three dimensions), similar to how atoms and molecules are assembled into matter. For this reason it is very important to understand the basic principles governing the synthesis, stability and interaction of these systems.

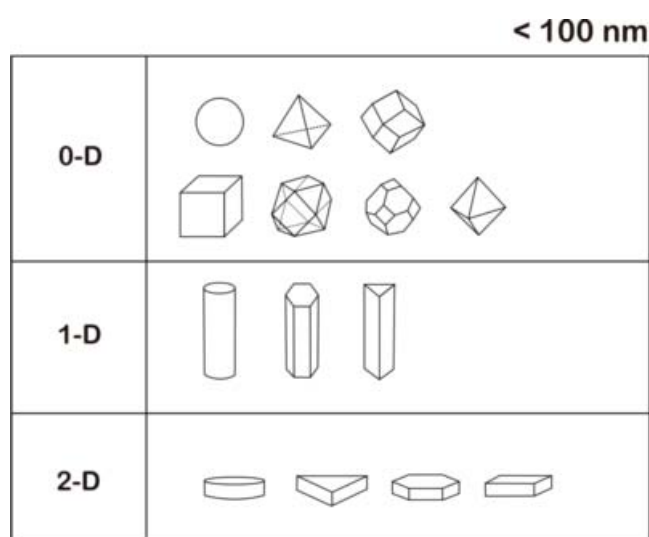


Figure 1.1: Geometrical shapes of basic NP building blocks at the nanometer scale.¹⁰

Basic building blocks can be classified by crystal symmetry and dimensionality (Figure 1.1). The zero-dimensional (0-D) building blocks such as small (dot) spheres, icosahedrons, and cubes are the most familiar shapes at the nanoscale. Rods, cylinders and wires are examples of one-dimensional (1-D) building blocks, whereas disks, plates and polygon shape structures belong to two-dimensional (2-D) building blocks group.

A wide number of approaches have been developed to accomplish SA such as template-assisted assembly,¹¹ surfactant-assisted assembly¹² and charge-assisted assembly.¹³ Showing how superstructures built-up with nano-building blocks can be achieved by specific interactions of molecules conjugated on the particle surface, e.g. molecular recognition methods such as antigen-antibody interactions. Alternatively, NPs are able to assemble into close-packed ordered superlattices under certain conditions.¹⁴ When NPs with highly monodisperse size (<5 %) and shape are segregated from the solution through slow evaporation of the solvent (allowing movement of the particles to suitable positions), closed-packed structures are formed via interactions between NPs. This packing can be tuned by changing parameters including particles size, shape and composition (which can add new interactions to the system). The resulting macroscopic properties of these superlattices are determined not only by the properties of each individual particle, but also by the interaction/coupling between the NPs, which are interconnected and isolated by a thin monolayer (ML) of organic molecules.¹⁵ SA is considered to be one of the most used strategies because of its simplicity, versatility, and ability to obtain spontaneous NPs patterns.

1.3 Inorganic Nanoparticles

In nanotechnology, a NP can be defined as a small elemental ensemble that behaves as a whole unit and present novel properties not exhibited in the characteristic bulk material. At the nanometer scale the confinement of electrons, phonons and photons leads to the appearance of new physical and chemical properties that make them “new” materials. Moreover, their size, morphology and structure determine not only their properties but also its reactivity. NPs are sized in the range of 1-100 nm and they are formed at least by hundreds or thousands of atoms organized within a structure, which can be non-crystalline, polycrystalline or a single crystal.

Both the thermodynamics and kinetics of reactions are different depending on the NP size. The reduction of the dimensionality affects to a variety of factors such as melting points (which depends of the coordination number of the participating atoms), optical properties, magnetic properties, reactivity and conductivity, among others. The smaller a particle becomes the more

the proportion of surface atoms, leading to an increased reactivity due to a rise of the active sites.

Some inorganic NPs display interesting optical properties, and the absorption and/or emission wavelengths can be controlled by particle size and surface functionalization.¹⁶ The surface Plasmon resonance (SPR) is an optical phenomenon also present in some metal particles, and consists in the parallel propagation of surface electromagnetic waves along the metal-dielectric interfaces. Plasmon resonance in metal NPs arises from the collective oscillations of the free conduction band electrons that are induced by the incident electromagnetic radiation (Figure 1.2 A). The surface, the surrounding environment and the agglomeration state play an important role in the observation of the SPR.¹⁷ As an example, SPR is the responsible of the intensive colors of spherical Au NPs dispersions, which present strong absorption bands in the ultraviolet-visible (UV-Vis) spectrum (which are not present in the bulk), as shows Figure 1.2 B. Instead, non-spherical Au structures generally present more than one plasmonic resonance due to the different electron dipolar oscillations in different directions (Figure 1.2 C). Moreover, the agglomeration of particles produces a red-shift of the resonance peak to longer wavelengths induced by the dipole coupling between the plasmons of

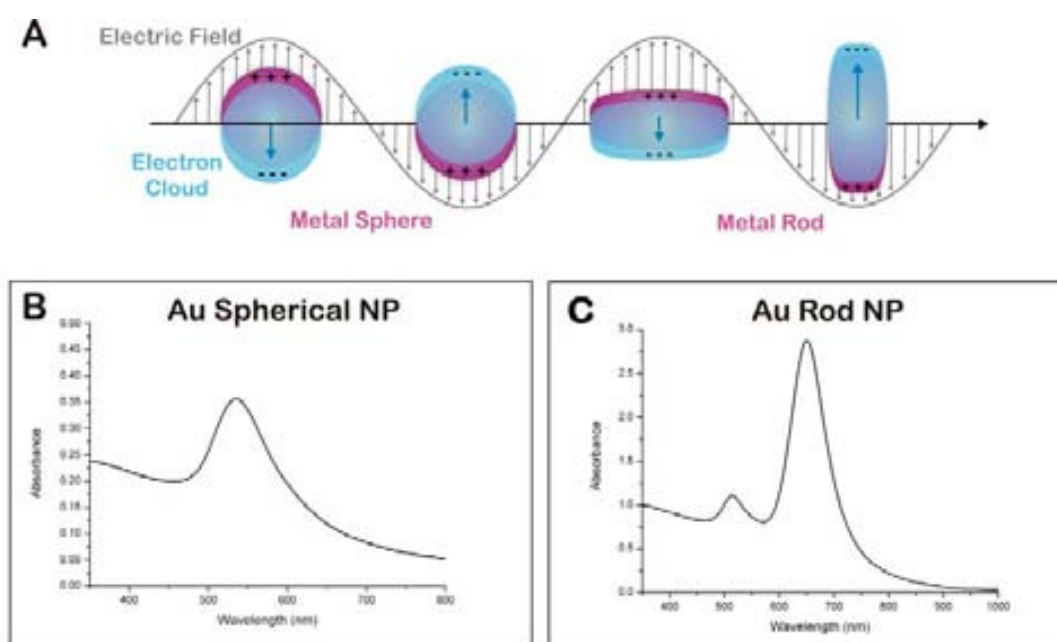


Figure 1.2: Scheme illustrating the excitation of the dipole surface Plasmon oscillations. B) and C) Characteristic UV-Vis spectra corresponding to spherical and rod shaped Au NPs, respectively. The spherical Au NP only display one plasmonic band (at 535 nm for this sample), while shape Au NPs exhibit two Plasmon bands, transverse and longitudinal (at 514 and 650 nm in this particular sample).

neighboring particles, fact that allow the Au NPs to be used as a sensor.

Another appearing optical property worthy to mention is the fluorescence emission in semiconductor quantum dots (QDs) (e.g. CdSe or PbS).¹⁸ When these particles are photo-excited, electron-hole pairs are generated and upon their recombination fluorescence light is emitted. This emission fluorescence can be very precisely chosen through variation of the size (an effect called quantum confinement). In this way, as the size of the nanocrystals (NCs) increase, the energy gap also increases and the more red-shifted is their wavelength fluorescence, thus yielding a tunability of colors from UV to infrared (IR).^{19,20}

1.3.1 Colloidal Stability of Nanoparticles

NPs can be synthesized either in aqueous or in organic solvents, and there are two possible mechanisms to provide them colloidal stability: electrostatic and steric stabilization. Colloid stability requires repulsive forces between colliding particles, for this reason electrical charges or ligand shells are used to screen the attraction.

In the case of electrostatically stabilized aqueous solutions, there is a competition between the van der Waals (vdW) attractive forces between the metal cores and the electrostatic repulsive forces from the charged surfaces. Derjaguin and Landau²¹ and Verwey and Overbeek²² worked deeply in the study of the factors affecting the dispersions stability, generating the known DLVO theory. This theory suggests that the stability of a colloidal system is determined by the sum of the vdW attractive forces and electrical double layer repulsive forces that exist between particles as they approach each other due to the Brownian motion they are undergoing.

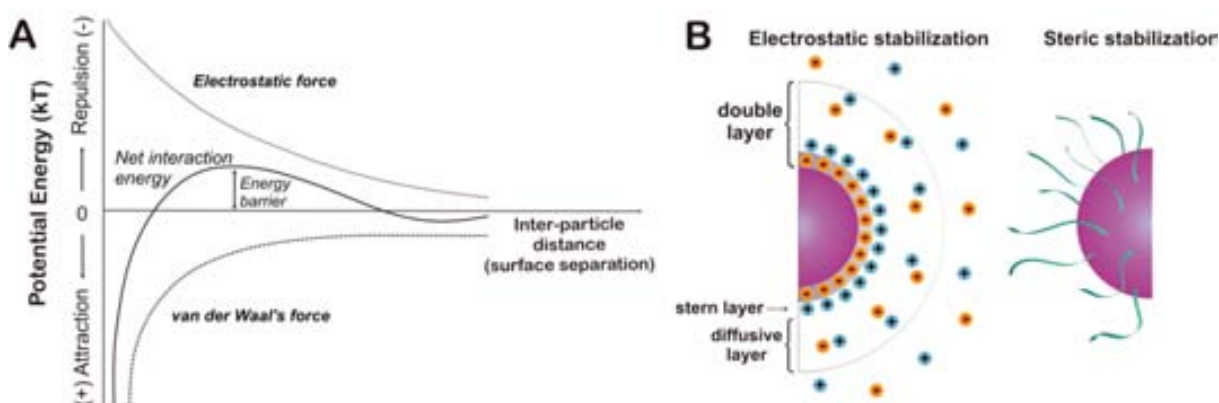


Figure 1.3: A) Schematic diagram showing the DLVO total interaction energy (solid black line), which is the sum of two components: the attractive vdW (dashed line) and the repulsive electric double layer (dotted line). B) Two main types of colloidal stabilization: electrostatic (left) and steric (right) stabilization.

As depicted in Figure 1.3 A, vdW forces will predominate at both large and small distances, while the double-layer repulsion may predominate at intermediate distances. Numerous examples of the application of the DLVO theory, i.e. to Au NPs, can be found in the literature.²³ In any colloidal-aqueous system, the surface charge on the particle with a counterion concentration change in the surrounding environment results in an electric double layer. The electrical double layer consist of two regions, the inner compact layer (Stern layer²⁴) and the diffusive layer (Figure 1.3 B, left). And the calculated total potential energy is known to have two minima when the size of the double layer is smaller than the particle radius. In the case of organic solutions, the total stability of the dispersion is again a competition of vdW attractive forces of the metal cores and, in this case, the steric repulsive forces from the ligand shells. The molecules adsorbed on the particle surface form a physical barrier that prevents the aggregation of the particles (Figure 1.3 B, right).

1.3.2 Synthetic Processes of Inorganic Nanoparticles

Size and shape control are crucial parameters that have to be consider during the synthesis of high quality NPs with specific properties. While the size of the NPs plays a significant role in sensory, biological systems, and catalysis, the shape control is also important due to their unique applications in sensors, photochemistry, optoelectronics and also fuel cell catalysis.^{9,25,26} Besides, there are other factors that must also be considered such as the monodispersity, avoid agglomeration and a well control of the surface functionalization (or state).

There are a wide variety of both physical and chemical synthetic methods for obtaining NPs,²⁷⁻²⁹ which can be divided in three main groups: i) mechanical methods (e.g. grinding or milling), ii) gas-phase methods (e.g. chemical vapor deposition or laser ablation deposition) and iii) liquid- phase synthesis (e.g. hydrothermal synthesis or sol-gel process). Mechanical breakdown methods present important technical advantages allowing the obtention of large quantities of product with reduced costs. However, they often are limited by agglomeration and contamination problems, and are not suitable for obtaining very small particles (<50 nm). Gas-phase methods are normally used in continuous systems and are based on homogeneous nucleation of a supersaturated vapor and subsequent particle grow by collision and condensation. These processes form crystalline NPs with “naked” surface and also result into agglomeration. Finally, in the liquid-phase methods, the size and the agglomeration are effectively controlled due to the functionalization of the NPs surface with organic molecules, also known as surfactants. In some cases, these molecules are used as shape control agents due to their selected binding to some crystalline faces of the NPs, favoring the growth in specific

directions. Thus, liquid-phase methods are the most frequently used for the synthesis of NPs due to the wide variety of different sizes, shapes and surface functionalities that can be obtained.^{9,30}

In the liquid-phase methods can be found different synthetic approaches such as chemical reduction of metal salts or thermal decomposition of organometallic complexes. Chapter 2 of this thesis shows various syntheses of transition metal NPs via these two pathways. In the case of metal ion reduction, many reductants such as sodium citrate, polyols, or H₂, have been used. In the organic phase, the reduction has to be performed by organic soluble reducing agents such as lithium superhydride. In particular, organic phase synthetic methods are one of the most used because present many advantages such as the high crystallinity and monodispersity of the obtained NPs.³¹ Many metallic particles, in particular those of Pt group metals, have been synthesized by the method known as polyol process, in which the reduction is performed into high-boiling point alcohols. Reactions by thermal decomposition of organometallic compounds were performed in hot surfactant solutions.

Regarding the mechanism, the general approach for producing uniform colloidal NCs in solution involves two important processes consisting on an initial very fast and homogeneous nucleation phase followed by a slow growth phase of the previously formed nuclei, as worked out by La Mer and Dinegar.³² Figure 1.4 shows the general kinetics for this mechanism, where it can be distinguished three stages. In **stage I**, the concentration of monomer constantly increases with time. Even under saturated conditions, the precipitation does not occur because the energy barrier for the spontaneous nucleation is very high. In **stage II** (when nucleation occurs), the degree of supersaturation is high enough to overcome the energy barrier of nucleation, thus forming stable nuclei. In **stage III**, the nucleation is effectively stopped due

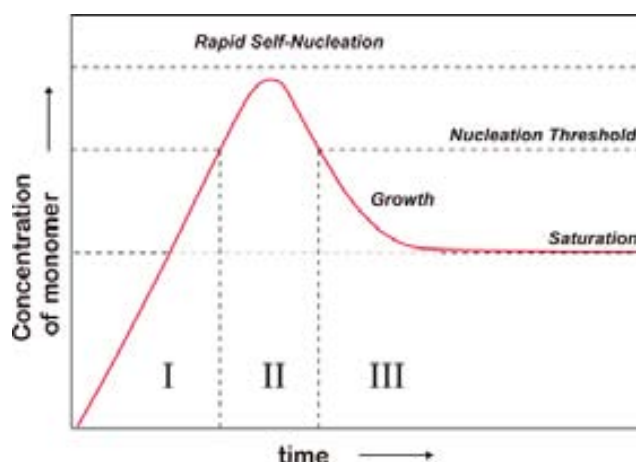


Figure 1.4: General kinetics of colloidal nucleation and growth mechanism of particles described by LaMer and Dinegar.

to the depletion of monomer concentration, and the particles keep growing as long as the solution is supersaturated. To simplify, nucleation takes place because the supersaturated solution is thermodynamically unstable and generates extremely small size nuclei particles. And after the nuclei are formed from the solution, they grow via deposition of the soluble species onto the solid surface (molecular addition).

1.4 Magnetic Characteristics of Nanoparticles

1.4.1 Magnetic Properties of Solids

If a magnetic material is placed in a magnetic field of strength H , the individual atomic moments in the material contribute to its overall response, the magnetic induction:

$$B = \mu_0(H + M) \qquad \text{Equation 1.1}$$

where μ_0 is the permeability of the free space, and the magnetization $M=mV$ is the magnetic moment per unit volume, where m is the magnetic moment on a volume V , of the material. All materials are magnetic to some extent, with their response depending on their atomic structure and temperature.

Thus, materials can be classified depending on their response towards an external field. Most materials display little magnetism even if it is only in the presence of an applied field; these are classified either as paramagnets or diamagnets. However, some materials exhibit ordered magnetic states and are magnetic even without an applied field; these are classified as ferromagnets, ferrimagnets and antiferromagnets. In the latest, the prefix refers to the nature of the coupling interaction between the electrons within the material.³³

They may be conveniently classified in term of their volumetric magnetic susceptibility (χ)

$$M = \chi H = \frac{C}{T} H \qquad \text{Equation 1.2}$$

where M describes the magnetization induced in a material by a magnetic field H , C is a material - specific Curie constant and T is the temperature. In SI units χ is dimensionless and both M and H are expressed in Am^{-1} .

Diamagnetism is a property of all matter. A **diamagnetic (DM)** material do not have

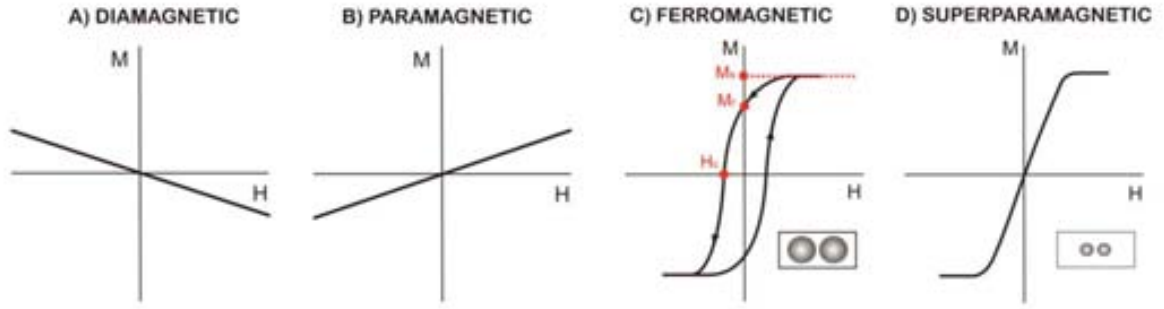


Figure 1.5: Magnetic responses associated with different classes of magnetic materials. M-H curves are shown for A) diamagnetic, B) paramagnetic, C) superparamagnetic and D) ferromagnetic materials.

unpaired electrons in the orbital shells (magnetic dipoles) resulting in no net magnetic moment in the absence of an external field. The magnetization responds in the opposite direction to the external field, thus the susceptibility is always negative (Figure 1.5 A). Instead, in **paramagnetic (PM)** materials some atoms or ions show a permanent magnetic moment even in the absence of an applied magnetic field. These dipoles are not interacting and randomly oriented in the absence of magnetic field, due to the thermal agitation, resulting in an overall zero net magnetic moment. The magnetization of a paramagnet responds in the direction of the applied field, therefore the susceptibility is always positive (Figure 1.5 B).

In **ferromagnetic (FM)** materials, the magnetic order observed is due to the interaction between spins of neighboring atoms in the lattice, which for a pair of atoms, i and j , takes the form,

$$\hat{H}_{ex}^{ij} = -J_{ij}\mu_i \cdot \mu_j \quad \text{Equation 1.3}$$

where J_{ij} is the exchange coupling constant for that specific pair of ions and μ is the spin moment. And the total exchange energy is the sum of overall magnetic ions, i.e.,

$$\hat{H}_{ex}^{ij} = -\sum_{i,j} J_{ij} \mu_i \cdot \mu_j \quad \text{Equation 1.4}$$

A positive J_{ij} favors a parallel alignment of the moments, while a negative J_{ij} results in an antiparallel ordering in the moments. This is known as FM and **antiferromagnetic (AFM)** order, respectively. There is a third possibility, the **ferrimagnetic** order, which is similar to the AFM but where the magnitude of the spins differs, which results into an overall effective

net magnetic moment. In the case of FM order, the exchange interaction favors parallel alignment of spins forming regions called domains. Usually the domains are randomly oriented and the material is demagnetized, and when an external magnetic field is applied, the magnetic domains align up along the field magnetizing the material. All materials present a maximum temperature, called the Curie temperature (T_c), where the FM behavior disappears. The thermal energy becomes large enough to destroy the magnetic order within the material (Equation 1.5) and, thus, becomes paramagnetic (Figure 1.6).

$$\hat{H}_{ex}^{ij} = - \sum_{i,j} J_{ij} \mu_i \quad \text{Equation 1.5}$$

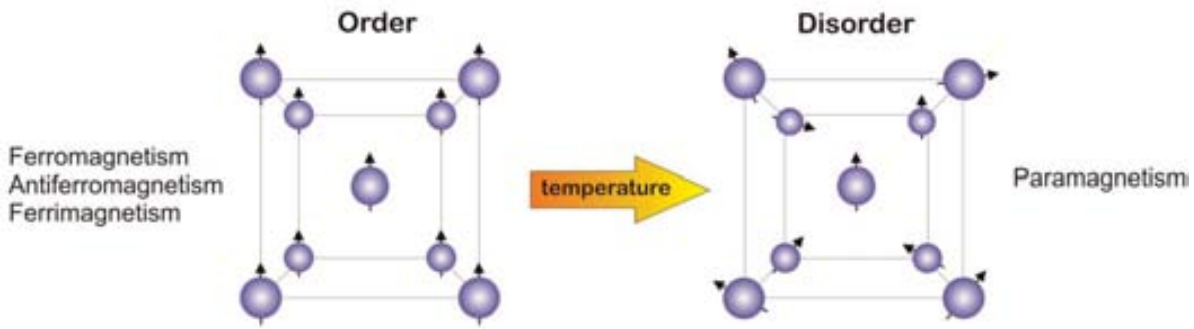


Figure 1.6: Evolution of the magnetic behavior with the increase of the temperature.

The susceptibility in ordered materials depends not just on temperature, but also on H , which gives rise to the characteristic sigmoidal shape of the $M-H$ curve, with M approaching a saturation value for large values of H (M_G). Furthermore, in FM and ferrimagnetic materials one often see hysteresis, which is an irreversibility in the magnetization process that is related to the pinning of the magnetic domain walls at impurities or grain boundaries within the material, as well as to intrinsic effects such as the magnetic anisotropy of the crystalline lattice. This gives rise to the open $M-H$ curve called **hysteresis loop** (Figure 1.5 C). The shapes of these loops are determined, in part, by particles size: in large particles, there is a multi-domain ground state which leads to a narrow hysteresis loop since it takes relatively little field energy to make the domain walls move; while in smaller particles, there is a single domain ground state which leads to a broad hysteresis loop. Furthermore, at even smaller sizes, (tens of nanometers or less, depending on the material) one can see **superparamagnetism**, where the magnetic moment of the particle as a whole is free to fluctuate in response to the thermal energy, while the individual atomic moments maintain their ordered state relative to each other.

This leads to the antihysteretic, but still sigmoidal, $M-H$ curve shown in Figure 1.5 D.

1.4.2 Magnetic Nanoparticles

A magnetic NP has a net moment that is the sum of the spins of all its constituent atoms. These atoms are organized within a crystalline structure that determines their magnetic properties. Magnetic NPs show a wide variety of unusual magnetic properties compared to the respective bulk materials, which arise from finite size and surface effects. They exhibit unique phenomena such as superparamagnetism, high field irreversibility and high saturation field. In addition, exchange anisotropy can be caused by a thin layer of AFM oxide formed around the FM core of the NPs as a consequence of exposure to air.³⁴ All these phenomena are attributed to size and surface effects that dominate the behavior of magnetic particles in the nanosized range.³⁵ Co NPs are a typical example where it can be observed the previously described phenomena.

Inside a material, the spins form domains where the individual moments of the atoms are aligned with each other, and their formation is highly related with the size of the particle. In one hand, in big particles the energy considerations suits the formation of domains. On the other hand, when the size of the particle decreases the number of domains also decreases and it becomes a single domain. If the particle size is reduced, there is a critical volume below which it costs more energy to create a domain wall than to support the external magnetostatic energy of the single-domain state. This critical diameter, which typically lies in the range of a few tens of nanometers, depends on the type of material and it is influenced by the contribution from various anisotropic energy terms.

1.4.3 Magnetic Anisotropy

The different directions along which magnetostatic energies have minimum/maximum values are called directions (or axes) of easy/hard magnetization, respectively. Magnetic anisotropy is the dependence of the internal energy of a system on the direction of the spontaneous magnetization. The energy of an atomic moment in the crystalline structure depends on the orientation of this magnetic moment with respect to the crystallographic axis. The exchange energy (Equation 1.3) is determined by the relative orientation of the moments with respect to each other, not by the absolute orientation with respect to the crystal axes. Thus, the magnetic anisotropy energy contains contributions from several other sources. The dominant contribution comes from physical **anisotropy** (K) such as crystal lattice, shape, stress and surface anisotropy, that favors certain M orientations.

$$K = K_{crystal} + K_{shape} + K_{stress} + K_{surface} \quad \text{Equation 1.6}$$

Magnetocrystalline anisotropy is due to the anisotropy of the crystal lattice, and is the energy necessary to deflect the magnetic moment from the easy to the hard direction in a single crystal, Shape anisotropy is due to demagnetization (magnetostatic) effects in each direction of the NP shape, strain anisotropy is due to magnetostriction, if the particle is subjected to stress, and surface anisotropy is due to the reduced symmetry of the surface sites. The resulting associated energy is, in the simplest case, written as,

$$E_K(\theta) = KV \sin^2\theta \quad \text{Equation 1.7}$$

where K is the effective anisotropy energy constant (containing contribution of all the sources mentioned above) and is typically on the order of 10^3 - 10^5 J/m³ in magnetic NPs, where V is the particle volume, and θ is the angle between the magnetization and easy axis. This direct proportionality between ΔE and V is the reason why superparamagnetism (the thermally activated flipping of the net moment direction) becomes important for small particles, since for them ΔE is comparable to $K_B T$ at room temperature (RT) (see next section).

1.4.4 Superparamagnetism

In the most common cases, where the magnetic anisotropy is unidirectional (even in spherical NPs defects favours a single easy magnetization axis), energy contains two minima states ($\theta=0$ and $\theta=180$) with opposite magnetization (Figure 1.7), separated by an energy barrier (ΔE). The relaxation time, τ , between the two minima is given by the Arrhenius law:

$$\tau = \tau_0 \exp\left(\frac{\Delta E}{K_B T}\right) \quad \text{Equation 1.8}$$

where ΔE is the energy barrier to the moment reversal, K_B is the Boltzmann's constant, T is the temperature, $K_B T$ is the thermal energy and τ_0 is the moment relaxation time, that may be considered as an "attempt time", typically in the range of 10^{-11} - 10^{-9} s for non interacting superparamagnetic (SPM) NPs.

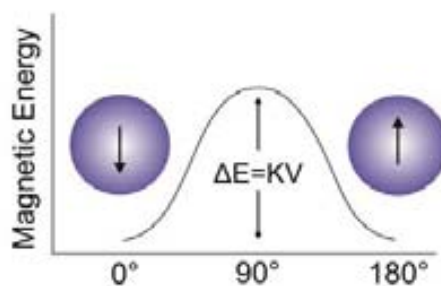


Figure 1.7: Scheme of energy barrier separating states with opposite magnetization due to anisotropy.

It is important to recognize that observations on superparamagnetism are implicitly dependent not just on the temperature, but also on the measuring time (τ_m) of the experimental technique being used. If $\tau < \tau_m$ the flipping is fast relative to the experimental time window and the particles appear to be like a paramagnetic system (SPM state). On the contrary, if $\tau > \tau_m$ the relaxation appears so slow that thermodynamical non-equilibrium properties are observed (blocked state). The temperature at which $\tau = \tau_m$ (where the flipping is slow and quasi-static properties are observed) is denoted as the (SPM) blocking temperature (T_B), and is defined as the mid-point between these two states. T_B increases with increasing NP size and for a given size increases when decreasing measuring time. The highest possible value of T_B is represented by the Curie (or Néel) temperature, T_c (or T_N), at which the magnetic moments within each particle decouples.

1.4.5 Exchange Bias: FM-AFM Coupled Systems

The physical origin of exchange bias, or exchange anisotropy, is rather generally accepted to be due to the exchange coupling between the AFM and FM components of the interface. The magnetic exchange can provide an extra source of anisotropy, leading to increased magnetization stability. In materials composed of FM–AFM interfaces, the main tell-tale indication of the existence of exchange bias is a shift in the magnetization curve (exchange field, H_{ex}) if performed after cooling the sample below the AFM ordering temperature (T_N) under an applied field. Accompanying the loop shift are other related properties, the most common in nanostructures is probably an increase of the coercivity (H_c).

1.4.6 Inter-particle Interactions: Dipolar Interactions

Magnetic metal particles experience strong vdW attractions, which combined with their

magnetic dipole interactions, make the stabilization of these systems very challenging. Highly ordered structures of NCs such as two or three dimensional assemblies are also interesting because these NCs can act as building blocks in future devices for potential applications such as data storage, permanent magnetic composites and biomedicine.³⁶

The SPM behavior depends on inter-particle interactions. Additionally, at low temperatures, the interactions between NPs become more important and can have strong influence in their dynamics. The most important type of magnetic interactions in NPs is the **dipole-dipole interaction**, which refers to the direct interaction between magnetic moments of neighboring particles. Such interactions normally leads to increased disorder and spin-glass like behavior, however ordering interactions are also possible. **Dipolar ferromagnetism** in the absence of an external applied magnetic field was first predicted by Luttinger and Tisza,³⁷ who found a FM ground state for a face-centered-cubic (fcc) lattice of point dipoles. Its importance falls on the presence of two main features: long-range character and rather large value of the typical magnetic moment of an individual NP (10^3 - 10^4 Bohr's magnetons, μ_B). Dipolar interactions are present in all magnetic spin systems, but in large magnetic materials are usually negligible compared to exchange interactions. However, decreasing the single particle size usually reduces the anisotropy energy or modifies the easy magnetization axes increasing the influence of dipolar interactions. Dipole interaction energy for a particle is the order of

$$E_d \approx \frac{\mu_0 \mu^2}{4\pi d^3} \quad \text{Equation 1.9}$$

where μ is the average magnetic moment, d the average distance between the particles, and μ_0 is the permeability of free space.

In fact, dipolar interactions play an important role in determining cooperative phenomena at the molecular scale and in the final properties of the material.² Dipoles display a fondness for arranging themselves into highly inhomogeneous structures. This is a consequence of the very strong anisotropy of the dipole-dipole interaction, which couples the orientations of the dipole moments with that of the inter-particle vector, what is different from the isotropic vdW interaction. Dipolar interactions are anisotropic and can favor AFM and FM alignments of the magnetic moments, depending on geometry. Furthermore, the dipolar interaction tends to be frustrated,³⁸ and NP systems with dipolar interactions are anticipated to easily demonstrate spin-glass properties due to the random distribution of particle easy axes and positions.³⁹

1.5 Self-Assembly Process

The central role of the SA in life is one of the most important reasons that lead to its study. SA can be defined by a spontaneous organization of components into patterns and structures without human intervention, and is common throughout nature and technology.¹ In addition, SA is one of the few practical strategies for making ensembles of nanostructures, and it therefore is an essential part of nanotechnology. The concept of SA is increasingly used in many disciplines with different nuances in order to break nature's code for SA.¹

Dispersed colloidal NPs self-assemble into complex structures when segregated from the solvent, either by evaporation or precipitation. Different micro and macroscopic structures like opals, fractals, mixed structures and other forms based in NPs have been observed⁴⁰ as a result of the balance between electrostatic forces, surface tension, entropy, topography, substrate affinity and, most importantly, the size, shape and concentration of the particles.⁴¹ The study of these systems is a key issue for applications and for fundamental investigations.

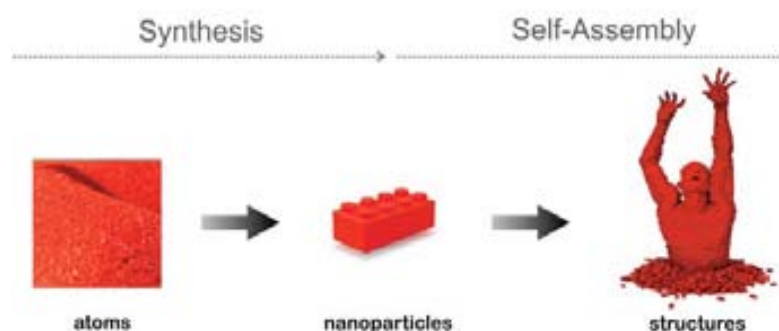


Figure 1.8: Scheme showing a comparison of how NPs can be used as the building blocks for assembling new structures in a similar manner to assembling “LEGO” blocks.⁴²

In the SA process, it is important to understand the various interactions between NPs, substrates and solvents, which lead to the patterns formed. There are several competing interactions/forces between particles that control the SA behavior, such as Brownian motion, electrostatic attraction and repulsion, vdW attraction, steric repulsion, and capillary force, among others. Since a common method for initiating aggregation of NPs is to evaporate their solvent, the drying kinetics, substrate roughness, solvent wetting/dewetting, hydrodynamic effects, and self-diffusion of the NPs on the substrate also play important role in SA process, leading to unusual non-equilibrium structures. Furthermore, the evaporation rate of the solvent affects particle/particle interaction since the relatively weak attraction between NPs, which are

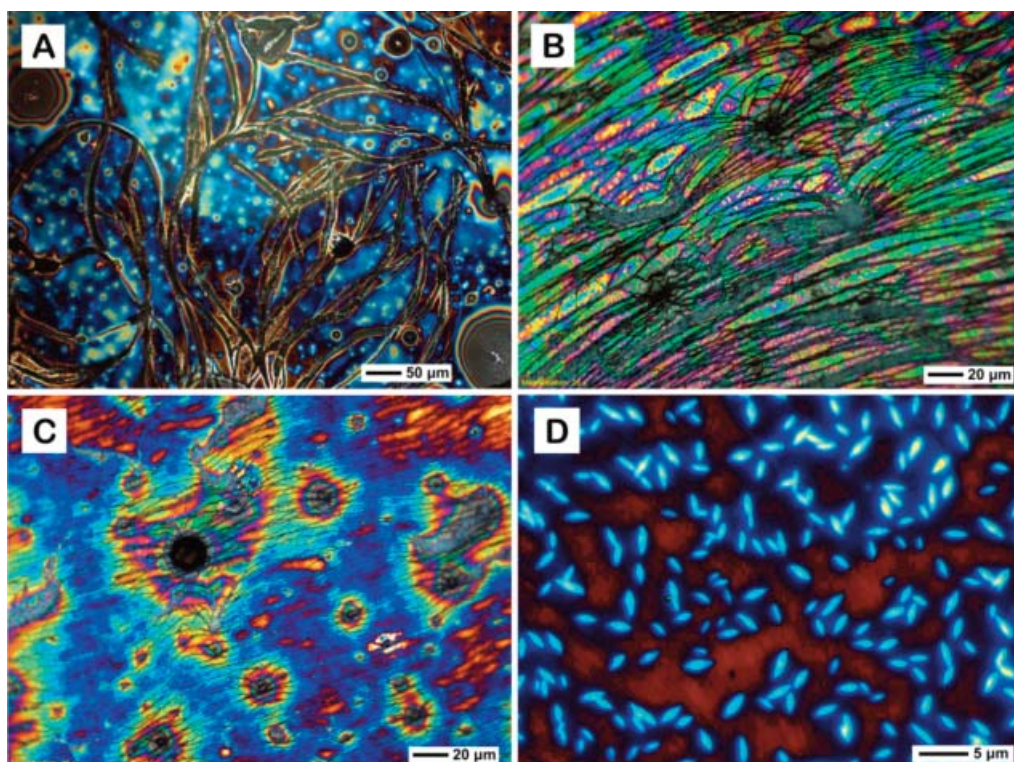


Figure 1.9: A-D) Optical microscope images of different Co NPs self-assembled structures formed by solvent evaporation.

efficiently screened in dilute solution, becomes noticeable as the solvent evaporates, initiating assembly of slowly evolving structures. The quality of assembly is also determined by other factors such as the solvent evaporation rate, the ionic strength, the surfactant concentration and the particle size and shape distributions. For the SA of anisotropic shaped NPs such as nanorod (NR), nanowire (NW), and nanodisk (ND), the situation becomes even more complex. For nanostructured materials built from magnetic NPs new effects such as proximity, long-range interactions, long-range order, domain walls, hysteresis and collective behavior, among others, are also involved in the SA process, and are subject of current investigation. In this context, magnetic dipolar interactions that are not screened or interfered by the medium are an interesting piece of puzzle to understand and control such processes.

Making sure that the components assemble themselves correctly is not an easy task, because the forces at work are so small. Self-assembling particles can get trapped into undesirable conformations, generating defects that are impossible to avoid. Another important factor that we have to take in account is that the most synthesized particles contain a surfactant layer, which maintain them separated some nanometers. This means that exchange interactions between NPs, even in the dense assemblies, is negligible and their mutual interactions are,

therefore, dominated by long-range dipole-dipole interactions. Thus, dipolar interactions play an important role in determining cooperative phenomena at the molecular scale and the final properties of the material made of magnetic NPs.⁴³

There is a specific case of SA of NCs, also considered as a growth mechanism, known as oriented attachment. Oriented attachment involves spontaneous self-organization of adjacent particles, sharing a common crystallographic orientation, followed by joining of these particles at a planar interface. Bonding between the particles reduces overall energy by removing surface energy associated with unsatisfied bonds.^{44,45}

1.6 References

1. Whitesides, G. M.; Grzybowski, B. "Self-Assembly at All Scales". *Science* **2002**, 295, 2418-2421.
2. Zeng, H.; Li, J.; Liu, J. P.; Wang, Z. L.; Sun, S. "Exchange-Coupled Nanocomposite Magnets by Nanoparticle Self-Assembly". *Nature* **2002**, 420, 395-398.
3. Li, Y.; Somorjai, G. A. "Nanoscale Advances in Catalysis and Energy Applications". *Nano Letters* **2010**, 10, 2289-2295.
4. Pankhurst, Q. A.; Connolly, J.; Jones, S. K.; Dobson, J. "Applications of Magnetic Nanoparticles in Biomedicine". *Journal of Physics D-Applied Physics* **2003**, 36, R167-R181.
5. Arbiol, J.; Estrade, S.; Prades, J. D.; Cirera, A.; Furtmayr, F.; Stark, C.; Laufer, A.; Stutzmann, M.; Eickhoff, M.; Gass, M. H.; Bleloch, A. L.; Peiro, F.; Morante, J. R. "Triple-Twin Domains in Mg Doped GaN Wurtzite Nanowires: Structural and Electronic Properties of This Zinc-Blende-Like Stacking". *Nanotechnology* **2009**, 20.
6. Sanchez, A.; Recillas, S.; Font, X.; Casals, E.; Gonzalez, E.; Puentes, V. "Ecotoxicity of, and Remediation with, Engineered Inorganic Nanoparticles in the Environment". *Trends in Analytical Chemistry* **2011**, 30, 507-516.
7. Gubin, S. P.; Koksharov, Y. A. "Preparation, Structure, and Properties of Magnetic Materials Based on Co-Containing Nanoparticles". *Inorganic Materials* **2002**, 38, 1085-1099.
8. Kessler, R. "Engineered Nanoparticles in Consumer Products Understanding a New Ingredient". *Environmental Health Perspectives* **2011**, 119, 121-125.

- 9.** Burda, C.; Chen, X.; Narayanan, R.; El-Sayed, M. A. "Chemistry and Properties of Nanocrystals of Different Shapes". *Chemical Reviews* **2005**, 105, 1025-1102.
- 10.** Rotello, V. *Nanoparticles: Building Blocks for Nanotechnology* 1st ed.; Springer, **2003**.
- 11.** Yin, Y.; Lu, Y.; Gates, B.; Xia, Y. "Template-Assisted Self-Assembly: A Practical Route to Complex Aggregates of Monodispersed Colloids with Well-Defined Sizes, Shapes, and Structures". *Journal of the American Chemical Society* **2001**, 123, 8718-8729.
- 12.** Corma, A.; Atienzar, P.; Garcia, H.; Chane-Ching, J.-Y. "Hierarchically Mesostructured Doped CeO₂ with Potential for Solar-Cell Use". *Nat Mater* **2004**, 3, 394-397.
- 13.** Murthy, V. S.; Cha, J. N.; Stucky, G. D.; Wong, M. S. "Charge-Driven Flocculation of Poly(L-Lysine)Gold Nanoparticle Assemblies Leading to Hollow Microspheres". *Journal of the American Chemical Society* **2004**, 126, 5292-5299.
- 14.** Wang, Z. L. "Structural Analysis of Self-Assembling Nanocrystal Superlattices". *Advanced Materials* **1998**, 10, 13-30.
- 15.** Pileni, M. P. "Nanocrystal Self-Assemblies: Fabrication and Collective Properties". *Journal of Physical Chemistry B* **2001**, 105, 3358-3371.
- 16.** Kelly, K. L.; Coronado, E.; Zhao, L. L.; Schatz, G. C. "The Optical Properties of Metal Nanoparticles: The Influence of Size, Shape, and Dielectric Environment". *Journal of Physical Chemistry B* **2003**, 107, 668-677.
- 17.** Mie, G. "Beiträge Zur Optik Trüber Medien, Speziell Kolloidaler Metallösungen". *Annalen der Physik* **1908**, 330, 377-445.
- 18.** Nie, S. M.; Emery, S. R. "Probing Single Molecules and Single Nanoparticles by Surface-Enhanced Raman Scattering". *Science* **1997**, 275, 1102-1106.
- 19.** Bruchez, M.; Moronne, M.; Gin, P.; Weiss, S.; Alivisatos, A. P. "Semiconductor Nanocrystals as Fluorescent Biological Labels". *Science* **1998**, 281, 2013-2016.
- 20.** Chan, W. C. W.; Nie, S. "Quantum Dot Bioconjugates for Ultrasensitive Nonisotopic Detection". *Science* **1998**, 281, 2016-2018.
- 21.** Derjaguin, B. V.; Landau, L. "Theory of the Stability of Strongly Charged Lyophobic Sols and of the Adhesion of Strongly Charged Particles in Solutions of Electrolytes". *Acta Phys. Chim. URSS* **1941**, 14, 633-662.

- 22.** Verwey, E. J. W.; Overbeek, J. T. G. *Theory of the Stability of Lyophobic Colloids*; Dover Publications, **1999**.
- 23.** Laaksonen, T.; Ahonen, P.; Johans, C.; Kontturi, K. "Stability and Electrostatics of Mercaptoundecanoic Acid-Capped Gold Nanoparticles with Varying Counterion Size". *Chemphyschem* **2006**, 7, 2143-2149.
- 24.** Stern, O. "The Theory of the Electrolytic Double Shift". *Zeitschrift Fur Elektrochemie Und Angewandte Physikalische Chemie* **1924**, 30, 508-516.
- 25.** Robinson, R. D.; Sadtler, B.; Demchenko, D. O.; Erdonmez, C. K.; Wang, L.-W.; Alivisatos, A. P. "Spontaneous Superlattice Formation in Nanorods through Partial Cation Exchange". *Science* **2007**, 317, 355-358.
- 26.** Senthil Kumar, P.; Pastoriza-Santos, I.; Rodriguez-Gonzalez, B.; Garcia de Abajo, F. J.; Liz-Marzan, L. M. "High-Yield Synthesis and Optical Response of Gold Nanostars". *Nanotechnology* **2008**, 19.
- 27.** Sun, S. H.; Murray, C. B. "Synthesis of Monodisperse Cobalt Nanocrystals and Their Assembly into Magnetic Superlattices (Invited)". *Journal of Applied Physics* **1999**, 85, 4325-4330.
- 28.** Peng, X. G.; Manna, L.; Yang, W. D.; Wickham, J.; Scher, E.; Kadavanich, A.; Alivisatos, A. P. "Shape Control of Cdse Nanocrystals". *Nature* **2000**, 404, 59-61.
- 29.** Jana, N. R.; Gearheart, L.; Murphy, C. J. "Seeding Growth for Size Control of 5-40 Nm Diameter Gold Nanoparticles". *Langmuir* **2001**, 17, 6782-6786.
- 30.** Cushing, B. L.; Kolesnichenko, V. L.; O'Connor, C. J. "Recent Advances in the Liquid-Phase Syntheses of Inorganic Nanoparticles". *Chemical Reviews* **2004**, 104, 3893-3946.
- 31.** Puntès, V. F.; Krishnan, K. M.; Alivisatos, A. P. "Colloidal Nanocrystal Shape and Size Control: The Case of Cobalt". *Science* **2001**, 291, 2115-2117.
- 32.** LaMer, V. K.; Dinegar, R. H. "Theory, Production and Mechanism of Formation of Monodispersed Hydrosols". *Journal of the American Chemical Society* **1950**, 72, 4847.
- 33.** Morrish, A. H. *The Physical Principles of Magnetism*; Wiley-IEEE Press: New York, **2001**.

- 34.** Tartaj, P.; Morales, M. D.; Veintemillas-Verdaguer, S.; Gonzalez-Carreno, T.; Serna, C. J. "The Preparation of Magnetic Nanoparticles for Applications in Biomedicine". *Journal of Physics D-Applied Physics* **2003**, 36, R182-R197.
- 35.** Batlle, X.; Labarta, A. "Finite-Size Effects in Fine Particles: Magnetic and Transport Properties". *Journal of Physics D-Applied Physics* **2002**, 35, R15-R42.
- 36.** Sun, S. "Recent Advances in Chemical Synthesis, Self-Assembly, and Applications of Fept Nanoparticles". *Advanced Materials* **2006**, 18, 393-403.
- 37.** Luttinger, J. M.; Tisza, L. "Theory of Dipole Interaction in Crystals". *Physical Review* **1946**, 70, 954-964.
- 38.** Chan, D. C. F.; Kirpotin, D. B.; Bunn, P. A. "Synthesis and Evaluation of Colloidal Magnetic Iron-Oxides for the Site-Specific Radiofrequency-Induced Hyperthermia of Cancer". *Journal of Magnetism and Magnetic Materials* **1993**, 122, 374-378.
- 39.** Poddar, P.; Telem-Shafir, T.; Fried, T.; Markovich, G. "Dipolar Interactions in Two- and Three-Dimensional Magnetic Nanoparticle Arrays". *Physical Review B* **2002**, 66, 060403.
- 40.** Murray, C. B.; Kagan, C. R.; Bawendi, M. G. "Synthesis and Characterization of Monodisperse Nanocrystals and Close-Packed Nanocrystal Assemblies". *Annual Review of Materials Science* **2000**, 30, 545-610.
- 41.** Puentes, V. F.; Bastus, N. G.; Pagonabarraga, I.; Iglesias, O.; Labarta, A.; Batlle, X. "Nucleation Phenomenon in Nanoparticle Self-Assemblies". *International Journal of Nanotechnology* **2005**, 2, 62-70.
- 42.** <http://brickartist.com/lego-art/red.html>. © Copyright: See Author in the Original Source of This Image
- 43.** Zeng, H.; Li, J.; Liu, J. P.; Wang, Z. L.; Sun, S. H. "Exchange-Coupled Nanocomposite Magnets by Nanoparticle Self-Assembly". *Nature* **2002**, 420, 395-398.
- 44.** Penn, R. L.; Banfield, J. F. "Imperfect Oriented Attachment: Dislocation Generation in Defect-Free Nanocrystals". *Science* **1998**, 281, 969-971.
- 45.** Penn, R. L.; Banfield, J. F. "Morphology Development and Crystal Growth in Nanocrystalline Aggregates under Hydrothermal Conditions: Insights from Titania". *Geochimica et Cosmochimica Acta* **1999**, 63, 1549-1557.

Chapter 2

Synthesis of Metallic and Bimetallic Nanoparticles

The combination of size- and shape-dependent physical properties, together with their easy fabrication and processing, makes NPs promising building blocks for materials with designed functions.^{1,2} The properties of the individual particles as well as their mutual interactions determine important features of the NPs systems. Since magnetic and optical properties are highly dependent on the size, shape, crystalline and surface state of the NPs, their controlled synthesis with a narrow size distribution and uniform shape remains an important issue. Various methods have been developed for the synthesis of colloidal NPs.³⁻⁶ In particular, the thermal decomposition of metal carbonyls is known to produce well-defined metallic NCs.⁷

In this chapter, we investigate different synthetic routes towards metallic NPs, presenting different characteristic properties for their later use in SA processes. Firstly, we start with the synthesis of different size Co NPs and the study of their size-dependent magnetic properties, which are directly related with the oxidation state and crystal structure, among others. For this reason, it is important to control the oxidation processes of Co NPs. We observe the formation of different NPs such as Co/CoO core/shell and CoO hollow NPs. In addition, we study the synthesis of Pt NPs, and the influence of Co in the formation of PtCo bimetallic particles. We also explore the formation of Pt-Au heterodimers by using PtCo NPs both as a reaction catalyst and starting material. Finally, we finish this chapter with the study of the formation of long rod-shaped Au NCs, also using Pt NPs as catalytic starting of the reaction.

2.1 Synthesis of Co Nanoparticles

Magnetic NPs have been the subject of extensive research because they have the potential to be utilized in several applications such as ultra-high density recording media,^{8,9} contrast agent in magnetic resonance imaging,¹⁰ drug delivery¹¹ and as single electron transistors.^{8,9}

Co is a well-known FM material which is commonly used as an alloying element in permanent magnets.¹² It can be found in two forms: hexagonal close-packed (hcp) and face-centered cubic (fcc). The hcp phase is the bulk stable phase at RT, whereas fcc is stable at temperatures above 450 °C.¹³ At the nanoscale regime, Co particles present a wide range of interesting size-dependent structural, electrical, magnetic, and catalytic properties.¹⁴ Their net moment that is sum of the spin of all atoms, displaying quantum size effects, superparamagnetism, large magnetic anisotropies, and a maximum coercivity.¹⁵ In particular, because of their large surface area, Co NPs show high chemical reactivity, which makes them suitable for catalysis of intramolecular reactions.¹⁶ When the particle size is reduced, there is a critical volume below which it costs more energy to create a domain wall than to support the external magnetostatic energy of the single-domain state. This critical diameter typically, which lies in the range of a few tens of nanometers, depends on the material and it is influenced by the contribution from various anisotropic energy terms. Moreover, at this scale, a new metastable phase of cobalt called epsilon (ϵ -Co) can also be formed.^{4,13} This new phase is a primitive cubic phase (complex β -Mn phase) with 20 atoms in the elemental cell, and present properties in between the hcp and fcc phases. Gubin *et al.* described in detail different methods for the synthesis and magnetic properties of the different structures of Co particles.¹⁷

Liquid-phase synthetic routes are the most successful in the preparation of macroscopic amount of monodisperse Co NPs. Examples of liquid-phase processes are metal salt reduction,^{18,19} reverse micelles²⁰ and thermal decomposition of organometallic precursor⁷ (see also section 1.3.2). Among these routes, the organometallic route in the presence of tightly binded ligands are the more extended in the preparation of monodispersed ϵ -Co NPs. The rapid injection of organometallic reagents in a hot coordinating solvent produces temporally discrete homogeneous nucleation. The life time of the monomers in solution is short, and rapidly many small metal clusters form simultaneously. The surfactants (coordinating ligands) present in solution allows controlling the size and the shape of the growing particles by coating them with a close-packed ML. Also, this surfactant layer around the NPs prevents their agglomeration, providing steric hindrance, and protects the NPs against oxidation.

In this section, a general synthesis methodology to prepare different sized ϵ -Co NPs in organic solvent will be presented. This method was developed by Puentes *et.al.* and is based on

2.1 Synthesis of Co Nanoparticles

the thermal decomposition of dicobalt carbonyl in presence of oleic acid and trioctylphosphine oxide as surfactants.⁷ A detailed characterization of the particles will be also showed.

2.1.1 Experimental

For instrumentation details see Appendix A.1

2.1.1.1 Chemicals

Dicobalt carbonyl ($\text{Co}_2(\text{CO})_8$, moistened with 5-10 % hexane), trioctylphosphine oxide (TOPO, 99 %), oleic acid (OA, 99 %) and 1,2-dichlorobenzene anhydrous (DCB, 99 %), were purchased from Sigma-Aldrich and used as received without further purification.

2.1.1.2 Synthesis of ϵ -Co Nanoparticles

Synthesis of spherical ϵ -Co NPs was performed under Ar atmosphere and at high temperature. It involves the thermal decomposition of $\text{Co}_2(\text{CO})_8$ in a mixture of hot organic solvent and surfactants (OA+TOPO).^{7,21} A scheme of the synthesis set-up is shown in the Figure 2.1. A concentrate solution of $\text{Co}_2(\text{CO})_8$ (0.45-0.65 g in 2-3 mL of DCB anhydrous) was rapidly injected in a refluxing DCB anhydrous solution of 15 mL (bp = 181 °C).

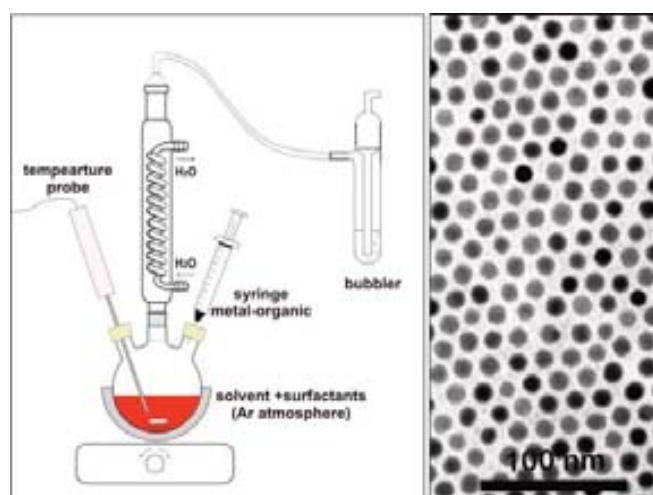


Figure 2.1: General scheme of the synthesis set-up (left) and TEM image of ~ 12 nm Co NPs (right).

The decomposition and nucleation occurs instantaneously upon injection. The lifetime of atoms in solution is short leading to the simultaneous formation of small metal clusters (Figure 2.2).

The surfactant mixture of OA and TOPO is present in the hot bath at concentrations of about 1%. Control of the bath temperature and the surfactant composition modifies the strength of the metallic particle-organic molecule bonding. Thus, by controlling the precursor/surfactant ratio, the reaction temperature and injection time, the size of the spherical particles could be controlled and varied between 6 and 17 nm. This method produced macroscopic quantities of ϵ -Co single and fairly monodisperse crystals.

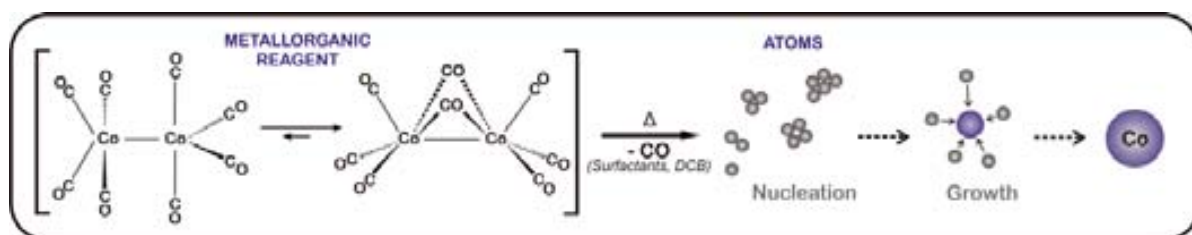


Figure 2.2: Schematic illustration of the synthesis of Co NPs by thermal decomposition.

2.1.2 Results and Discussion

2.1.2.1 Structural Characterization

According to a method previously reported,⁷ Co NPs with different mean sizes between 6 and 16 nm were obtained. The NPs has been characterized by transmission electron microscope (TEM), and the size distribution has been determined by image processing of several TEM images (>500 particles) using the Particle Size Analyzer (PSA) macro for ImageJ,²² confirming nearly symmetric distributions. Figure 2.3 shows TEM images of different size Co NPs. It can be observed that by systematically increasing the particle size, TEM images show an abrupt transition from self-assembled MLs to randomly oriented linear aggregates and branched chains or networks.⁷

High resolution TEM (HRTEM) observations of 15 nm Co NPs confirmed their crystallinity, and also showed the lattice fringes without observable defects. A typical HRTEM micrograph of a single Co NP is displayed in Figure 2.4 B (selected area), showing that it is a single crystal. The particle exhibits its $\langle 221 \rangle$ (1.99 Å) projection with no defects in the structure. The monocrystallinity of the NPs can also be certified by the dark field image (Figure 2.4 A), where again no defects can be observed.

Figure 2.5 show elemental composition maps of 15 nm Co NPs corresponding to the bright field images A and B, which are composed by three elements: Co, O and C. In the first analysis

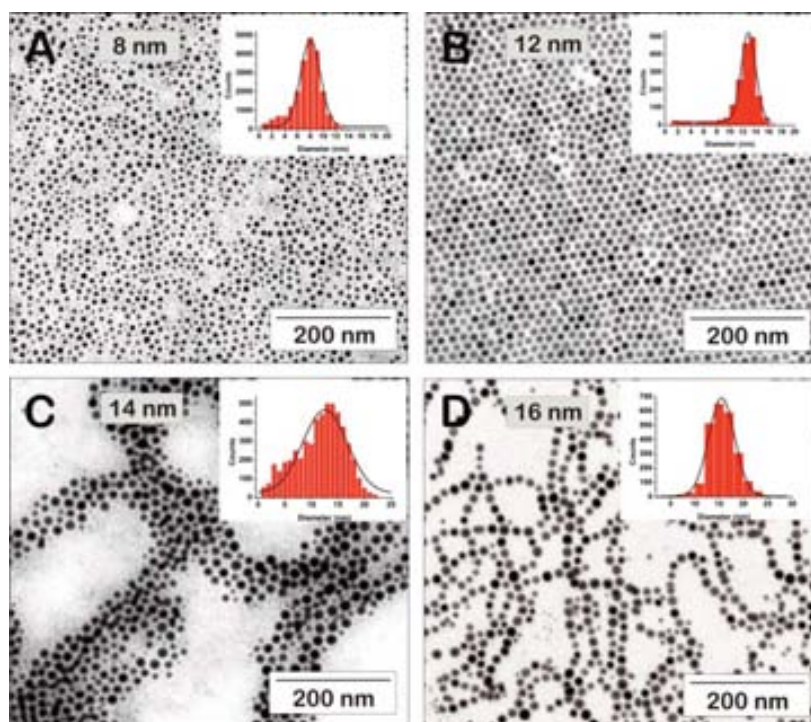


Figure 2.3: TEM images of Co NPs of different sizes with the corresponding size distribution: A) ~ 8 nm, B) ~12 nm, C) ~14 nm and D) ~ 16 nm. Each image is accompanied by its statistical size analysis.

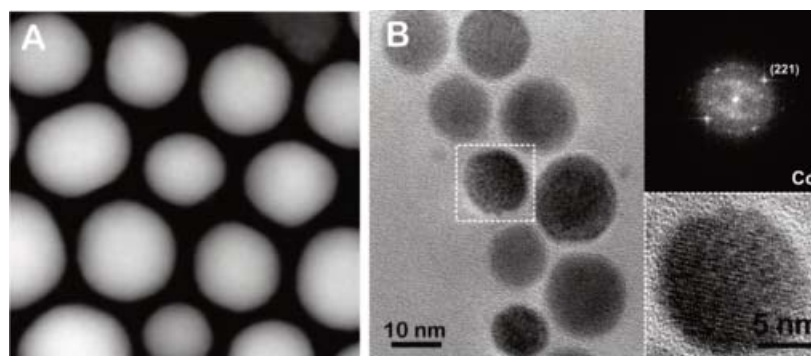


Figure 2.4: HAADF or Z-contrast image (A) and HRTEM image with the corresponding FFT power spectra (B) of ϵ -Co NPs, which shows the $\langle 221 \rangle$ projection (1.99 Å).

(A), some superficial oxidation can be observed. Despite the existence of the protecting organic layer at the surface of the NPs, a small degree of oxidation attributed to the surface can not be avoided when samples are exposed to air. Besides, in the second analysis (B), after a prolonged beam exposure of the sample (300 kV), it can be appreciated some changes in the particles.

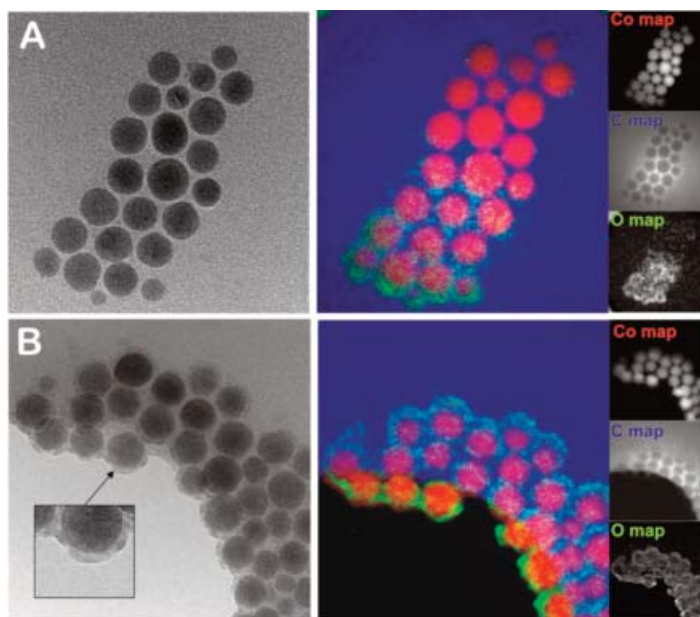


Figure 2.5: A,B) TEM images of two different regions of 15 nm Co NPs with their corresponding elemental color map, composed by Co (red), O (green) and C (insets).

The surfactant capping layer (OA) suffers some modification, similar to crystallization (Figure 2.5 B, inset). The color map shows more oxidation of the particles as well some outward diffusion of Co, as can be appreciated in the correspondent elemental map for Co. This indicates that we have to be careful with the interpretation of these measurements because the sample can be modified by the beam in some cases.

The x-ray powder diffraction (XRD) measurement of 12 nm ϵ -Co particles (Figure 2.6 A) gives us information about the crystalline phase of the material. Analyzing the Co samples, the

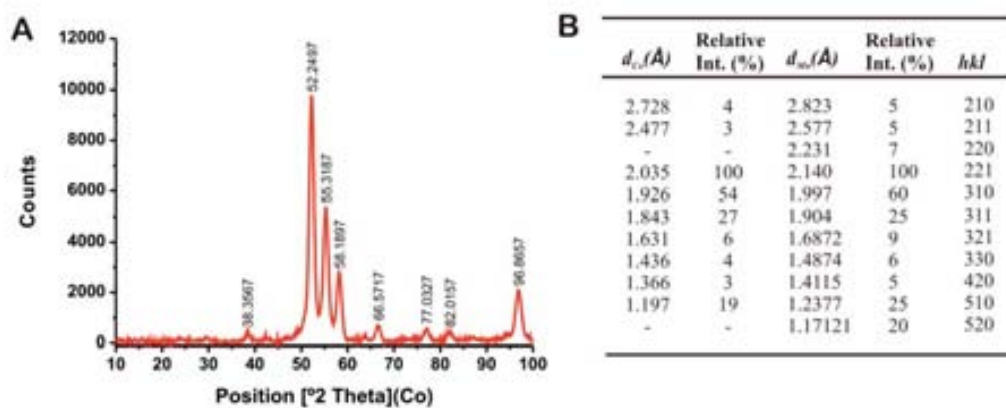


Figure 2.6: A) XRD pattern for the ϵ -Co NPs of 12 nm. B) Comparison of the crystalline structure of the obtained ϵ -Co NPs and the β -Mn structure.

2.1 Synthesis of Co Nanoparticles

most intensive 2θ Bragg peaks can be observed at 52.25° , 55.32° , 58.12° and 96.87° , which correspond to the (221), (310), (311) and (510) diffractions of the ϵ -Co phase, respectively. Figure 2.6 B shows a comparison of the d spacing and relative intensities of diffractions observed in our sample and those in a structure with β -Mn symmetry.⁴ No peaks corresponding to oxide phases of Co are observed.

2.1.2.2 Size-Dependent Properties

As previously mentioned, magnetic particles below a critical diameter can be considered as a single domain, and the particle behaves as a single magnetic dipole. The magnetic dipole of the particles can be free to rotate (superparamagnetism), when the thermal energy is enough

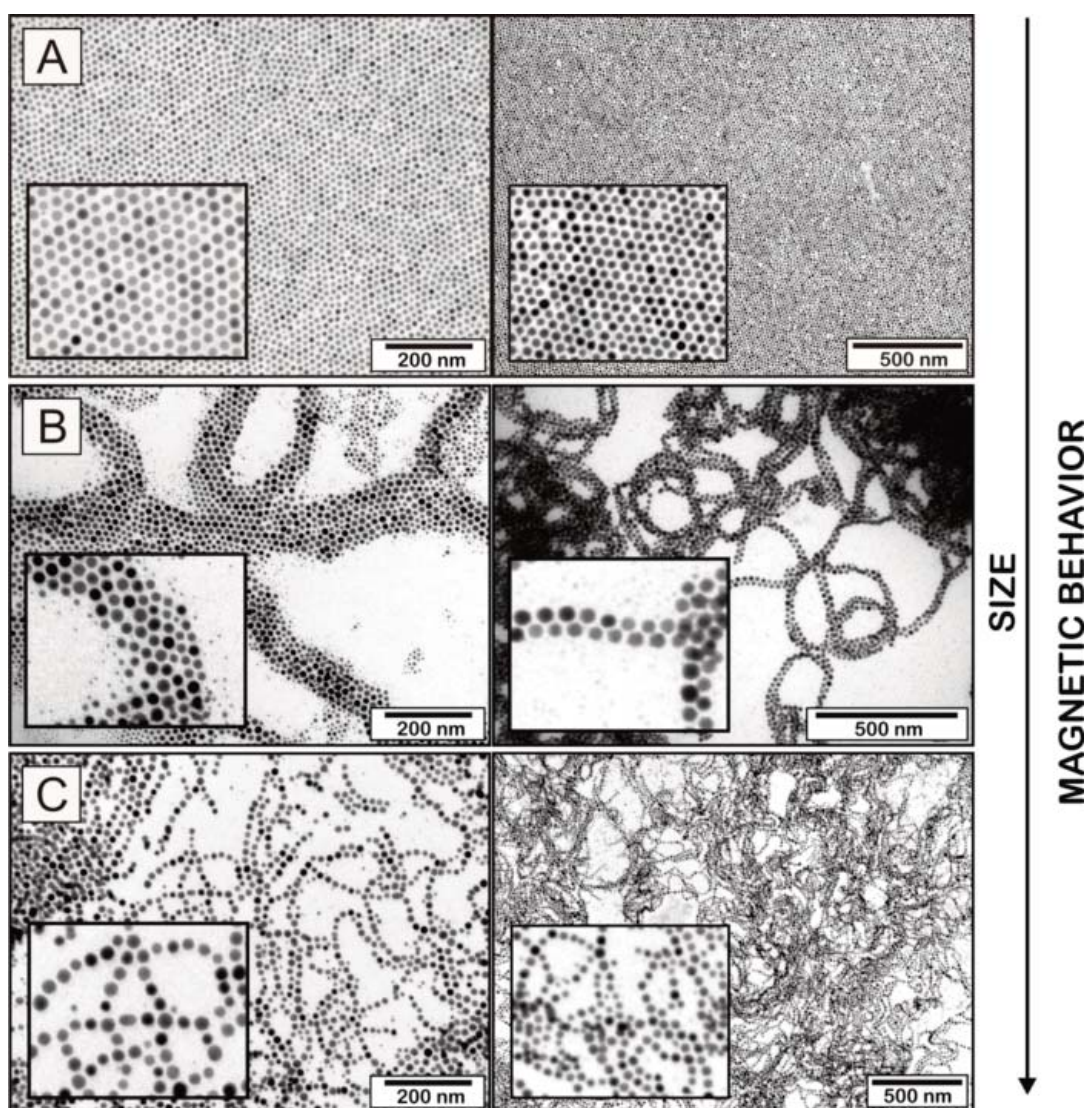


Figure 2.7: TEM images of Co NPs of different sizes showing the strong size-dependence of the magnetic properties: A) ~ 12 nm, B) ~ 14 nm and C) ~ 16 nm..

to exceed the energy barrier separating states with different magnetization direction due to anisotropy, or blocked in the anisotropy direction (ferromagnetism). In the case of Co NPs, it can be observed, by systematically increasing the particle size, an abrupt transition from MLs to linear and branched structures, witnessing the rise of stability and intensity of the NPs magnetic moment with diameter (Figure 2.7).

2.1.2.3 Magnetic Characterization

In order to study the magnetic properties of individual NPs, magnetic measurements were carried out on samples consisting in Co NPs embedded in air-tight paraffin wax (melting point, mp = 60-65 °C). Susceptibility curves (M vs T at low fields) for 6 nm Co NPs, obtained after a zero field cool (ZFC)-field cool (FC) process in a magnetic field of 100 Oe, are shown in the Figure 2.8 (A). A maximum in the ZFC branch is observed around the blocking temperature (T_B) \approx 130 K. The broadness of the peak indicates that the particles are present in a wide size distribution function. A second peak is observed in both ZFC and FC branches at $T \approx$ 45 K. We tentatively assign this peak to the presence of some Co oxide at the NP surface, which has the Néel transition close to this temperature. The magnetic susceptibility is measured in response to an alternating magnetic field (AC susceptibility) (Figure 2.8 B) do not show any frequency dependence of the position of this peak (marked by a red arrow), indicating that it corresponds to a thermodynamic transition. The paramagnetic upturn observed in the low temperature regime may be due to the existence of very small Co NPs with a very low T_B or to the presence of paramagnetic atoms coordinated to the OA or TOPO. Besides, the corresponding T_B for 10 nm Co NPs is close to RT (Figure 2.8 C).

Also, the magnetic behavior of a group of magnetic NPs can be described by a hysteresis

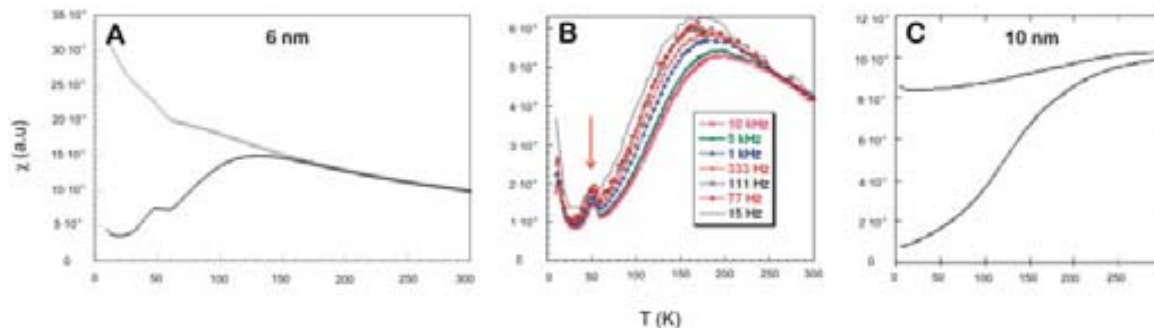


Figure 2.8: Magnetic susceptibility curves after ZFC-FC (100 Oe) process of 6 nm Co NPs. B) Temperature dependence of the AC susceptibility for 6 nm Co NPs. C) Magnetic susceptibility curves after ZFC-FC (100 Oe) of 10 nm Co NPs.

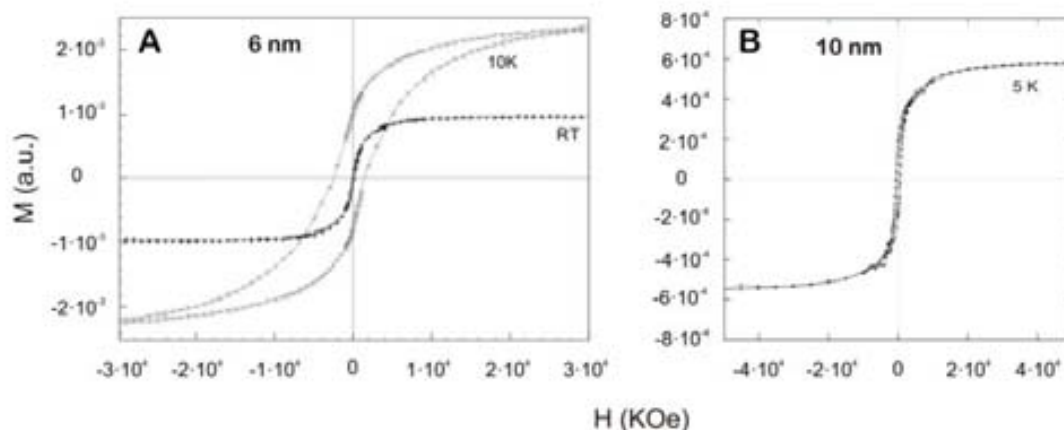


Figure 2.9: A) Hysteresis loop for 6 nm Co NPs at low temperature (10 K) and RT. B) Hysteresis loop for 10 nm Co NPs at low temperature (5 K).

loop, which measures the change of magnetic moment (M) over the strength of an applied magnetic field (H) at a specific temperature. Figure 2.9 A shows the $M(H)$ curves of dispersed average size 6 nm Co NPs at RT and 10 K. At RT the curve exhibits the typical features of SPM behavior (coercivity ~ 0). At 10 K the $M(H)$ curve exhibits a well developed hysteresis loop with a coercive field $H_c \approx 2$ kOe. There is also the existence of an exchange bias field (H_{ex}) likely generated by the oxide layer at the surface of the Co NP. Furthermore, hysteresis curve for 10 nm Co NPs at 5 K and with typical FM behavior shows low coercivity and a remanence around half of the saturation magnetization (Figure 2.9 B).

2.1.3 Summary

In this section, we have synthesized different size ϵ -Co NPs and we have characterized them by different techniques. We have determined by TEM images how the magnetic properties change with the particle size, also increasing the interaction between particles. When magnetostatic forces prevail over dispersion forces, the particles tend to form chains. In contrast, when magnetic interactions are weaker than other isotropic interactions, close packed structures are formed. Different intermediate structures can be observed during this transition.

2.2 Formation of Core/Shell Co/CoO and Hollow CoO Nanoparticles

Although Co NPs have very interesting properties that make them relevant in a wide range of scientific areas, their stability under the different conditions of study has to be considered in order to assure the successful results in the applications. The environmental fate and full life cycle analysis of the NPs is mandatory in order to develop certain type of applications. However, at the present moment there are just scarce and partial studies on the evolution of the NP characteristics once completed the synthetic stage.²³ In this context, Co can be considered as a model because it is a reactive metal, magnetic and traceable, and also a promising material for further applications.

Along this section two different phenomena will be studied: i) the chemical and morphological transformations occurring to Co NPs when they are removed from inert atmosphere conditions and exposed to air, and ii) the spontaneous formation of CoO hollow NPs via oxidation of Co NPs in aqueous environment at RT.

2.2.1 Exposure to Open-Air Conditions: Core/Shell Co/CoO Nanoparticles

The oxidation of Co NPs is an important issue in many applications, since it generally induces changes in the magnetic properties. For example, the use of Co NPs in heterogeneous catalysis depends on the degree of oxidation, which modifies the active sites.²⁴ Also, partial oxidation of Co NCs with a thin oxide layer resulting in a Co/CoO core/shell NP can result in exchange bias effects at the interface between FM Co and AFM CoO at low temperatures beating SPM transition.^{25,26} Therefore, it is important to study the oxidation process and the degree of oxidation in the NPs because it can affect their properties and their future applications.

2.2.1.1 Experimental

Formation of Core/Shell Co/CoO Nanoparticles

By exposure of the pre-synthesized Co NPs solution (Section 2.1) to the atmosphere, the Co NPs experiment a surface oxidation, and evolve to core/shell Co/CoO NPs.

2.2.1.2 Results and Discussion

When the Co NPs are exposed to air, the formation of a first thin oxide layer on the Co surface

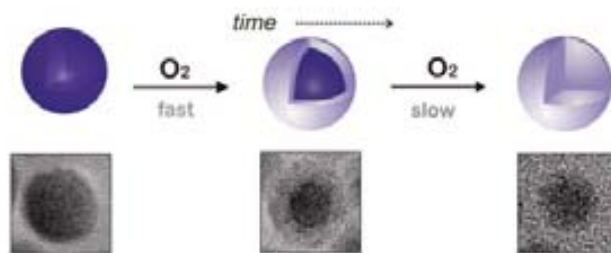


Figure 2.10: Schematic diagram illustrating the different oxidation processes observed for Co NPs in contact with air. Scheme not drawn to scale.

is very rapid, even at RT. Colloidal Co NPs solutions processed in air-free conditions, but subsequently exposed to the atmosphere, gave different thicknesses of oxide shell depending on the exposure time. This process occurs up to passivation or full oxidation, depending on the oxidizing environment and the stability of the NP (high crystalline and homogeneous coating), to form homogeneous CoO layers that effectively protect the Co core from oxidation. This thin oxide shell formation is shown even when they are exposed to atmosphere during transfer to a TEM grid and dried. It has previously been reported that oxidation of colloidal Co NPs upon extended exposure to air leads to the well known Co/CoO core/shell particles (Figure 2.10),^{26,27} where the external CoO shell partially passivates the surface of the NP as a function of its thickness. For 7 nm Co NPs, it was postulated that a 2 nm CoO shell is formed in 18 months.²⁸

Dynamic light scattering (DLS) measurements of ~12 nm Co NPs in DCB, under Ar atmosphere, show that the particles have a mean hydrodynamic radius of 13.1 ± 3.6 nm (Figure 2.11 A), confirming that the particles are not aggregated in solution. Once the vial is opened and the solution gets in contact with air, it can be observed a progressive increase of the size with time (Figure 2.11 B), indicating that starts an agglomeration process of the particles. Thus, we attributed this agglomeration to the oxidation process of the NPs. Z-potential measurements were also done as increasing time (Figure 2.11 C). At the initial times (when the sample was just taken out from the glove box), a negative z-potential value of -44.6 ± 4.2 mV was obtained. Over time, it was observed a decreasing of the potential from -44.6 mV to 0 mV in approximately 45 minutes. This fact can be an indicator of the oxidation process because the sample is in contact with air. The DLS and initial z-Potential values for Co NPs were similar to the values obtained for 12 nm OAM-capped Au NPs synthesized in toluene (Figure 2.11 A), which were measured as a control experiment. However, z-potential values of Au NPs remained constant over time (~ 50 mV), thus confirming that the potential fall observed in Co NPs was caused because their oxidation.

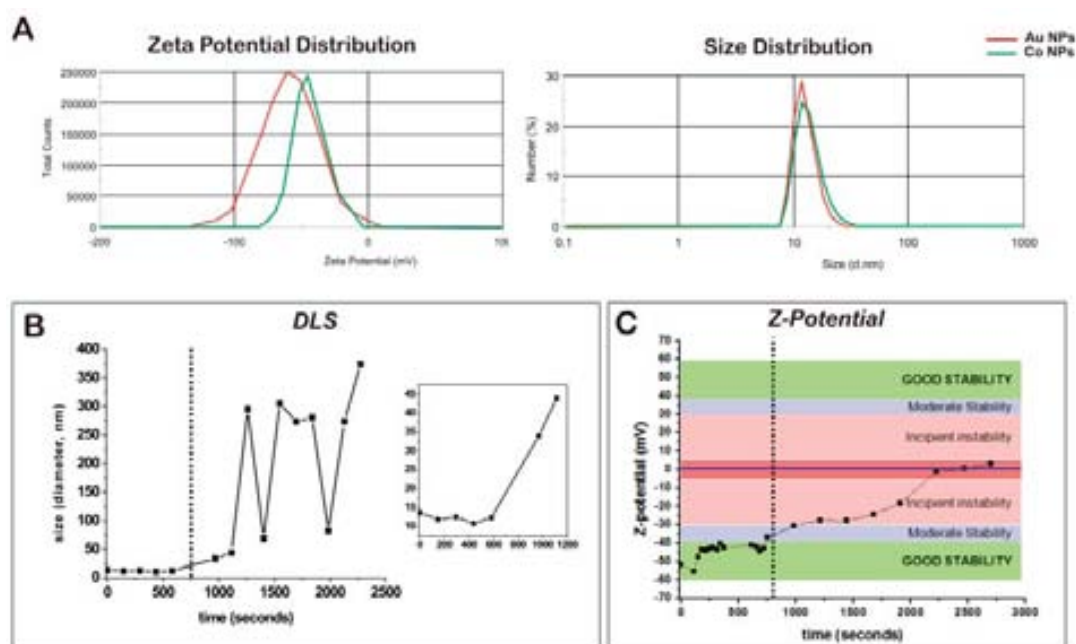


Figure 2.11: Comparison of DLS and z-Potential measurements of 12 nm Co NPs and Au NPs (A). Evolution of the DLS (B) and Z-potential (C) measurements of 12 nm Co NPs with time. The dashed line represents the time when the sample was exposed to the atmosphere.

2.2.2 Exposure to Water/Air Interface Conditions: Formation of Hollow CoO Nanoparticles

Hollow materials have been widely studied because their appealing applications in many areas of science and technology such as in catalysis²⁹ and plasmonics,³⁰ together with bioencapsulation,³¹ drug delivery^{32,33} or nanoelectronics,³⁴ where they are excellent benchmarks. Hollow spheres of different materials including those composed of carbon,³⁵ polymers,³² inorganic materials^{36,37} and metals^{38,39} have been synthesized previously. Diverse synthetic strategies have been developed to prepare hollow particles such as removal of a templating core,²⁹ galvanic replacement starting from reactive sacrificial templates,³⁸ or control of solid diffusion processes by Kirkendall effect.^{40,41} In the last, the porosity results from different solid-state diffusion rates of two reactants upon oxidation or alloying reactions. In the case of significant differences in the diffusion coefficients, accumulation of vacancies at the interface of the two components can lead to the formation of cavities. The first experimental proof of this phenomenon was reported by Smigelkas and Kirkendall in 1947.⁴² At the nanoscale, Alivisatos and co-workers obtained hollow oxides and chalcogenides nanostructures by reacting Co NPs

in solution with oxygen and either sulfur or selenium at 182 °C.⁴¹ Direct formation of CoO hollow NPs has also been reported via thermal decomposition of selected Co molecular precursor in open-air conditions at 150 °C.⁴³ And Cabot *et al.* studied the vacancy coalescence during the oxidation process in iron NPs in solution with a controlled oxygen flow and temperature, which leads to the formation of hollow iron oxide NPs.⁴⁴ Interestingly, the studies about the formation of hollow NPs in solution as a result of metal mobility make use of high temperatures under controlled conditions.

We have observed that at the air/water interface, the rate of the oxidation process is significantly accelerated thus resulting in the formation of different species: i) Co/CoO core/shell, ii) hollow CoO particles and iii) small CoO particles. In this section, we report a solution-phase formation of CoO hollow NPs via oxidation of Co NPs in aqueous environment at RT. The presence of water accelerates the oxidation of Co and modifies the reactivity at the surface of the NP, favoring the formation of hollow structures.

2.2.2.1 Experimental

Formation of Hollow CoO Nanoparticles

Oleic-acid stabilized ϵ -Co NPs ($2 \cdot 10^{16}$ NPs/ml) of a mean size of 10.3 ± 1.8 nm diameter were prepared following the explained procedure of the section 2.1. Afterwards, a few drops (0.3-0.5 mL) of the Co NP solution in DCB were deposited onto a water layer contained in a Petri dish, which remained uncovered in the hood thus allowing the slow evaporation of the DCB (bp = 181 °C) at RT. This is indeed the process to obtain MLs by the LBL technique, which has been previously employed to obtain large self-assembled MLs of CdSe at the water/air interface.⁴⁵

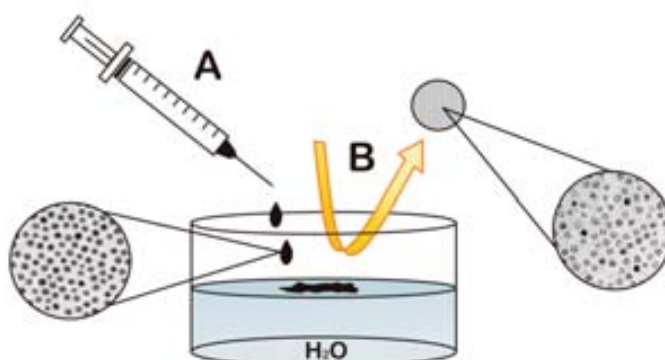


Figure 2.12: Schematic diagram showing the sample preparation process. A) Deposition of the Co NPs solution onto a water layer. B) Direct sample collection with a TEM grid. Scheme not drawn to scale.

For a straightforward observation of the morphological changes in the NPs without any further manipulation step, sample collection was directly performed with TEM grids (Figure 2.12). The samples were collected at different times: 0 h, 2.5 h, 5 h and 24 h. For instrumentation details of this subsection see Appendix A.2.

Recovery Process of Hollow CoO Nanoparticles

The maximum volume of water was removed from the bottom part of the Petri dish with the help of a syringe. Afterwards, the remaining solution was mixed with an equal volume of MeOH. The mixture was shaken with the aim of favor the precipitation of the particles, and then centrifuged at 6000 rpm during 20 min. After remove the supernatant, 2 mL of MeOH were added and the centrifugation process repeated. Finally, the supernatant was removed and the particles redispersed in a small volume of DCB (~0.5 mL).

2.2.2.2 Results and Discussion

Structural Characterization

Some drops of colloidal Co NP solution in DCB were casted onto distilled water and the morphological and structural evolution of the sample exposed to air, after different periods of time, was firstly characterized by TEM (Figures 2.13 A-D). A polycrystalline low contrast shell at the outer surface of the particles after 2.5 hr was observed. After 5 hr, the sample was mostly constituted of hollow particles together with a little population of smaller particles of 2-3 nm. After 24 hr, only CoO NPs of 2-3 nm were observed, which were assumed to be the result of disintegration of the CoO hollow particles caused by the large stresses upon the growth of the crystal domains.

In the case of hollow NPs, as the oxidation proceeded, the CoO shell grew outward from the initial Co NP diameter of 10.3 ± 1.8 nm to approach a particle size of 13.4 ± 3.3 nm for the hollow morphology (Figure 2.13 E). The external growth requires the diffusion of Co through the forming CoO shell and subsequently oxidation at the NP surface and inward diffusion of the equivalent number of vacancies (Kirkendall effect). The hole left inside the NP is smaller than the initial Co NP diameter, indicating some inward growth.⁴¹ Furthermore, after 5 h exposure, NPs can be recovered by centrifugation and redispersion in anhydrous DCB to preserve the formed hollow NPs (see experimental part for details).

As indicated by HRTEM (Figure 2.14), the shells around the NPs are polycrystalline composed by small crystals of 2-3 nm (Figure 2.14 A), like those previously reported for hollow spheres of Fe NPs also obtained by the Kirkendall effect.⁴¹ This is likely due to cracks produced

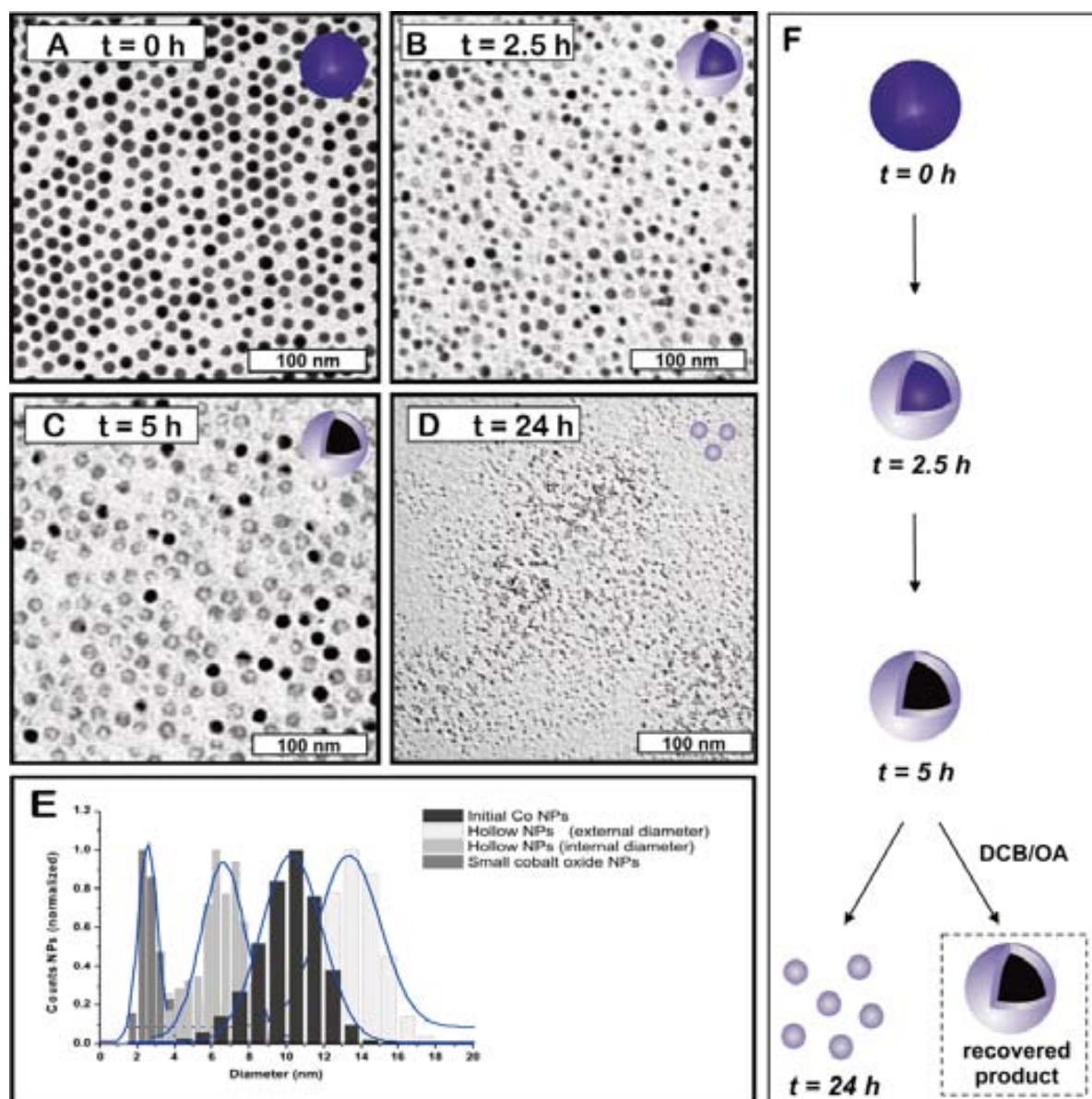


Figure 2.13: TEM images of the 10 nm Co NP on a distilled water surface after different times: A) 0 h, B) 2.5 h, C) 5 h and D) 24 h. E) Particle size distribution of Co NPs at initial time (dark gray), external diameter of hollow CoO NPs after 5 h of water exposure (line pattern), internal diameter of hollow CoO NPs after 5 h of water exposure (light grey) and CoO NPs after 24 h of water exposure, measured by taking the largest distance (medium gray). F) Scheme of the evolution of the Co NP with time.

during oxidation to release crystal stress at the Co/CoO interface (densities are 8.9 g/cm^3 for Co and 6.4 g/cm^3 for CoO). The detailed analysis of the HRTEM image, confirmed that the crystals correspond to Co oxide in the cubic phase ($Fm\bar{3}m$). Figure 2.14 B also shows the HRTEM images of a 2 nm CoO NP result of the disintegration of a hollow particle, and its

corresponding FFT power spectra. More expanded lattice spacing were also observed, which may correspond to intermediate O/OH species.

TEM shows the 2D projection of 3D objects, therefore careful analysis is needed to interpret shapes from TEM images. Figures 2.15 A and C show high angle annular dark field (HAADF) images of the samples at 2.5 h (intermediate state), in which the HAADF profile is proportional

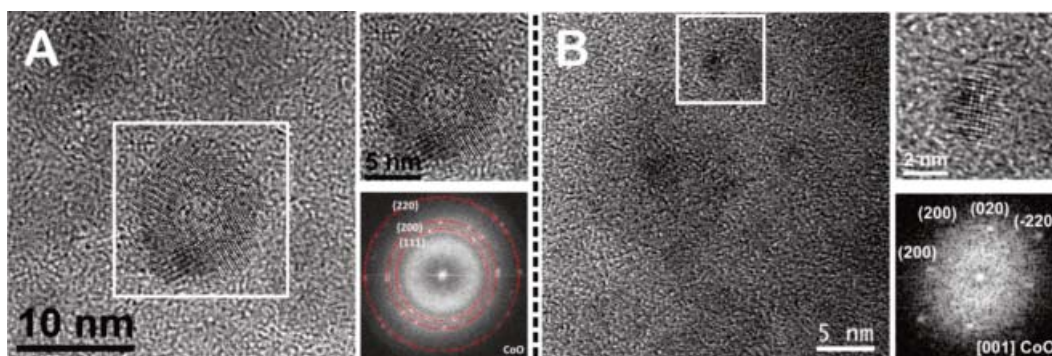


Figure 2.14: A) HRTEM images of a CoO hollow sphere (selected area) and its corresponding FFT power spectra pattern. B) HRTEM images and the corresponding FFT power spectra of a small CoO crystal near a sphere (selected area).

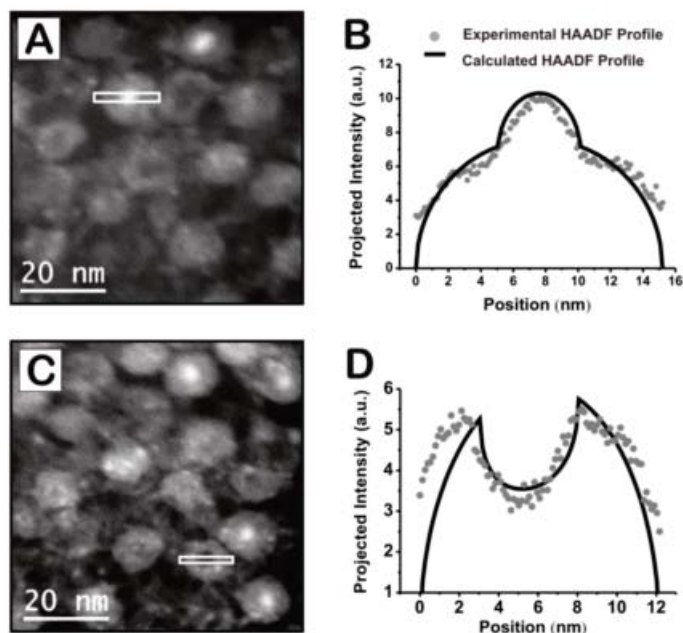


Figure 2.15: A,C) HAADF or Z-contrast STEM images of the particles in an intermediate state (2.5 hr). B,D) Comparison of intensities between the HAADF calculated (black line) and experimental (gray dots) for a core/shell Co/CoO sphere⁴⁷ and a hollow sphere,⁴⁸ measuring the selected line profiles showed in the images A and C, respectively.

2.2 Formation of Core/Shell Co/CoO and Hollow CoO Nanoparticles

to Z^2 and the thickness at every projected point. Assuming that the particles have spherical morphology, it could be observed two principal structures that coexist: i) hollow CoO particles in which the lower contrast in the center suggests the absence of material, and ii) core/shell Co/CoO particles with a denser core than the shell corresponding to the pure metal. Intensity profiles for the HAADF projections of a hollow sphere and a core/shell sphere have been calculated following the assumptions stated above together with a methodology published elsewhere.⁴⁶ In addition, a comparison between the HAADF calculated intensities and the experimentally observed intensities for the hollow sphere (Figure 2.15 D) as well as the core/shell Co/CoO sphere (Figure 2.15 B) are shown, in which the dotted line corresponds to the experimental data and the continuous line to the calculated profile. The proposed model is in good agreement with the experimental results indicating the accurate radial isotropy of the NPs which are homogeneously oxidized. The small discrepancy between calculated and experimental HAADF profiles is attributed to the shell of the spheres being polycrystalline instead of a continuous monocrystal, as a result of the multiple shell nucleation sites.

The formation of hollow structures at RT in a humid atmosphere (above the water there is a dense vapor layer of microns thickness in equilibrium) shows a good reproducibility and very strong size dependence, partially observed in similar experiments at higher temperature, such as in the oxidation of iron NPs.⁴⁴ As a consequence of this, different oxidation stories are observed in the same sample with little size dispersity (Figure 2.16). Small particles get fully oxidized with no observation of intermediate hollow structures, while the medium ones got hollow and the larger ones got core/shell or core-hollow/shell shapes. This is in agreement with

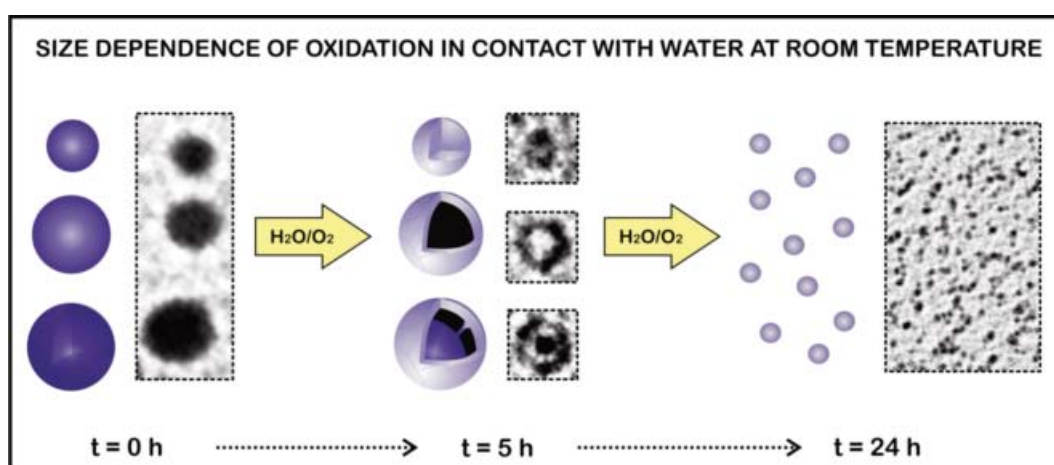


Figure 2.16: Schematic diagram illustrating the different oxidation processes observed in Co NPs in contact with water. It can be observed different intermediate species (CoO NPs, CoO hollow NPs and core/shell Co/CoO NPs) depending of the size of the NPs and time. Scheme not drawn to scale.

what would be predicted from the nanoscale Kirkendall effect since the atomic diffusion would be much slower for large growing shells. After 24 hr at the water interface, small fragments of CoO are observed irrespective to the initial size of the Co NPs, which can be explained because in large NPs the shell breaks before the oxidation of the whole particle is complete.

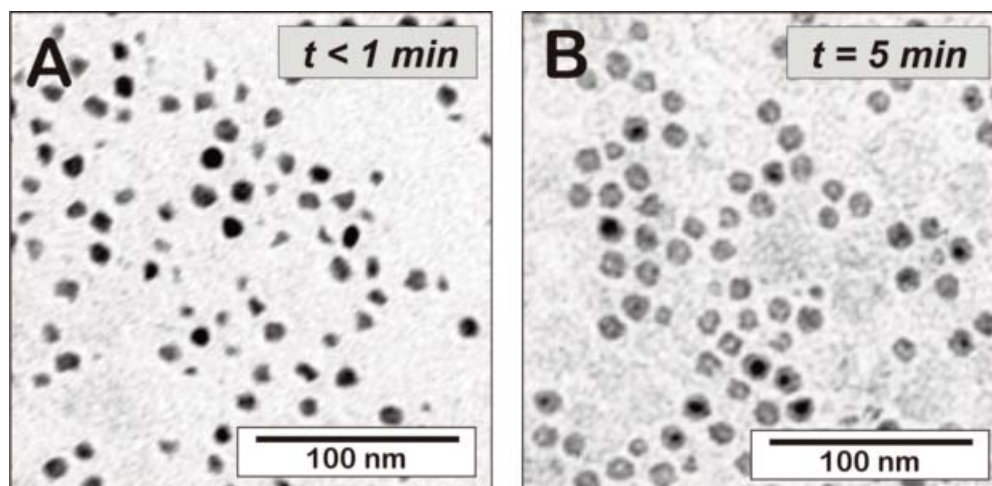


Figure 2.17: TEM image of Co NPs exposed to distilled water at 80 °C at different times: A) $t < 1$ min and B) $t = 5$ min.

The reactivity of Co and atomic diffusion in the solid is strongly dependent of the temperature. The effect of the temperature in the oxidation process was studied under the same conditions than before by deposition of colloidal Co NPs in DCB onto distilled water at higher temperature (up to 80 °C to avoid strong convection at the boiling point). In these conditions, at very short times (tens of seconds) it could be observed in the TEM images a selective etching of the particles, where the Co NPs get broken into irregular prism-like shapes (Figure 2.17 A). In this selective corrosion process, where oxidation dissolves the metal, some crystal faces have higher energy than others. Thus, we have observed that together with the oxidation there is a considerable disintegration of the Co NPs and an increased amount of Co ions are found in solution after precipitation of the oxidized NPs. Moreover, the hollow formation process is accelerated in the presence of hot water and core/shell Co/CoO and hollow CoO particles can be observed after 5 minutes (Figure 2.17 B).

Magnetic Characterization

The crystalline and morphological transformation of Co NPs was also followed by SQUID magnetometry, which is especially suited to study the different species (FM Co, AFM CoO, PM Co²⁺, and DM Co³⁺) present during the Co NPs evolution process, due to the strong coupling

between fine atomic structure and magnetic response. In Figure 2.18 we show DC magnetic susceptibility curves (under constant field), $\chi(T)$, of different samples after a ZFC and FC processes. The colloidal Co NPs were mixed homogeneously with air-tight paraffin wax (mp = 60-65 °C) to avoid inter-particle interactions. For the initial Co NPs sample prior to oxidation (Figure 2.18 A), the corresponding T_B is close to RT as expected for Co NPs of about 10 nm in diameter.¹⁴ After oxidation for 5 h in distilled water the $\chi(T)$ curve develops three peaks (Figure 2.18 B), together with a non-zero and almost constant magnetization measured between 100 K and 300 K, which indicates the presence of FM or interacting NPs. The higher temperature broad maximum around 150 K should correspond to residual Co NPs with a reduced diameter, and with some degree of oxidation at the surface.²⁶ From magnetic measurements at 70 K (well below the T_B of these residual Co NPs) this amount of metallic Co NPs can be estimated to be only around 1%. The peak at intermediate temperature (53 K) has been identified as corresponding to the CoO hollow particles,⁴⁹ while the low temperature peak at 8 K has been assigned to the tiny CoO particles formed when the hollow particles are broken down to pieces due to over-oxidation. In order to confirm the origin of the low temperature peak at 8 K, we have performed magnetic measurements of samples kept for 48 hr in distilled water, which resulted into complete oxidation and disintegration of the original Co NPs as shown by TEM. In this case, ZFC-FC susceptibility curves exhibit only a peak at about the expected temperature, namely 6-7 K (Figure 2.18 C). In addition, AC susceptibility measurements (under AC field) have also been performed to study the dynamic behavior of the magnetic system. AC susceptibility curves as a function of the AC frequency in a temperature range close to the observed T_B of the hollow particles are shown in the inset of Figure 2.18 B. The observed frequency dependence is indicative of a blocking process. However, attempts to fit the experimental data using the Arrhenius law end up always in values of the microscopic relaxation time $\tau_0 \sim 10^{-40}$ (it is expected to be around 10^{-11} for SPM NPs⁴⁷). These results are indicative of the existence of strong interaction between NPs or between different grains at the same NP. Besides, a quite accurate fit of the experimental data taking reasonable values of τ_0 ($\sim 10^{-9}$ - 10^{-10}) can be obtained by using the Vogel-Fulcher law

$$\tau = \tau_0 \exp\left(\frac{A}{T-T_0}\right) \quad \text{Equation 2.1}$$

with a T_0 value of about 40 K. This gives a T_B ' slightly below 10 K, which is very close to that obtained for residual disintegrated CoO NPs. Thus, the scenario is that hollow particles are polycrystalline and consist of tiny AFM CoO grains. Besides, in Figures 2.18 D-F we depict the

low temperature hysteresis curves at 5 K for the three different samples confirming the previous results. The original metallic Co NPs with typical FM behavior show low coercivity and a remanence of about half of the saturation magnetization (Figure 2.18 D). Figure 2.18 F displays

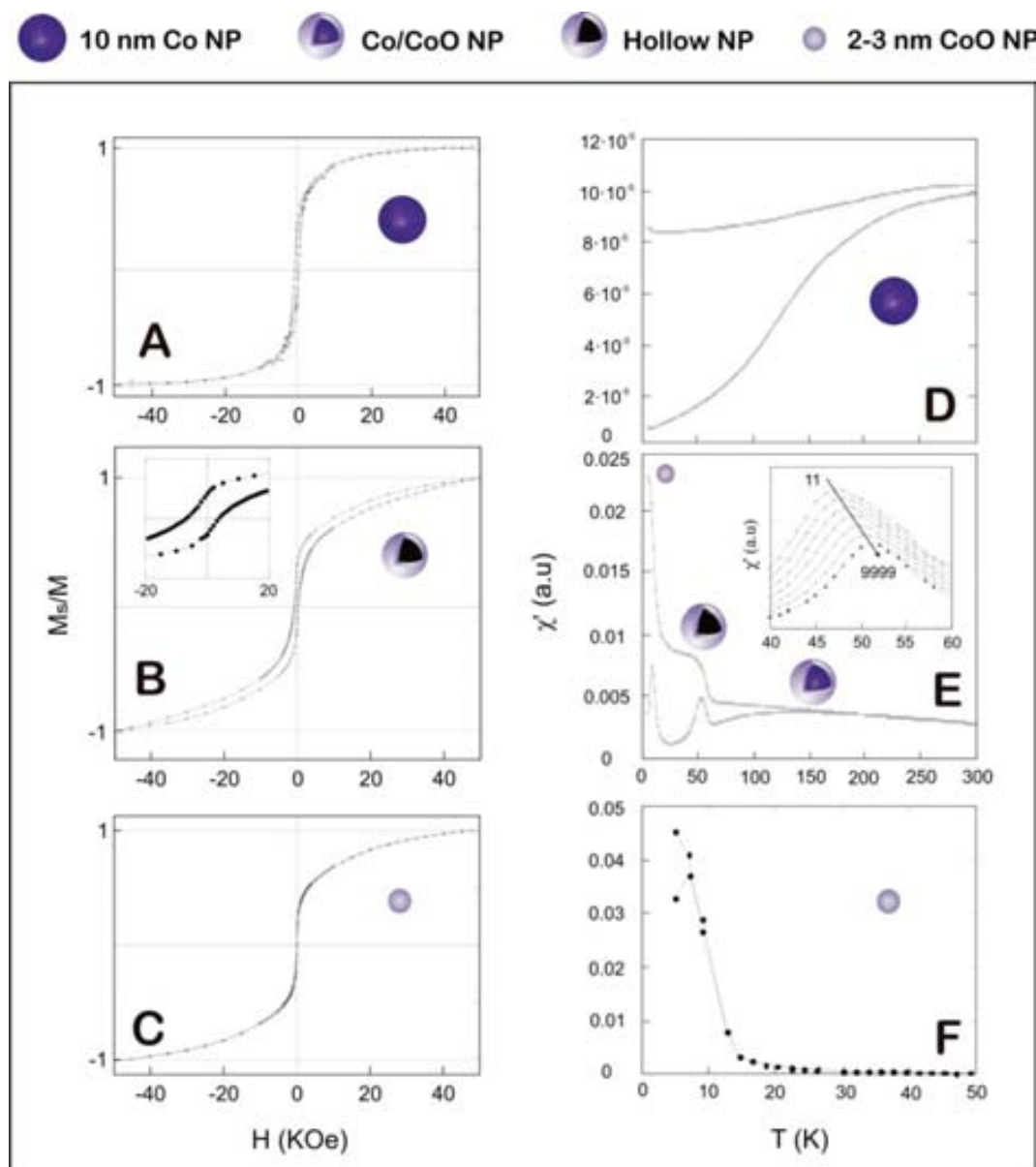


Figure 2.18: Magnetic susceptibility curves after ZFC-FC (100 Oe) process of A) the initial Co NP sample, B) the sample after 5 h of water exposure time and C) the sample after 48 h of water exposure. (Inset image in B corresponds to ac susceptibility at different frequencies (11, 33, 111, 333, 1111, 3333, 9999) for the corresponding sample). And hysteresis loops after FC (1 T) process for D) the initial sample at 5 K, E) of the sample after 5 hr water exposure at 5 K and F) for the sample after 48 h water exposure at 5 K. (Inset image E shows a detail of the loop).

the magnetization curve of the small CoO particles with a T_B (9 K) very close to the measurement temperature (10 K), showing low coercivity and remanence. On the other hand, in Figure 2.18 E, which corresponds in more than 70% to hollow NPs, the magnetization curve exhibits peculiar properties derived from its particular microstructure, which favors the appearance of strong magnetic frustration.⁵⁰ Thus, while the magnetization of the polycrystalline hollow particles mainly corresponds to the uncompensated spins at the surface and interfaces of these small AFM grains, the high T_B is due to the intense exchange interaction between neighboring grains in the same hollow NP. Consequently, while hysteresis loops are dominated by the individual grains, susceptibility measurements are dominated by their dipolar interactions. A similar behavior was also observed and described by Cabot *et al.*⁵¹

Formation Mechanism: Kirkendall Effect

Hollow polycrystalline NPs generally result when the outward diffusion of the core element A (Co) through the growing AB (CoO) composite is faster than the inward diffusion of the external element B (O₂). This situation has previously been determined, and simulated for the model case of 200 nm CdSe NPs, by the number of reactions at the A/AB and AB/solution interfaces; which subsequently depend on: the diffusion time of both elements through the shell, the A-B reaction probability at each interface, and the collision frequency of B with the particle (determined by the concentration and the diffusivity of B in solution). For equal reaction probabilities at each interface, the shell growth is controlled by the diffusivity of the metal through the shell, and this condition can be expressed as a ratio of self-diffusivities.⁵² As the self-diffusivity of Co²⁺ is estimated to be faster through the CoO shell ($\rho_{\text{CoO}} = 6.4 \text{ g/cm}^3$) than in the denser Co core ($\rho_{\text{Co}} = 8.9 \text{ g/cm}^3$), this leads to kinetically controlled Co/CoO nanostructures, with spherical cores in the case of larger particles supported by bridges and with very high metal/void interface areas.^{41,44} As can be observed in the Figure 2.16 (case of the bigger particles), by means of these bridges the mass transfer is facilitated, which leads to a shrinking of the metal core suspended in a CoO shell. At some point the bridges may get oxidized and mass transport slows down until dot-in-a-shell structures are observed.

Initially, one could expect that with the diffusion coefficients of Co in oxygen and oxygen in Co, to grow a second shell of CoO by Kirkendall effect at RT would take months. However, here we observe how it happens in a matter of hours. In fact, the diffusion coefficients at the nanoscale are altered by several orders of magnitude, and previous works have confirmed that diffusion processes are enhanced in NPs.^{53,54} In addition to the larger interfaces, number of defects at the surface and stress folds, the reaction time at the surface can be limited by the supply of the oxidizing agent in solution modulated by the presence of DCB.⁵² Finally, at low

enough oxygen concentration, the low collision frequencies but large reaction probability would limit the global reaction rate, allowing Co^{2+} ions to diffuse and load the outer shell surface while preventing the oxygen to diffuse inside leading to hollow NP formation at RT in short times.

2.2.3 Summary

In this section, it has been studied both the stability and reactivity of the Co NPs in different environments, in air and water-air interface. We show that the formation of hollow structures can be performed at RT and ambient conditions and not only under high temperatures and specific controlled conditions as previously reported. It has also been demonstrated that water has a critical role in the oxidation of Co NPs, which can be used to control and/or accelerate the formation of hollow particles. The reactivity of the external surface increases initially while O_2 penetration is slow, and then the Co mobility dominates the oxidation process.

2.3 Synthesis of Pt and PtCo Nanoparticles

The main problem with the Co NPs is their fast oxidation and consequently the change of the magnetic properties. Also Co is rather toxic, which makes them not biocompatible for medical applications even that present better magnetic properties than other magnetic materials like iron oxide. To solve this problem can be done two possibilities: cover the particles with a protective layer, which will avoid oxidation process and also will make them biocompatible; or form an alloy including a noble metal in the composition, which will reduce the tendency towards oxidation. With this idea we started to deal with bimetallic synthesis of different metals.

2.3.1 Synthesis of Pt and PtCo Nanoparticles Assisted by Metal Traces

The Pt system is of great interest because Pt NCs present unique optical and catalytic properties, which make them to be the focus of an extensive research in the recent years. The catalytic and electrocatalytic properties strongly depends on surface-to-volume ratio, shape and number of active catalytic sites.⁵⁵ The corner and edges of the particle are the most reactive sites due to the low coordination number they exhibit. Thus, different Pt NCs morphologies have been explored, finding that cubic Pt NCs seems to offer a greater potential as a catalyst.⁵⁶⁻⁵⁸

The rather extended methodology for a shape-controlled Pt NCs synthesis involves the use of capping agents that binds to a preferred crystal face of the growing crystal.⁷ Rampino⁵⁹ and El-Sayed⁶⁰ reported pioneering works reporting the synthesis of polydisperse cubic Pt NCs from the reduction of a Pt salts in the presence of different capping agents. Later on, Zhu and Alivisatos reported a similar synthesis using different temperatures and different capping agents, and also performing a size selection by centrifugation.⁶¹ More recently, Xia reported a more monodisperse and high yield synthesis of cubic Pt NCs (and other morphologies) employing poly(vinylpyrrolidone) (PVP) as surfactant with ethylene glycol serving as both a reducing agent and solvent.^{62,63} Subsequently, a wide variety of synthetic methods has been reported in order to achieve the desired Pt NC size and shape.⁶⁴⁻⁷¹

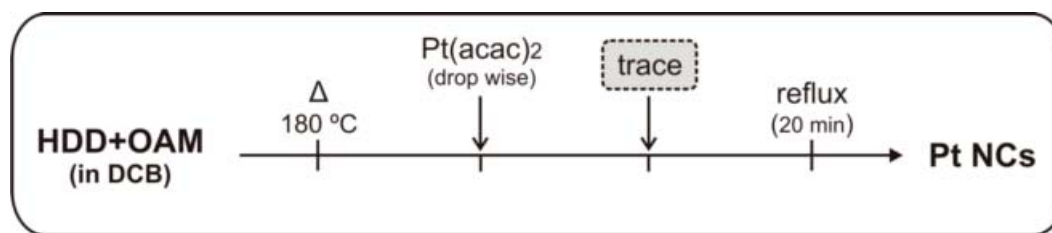
In this section, it will be explored how different small amounts of metal traces (we use the term “trace” to refer a small quantity of a specie, below 5%) can interfere with the Pt NCs growth and modify the final shape. Traces such a Co NCs,⁷ Co²⁺ ions and Au NCs⁷² has been used to compare changes in the morphology and better understand the growth mechanism. The NCs studied in this chapter are referred to as Pt NCs even when some contain a small amount of Co.

2.3.1.1 Experimental

For instrumentation details of this subsection see Appendix A.3.1

Chemicals. Platinum(II) acetylacetonate (Pt(acac)₂, 98%) was purchased from Strem Chemicals and used as received. Oleylamine (OAM, 70%), 1,2-dichlorobenzene anhydrous (DCB, 99%), oleic acid (OA, 99%), 1,2-hexadecanediol (HDD, 90%), cobalt(II) acetylacetonate (Co(acac)₂, 97%), cobalt carbonyl moistened with 5-10% hexane (Co₂(CO)₈, 90-95%), cobalt (II) chloride (CoCl₂, 98%) and super-hydride lithium triethylborohydride (in 1M tetrahydrofuran, THF) were purchased from Sigma-Aldrich and used as received. All chemicals were stored and prepared for synthesis in a UNILab MBraun glove box unless otherwise stated. The synthesis of Co NCs⁷ and Au NCs⁷² follow the previously reported procedures and the NC purification was performed in the presence of methanol or acetone followed by dispersion in DCB or toluene, respectively.

General Synthesis. Unless otherwise stated, all syntheses were performed under an Ar atmosphere using the standard Schlenk-line setup. In a typical synthesis, a solution containing 92 mg of HDD (0.36 mmol), 45 μ L of OAM and 10 mL of DCB was added to a 3-neck round-



trace = Co NCs, Co(CO)₈, Co(acac)₂, CoCl₂, Au NCs

Figure 2.19: Scheme of the general synthesis procedure to obtain different Pt NPs where the only variable is the different traces added to the synthesis.

bottom flask equipped with a condenser. The solution temperature was increased to 180 °C using a glycerol oil bath over a time period of ~30-60 min. Once the boiling temperature of DCB was reached, a 3 mL solution of DCB containing 45 mg of Pt(acac)₂ (0.11 mmol) was added drop-wise to the solution at a rate of 0.5 mL/min. 100 μL of trace (0.0018 mmol) was then added immediately to the solution. The solution was refluxed at 180 °C for 20 min and gradually cooled down to RT before being transferred to an Ar filled vial. In order to remove the excess capping/reducing agent or ions, the Pt NCs were purified by precipitation in methanol (or ethanol), followed by brief centrifugation and redispersion in DCB.

2.3.1.2 Results and Discussion

Various Pt NC morphologies has been produced with the synthetic procedure described above, without modification of the reaction conditions, composition, and concentration other than the presence of different Co traces (<5%). Under the reported conditions, a typical Pt NC synthesis, in the absence of any metallic trace, produces polypod or multipod structures (Figure 2.20 A). These particles have a multiarmed morphology, which each arm is made of small Pt NCs. The size of the polypods estimated from TEM observations ranges from 2- 3 nm for the individual Pt NCs, and up to 8-9 nm for a single polypod structure (measured by taking the longest distance between two end points on each arm). The polycrystalline polypods observed in the HRTEM (Figure 2.20 A, inset) are attributed to the *cementation* of individual Pt NCs. It is used the term “cemented” NCs when referring to the coalescence, or pasting, of two or more individual NCs in the presence of monomer in the early stages of NC growth.^{73,74} The *cementation* process occurs due to the presence of free precursors left in the solution and the constant deattachment/reattachment of the surfactants on the NC surface, allowing to the NCs to rapidly grow/attach to their neighbors. In some cases, single crystalline polypods were also

2.3 Synthesis of Pt and PtCo Nanoparticles

observed, suggesting that the origin of the polypod morphology is not due to epitaxial growth of the polypod arms rather a result of NC coalescence. This fact can be explained by the natural tendency for the NC to favor oriented attachment^{75,76} and the known atomic reorganization that occurs during their growth and subsequent evolution.⁷⁷ The FFT pattern obtained from HRTEM (Figure 2.20 A, inset) shows that the NCs crystallize on the Pt cubic structure, showing the (111) and (002) Pt planes at 0.226 and 0.196 nm, respectively.

To deviate from polypod synthesis, metallic Co was introduced as a trace and reducer. The metallic Co can be introduced as pre-synthesized Co NCs or Co carbonyl ($\text{Co}_2(\text{CO})_8$), since in the reported conditions the metallorganic precursor instantaneously decomposes and becomes Co NCs. Co NCs have been employed at a low concentration (<5%) into the syntheses where their main role includes acting as a chemical compound (i.e. a metal reducer) and interfering with the Pt NC growth modifying the final shape. Thus, under the same conditions of the polypod synthesis, the presence of $\text{Co}_2(\text{CO})_8$ yields highly monodisperse cubic Pt NCs (Figure 2.20 B). The obtained cubes form a highly ordered arrangement on the TEM substrate (carbon coated Cu grid) with a well-defined interparticle spacing, demonstrating their narrow size distribution. The particles have an average size determined from the TEM images of 7.6 ± 0.8 nm, which is similar to the previously reported but synthesized using different conditions.⁷⁸ The HRTEM image and the corresponding FFT pattern (Figure 2.21 B, inset) show that the single Pt cubes have a preferential orientation with crystallization along the family of {100} facets. It is known that the cubic morphology of the fcc NCs is highly dependent of the relatively slower growth rate along the (100) direction with respect to the (111).^{56-58,79} Thus, the alteration in the morphology from polypod to cubic structure might also be attributed to the interaction between the Co and Pt atoms.

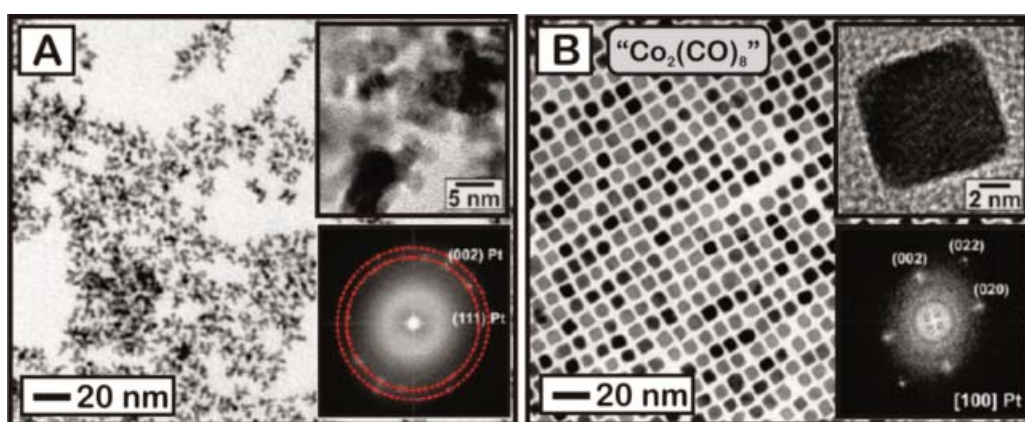


Figure 2.20: TEM images of the Pt NCs synthesized in the absence (A) and presence (B) of a $\text{Co}_2(\text{CO})_8$ metallic trace. Inset: HRTEM image and FFT patterns of the corresponding NCs.

Co carbonyl traces decompose instantaneously resulting in the formation of Co NCs at a rate much faster than Pt nucleation (Pt nuclei is observed after a few minutes while Co NCs are formed within the first seconds). The Co NCs function as a metal strong reducer (in addition to the weak reducing agent already present in the solution, HDD) that becomes pyrophoric at the nanoscale and modifies the reaction kinetics. Besides, no free Co NCs were observed in the TEM grid, fact that suggests that all the Co NCs were sacrificed at 180 °C to aid in the formation of the cubic shape.

As a control experiment, Pt NCs synthesis was also performed in the presence of CoCl_2 , and Pt polypod NCs were consistently obtained (Figure 2.21 A). The size of the individual Pt NCs and the polypods, calculated from the TEM images, were 2-3 nm and 8 nm, respectively. It is interesting to note that while the $\text{Co}_2(\text{CO})_8$ gives cubic-like structures, CoCl_2 yields polypod structures under the same synthesis conditions, a morphology similar to that produced in a typical Pt NCs synthesis. This suggest that the Co^{2+} from CoCl_2 is not reduced to Co^0 at the right times during the synthetic process. Also, the synthesis using $\text{Co}(\text{acac})_2$ as a trace, a well known precursor for the synthesis of Co and alloy NCs, was performed. In this case, the synthesis showed three different morphologies, under the same experimental conditions, which we categorized as: i) polypods (Figure 2.21 B), ii) small cemented cubes (Figure 2.21 C) and iii) large cemented cubes (Figure 2.21 D). Different batches of synthesis could produce three different NC morphologies as the synthesis was routinely repeated and, interestingly, these different morphologies did not coexist in the same batch. The monodispersity observed suggests that there is a critical stage at the beginning of the synthesis where the size and shape of the Pt NCs are determined.

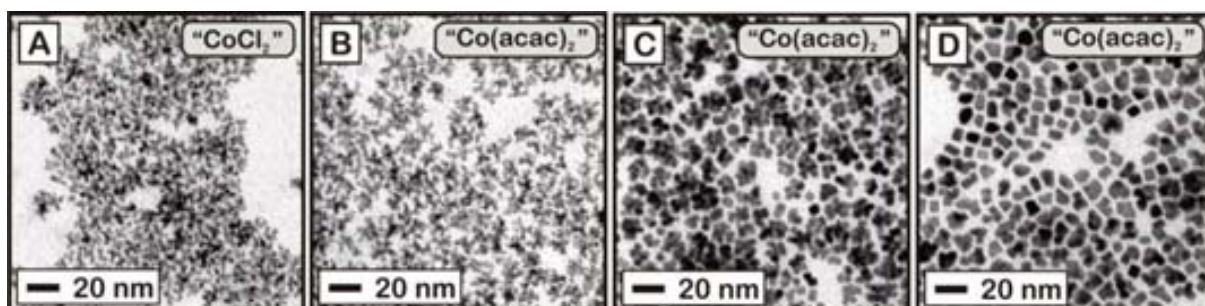


Figure 2.20: TEM images of Pt NCs synthesized using CoCl_2 (A) and $\text{Co}(\text{acac})_2$ (B-D) as traces. In the syntheses where $\text{Co}(\text{acac})_2$ was used as a trace, three different morphologies are observed. The individual sized of the NCs are 2-3 nm (B), ~5 nm (C) and ~7 nm (D). The size of the polypods and cemented cubes are 6-8 nm (B), ~12 nm (C) and ~14 nm (D).

2.3 Synthesis of Pt and PtCo Nanoparticles

In order to understand the role and intake of Co when using $\text{Co}(\text{acac})_2$ precursor, ICP-MS analysis of two samples with different morphologies (polypods and cemented cubes) was carried out (see Table 2.1). In the case where polypod Pt NCs are obtained, only 0.3% of Co was detected in the purified NC samples, while the majority of the Co remained in solution. But in the case where cemented cubes are obtained, ICP-MS results show a higher fraction of Co in the purified NCs, up to 4.74%, while the supernatant contains only the 0.08% of Co.

It can be concluded that $\text{Co}(\text{acac})_2$ can be partially reduced by HDD under the experimental conditions. In the case where Co^{2+} is not reduced to Co^0 , polypods are observed, which is similar to the case using CoCl_2 or in the absence of traces. When the Co^{2+} is reduced to Co^0 , cemented cubic NCs are formed, which is similar to the case of $\text{Co}_2(\text{CO})_8$ and indicates the presence of metallic Co in the NC.




Metallic trace	% Co	% Pt	Shape	TEM
$\text{Co}_2(\text{CO})_8$	2.68	97.32	cubes	
$\text{Co}(\text{acac})_2$	0.30	99.70	polypods	
$\text{Co}(\text{acac})_2$	4.74	95.26	cemented cubes	

Table 2.1: Comparison of the atomic % of Co and Pt obtained for purified Pt NCs using $\text{Co}_2(\text{CO})_8$ and $\text{Co}(\text{acac})_2$ as traces obtained by ICP-MS.

As a last control experiment, Pt NCs were also synthesized in the presence of pre-synthesized Au NCs⁷² (a non Co source of atoms) while maintaining the same conditions to the previously described syntheses. It was observed the formation of polypod Pt NCs along with the “well-preserved” OAM capped Au NCs, indicating that the Au NCs were inactive. The XRD spectrum (Figure 2.23 F) shows an overlap of the Pt and Au NC (111) and (200) fcc peaks. These results are consistent with the TEM images which show that the Au NCs were not sacrificed due to the more noble character of Au with respect to Pt (Figure 2.22).

Figure 2.23 shows the crystalline structure of the Pt NCs, in the absence and in the presence of a each specific trace ($\text{Co}_2(\text{CO})_8$, CoCl_2 , $\text{Co}(\text{acac})_2$, pre-synthesized Co NCs and Au NCs) analyzed using XRD. The 2θ Bragg peaks obtained at 39.97° , 46.48° , 67.81° , 81.66° and 86.27° (Figure 2.23 A-E) correspond to the (111), (200), (220), (311) and (222) Pt fcc diffractions, respectively. There is a slight shift in the measured 2θ Bragg peaks compared with the

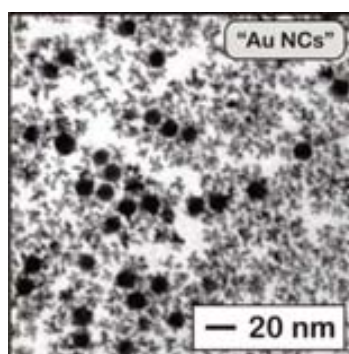


Figure 2.22: TEM image of Pt NCs synthesized in the presence of pre-synthesized and purified Au NCs as metallic trace.

theoretical peaks for bulk Pt (39.76° , 46.24° , 67.47° , 81.27° and 85.71°).⁸⁰ This shift indicates that may be a compression of the Pt crystal lattice due to the high surface tension of the NCs and the incorporation of Co to form a PtCo alloy structure, which can be explained by Vegard's law.

The Vegard's law⁸¹ (Equation 2.2) is an approximate empirical rule which holds that a linear relation exists, at constant temperature, between the crystal lattice constant of an alloy and the concentrations of the constituent elements. Assuming this linear relationship also applies to our case, the presence of Co was calculated to be 3.1 % (Equation 2.3).

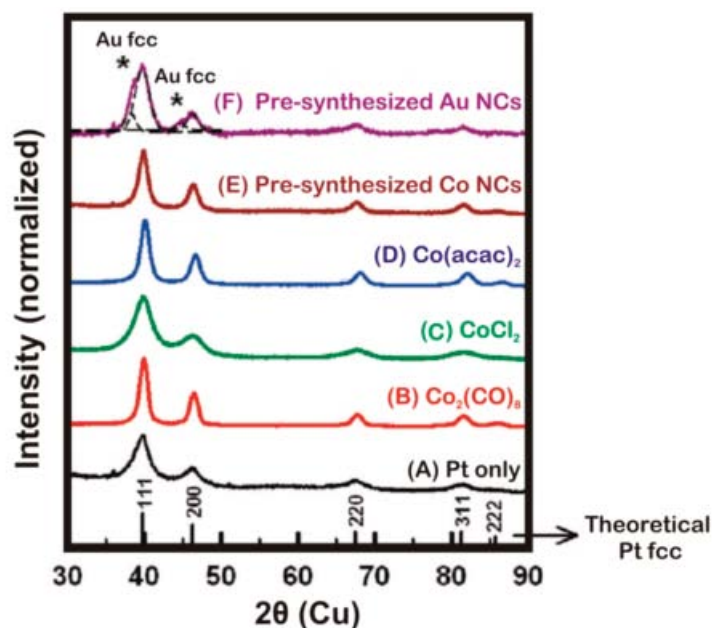


Figure 2.23: XRD spectra for the Pt NCs synthesized in the absence (A) and presence of trace $\text{Co}_2(\text{CO})_8$ (B), CoCl_2 (C), $\text{Co}(\text{acac})_2$ (D), pre-synthesized Co NCs (E), and Au NCs (F).

$$a_{PtCo}(x) = (1 - x)a_{Pt} + xa_{Co} \quad \text{Equation 2.2}$$

$$x = 100\% \cdot \frac{(a_{Pt} - a_{PtCo})}{(a_{Pt} - a_{Co})} = 100\% \cdot \frac{(3.917 - 3.095)}{(3.917 - 3.533)} = 3.1\% \quad \text{Equation 2.3}$$

The Pt and Co NCs lattice parameter (a) used in this calculation are 3.917 Å for 100 % Pt and 3.533 Å for 100 % Co NCs. The lattice parameter of the Pt NCs synthesized in the presence of Co is 3.905 Å.

From all the generated experimental data, some insight on the mechanism for the shape control of Pt NCs can be obtained. As illustrated in Figure 2.24, under the right conditions, and in the presence of sufficient monomer concentration (1), there is an initial burst nucleation of small shapeless Pt nuclei (2-3 nm). While nucleation decreases the initial Pt concentration, which in turn slows down the nucleation rate, there is still a significant amount of Pt precursor remaining in the solution. At this stage, both nuclei and monomer coexist (2). When this process is carried out in the presence of HDD as the only reducing agent, a slow reduction rate leads to a large amount of monomer that homogeneously crystallize into a large number of nuclei, which are in close proximity to each other in a Pt-monomer-rich environment. This situation would favor a coalescence mode, resulting in the progressive cementation of the NCs into polypod structures of different degree of aggregation (3a and 3b), which likely depend on the ratio of the free Pt cations vs the formed nuclei. Besides, in the presence of Co NCs, a fast reduction of a portion of the Pt monomer would lead to the initial appearance of fewer nuclei, which are isolated in the Pt-monomer rich environment, favoring a growth mode over coalescence. This situation would lead to the formation of larger NC that may display cubic structures (4).

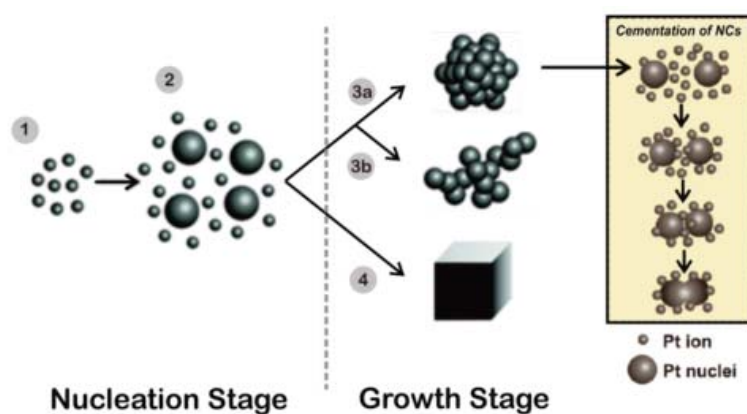


Figure 2.24: Schematic diagram illustrating the growth mechanism of the Pt NCs.

2.2.1.3 Summary

Unlike previous works where different shapes were obtained with different experimental procedures (modifying reducers, surfactants, concentration, temperatures, etc.), it has been demonstrated that Pt NCs of different morphologies can be achieved by using a fixed set of conditions and varying only the presence of different traces. In the presence of metallic Co at low concentration (<5%), highly monodispersed cubic NCs are obtained, while in its absence poly-pods are observed. The role of Co is to act as strong reducer to rapidly generate a small amount of nuclei and promote cubic growth as shape directing agent. It is important to note that these different morphologies do not coexist in the same preparation, indicating that the size and shape are determined at an early stage and all the NCs are simultaneously affected. It is worthy to mention one possible application of these Co doped Pt NCs as catalyst, as has been recently reported for improving the oxygen reduction reaction in fuel cell technology.⁸²

2.3.2 Synthesis of Pt and PtCo Nanoparticles by Using Competing Reducers

Generally, the kinetics of the NCs synthesis can be manipulated by changing different parameters such the concentration, the temperature, reducing power, and additives or surfactants, which have an impact on both the nucleation rate and the nuclei stability. Despite the wide number of reports on the importance of the kinetic control in NC growth, the use of mixtures of reducers has been not explored. In the previous subsection has been studied the shape-control of Pt NCs in the presence of different Co traces and other metals (<5%),⁸³ where Co trace can function as both a metal reducer and shape directing agent. Recently, Zou *et al.* reported the use of metal as reducers where tungsten was added as a foreign element to reduce the Pt precursor. They found that tungsten has an influence of the kinetic control on NC morphology, since without the presence of $W(CO)_6$ their morphology appeared to be much less controlled.⁸⁴

In this subsection is explored the synthesis of Pt NCs in the presence of Co^0 with a broad range of reducer compositions and concentrations with the aim of better understand this shape-control process. Therefore, two competing reducers are used in a one-pot synthesis to kinetically control the NC growth. It is showed that Pt and PtCo NCs with different morphologies can be obtained by systematically varying the concentration of two competing reducing agents while maintaining a fixed set of reaction conditions. Moreover, it is observed an important competitive relationship between the two different reduces, and also how the NC growth toward

a particular shape can be influenced at very early stages. Unlike other NCs synthesis where the size is controlled by varying the precursor/reducer ratio,⁸⁵ chain lengths of capping agents⁸⁶ or changing reaction temperatures,⁸⁷ herein it is observed a change in both the shape and the size as we vary the Co and HDD concentrations. Finally, a control experiment substituting the Co by lithium triethylborohydride as stronger reducing agent confirmed the proposed mechanism.

2.3.2.1 Experimental

For instrumentation details of this subsection see Appendix A.3.2

Chemicals. Platinum(II) acetylacetonate ($\text{Pt}(\text{acac})_2$, 98%) was purchased from Strem Chemicals and used as received. Oleylamine (OAM, 70%), 1,2-dichlorobenzene anhydrous (DCB, 99%), 1,2-hexadecanediol (HDD, 90%), superhydride lithium triethylborohydride (in 1 M THF) and Co carbonyl moistened with 5-10% hexane ($\text{Co}_2(\text{CO})_8$, 90-95%) were purchased from Sigma-Aldrich and used as received. All chemicals were stored and prepared for synthesis in a UNILAB MBraun glovebox unless otherwise stated.

Synthesis. All the syntheses were performed under an Ar atmosphere using the standard Schlenkline setup to avoid interactions between the NCs and O_2 , H^+ , or OH^- species, and the $\text{Pt}(\text{acac})_2$ concentration was constant in all syntheses. To remove the excess capping, reducing agent and ions, the PtCo NCs were purified by precipitation in methanol followed by brief centrifugation and redispersion in DCB prior to being subjected to further analysis (XRD, ICP-MS, EDX).

Increasing Co Content. In the synthesis where the concentration of HDD remained constant while the Co concentration was systematically increased, a solution containing 95 mg of HDD (0.37 mmol), 45 μL of OAM, and 10 mL of DCB was added to a 3-neck round-bottom flask equipped with a condenser and stirred under an Ar atmosphere. The solution temperature was increased to 180 °C using a glycerol oil bath over a time period of ~30-60 min. Once the boiling temperature of DCB was reached, a 3 mL solution of DCB containing 45 mg of $\text{Pt}(\text{acac})_2$ (0.11 mmol) was added dropwise at a rate of 0.5 mL/min. A 100 μL portion of Co trace prepared from $\text{Co}_2(\text{CO})_8$ (ranging from 0 to 54 μmol) was then added immediately to the solution. The solution was refluxed at 180 °C for 20 min and gradually cooled down to RT before being transferred to an Ar filled vial.

Increasing Hydride Content. In a set of control syntheses, the Co was replaced with a stronger reducing agent, lithium triethylborohydride. In this case, the HDD amount remained constant at 0.37 mmol while the hydride concentration was varied from 0.2 to 40 μmol (taken at 100 μL each time). The remaining synthesis was conducted following the method described above.

Increasing HDD Content. In the synthesis where the concentration of HDD was varied while maintaining a constant Co concentration, different amounts of HDD ranging from 0 to 1.5 mmol, and a constant concentration of Co trace prepared from $\text{Co}_2(\text{CO})_8$ (100 μL containing 2.2 μmol of Co) were added to the synthesis following the method previously described.

2.3.2.2 Results and Discussion

As described in the previous subsection (2.3.1), synthesis of Pt NCs in the presence of HDD and OAM produces Pt polypod NCs. However, if a small amount of $\text{Co}_2(\text{CO})_8$ (<5%) is added, the evolution of the reaction is much faster and cubic NCs are obtained. Herein, using the experimental procedure described in the experimental section, the reduction of Pt ions has been examined in the presence of two competing reducing agents (HDD and Co) with different reducing strengths. The reduction potential of Pt^{2+} (Pt^{2+}/Pt , $E^\circ_{\text{red}} = +1.20 \text{ V}^{88}$) has been achieved using HDD,⁸³ but the exact reduction potential of HDD is not yet determined. Just a reduction potential range can be delimited by comparing with other reported studies at similar conditions, in which HDD was able to reduce Cu^{2+} (Cu^{2+}/Cu , $E^\circ_{\text{red}} = +0.34 \text{ V}^{89}$) and Fe^{2+} (Fe^{2+}/Fe , $E^\circ_{\text{red}} = -0.44 \text{ V}^{90}$). Besides, the redox potential of Co^{2+} is -0.28 V^{88} , which can provide a faster and effective reduction of the Pt ions. In the following experiments, the same synthetic procedure is systematically performed by varying the concentration of only one reducer (HDD, Co and hydride).

Increasing the Co content. Polypod structures with a multiarmed morphology, which each arm is comprised small cemented Pt NCs,⁸³ were observed when de HDD was presented as sole reducing agent ($[\text{Co}] = 0$) (Figure 2.25A). The increase in Co concentration is determined from the ratio $[\text{Co}]/[\text{Pt}]$ and represented by the value of x , which take values from 0 to 0.466. When Co was added to the synthesis ($x = 0.005$), a morphological change from polypod to cuboctahedron PtCo NCs could be observed (Figure 2.25, from B to D). It was produced an increase in the NC size from 2.7 nm to 9.8 nm, being this dramatic change an effect of having

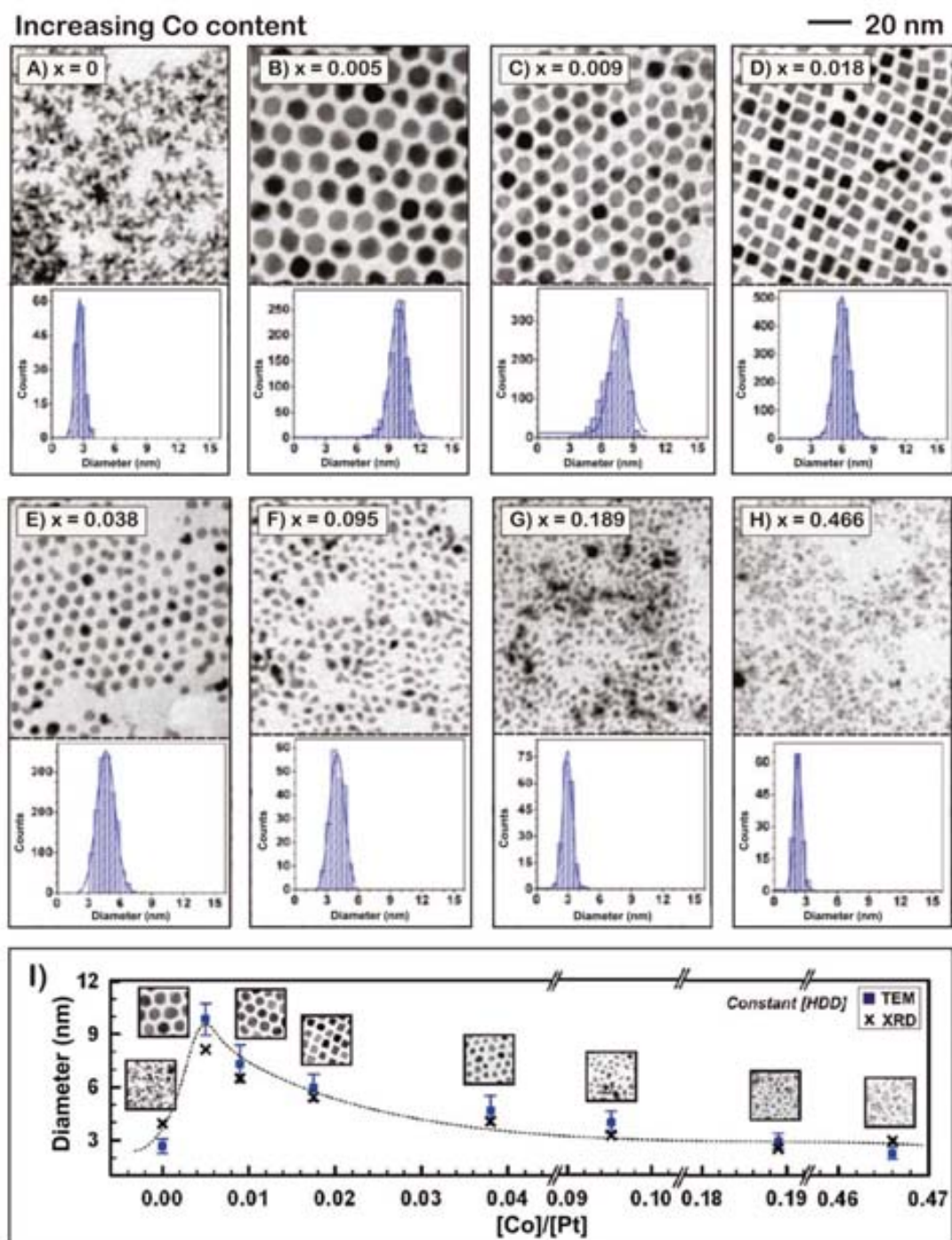


Figure 2.25: A-H) TEM images with the corresponding statistical size analysis of the PtCo NCs synthesized by increasing the Co concentration while maintaining constant HDD and Pt precursor concentrations (x represents the $[Co]/[Pt]$ ratio). I) Plot of $[Co]/[Pt]$ ratio versus NC diameter (nm) obtained by TEM (solid squares) and XRD (x mark). NOTE: There is a dotted line and a scale break (in the x-axis) to better represent a decreasing trend in the PtCo NC sizes.

two different reducers in on-pot synthesis (even with the small amount of Co). The rise of Co content from $x = 0.005$ to 0.038 further altered the NC shape as Co began to play a more prominent role as a reducer and shape directing agent. Figure 2.25 represents the shape evolution of PtCo NCs from polypods to spherical and cubic morphologies, with NC sizes ranging from 7.3 nm (Figure 2.25 C) to 4.7 nm (Figure 2.25 E). More increasing of Co content from $x=0.095$ to 0.466 gave rise to an even faster Pt ion reduction, and resulted in the disappearance of the monodispersed shapes and the appearance of irregular shaped and flake-like NCs (Figure 2.25, F-H), which appear similar to those obtained using only HDD as the reducer (Figure 2.25 A). The polycrystalline polypods and flake-like NCs have average crystal sizes ranging from 3.9 nm (Figure 2.25 F) to 2.3 nm (Figure 2.25 H).

The PtCo alloys were further analyzed using XRD (Figure 2.26 B), showing the evolution of their crystalline structure as the Co content increased. The 2θ Bragg peaks correspond to the known (111), (200), (220), (311), and (222) diffractions of the Pt fcc structure. There is a slight shift in the measured 2θ Bragg peaks as x varies from 0 (a) to 0.466 (h), which can be attributed to a compression of the Pt crystal lattice because of the incorporation of increasing amounts of Co into the NC structure forming a solid solution. The %Co content (with respect to Pt) was calculated using the Vegard's law (Equation 2.2) by comparing the lattice parameters (a) obtained from the measured 2θ Bragg peaks with those of pure Pt NCs ($a = 3.917$ Å) and Co NCs ($a = 3.533$ Å), as previously described in subsection 2.3.1 (page 51) These values were also compared to the theoretical %Co added to the synthesis, together with the elemental composition analysis from ICP-MS (Figure 2.26 A). It is observed that as [Co]/[Pt] ratio increases from 0 to 0.466 , the theoretical Co content increases from 0 to 31.8%, and this is in agreement with the trend obtained by XRD and ICP-MS.

Moreover, the NCs sizes were determined from the XRD measurements using the Scherrer equation (Equation 2.4), because the broadening of the peaks is an indication of the crystal size.

$$\tau = \frac{K\lambda}{\beta \cos\theta} \quad \text{Equation 2.4}$$

where K is the shape factor (typical value of about 0.9), λ is the x-ray wavelength, β is the line broadening at half the maximum intensity (full width at half maximum, FWHM) in radians, and θ is the angle. The obtained sizes are in good agreement with those obtained from TEM images, indicating that the particles are single crystals (Figure 2.26 A).

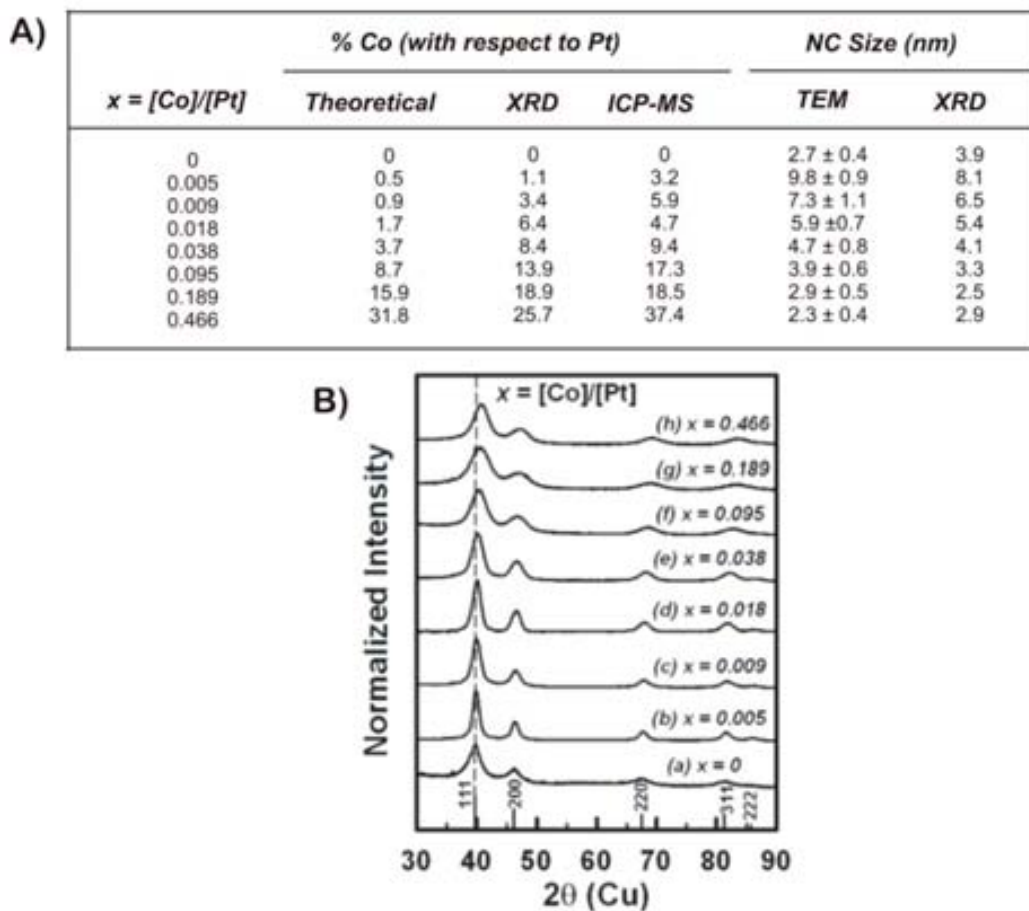


Figure 2.26: A) Tabulated comparison of the atomic % of Co obtained from the theoretical synthesis, calculated from Vegard's law (XRD) and ICP-MS (left); and a comparison of the PtCo NCs size determined from TEM images and calculated using the Scherrer equation (XRD) as the Co content varies (right). B) XDR patterns for the PtCo NCs synthesized in the presence of increasing Co content ($x=[\text{Co}]/[\text{Pt}]$) with constant HDD and Pt precursor concentrations.

The different morphologies obtained with increasing $[\text{Co}]/[\text{Pt}]$ ratio can be divided in three regimes:

- I.** The polypods morphology is consistently observed in the absence of Co. Likely, the slow reduction rate of HDD leads to a large amount of monomer that simultaneously crystallize into a large amount of Pt nuclei, which grow into polypod structures due to a cementation process.⁸³
- II.** The spherical/cubic PtCo NCs are observed when small Co amounts are added to the synthesis. The reduction competition between HDD and Co leads to a fast reduction of a

portion of the Pt monomers and the formation of a smaller number of nuclei, enabling growth towards larger sizes.

III. The progressive increase in Co content produces a fast homogeneous reduction of more Pt monomers (faster but equivalent to HDD reduction), causing the formation of irregular flake-like NCs (comparable to the polypod morphology).

It is important to mark up that high concentration of Co does not lead to shape control indicating that the NC size and shape control is determined by the relative concentrations ([Co]/[Pt] ratio) and reducing strengths of the reducers. The ensemble of data suggests that during synthesis, the metallic Co reduces the Pt^{2+} ions and in the process becomes oxidized. The incorporation of Co into the Pt NCs as a metal further suggests that the oxidized Co is later reduced back to Co^0 , probably with the assistance of the Pt NCs as a catalyst.

Increasing the Hydride content (Replacing Co by Hydride). As a control experiment, the role of the second reducer by replacing the Co by a stronger reducer, lithium triethylborohydride ($\text{H}_2/2\text{H}^-$, $E^\circ = -2.25 \text{ V}^{88}$) was examined. The NCs produced in this case are purely Pt NCs, unlike the PtCo alloys produced when using Co as a second reducer. Figure 2.27 shows the morphological trends which are similar to the previously observed when using Co, thus confirming the competitive reducing role between HDD and hydride. The increase in hydride concentration is represented by the value of y , which is determined from the ratio of $[\text{Hydride}]/[\text{Pt}]$.

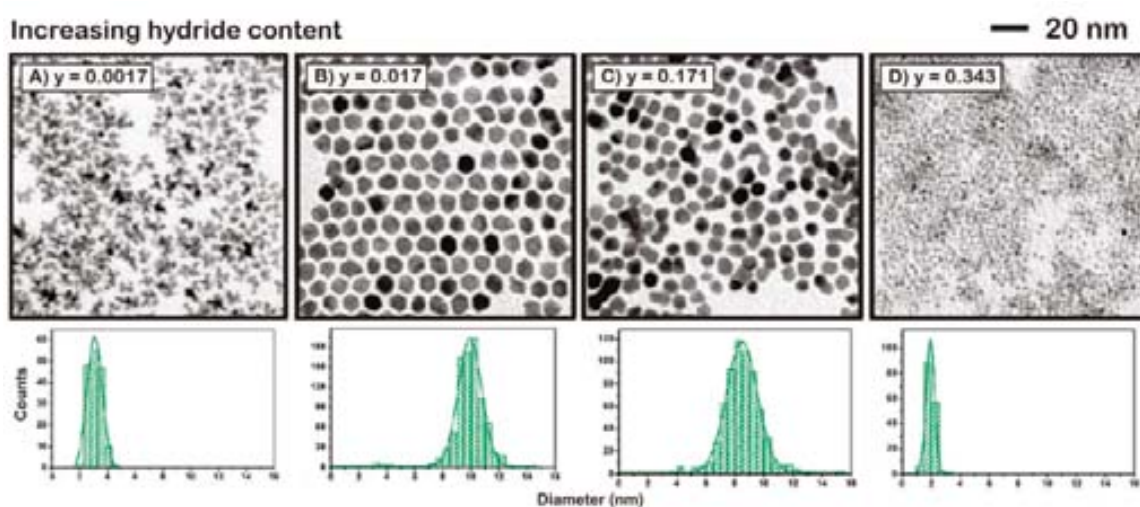


Figure 2.27: TEM images with the corresponding statistical size analysis of the Pt NCs synthesized by increasing the hydride concentration while maintaining constant HDD and Pt precursor concentrations (y represents the $[\text{Hydride}]/[\text{Pt}]$ ratio).

2.3 Synthesis of Pt and PtCo Nanoparticles

The table 2.2 summarizes the evolution on the particle size and shape when increases the hydride concentration. The differences in the polypod morphology in Figures 2.27 A and B, signify that the different reducing strengths of HDD and hydride.





$y = [\text{Hydride}]/[\text{Pt}]$	Size (nm)	Shape	TEM
0.0017	3.1 ± 0.1	Polypod	
0.017	9.8 ± 1.3	Cuboctahedral	
0.171	8.5 ± 1.3	Cuboctahedral/ Spherical	
0.343	1.9 ± 0.3	Cemented Pt NCs	

Table 2.2: Comparison of the size and shape evolution of the NCs obtained by increasing hydride content in the synthesis.

Increasing the HDD content. With the aim of examine the role of HDD in the process, the HDD amount added to the synthesis was varied while maintaining constant Co and Pt concentrations. The increase in HDD concentration is represented by the value of z , which is determined from the ratio of $[\text{HDD}]/[\text{Pt}]$. Figure 2.28 shows a representative set of TEM images of the evolution of the NCs morphology as z varies from 0 to 13,24. It can be observed a wide range of morphologies indicating that it is not just the differential reducing rate, but also the absolute rate which tunes and affects the NC morphology. In detail, a flake-like morphology was observed at $z = 0$ (Figure 2.28 A), illustrating the characteristic shape produced when only one reducer is present in the synthesis. By the addition of different amounts of HDD, the emergence of different shape PtCo NCs from of aggregated spheres (Figure 2.28 B,C) to a mixture of shaped NCs (Figure 2.27 D,E) and eventually monodispersed cubic NCs (Figure 2.28 F,G) were observed. It is interesting the appearance of two NC size species at $z = 4.58$, as this is different from the typical synthesis where only one NC size is normally observed (Figure 2.28 H). The continued increase in HDD concentration led to the appearance of an oval and triangular shaped NCs (Figure 2.28 I,J) instead of the previously seen flake-like morphology, showing the high degeneracy of the system.

The PtCo NCs were also analyzed using XRD (Figure 2.29 C), confirming their crystalline structure, and the content of Co (%) in the PtCo alloy was calculated using Vegard's law. The values obtained oscillate between 2 and 5 %, which are close to the theoretical % Co added to the synthesis and the values of the elemental composition analysis determined by ICP-MS (Figure 2.29 A). There is no particular trend apparent between the % Co and z value, showing that in a high HDD concentration environment, the Co plays a less significant role. Also, NC

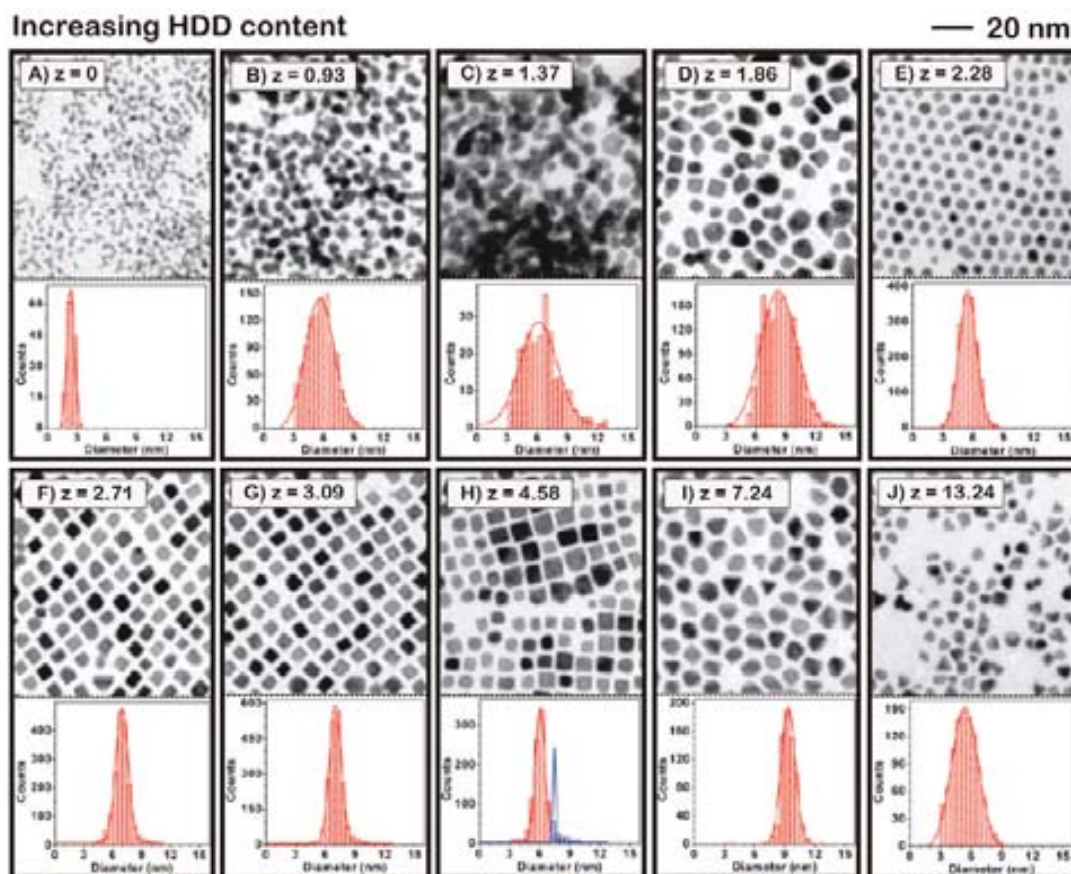


Figure 2.28: TEM images and the corresponding statistical size analysis of the PtCo NCs synthesized by increasing the HDD concentration while maintaining constant Co and Pt precursor concentrations (z represents the $[HDD]/[Pt]$ ratio).

sizes were determined from the Scherrer equation (equation 2.1) and compared with the sizes obtained from TEM images (Figure 2.29 A). The calculated sizes are remarkably close, again showing good agreement between both techniques (Figure 2.29 B).

Finally, we can conclude that when HDD is present as a sole reducer, there is not competition in the reducing rate, and polypod-type morphology is observed (Figure 2.30, R_1). However, in the presence of both HDD and Co, a competition between two reducers leads to large shaped NCs. Depending on the proportion of both reducers, may be a balanced competition between them or one reducer may dominate the other (Figure 2.30, R_1+R_2). Eventually, the continued increase in Co concentration leads to an even faster reducing rate and the appearance of flake-like NCs, similar to the polypod structures obtained using solely HDD (Figure 2.30, R_2). Experiments substituting superhydride for $Co_2(CO)_8$ show the same behavior, but without the shape control effect induced by the Co.

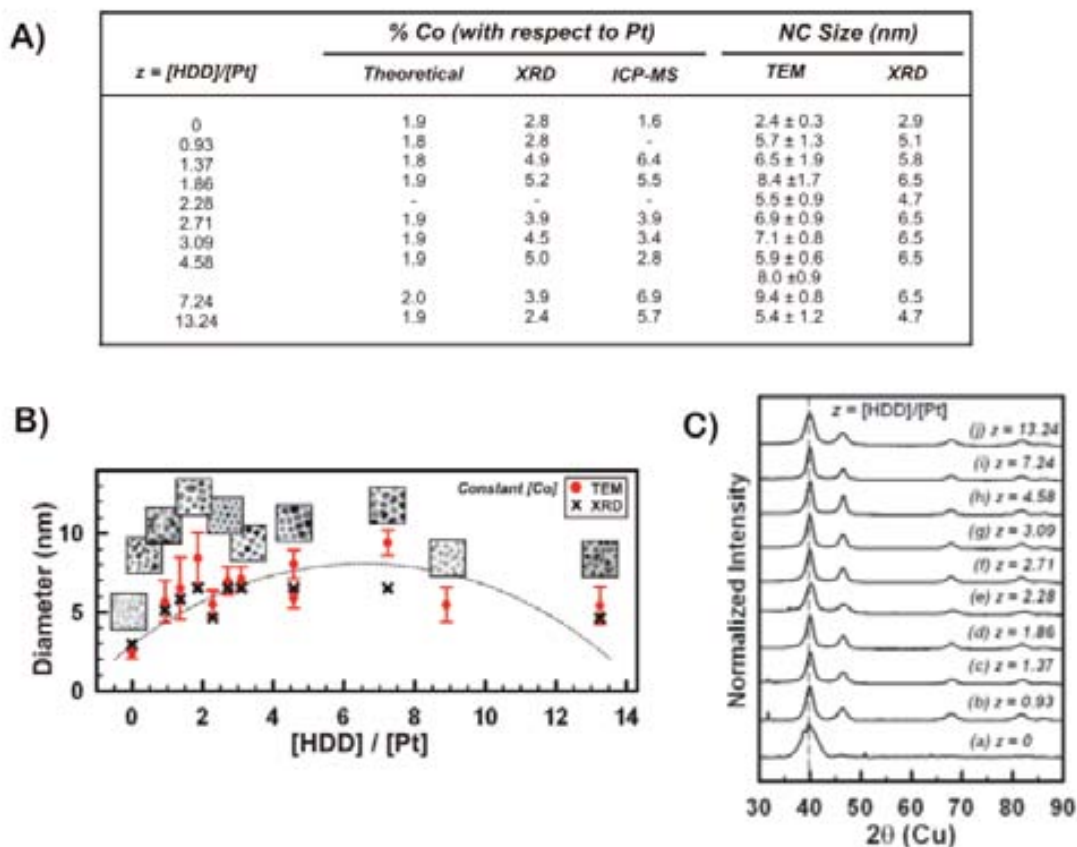


Figure 2.29: A) Table comparing the % Co inside the PtCo NCs (using XRD and ICP-MS) and the PtCo NCs size (using TEM and XRD) at different $[\text{Co}]/[\text{Pt}]$ ratios. B) Plot of $[\text{Co}]/[\text{Pt}]$ versus PtCo NC diameter (nm) obtained from TEM (solid circle) and XRD (x mark). The dotted line is drawn to better represent the change in NC size. C) XRD patterns for the PtCo NCs synthesized in the presence of increasing HDD content while maintaining constant Co and Pt precursor concentrations (z represents the $[\text{HDD}]/[\text{Pt}]$ ratio).

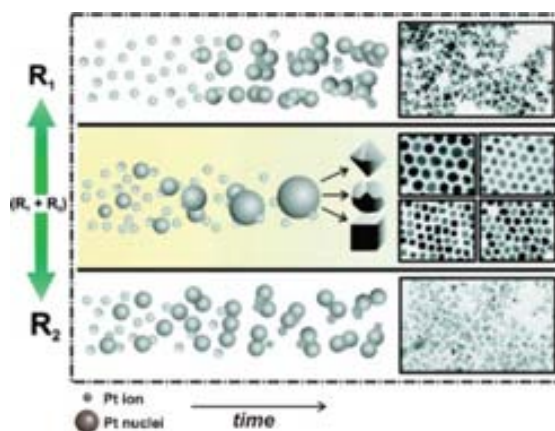


Figure 2.30: Schematic diagram illustrating the growth mechanism of Pt (and PtCo) NCs in the presence of a sole reducer (R_1 or R_2) or a mixture of reducers (R_1+R_2), where R_1 represents HDD and R_2 represents Co.

2.3.2.3 Summary

The synthesis of Pt and PtCo alloy NCs in the presence of one or two reducing agents has been studied. Upon the addition of Pt precursor, an initial burst nucleation of small, amorphous Pt nuclei results in a dramatic decrease on the concentration and availability of the Pt precursor, and thus opens a getaway for the NC growth phase. The existence of both freshly formed nuclei and precursor at the beginning of the reaction represents a highly susceptible and vulnerable stage, where the size and shape of NCs can be easily manipulated.⁷⁷ The relative concentrations of available precursor and the growing nuclei can be altered to have an impact on the growth kinetics by mixing reducers in such a way that they compete to reduce the Pt ions. The presence of only one reducer produces polypod-type morphologies. On the other hand, when the synthesis contains two competing reducers, shaped NCs are obtained. Different morphologies can be produced by taking advantage of the susceptibility of the system to minor changes during the early reaction stages.

2.4 Synthesis of Bimetallic Au/Pt Heterostructures

From the mixed Pt/Co systems, in this section we move to explore Pt/Au systems, where in this case the Pt is the reactive specie and Au the noble one. Hybrid NCs represent a new class of structures where different inorganic materials are joined together in the absence of a mediator (i.e. molecular linker) and bring about materials with novel properties.^{91,92} The most studied geometries are core/shell NCs, where the outer material is uniformly grown around the metallic core.⁹³ But recently, special interest is also being directed towards asymmetrical structures, which are grown with two materials (such as metal/metal,⁹⁴⁻⁹⁶ semiconductor/metal,^{97,98} metal oxide/metal^{99,100} and metal oxide/semiconductor¹⁰¹) epitaxially joined through an interfacial area. In the last years, a wide variety of morphologies such as dumbbells,^{102,103} clover-like⁹⁶ and rod with metal tip^{94,104} have been reported, where their shape depends on how growth can occur (i.e. at specific facets or domains of the NCs).

While a common theme for most of the reported heterodimers is the use of high temperatures during the synthetic process, herein we show a RT synthesis of AuPt heterodimers using a simple protocol.

2.4.1 Experimental

For instrumentation details of this section see Appendix A.4

2.4.1.1 Chemicals

Platinum(II) acetylacetonate [Pt(acac)₂, 98%] was purchased from Strem Chemicals and used as received. Au(III) chloride trihydrate (HAuCl₄·3H₂O, 99%), oleylamine (OAM, 70%), 1,2-dichlorobenzene anhydrous (DCB, 99%), 1,2-hexadecanediol (HDD, 90%), Co carbonyl moistened with 5-10% hexane [Co₂(CO)₈, 90–95%] and 1-undecanol (UD, 98%) were purchased from Sigma-Aldrich and used as received. All chemicals were stored and prepared for synthesis in a UNILab MBraun glove box unless otherwise stated.

2.4.1.2 Synthesis of Pt Nanocrystals

The Pt NCs used in the AuPt heterodimer synthesis were synthesized and purified using a procedure described previously (Chapter 2, Section 2.3.1). Briefly, a solution containing 95 mg of HDD (0.37 mmol), 45 μL of OAM and 10 μL of DCB was added to a 3-neck round-bottom flask equipped with a condenser and stirred under an Ar atmosphere. The solution temperature was increased to 180 °C using a glycerol oil bath over a time period of ~30 to 60 min. Once the boiling temperature of DCB was reached, a 3 mL solution of DCB containing 45 mg of Pt (acac)₂ (0.11 mmol) was added drop-wise at a rate of 0.5 mL/min. 100 μL of Co trace prepared from Co₂(CO)₈ (2 μmol) was then added immediately to the solution. The solution was refluxed at 180 °C for 20 min and gradually cooled down to RT before being transferred to an Ar filled vial. The atomic Pt concentration immediately after synthesis and purification was 0.56 mg/mL (measured by ICP-MS). The concentration of Pt NCs was 1.21 × 10¹⁴ NC per mL (calculated assuming cubic NCs of side length 6 nm, Pt density of 21.45 g/cm and atomic Pt concentration 0.56 mg/mL).

2.4.1.3 Synthesis of AuPt Heterodimers at Room Temperature

A previously purified 0.3 mL solution of Pt NCs in DCB was mixed with 2.7 mL solution of 1% OAM in DCB. Next, 3 mL solution of AuCl⁴⁻ in DCB (0.79 mM stock prepared with 5% UD to ensure its complete dissolution) was then added, and the resulting solution was stirred at RT for different time intervals. The final fractions of OAM and UD in the solution were 0.45% and 2.5%, respectively. The growth of the heterodimers was monitored using TEM and UV-Vis, and the solution was purged with N₂ after each measurement and stored in a darkened environment.

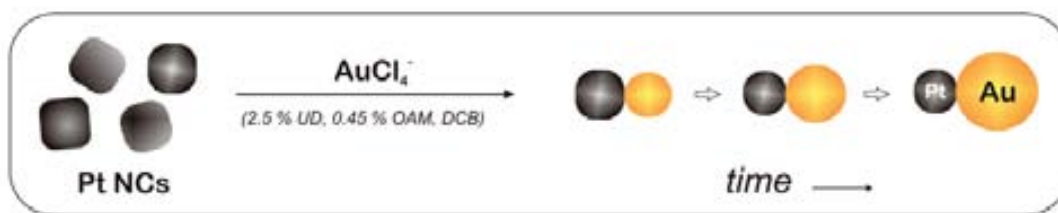


Figure 2.31: Schematic representation of the Pt/Au heterodimer formation.

2.4.2 Results and Discussion

Pt seeds play a very important role for the nucleation and growth of Au on Pt NCs to form heterodimer structures at RT in the presence of OAM as reducer. The Pt NCs drastically accelerates the reaction by acting both as seed platforms for the Au nucleation and possibly as a catalytic reducer especially when the initial concentration of Au ions in solution is high.

2.4.2.1 The Reaction Time.

The growth of the Au domains on the Pt seeds was followed with time. The initial solution appeared brownish due to the presence of Pt NC seeds, but it eventually evolved to pink/reddish after 24 h. TEM samples taken at different reaction times show that the size of the growing Au NCs increased from ~ 8 nm, at 24 h, to ~ 9 -10 nm, at 72 h, and remained constant afterwards (Figure 2.32). After 96 h of reaction, two different heterodimer structures were observed: i) some having a peanut-like structure and ii) others showing a smooth merging between Au and Pt NCs. In order to evaluate the effect of an excess of Au^{3+} ions in solution, more Au precursor was added to the reaction mixture after 196 h and stirred for an additional 4 days. It was observed an increase in the size of the pre-existing Au domains to 15.6 nm, along with some free Au NCs. Also, multiple heterojunctions in each particle (i.e. Au-Pt-Au) were not observed as happens at higher temperatures.⁹⁶

The formation of Au/Pt heterodimers can be explained as follows. As Au begins to nucleate onto a particular facet of a Pt seed (most likely on the 111 surface), electrons are transferred from the Pt to the Au between their Fermi levels across the interface.⁹⁹ The charge distribution is thus modified to compensate for the potential at the Au/Pt interface and the other exposed Pt facets become much less effective points for the nucleation of Au. Therefore, when more Au^{3+} precursor is added to the existing heterodimers, the slight lattice mismatch tends to favor the growth of Au ions on Au NC rather than on another facet of Pt NCs. Also, at RT, the required energy for the nucleation is higher than for the growth, favoring the heterodimer formation.

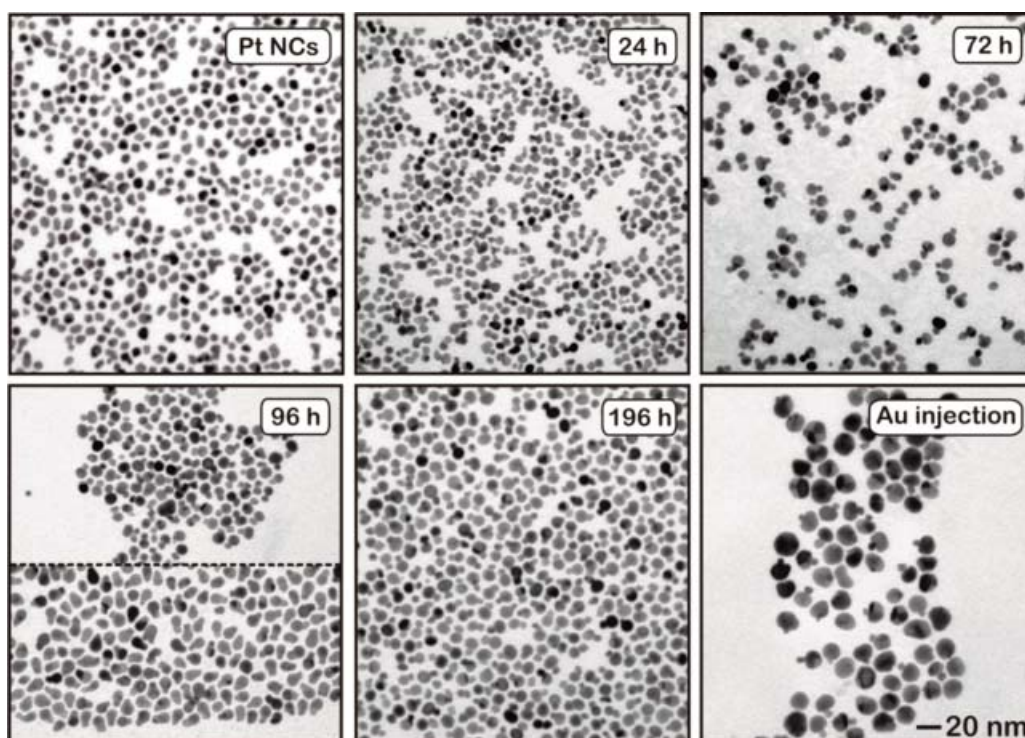


Figure 2.32: TEM images of the Pt/Au heterodimer evolution with time.

2.4.2.2 Structural Characterization

The HRTEM analysis of the heterodimers (Figure 2.33) shows how Au-domains growth epitaxially on top of Pt seeds, and some of the Au NCs domains exhibit twin dislocations and are faceted. The FFT power spectrum analysis (Figure 2.33 A) shows that both NCs are oriented along the $[110]$ zone axis and the pattern also presents the typical striking lines for such twinned and faceted NCs. Geometrical Phase Analysis (GPA)^{105,106} of the heterodimers was carried out in order to confirm the changes in the cell parameter or fringe deformation due to the chemical variation along the NCs (Figure 2.33 B). Taking into account that the interplanar distances of the $\{111\}$ planes are 0.236 and 0.226 nm for Au and Pt respectively, we would expect a variation of 4% in the fringe distance between both parts. The results obtained with GPA match with the predicted variations and show the two different metals with the fringe deformation in color maps (%).

The crystalline structures of the heterodimers were also characterized by powder XRD and compared with the diffraction pattern of individual Au and Pt NCs. The determined XRD spectrum shows a mixture of the two patterns originating from nanosized Au and Pt particles (Figure 2.34 A). The evolution of the heterodimer formation has been also followed with time by UV-Vis spectroscopy giving us information of the surface SPR, a direct measurement of the electron cloud of the conforming metals (Figure 2.34 B). While Pt NCs do not have maximum

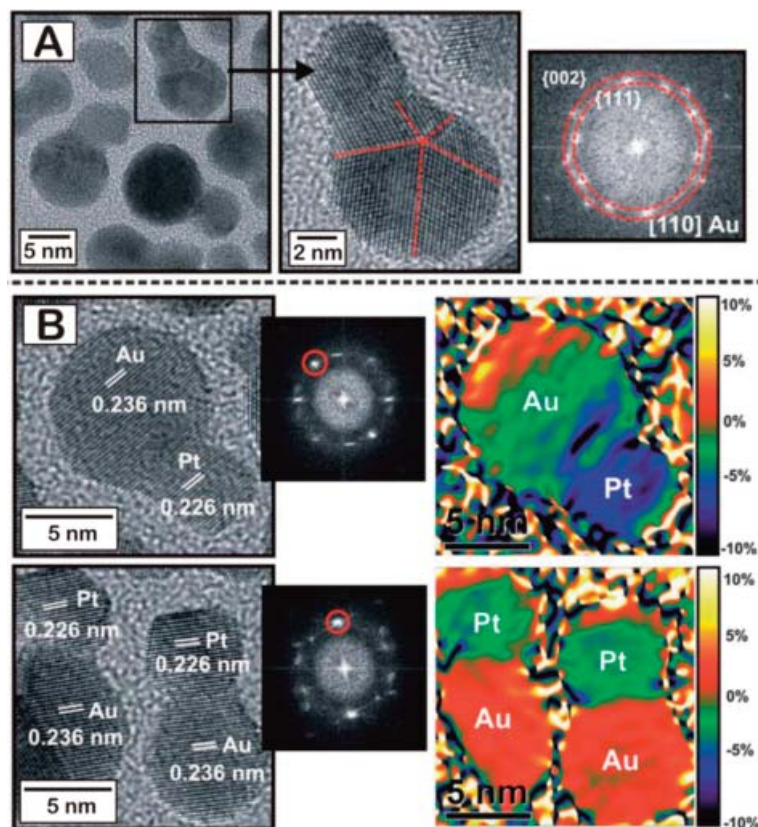


Figure 2.33: A) HRTEM image and B) GPA of the heterodimers with the corresponding FFT power spectra. The red circles in the FFT indicates the (111) spot used for the GPA. Colored areas correspond to crystal domains of the same lattice parameters, which go in the sense blue, green, and red towards a higher density of the material.

SPR band in the visible range ($t = 0$ h), a small band begins to emerge after 10 h of reaction. A maximum SPR was observed at 24 h of reaction, corresponding to the growth of the Au NCs attached on the Pt seeds. As time progressed, more prominent and narrower SPR bands were observed (~ 537 - 543 nm) due to the continuous growth of the Au NCs and increase of monodispersity of the NC size. During the heterodimer evolution, a slight blue-shift of ~ 6 nm was observed. This is consistent since the growth of larger Au NCs red-shifts the Plasmon while the presence of Pt induces a charge transfer to the Au and causes the blue-shift. Thus, when more Au^{3+} precursor was added, a red-shift of the band and an increase in the absorbance were observed.

Heterodimers exhibit unique optical properties due to the coupling and the electronic effects of the two different metals domains. While individual Au NCs (5-20 nm in size) exhibit a SPR around ~ 520 nm,¹⁰⁷ the heterodimers were detected in the 540-550 nm region. This red-shift suggests an effective coupling where the electronic structure of Au is modified by the presence of the Pt seeds.

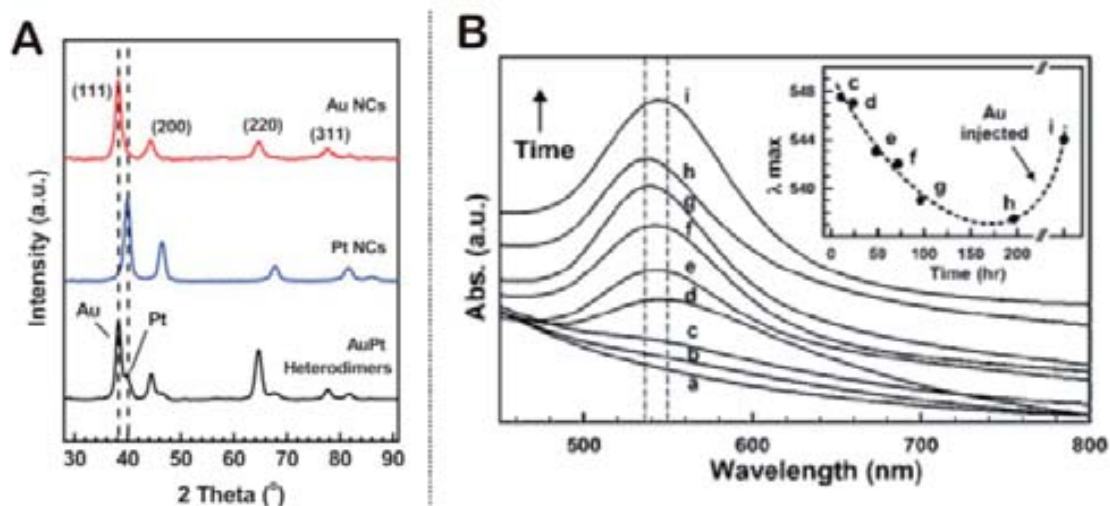


Figure 2.34: A) Powder XRD spectra comparing Au NCs, Pt NCs and heterodimer crystalline structures after 114 h of reaction at RT. B) UV-Vis spectra for the heterodimers at different reaction time: 0 h (a), 6 h (b), 10 h (c), 24 h (d), 48 h (e), 72 h (f), 96 h (g), 196 h (h) and after additional Au³⁺ injection (i). Inset: plot of maximum absorbance peak (λ) vs time. The dotted line illustrates the change in λ .

2.4.2.3 Role of Pt Nanocrystals

Control studies were performed to determine the role of the Pt seeds in the heterodimer formation. When the synthesis was repeated in the absence of Pt NCs, lightly pinkish colored solution is observed only after 196 h. Analysis by TEM showed polydispersed non-spherical Au NCs (Figure 2.35), thus confirming the role of the OAM as a mild reducer of the Au³⁺ as it has been reported previously elsewhere.^{96,108} It can be observed a dramatic decrease of the reaction rate when comparing with the presence of Pt NCs (from 196 h to 24 h), indicating that the Pt seeds strongly favor the nucleation of Au. This fact can be understood in terms of Pt NCs acting as both, i) nucleation center and/or ii) catalyzing the reduction of Au ions when the initial concentrations are very high.

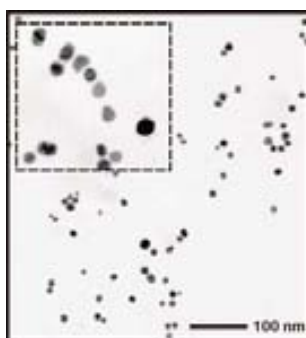


Figure 2.35: Control experiment: synthesis without Pt seeds.

To determine if the Pt NCs suffer an etching and dissolution during the formation of the heterodimers due to their reductive role, the synthesis was repeated both in the presence and absence of Au^{3+} precursor for 24 h. The suspended particles were precipitate and the supernatant analyzed by ICP-MS. The chemical analysis of the resulting supernatant did not show a significant presence of Pt^{2+} in neither solutions (0.2 and 0.3 % of the mass in the absence and presence of Au^{3+} , respectively). These results further corroborate the role of the OAM as the reducer in these reactions.

The heterodimer structures were also synthesized in the presence of different Au^{3+} precursor concentrations while maintaining a constant concentration of Pt NCs (10nM) (Figure 2.36). The results show that the heterodimers became more apparent as the initial concentration of Au^{3+} increased. The main diameter of the Au domains increased from 7.9 ± 1.0 nm to 9.1 ± 1.4

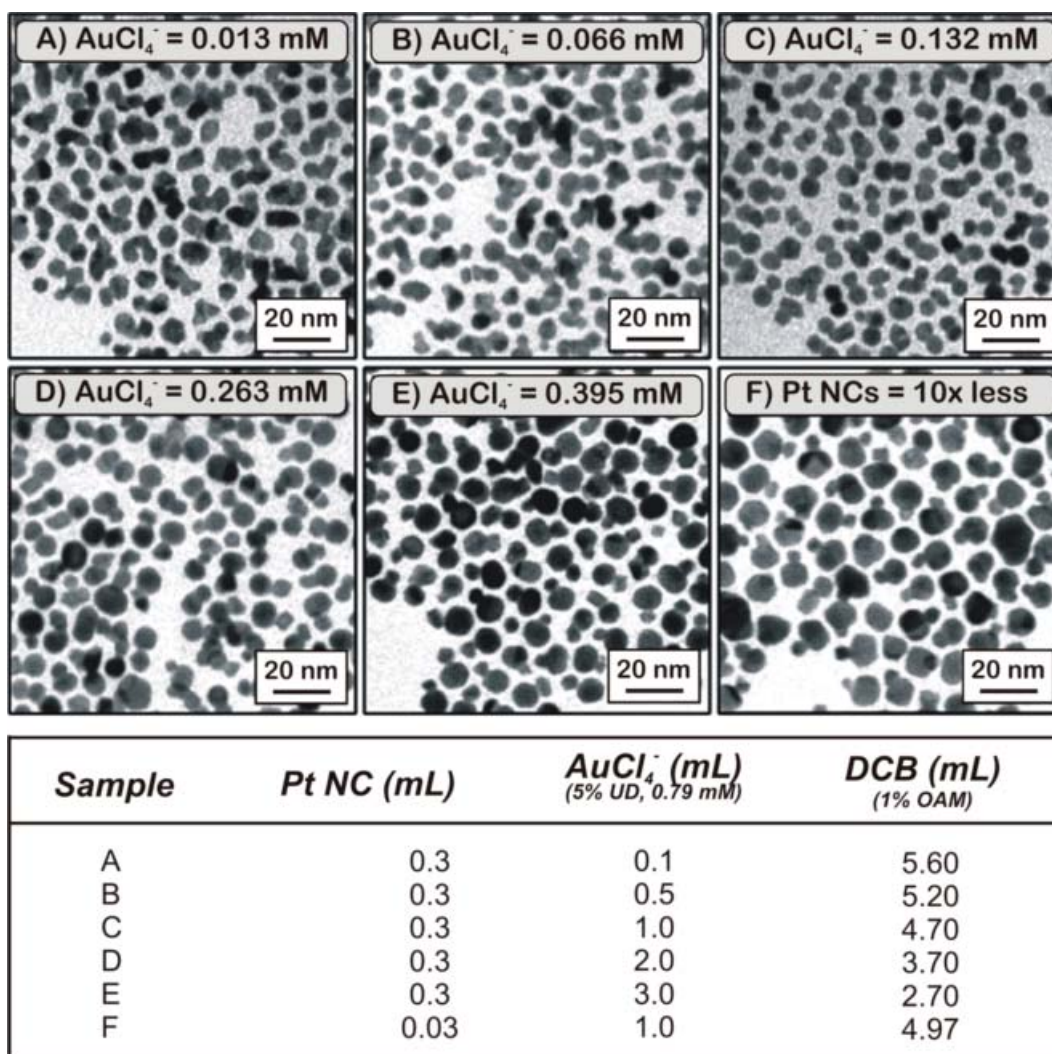


Figure 2.36: TEM images of the heterodimer structures with increasing Au^{3+} precursor concentration (A-E) and decrease of the Pt NCs amount (F), sampled after 96 h of reaction.

nm (Figure 2.36, A-E), thus indicating that the growth of Au NCs is directly related to the increased availability of Au³⁺ ions to be reduced on top of the Au domains. By the contrary, when the Pt seed concentration was decreased ten times while maintaining Au precursor constant and similar to Figure 2.36 C, the size of the Au domains was 10.6±1.9 nm (Figure 2.36 F).

2.4.3 Summary

In this section, we have reported a method for the synthesis of AuPt heterodimers performed at RT using OAM as the reducer and PtNCs as seeds. The presence of Pt NCs markedly accelerates the nucleation rate of Au, which suggests its role as both nucleation platforms and initial catalytic reducer. HRTEM showed an epitaxial growth of Au on Pt, favored by the slow growth conditions. These soft conditions also allows an easily monitorization of the SPR band shift with time.

2.5 Synthesis of Extremely Long Rod Shaped Au Nanocrystals

As it is well known, properties of materials at the nanometer scale, including optical, magnetic, electronic, crystallographic and catalytic, are size and shape dependent and often different from their corresponding bulk materials.¹⁰⁹⁻¹¹³ Optical properties are especially important when the particles have high aspect ratios (length/width). Spherical particles show a single SPR but in particles with shape anisotropy, such Au nanorods (Au NRs), a second surface Plasmon band is typically observed at lower energies. The two different Plasmon absorption bands are related to the two different oscillations of the electrons: transversal, across the short dimension, and longitudinal, along the long axis; being the second very sensitive to the aspect ratio.¹¹⁴ This characteristic makes that the Au NRs present very interesting optical properties such as enhancement of the fluorescence over bulk metal nanospheres, which make them able to be used in sensory applications.^{115,116}

Different approaches have been attempted to produce long Au NRs such as lithography,¹¹⁷ template-mediated synthesis^{118,119} and reduction methods in aqueous surfactant media. In the last method mentioned there are two known approaches: the electrochemical¹²⁰ or photochemical¹²¹ method and the seed-mediated growth method.¹²² Among all methods, the

seed-mediated growth is one of the most commonly used, where previously synthesized small particles (seeds) are used as nuclei for the anisotropic growth of the NRs. Moreover, the use of cationic surfactant CTAB is a crucial parameter in the synthesis of Au NRs by a seed-mediated growth method.

The growth mechanism of Au NRs remains a subject of debate, but all mechanisms are based on the crystal growth inhibition, which is closely related to the crystalline structure and thermodynamic stability of the different facets of the fcc structure of the metallic Au. CTAB is used as a structural directing agent due to its preferential adsorption on the (100) surface. Murphy and co-workers proposed the growth mechanism of Au NRs governed by preferential adsorption of CTAB to different crystal faces during the growth in a bilayer conformation.¹²³⁻¹²⁵ Also they developed a rod synthesis where aspect ratio (AR) was controlled by varying the ratio of seeds to the metal salt, and rods with AR between 2 and 18 can be synthesized by using this three-step seed-mediated approach.¹²² Later on, it was discovered that with the addition of an appropriate amount of nitric acid to the growth solution, and Au NRs with high AR (>20) can be produced in a high yield.^{126,127} Huang *et al.* also discovered that rods growth was promoted in acidic solutions, and they were able to increase the AR to over 200 with also decreasing the amount of initial seeds.¹²⁸ However, large amounts of Au precursor were needed to obtain long rods, thus the reaction required to be multi-step to avoid new nucleation. In this section we present a one-step synthesis, based in the seed-mediated growth method, which produces high AR Au NRs at RT and using Pt seeds as nuclei.

2.5.1 Experimental

For instrumentation details of this section see Appendix A.5

2.5.1.1 Chemicals

Hydrogen tetrachloroaurate trihydrate ($\text{HAuCl}_4 \cdot 3\text{H}_2\text{O}$), potassium tetrachloroplatinate(II) (K_2PtCl_4), cetyl trimethylammonium bromide (CTAB) 95%, sodium citrate, sodium borohydride (NaBH_4) and ascorbic acid (AA) were purchased from Sigma-Aldrich and used as received without further purification.

2.5.1.2 Synthesis of CTAB Stabilized Pt Seed Nanoparticles

The synthesis of Pt NPs stabilized in CTAB was carried out following the method described by Grzelczak *et al.*¹²⁹ A mixture of 9.63 mL of CTAB (0.1 M) with 50 μL of K_2PtCl_4 (0.05 M)

was heated up to 40 °C for 5 min until the solution became clear. After adding 0.3 mL of NaBH₄ (0.06 M), the vial was capped immediately. After 10 min, the vial was opened and stirred for several minutes for the total decomposition of the NaBH₄.

2.5.1.3 Synthesis of CTAB Stabilized Au Seed Nanoparticles

The synthesis of Au NPs stabilized in CTAB was prepared via the method developed by Nikoobakht and El-Sayed.¹³⁰ Briefly, 5 mL of CTAB (0.2 M) were mixed with 5 mL of HAuCl₄ (0.0005 M). Next, 0.6 mL of freshly prepared NaBH₄ (0.01 M) solution were added to the mixture while vigorous stirring, which resulted in the formation of a light-brown solution within a few seconds. Stirring of the solution was continued for 2 min.

2.5.1.4 Synthesis of Au Rods Using Pt Seed Nanoparticles

A growth solution was prepared by mixing 5 mL of CTAB (0.2 M) and 5 mL of HAuCl₄ (0.001 M). After that, 50 µL of AA (0.1 M) were added as a mild reducing agent, changing the growth solution from dark yellow to colorless (reducing Au³⁺ to Au¹⁺). Then, a volume between 5 and 30 µL of the pre-synthesized Pt seeds was added and gently mixed for 10 seconds. The solution was kept at RT for 1 month. The evolution of the reaction was followed by UV-Vis and TEM.

2.5.1.5 Synthesis of Au Nanorods Using Au Seed Nanoparticles

Three different growth solutions were prepared by addition of three different volumes (0.015 mL, 0.15 mL and 1.5 mL) of K₂PtCl₄ (0.004 M) to 5 mL of CTAB (0.2M). Next, 5 mL of HAuCl₄ (0.001 M) and 55 µL of AA (0.1 M) solution were added to each growth solution by means of a step-by-step addition, and then gently mixed for 10 seconds. It is worth noting that the three solutions above are identical except for the Pt ion content. The final step was the addition of 12 µL of the pre-synthesized Au seedNP solution to the growth solutions. The solutions were kept at RT.

2.5.2 Results and Discussion

2.5.2.1 Structural Characterization

Following the procedures reported in the experimental section, high AR Au NRs have been obtained when Pt-CTAB capped NPs were used as seeds. Figure 2.37 shows TEM images of the Au rods after 1 day (A) and 1 month (B). In the size distribution diagram it can be observed that after one day reaction the Au NRs have a length between 100 and 600 nm (Figure 2.37 A, inset),

and a medium width of 26 ± 5 nm. The synthesis of NRs is accompanied by the formation of spherical particles and plates as by-products. After 1 month, the Au rods have grown until reach a lengths of several microns ($>10 \mu\text{m}$) and a widths of 36 ± 11 nm (Figure 2.37 B,C).

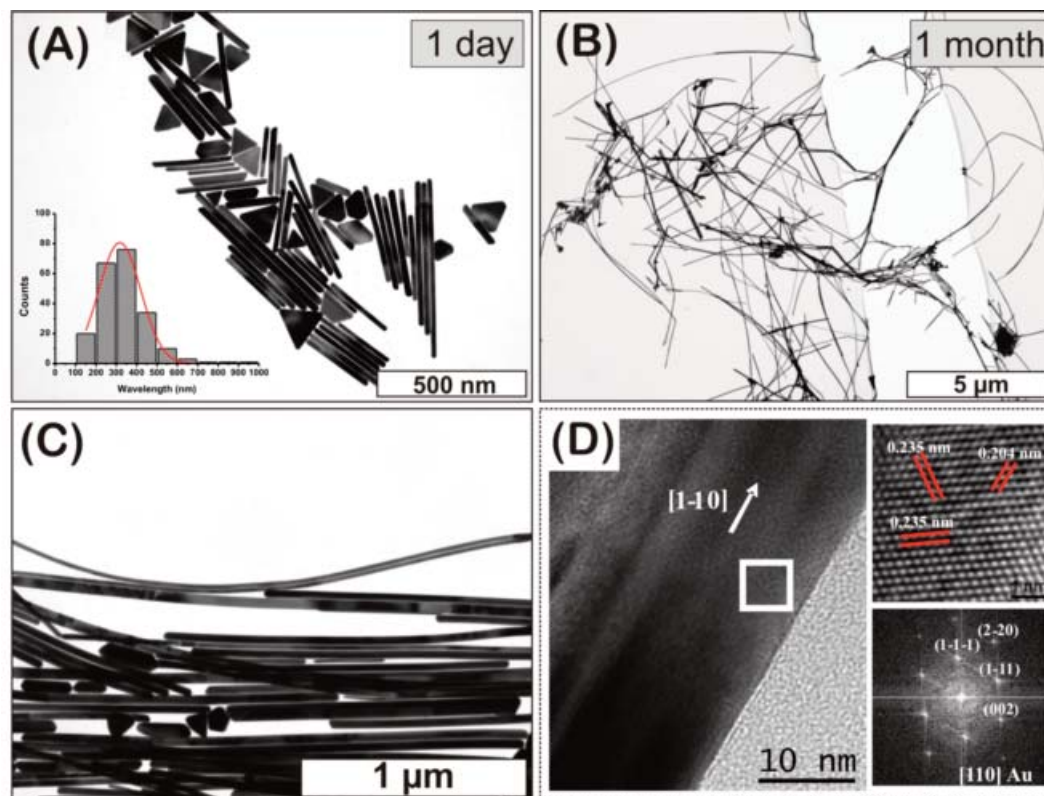


Figure 2.37: TEM images of the Au NRs produced by one-step seed-mediated growth method in presence of metallic Pt at different times: 1 day (A) and 1 month (B) and (C); inset in A: size distribution diagram of the length of Au NRs at 1 day reaction time. D) HRTEM image of one of the Au rods with its associated FFT power spectra.

The Au NRs perfectly crystallize in the Au fcc cubic structure. Their growth direction is always along the $[1-10]$ axis (Figure 2.37 D), and remarkably all the NRs are single crystal. However, the NRs contain plenty of crystalline $\{111\}$ twin and/or stacking fault defects parallel to the growth axis. Figure 2.38 shows HRTEM images of a twinned Au NR, found on a rotated orientation (e.g. $[112]$ zone axis), on the top part (growth front, A) and some middle section (B). In both cases the presence of twins and stacking faults is evidenced clearly crossing the entire length of the NR. These twins tend to occur as rotation along the $\{111\}$ planes parallel to their growth axis and in the central part of the NR. We have analyzed with the FFT power spectra both the central and the lateral part of the NR finding the presence of multiple spots on the $(-1-11)$ axis in the central part, meaning that the twins are partially ordered. In fact, as shown

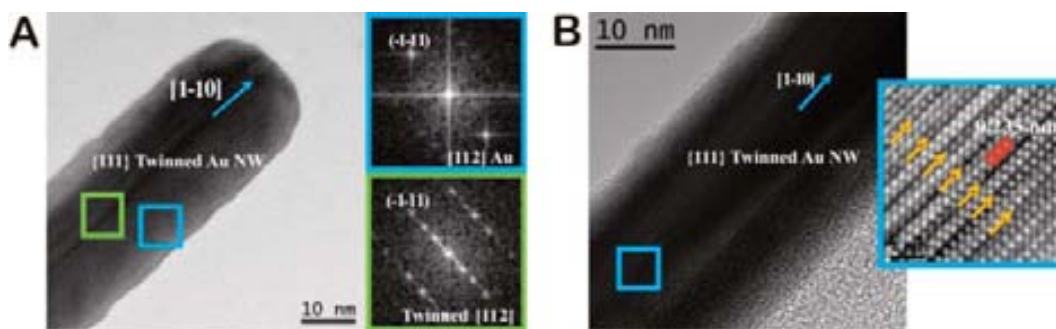


Figure 2.38: Panel of HRTEM images of A) the top part (growth front) of a twinned Au NR, with the corresponding FFT patterns of the selected areas, and B) a middle section of the same NR showing the twin ordered superstructure.

on the yellow arrows, these twins may occur every 2 or 3 (-1-11) atomic planes forming a kind of ordered superstructure.

The presence of {111} twins parallel to the zone axis is a common feature found in NWs composed of cubic crystalline materials, e.g. in Si NWs.¹³¹ But moreover, the presence of twins mainly in NWs have been shown recently to have a finest effect, by changing the local stacking of the atomic planes and thus creating different structural polytypes localized in some areas of the NW, which can present different optical and electrical properties.¹³²⁻¹³⁶

The main feature of these Au NRs is their extremely length, up to tenths of microns, fact that even allow us to see them by optical microscope (Figure 2.39 A). Figures 2.39 B and C also show SEM images of the Au NRs deposited onto HOPG substrate. The EELS spectra analysis realized to the sample indicates that both particles (by-products) and Au NRs are formed by pure Au and no signal of Pt (both overlapping in the EELS spectra) was found.

In the reported mechanism for the Au NR formation, the surfactant plays an important role. First, the CTAB interacts with $[\text{AuCl}_4]^-$ before the reduction process is induced, leading to the formation of $[\text{AuCl}_4]^-$ -CTAB metallo-micelles. Later, the AA reduces Au^{3+} to Au^{1+} (process confined in the metallo-micelle) and subsequently the seeds induce the catalytic reduction of Au^{1+} to Au^0 . And, finally, the adsorption of CTAB on the growing surface confines the direction growth. Generally, a high concentration of CTAB it is required for NR growth (0.1 M), even though its critical micelle concentration (cmc) is 100 times lower (0.9 mM). The rate of the reaction is controlled by the collisions of the metallo-micelles, formed by the Au^{1+} ions trapped in the CTAB, with the Pt seeds. The cmc is determined by the temperature of the solution, and working at RT allows us to decrease the solubility of CTAB and, in that way, slow down the reaction. Thus, reducing the solubility allows decrease the availability of Au ions for the growth process and also avoid new nucleation. Considering this, we have a kinetic control of the

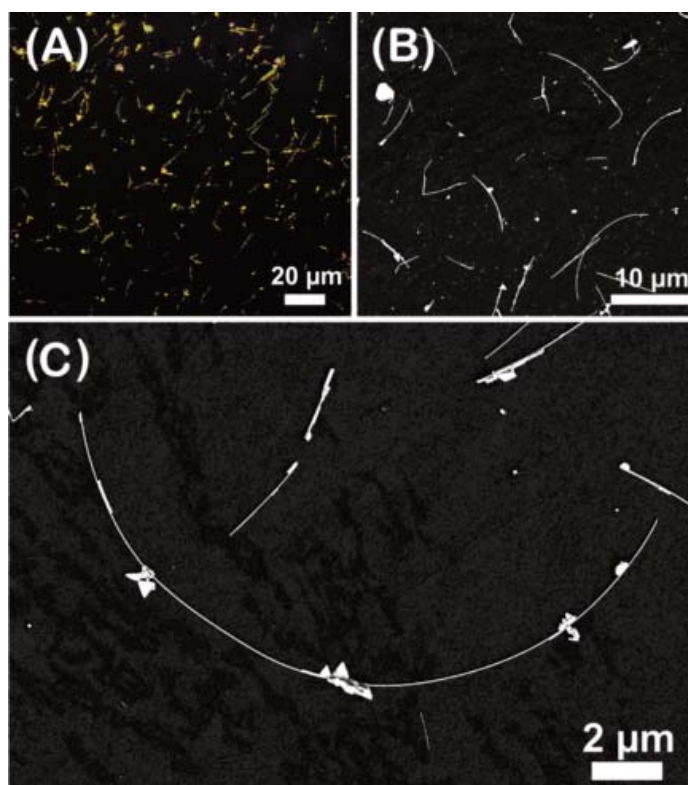


Figure 2.39: Optical microscope image of the extremely Au NRs deposited onto a mica substrate (A) and SEM images of the Au NRs deposited HOPG substrate (B and C).

synthesis favoring the formation of the extra long Au NRs. However, secondary nucleation was not completely avoided and some by-products as big particles and plates appeared as the NR grew longer. Furthermore, it has been established that the morphology of the final particles is mainly determined by the number of twin defects present in the initial seeds.¹³⁷ Considering that, the by-products obtained can also be attributed to the possible polydisperse morphology of the Pt seeds, due that we also observed Au plates of the order of microns.

2.5.2.2 Effect of Pt²⁺ and Pt Seeds in the Synthesis

Control studies were performed to further substantiate the role of Pt in the NRs formation. For study if the Pt ions had some effect in the growth process, we performed some experiments varying the amount of Pt²⁺ in the synthesis. The procedure reported in the experimental section was followed using in this case Au seeds synthesized in CTAB, instead of Pt seeds, with the objective of had the presence of Pt in the system only in ionic form. It could be observed (Figure 2.40) that as the amount of Pt²⁺ increases, the rod size decreases until produce polydisperse Au NPs of ~200 nm in diameter as main product. From that, it can be conclude that the presence of Pt²⁺ avoids the formation of rods, and is the presence of the Pt as metallic particle that helps the extremely long Au NRs formation.

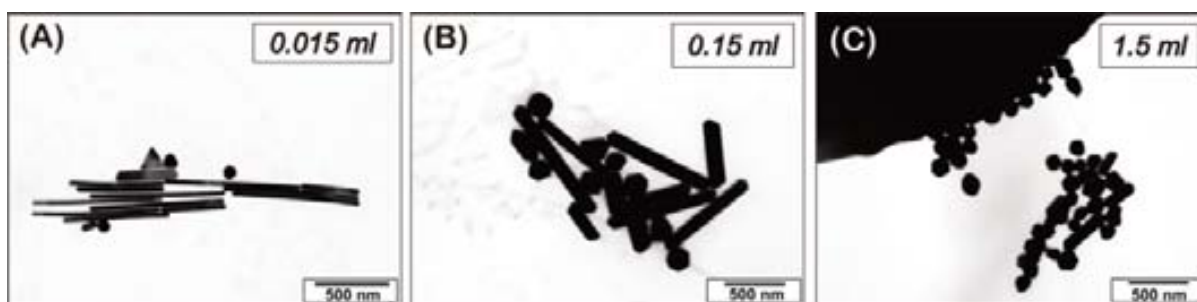


Figure 2.40: TEM images showing the Pt salt (K_2PtCl_4) effect in the synthetic process. Volumes of K_2PtCl_4 solution (0.004 M) added: 0.015 mL (A), 0.15 mL (B) and 1.5 mL (C). As the bigger the amount of Pt seeds the lower the formation of rods.

Furthermore, sometimes it was observed a narrower tip at the end of the rods at short times of the synthesis (Figure 2.41). This, at least, remembers the colloidal synthesis of Ge NRs published by Korgel *et al.* based on metal NC-seeded solution-liquid solid (SLS) growth.¹³⁸

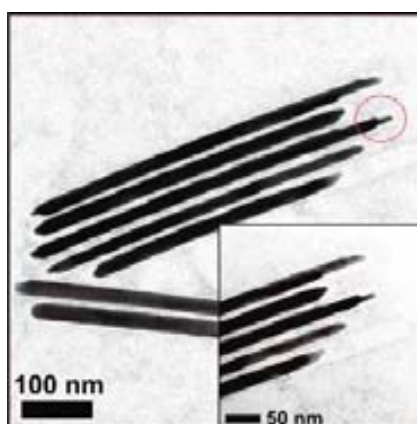


Figure 2.41: TEM image of Au NRs at 1 day reaction, where it can be observed an elongated tip at the end of the NRs.

2.5.2.3 Effect of Different Amount of Pt Seeds in the Synthesis

It has also been studied the effect of the variation of the amount of Pt seeds. As the amount of seeds increased, more by-products such as spherical particles, plates and shorter rods were obtained, as well as less proportion of long NRs were observed. Therefore, we can also conclude that large amounts of seeds favored the formation of more nucleations, thus obtaining less long NR (Figure 2.42). Besides, if none seeds were added to the growth solution no changes were observed.

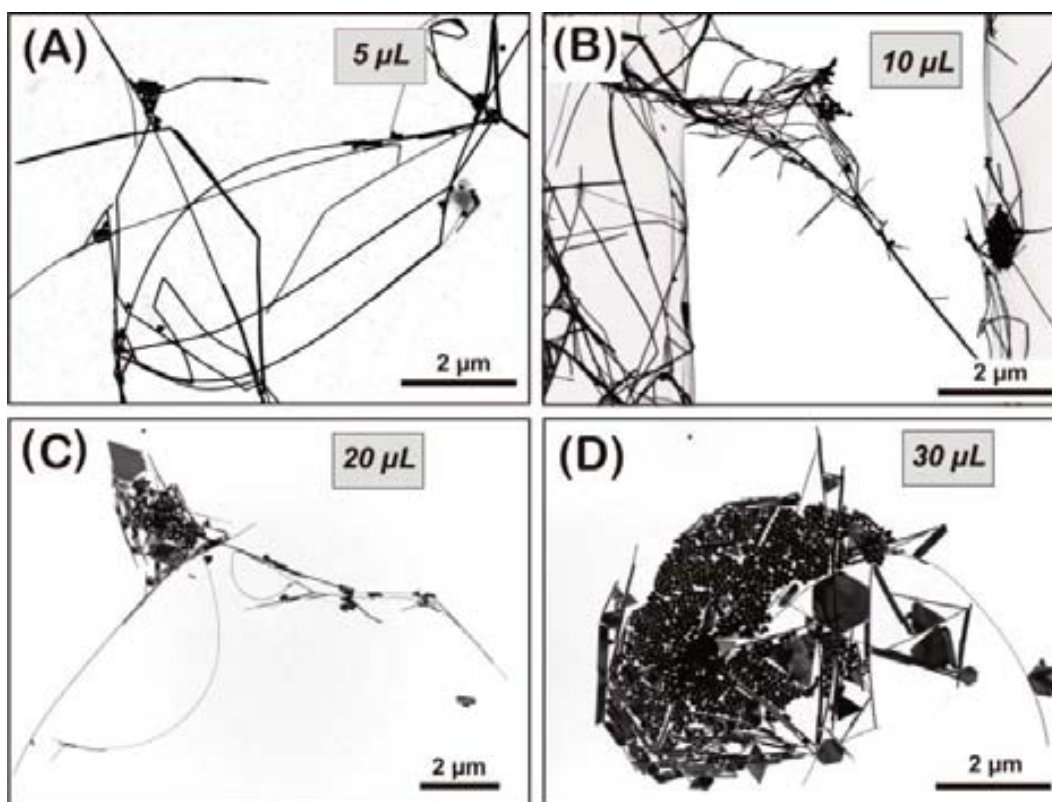


Figure 2.42: The effect of Pt seeds in the synthetic process. TEM images of different samples where different volumes of seeds were added: 5 μL (A), 10 μL (B), 20 μL (C) and 30 μL (D).

2.5.3 Summary

Au NRs of several microns have been synthesized in the presence of Pt NPs in aqueous solution, at smooth conditions and at RT. It has been demonstrated that the catalytic activity of the Pt seeds can be used for the seed-mediated growth and RT reduction of Au^{3+} in aqueous CTAB solution, leading to high AR rods to over 200. It can be also assured that the Pt is involved in the formation of the long NRs in form of metallic NPs and it is not taking an active part as an ion. A possible applicability of these structures can consist in their implementation into electronic systems which will allow study fundamental aspects of electronic transport.

2.6 Conclusions

This chapter has been devoted to a detailed description of the synthesis of different metallic and bimetallic particles, as well as to a detailed structural characterization.

In the case of magnetic Co NPs, their magnetic characterization has been also performed. Due to the high dependence of the magnetic properties with the oxidation state, the oxidation studies of the Co NPs became an important subject. Some interesting oxides such as CoO hollow NPs has been deeply studied. The Co NPs will be subject of intense research in the next chapters, which are centered in the better understand of their SA process and the interactions that are involved, by different techniques.

The synthesis of diverse Pt NPs and PtCo alloy NPs has been reproducibly synthesized as monodisperse and crystalline NCs in stable colloidal solution. Various NCs shapes has been obtained with subtle changes, which indicate the high susceptibility and mutability of the NC shape in front to the modification of the reaction kinetics at the early reduction stages. It has been also determined the role of the Co NPs as shape-directing agents during the synthetic process. Moreover size and shape control has been obtained by combining different reducers, and the importance of the competitive role between reducing agents has been explored.

We reported the synthesis of AuPt heterodimers by using a simple protocol, and the role of both OAM and Pt NCs in the reduction and nucleation of Au has also been investigated. The synthesis presented two significant aspects: firstly, the synthesis was conducted at RT, which enabled the heterodimer growth to progress at a slower rate and thus allowed monitoring of the Au nucleation process; and secondly, these conditions allowed epitaxial growth with no crystal modification at the Au-Pt interphase.

Finally, Au long NRs have been synthesized through one-step synthetic process based in the commonly used seed-mediated growth method for synthesizing Au rods. Our modified process produces high aspect ratio gold NRs at RT by using Pt seed as nuclei and reaction catalyst. The Au NRs perfectly crystallize in the Au fcc cubic structure and remarkably all are single crystal. Moreover, the grow direction was always along the [1-10] axis and contain plenty of crystalline twins parallel to the grow axis.

2.7 References

1. Alivisatos, A. P. "Nanocrystals: Building Blocks for Modern Materials Design". *Endeavour* **1997**, 21, 56-60.
2. El-Sayed, M. A. "Small Is Different: Shape-, Size-, and Composition-Dependent Properties of Some Colloidal Semiconductor Nanocrystals". *Accounts of Chemical Research* **2004**, 37, 326-333.
3. Yin, Y.; Alivisatos, A. P. "Colloidal Nanocrystal Synthesis and the Organic-Inorganic Interface". *Nature* **2005**, 437, 664-670.
4. Sun, S. H.; Murray, C. B. "Synthesis of Monodisperse Cobalt Nanocrystals and Their Assembly into Magnetic Superlattices (Invited)". *Journal of Applied Physics* **1999**, 85, 4325-4330.
5. Peng, X.; Manna, L.; Yang, W.; Wickham, J.; Scher, E.; Kadavanich, A.; Alivisatos, A. P. "Shape Control of Cdse Nanocrystals". *Nature* **2000**, 404, 59-61.
6. Jana, N. R.; Gearheart, L.; Murphy, C. J. "Seeding Growth for Size Control of 5–40 Nm Diameter Gold Nanoparticles". *Langmuir* **2001**, 17, 6782-6786.
7. Puntès, V. F.; Krishnan, K. M.; Alivisatos, A. P. "Colloidal Nanocrystal Shape and Size Control: The Case of Cobalt". *Science* **2001**, 291, 2115-2117.
8. Black, C. T.; Murray, C. B.; Sandstrom, R. L.; Sun, S. "Spin-Dependent Tunneling in Self-Assembled Cobalt-Nanocrystal Superlattices". *Science* **2000**, 290, 1131-1134.
9. Sun, S.; Murray, C. B.; Weller, D.; Folks, L.; Moser, A. "Monodisperse FePt Nanoparticles and Ferromagnetic FePt Nanocrystal Superlattices". *Science* **2000**, 287, 1989-1992.
10. Pankhurst, Q. A.; Connolly, J.; Jones, S. K.; Dobson, J. "Applications of Magnetic Nanoparticles in Biomedicine". *Journal of Physics D-Applied Physics* **2003**, 36, R167-R181.
11. Dobson, J. "Magnetic Nanoparticles for Drug Delivery". *Drug Development Research* **2006**, 67, 55-60.
12. Goldman, A. *Handbook of Modern Ferromagnetic Materials* (the Springer International Series in Engineering and Computer Science); Springer, **1999**.

- 13.** Dinega, D. P.; Bawendi, M. G. "A Solution-Phase Chemical Approach to a New Crystal Structure of Cobalt". *Angewandte Chemie International Edition* **1999**, 38, 1788-1791.
- 14.** Puentes, V. F.; Krishnan, K. M.; Alivisatos, P. "Synthesis, Self-Assembly, and Magnetic Behavior of a Two-Dimensional Superlattice of Single-Crystal Epsilon-Co Nanoparticles". *Applied Physics Letters* **2001**, 78, 2187-2189.
- 15.** S, R. "Allotropic Phase Transformations in Hcp, Fcc and Bcc Metastable Structures in Co-Nanoparticles". *Materials Science and Engineering: A* **2001**, 304-306, 923-927.
- 16.** Son, S. U.; Lee, S. I.; Chung, Y. K.; Kim, S.-W.; Hyeon, T. "The First Intramolecular Pauson-Khand Reaction in Water Using Aqueous Colloidal Cobalt Nanoparticles as Catalysts". *Organic Letters* **2001**, 4, 277-279.
- 17.** Gubin, S. P.; Koksharov, Y. A. "Preparation, Structure, and Properties of Magnetic Materials Based on Co-Containing Nanoparticles". *Inorganic Materials* **2002**, 38, 1085-1099.
- 18.** Petit, C.; Pileni, M. P. "Nanosize Cobalt Boride Particles: Control of the Size and Properties". *Journal of Magnetism and Magnetic Materials* **1997**, 166, 82-90.
- 19.** Guo, F.; Zheng, H. G.; Yang, Z. P.; Qian, Y. T. "Synthesis of Cobalt Nanoparticles in Ethanol Hydrazine Alkaline System (Ehas) at Room Temperature". *Materials Letters* **2002**, 56, 906-909.
- 20.** Lisiecki, I.; Pileni, M. P. "Synthesis of Well-Defined and Low Size Distribution Cobalt Nanocrystals: The Limited Influence of Reverse Micelles". *Langmuir* **2003**, 19, 9486-9489.
- 21.** Puentes, V. F.; Zanchet, D.; Erdonmez, C. K.; Alivisatos, A. P. "Synthesis of Hcp-Co Nanodisks". *Journal of the American Chemical Society* **2002**, 124, 12874-12880.
- 22.** <https://docs.google.com/Doc?docid=oAYx6u-E8P2NUZDJkOTg2c18xZm41a2YzZjk&hl=en&pli=1>
- 23.** Bastús, N. G.; Casals, E.; Vazquez-Campos, S.; Puentes, V. "Reactivity of Engineered Inorganic Nanoparticles and Carbon Nanostructures in Biological Media." *Nanotoxicology* **2008**, 2(3), 99-112.
- 24.** Son, S. U.; Lee, S. I.; Chung, Y. K.; Kim, S. W.; Hyeon, T. "The First Intramolecular Pauson-Khand Reaction in Water Using Aqueous Colloidal Cobalt Nanoparticles as

Catalysts". *Organic Letters* **2002**, 4, 277-279.

25. Skumryev, V.; Stoyanov, S.; Zhang, Y.; Hadjipanayis, G.; Givord, D.; Nogues, J. "Beating the Superparamagnetic Limit with Exchange Bias". *Nature* **2003**, 423, 850-853.

26. Tracy, J. B.; Weiss, D. N.; Dinega, D. P.; Bawendi, M. G. "Exchange Biasing and Magnetic Properties of Partially and Fully Oxidized Colloidal Cobalt Nanoparticles". *Physical Review B* **2005**, 72.

27. Braidy, N.; Behal, S.; Adronov, A.; Botton, G. A. "Investigation of the Oxide Shell Forming on ϵ -Co Nanocrystals". *Micron* **2008**, 39, 717-722.

28. Wiedwald, U.; Lindner, J.; Spasova, M.; Frait, Z.; Farle, M. "Effect of an Oxidic Overlayer on the Magnetism of Co Nanoparticles". *Phase Transitions* **2005**, 78, 85-104.

29. Kim, S. W.; Kim, M.; Lee, W. Y.; Hyeon, T. "Fabrication of Hollow Palladium Spheres and Their Successful Application to the Recyclable Heterogeneous Catalyst for Suzuki Coupling Reactions". *Journal of the American Chemical Society* **2002**, 124, 7642-7643.

30. Oldenburg, S. J.; Averitt, R. D.; Westcott, S. L.; Halas, N. J. "Nanoengineering of Optical Resonances". *Chemical Physics Letters* **1998**, 288, 243-247.

31. Marinakos, S. M.; Novak, J. P.; Brousseau, L. C.; House, A. B.; Edeki, E. M.; Feldhaus, J. C.; Feldheim, D. L. "Gold Particles as Templates for the Synthesis of Hollow Polymer Capsules. Control of Capsule Dimensions and Guest Encapsulation". *Journal of the American Chemical Society* **1999**, 121, 8518-8522.

32. Caruso, F.; Caruso, R. A.; Mohwald, H. "Nanoengineering of Inorganic and Hybrid Hollow Spheres by Colloidal Templating". *Science* **1998**, 282, 1111-1114.

33. Im, S. H.; Jeong, U. Y.; Xia, Y. N. "Polymer Hollow Particles with Controllable Holes in Their Surfaces". *Nature Materials* **2005**, 4, 671-675.

34. Erlebacher, J.; Aziz, M. J.; Karma, A.; Dimitrov, N.; Sieradzki, K. "Evolution of Nanoporosity in Dealloying". *Nature* **2001**, 410, 450-453.

35. Yoon, S. B.; Sohn, K.; Kim, J. Y.; Shin, C. H.; Yu, J. S.; Hyeon, T. "Fabrication of Carbon Capsules with Hollow Macroporous Core/Mesoporous Shell Structures". *Advanced Materials* **2002**, 14, 19-21.

36. Henkes, A. E.; Vasquez, Y.; Schaak, R. E. "Converting Metals into Phosphides: A General

Strategy for the Synthesis of Metal Phosphide Nanocrystals". *Journal of the American Chemical Society* **2007**, 129, 1896.

37. Peng, S.; Sun, S. H. "Synthesis and Characterization of Monodisperse Hollow Fe₃O₄ Nanoparticles". *Angewandte Chemie-International Edition* **2007**, 46, 4155-4158.

38. Sun, Y. G.; Mayers, B.; Xia, Y. N. "Metal Nanostructures with Hollow Interiors". *Advanced Materials* **2003**, 15, 641-646.

39. Vasquez, Y.; Sra, A. K.; Schaak, R. E. "One-Pot Synthesis of Hollow Superparamagnetic CoPt Nanospheres". *Journal of the American Chemical Society* **2005**, 127, 12504-12505.

40. Fan, H. J.; Gosele, U.; Zacharias, M. "Formation of Nanotubes and Hollow Nanoparticles Based on Kirkendall and Diffusion Processes: A Review". *Small* **2007**, 3, 1660-1671.

41. Yin, Y. D.; Rioux, R. M.; Erdonmez, C. K.; Hughes, S.; Somorjai, G. A.; Alivisatos, A. P. "Formation of Hollow Nanocrystals through the Nanoscale Kirkendall Effect". *Science* **2004**, 304, 711-714.

42. Smigelskas, A. D.; Kirkendall, E. O. "Zinc Diffusion in Alpha-Brass". *Transactions of the American Institute of Mining and Metallurgical Engineers* **1947**, 171, 130-142.

43. Mourdikoudis, S.; Simeonidis, K.; Tsiaoussis, I.; Dendrinou-Samara, C.; Angelakeris, M.; Kalogirou, O. "Impact of Synthesis Parameters on Structural and Magnetic Characteristics of Co-Based Nanoparticles". *Journal of Nanoparticle Research* **2009**, 11, 1477-1484.

44. Cabot, A.; Puentes, V. F.; Shevchenko, E.; Yin, Y.; Balcells, L.; Marcus, M. A.; Hughes, S. M.; Alivisatos, A. P. "Vacancy Coalescence During Oxidation of Iron Nanoparticles". *Journal of the American Chemical Society* **2007**, 129, 10358.

45. Rizzo, A.; Nobile, C.; Mazzeo, M.; De Giorgi, M.; Fiore, A.; Carbone, L.; Cingolani, R.; Manna, L.; Gigli, G. "Polarized Light Emitting Diode by Long-Range Nanorod Self-Assembling on a Water Surface". *ACS Nano* **2009**, 3, 1506-1512.

46. Lima, E.; Vargas, J. M.; Zysler, R. D.; Rechenberg, H. R.; Cohen, R.; Arbiol, J.; Goya, G. F.; Ibarra, A.; Ibarra, M. R. "Single-Step Chemical Synthesis of Ferrite Hollow Nanospheres". *Nanotechnology* **2009**, 20.

- 47.** Dormann, J. L.; Fiorani, D.; Tronc, E. Magnetic Relaxation in Fine-Particle Systems. In *Advances in Chemical Physics*, Vol 98; Prigogine, I., Rice, S. A., Eds., **1997**; pp 283-494.
- 48.** Bao, Y. P.; Beerman, M.; Pakhomov, A. B.; Krishnan, K. M. "Controlled Crystalline Structure and Surface Stability of Cobalt Nanocrystals". *Journal of Physical Chemistry B* **2005**, 109, 7220-7222.
- 49.** Cabot, A.; Alivisatos, A. P.; Puntès, V. F.; Balcells, L.; Iglesias, O.; Labarta, A. "Magnetic Domains and Surface Effects in Hollow Magnetite Nanoparticles". *Physical Review B* **2009**, 79.
- 50.** Yoshikawa, H.; Hayashida, K.; Kozuka, Y.; Horiguchi, A.; Awaga, K.; Bandow, S.; Iijima, S. "Preparation and Magnetic Properties of Hollow Nano-Spheres of Cobalt and Cobalt Oxide: Drastic Cooling-Field Effects on Remnant Magnetization of Antiferromagnet". *Applied Physics Letters* **2004**, 85, 5287-5289.
- 51.** Cabot, A.; Alivisatos, A. P.; Puntès, V. F.; Balcells, L.; Iglesias, O.; Labarta, A. "Magnetic Domains and Surface Effects in Hollow Magnetite Nanoparticles". *Physical Review B* **2009**, 79, 7.
- 52.** Cabot, A.; Smith, R. K.; Yin, Y.; Zheng, H.; Reinhard, B. r. M.; Liu, H.; Alivisatos, A. P. "Sulfidation of Cadmium at the Nanoscale". *ACS Nano* **2008**, 2, 1452-1458.
- 53.** Das, D.; Chatterjee, P. P.; Manna, I.; Pabi, S. K. "A Measure of Enhanced Diffusion Kinetics in Mechanical Alloying of Cu-18 At.% Al by Planetary Ball Milling". *Scripta Materialia* **1999**, 41, 861-866.
- 54.** Guisbiers, G.; Buchaillet, L. "Size and Shape Effects on Creep and Diffusion at the Nanoscale". *Nanotechnology* **2008**, 19.
- 55.** Li, Y.; Somorjai, G. A. "Nanoscale Advances in Catalysis and Energy Applications". *Nano Letters* **2010**, 10, 2289-2295.
- 56.** Subramannia, M.; Pillai, V. K. "Shape-Dependent Electrocatalytic Activity of Platinum Nanostructures". *Journal of Materials Chemistry* **2008**, 18, 5858-5870.
- 57.** Tian, N.; Zhou, Z.-Y.; Sun, S.-G. "Platinum Metal Catalysts of High-Index Surfaces: From Single-Crystal Planes to Electrochemically Shape-Controlled Nanoparticles". *Journal of Physical Chemistry C* **2008**, 112, 19801-19817.

- 58.** Xia, Y.; Xiong, Y.; Lim, B.; Skrabalak, S. E. "Shape-Controlled Synthesis of Metal Nanocrystals: Simple Chemistry Meets Complex Physics?". *Angewandte Chemie-International Edition* **2009**, 48, 60-103.
- 59.** Rampino, L. D.; Nord, F. F. "Preparation of Palladium and Platinum Synthetic High Polymer Catalysts and the Relationship between Particle Size and Rate of Hydrogenation". *Journal of the American Chemical Society* **1941**, 63, 2745-2749.
- 60.** Ahmadi, T. S.; Wang, Z. L.; Green, T. C.; Henglein, A.; ElSayed, M. A. "Shape-Controlled Synthesis of Colloidal Platinum Nanoparticles". *Science* **1996**, 272, 1924-1926.
- 61.** Zhu, J.; Konya, Z.; Punter, V. F.; Kiricsi, I.; Miao, C. X.; Ager, J. W.; Alivisatos, A. P.; Somorjai, G. A. "Encapsulation of Metal (Au, Ag, Pt) Nanoparticles into the Mesoporous Sba-15 Structure". *Langmuir* **2003**, 19, 4396-4401.
- 62.** Chen, J. Y.; Herricks, T.; Xia, Y. N. "Polyol Synthesis of Platinum Nanostructures: Control of Morphology through the Manipulation of Reduction Kinetics". *Angewandte Chemie-International Edition* **2005**, 44, 2589-2592.
- 63.** Herricks, T.; Chen, J. Y.; Xia, Y. N. "Polyol Synthesis of Platinum Nanoparticles: Control of Morphology with Sodium Nitrate". *Nano Letters* **2004**, 4, 2367-2371.
- 64.** Demortiere, A.; Launois, P.; Goubet, N.; Albouy, P. A.; Petit, C. "Shape-Controlled Platinum Nanocubes and Their Assembly into Two-Dimensional and Three-Dimensional Superlattices". *Journal of Physical Chemistry B* **2008**, 112, 14583-14592.
- 65.** Mahmoud, M. A.; Tabor, C. E.; El-Sayed, M. A.; Ding, Y.; Wang, Z. L. "A New Catalytically Active Colloidal Platinum Nanocatalyst: The Multiarmed Nanostar Single Crystal". *Journal of the American Chemical Society* **2008**, 130, 4590-+.
- 66.** Ren, J.; Tilley, R. D. "Shape-Controtled Growth of Platinum Nanoparticles". *Small* **2007**, 3, 1508-1512.
- 67.** Ren, J.; Tilley, R. D. "Preparation, Self-Assembly, and Mechanistic Study of Highly Monodispersed Nanocubes". *Journal of the American Chemical Society* **2007**, 129, 3287-3291.
- 68.** Song, H.; Kim, F.; Connor, S.; Somorjai, G. A.; Yang, P. D. "Pt Nanocrystals: Shape Control and Langmuir-Blodgett Monolayer Formation". *Journal of Physical Chemistry B* **2005**, 109, 188-193.

- 69.** Teng, X. W.; Yang, H. "Synthesis of Platinum Multipods: An Induced Anisotropic Growth". *Nano Letters* **2005**, 5, 885-891.
- 70.** Tian, N.; Zhou, Z.-Y.; Sun, S.-G.; Ding, Y.; Wang, Z. L. "Synthesis of Tetrahedral Platinum Nanocrystals with High-Index Facets and High Electro-Oxidation Activity". *Science* **2007**, 316, 732-735.
- 71.** Tsung, C.-K.; Kuhn, J. N.; Huang, W.; Aliaga, C.; Hung, L.-I.; Somorjai, G. A.; Yang, P. "Sub-10 Nm Platinum Nanocrystals with Size and Shape Control: Catalytic Study for Ethylene and Pyrrole Hydrogenation". *Journal of the American Chemical Society* **2009**, 131, 5816-5822.
- 72.** Hiramatsu, H.; Osterloh, F. E. "A Simple Large-Scale Synthesis of Nearly Monodisperse Gold and Silver Nanoparticles with Adjustable Sizes and with Exchangeable Surfactants". *Chemistry of Materials* **2004**, 16, 2509-2511.
- 73.** Maheshwari, V.; Kane, J.; Saraf, R. F. "Self-Assembly of a Micrometers-Long One-Dimensional Network of Cemented Au Nanoparticles". *Advanced Materials* **2008**, 20, 284.
- 74.** Pong, B.-K.; Elim, H. I.; Chong, J.-X.; Ji, W.; Trout, B. L.; Lee, J.-Y. "New Insights on the Nanoparticle Growth Mechanism in the Citrate Reduction of Gold(III) Salt: Formation of the Au Nanowire Intermediate and Its Nonlinear Optical Properties". *Journal of Physical Chemistry C* **2007**, 111, 6281-6287.
- 75.** Banfield, J. F.; Welch, S. A.; Zhang, H. Z.; Ebert, T. T.; Penn, R. L. "Aggregation-Based Crystal Growth and Microstructure Development in Natural Iron Oxyhydroxide Biomineralization Products". *Science* **2000**, 289, 751-754.
- 76.** Cho, K. S.; Talapin, D. V.; Gaschler, W.; Murray, C. B. "Designing Pbse Nanowires and Nanorings through Oriented Attachment of Nanoparticles". *Journal of the American Chemical Society* **2005**, 127, 7140-7147.
- 77.** Zheng, H.; Smith, R. K.; Jun, Y.-w.; Kisielowski, C.; Dahmen, U.; Alivisatos, A. P. "Observation of Single Colloidal Platinum Nanocrystal Growth Trajectories". *Science* **2009**, 324, 1309-1312.
- 78.** Wang, C.; Daimon, H.; Lee, Y.; Kim, J.; Sun, S. "Synthesis of Monodisperse Pt Nanocubes and Their Enhanced Catalysis for Oxygen Reduction". *Journal of the American Chemical Society* **2007**, 129, 6974.

- 79.** Chen, J.; Lim, B.; Lee, E. P.; Xia, Y. "Shape-Controlled Synthesis of Platinum Nanocrystals for Catalytic and Electrocatalytic Applications". *Nano Today* **2009**, 4, 81-95.
- 80.** <http://database.iem.ac.ru/mincryst/>.
- 81.** Denton, A. R.; Ashcroft, N. W. "Vegard Law". *Physical Review A* **1991**, 43, 3161-3164.
- 82.** Paulus, U. A.; Wokaun, A.; Scherer, G. G.; Schmidt, T. J.; Stamenkovic, V.; Radmilovic, V.; Markovic, N. M.; Ross, P. N. "Oxygen Reduction on Carbon-Supported Pt-Ni and Pt-Co Alloy Catalysts". *Journal of Physical Chemistry B* **2002**, 106, 4181-4191.
- 83.** Lim, S. I.; Ojea-Jimenez, I.; Varon, M.; Casals, E.; Arbiol, J.; Puntès, V. "Synthesis of Platinum Cubes, Polypods, Cuboctahedrons, and Raspberries Assisted by Cobalt Nanocrystals". *Nano Letters* **2010**, 10, 964-973.
- 84.** Zhang, J.; Yang, H.; Fang, J.; Zou, S. "Synthesis and Oxygen Reduction Activity of Shape-Controlled Pt₃Ni Nanopolyhedra". *Nano Letters* **2010**, 10, 638-644.
- 85.** Jana, N. R.; Peng, X. G. "Single-Phase and Gram-Scale Routes toward Nearly Monodisperse Au and Other Noble Metal Nanocrystals". *Journal of the American Chemical Society* **2003**, 125, 14280-14281.
- 86.** Schadt, M. J.; Cheung, W.; Luo, J.; Zhong, C.-J. "Molecularly Tuned Size Selectivity in Thermal Processing of Gold Nanoparticles". *Chemistry of Materials* **2006**, 18, 5147-5149.
- 87.** Zheng, N.; Fan, J.; Stucky, G. D. "One-Step One-Phase Synthesis of Monodisperse Noble-Metallic Nanoparticles and Their Colloidal Crystals". *Journal of the American Chemical Society* **2006**, 128, 6550-6551.
- 88.** F. Cotton; Wilkinson, G. *Advanced Inorganic Chemistry*; 4th ed.: New York, **1980**.
- 89.** Mott, D.; Galkowski, J.; Wang, L.; Luo, J.; Zhong, C.-J. "Synthesis of Size-Controlled and Shaped Copper Nanoparticles". *Langmuir* **2007**, 23, 5740-5745.
- 90.** Sun, S. H.; Zeng, H. "Size-Controlled Synthesis of Magnetite Nanoparticles". *Journal of the American Chemical Society* **2002**, 124, 8204-8205.
- 91.** Carbone, L.; Cozzoli, P. D. "Colloidal Heterostructured Nanocrystals: Synthesis and Growth Mechanisms". *Nano Today* **2010**, 5, 449-493.
- 92.** Hao, R.; Xing, R.; Xu, Z.; Hou, Y.; Gao, S.; Sun, S. "Synthesis, Functionalization, and

Biomedical Applications of Multifunctional Magnetic Nanoparticles". *Advanced Materials* **2010**, 22, 2729-2742.

93. Cao, Y. W.; Banin, U. "Growth and Properties of Semiconductor Core/Shell Nanocrystals with Inas Cores". *Journal of the American Chemical Society* **2000**, 122, 9692-9702.

94. Camargo, P. H. C.; Xiong, Y.; Ji, L.; Zuo, J. M.; Xia, Y. "Facile Synthesis of Tadpole-Like Nanostructures Consisting of Au Heads and Pd Tails". *Journal of the American Chemical Society* **2007**, 129, 15452.

95. Habas, S. E.; Lee, H.; Radmilovic, V.; Somorjai, G. A.; Yang, P. "Shaping Binary Metal Nanocrystals through Epitaxial Seeded Growth". *Nature Materials* **2007**, 6, 692-697.

96. Wang, C.; Tian, W.; Ding, Y.; Ma, Y.-q.; Wang, Z. L.; Markovic, N. M.; Stamenkovic, V. R.; Daimon, H.; Sun, S. "Rational Synthesis of Heterostructured Nanoparticles with Morphology Control". *Journal of the American Chemical Society* **2010**, 132, 6524-6529.

97. Gu, H. W.; Zheng, R. K.; Zhang, X. X.; Xu, B. "Facile One-Pot Synthesis of Bifunctional Heterodimers of Nanoparticles: A Conjugate of Quantum Dot and Magnetic Nanoparticles". *Journal of the American Chemical Society* **2004**, 126, 5664-5665.

98. Yang, J.; Elim, H. I.; Zhang, Q.; Lee, J. Y.; Ji, W. "Rational Synthesis, Self-Assembly, and Optical Properties of Pbs-Au Heterogeneous Nanostructures Via Preferential Deposition". *Journal of the American Chemical Society* **2006**, 128, 11921-11926.

99. Yu, H.; Chen, M.; Rice, P. M.; Wang, S. X.; White, R. L.; Sun, S. H. "Dumbbell-Like Bifunctional Au-Fe₃O₄ Nanoparticles". *Nano Letters* **2005**, 5, 379-382.

100. Figuerola, A.; Fiore, A.; Di Corato, R.; Falqui, A.; Giannini, C.; Micotti, E.; Lascialfari, A.; Corti, M.; Cingolani, R.; Pellegrino, T.; Cozzoli, P. D.; Manna, L. "One-Pot Synthesis and Characterization of Size-Controlled Bimagnetic Fept-Iron Oxide Heterodimer Nanocrystals". *Journal of the American Chemical Society* **2008**, 130, 1477-1487.

101. Kwon, K. W.; Shim, M. "Gamma-Fe₂O₃/Ii-Vi Sulfide Nanocrystal Heterojunctions". *Journal of the American Chemical Society* **2005**, 127, 10269-10275.

102. Shi, W.; Zeng, H.; Sahoo, Y.; Ohulchanskyy, T. Y.; Ding, Y.; Wang, Z. L.; Swihart, M.; Prasad, P. N. "A General Approach to Binary and Ternary Hybrid Nanocrystals". *Nano Letters* **2006**, 6, 875-881.

- 103.** Wang, C.; Xu, C.; Zeng, H.; Sun, S. "Recent Progress in Syntheses and Applications of Dumbbell-Like Nanoparticles". *Advanced Materials* **2009**, 21, 3045-3052.
- 104.** Mokari, T.; Rothenberg, E.; Popov, I.; Costi, R.; Banin, U. "Selective Growth of Metal Tips onto Semiconductor Quantum Rods and Tetrapods". *Science* **2004**, 304, 1787-1790.
- 105.** Hytch, M. J.; Snoeck, E.; Kilaas, R. "Quantitative Measurement of Displacement and Strain Fields from Hrem Micrographs". *Ultramicroscopy* **1998**, 74, 131-146.
- 106.** Johnson, C. L.; Snoeck, E.; Ezcurdia, M.; Rodriguez-Gonzalez, B.; Pastoriza-Santos, I.; Liz-Marzan, L. M.; Hytch, M. J. "Effects of Elastic Anisotropy on Strain Distributions in Decahedral Gold Nanoparticles". *Nature Materials* **2008**, 7, 120-124.
- 107.** Njoki, P. N.; Lim, I. I. S.; Mott, D.; Park, H. Y.; Khan, B.; Mishra, S.; Sujakumar, R.; Luo, J.; Zhong, C. J. "Size Correlation of Optical and Spectroscopic Properties for Gold Nanoparticles". *Journal of Physical Chemistry C* **2007**, 111, 14664-14669.
- 108.** Pellegrino, T.; Fiore, A.; Carlino, E.; Giannini, C.; Cozzoli, P. D.; Ciccarella, G.; Respaud, M.; Palmirotta, L.; Cingolani, R.; Manna, L. "Heterodimers Based on Copt3-Au Nanocrystals with Tunable Domain Size". *Journal of the American Chemical Society* **2006**, 128, 6690-6698.
- 109.** Creighton, J. A.; Eadon, D. G. "Ultraviolet Visible Absorption-Spectra of the Colloidal Metallic Elements". *Journal of the Chemical Society-Faraday Transactions* **1991**, 87, 3881-3891.
- 110.** El-Sayed, M. A. "Some Interesting Properties of Metals Confined in Time and Nanometer Space of Different Shapes". *Accounts of Chemical Research* **2001**, 34, 257-264.
- 111.** Hu, J. T.; Odom, T. W.; Lieber, C. M. "Chemistry and Physics in One Dimension: Synthesis and Properties of Nanowires and Nanotubes". *Accounts of Chemical Research* **1999**, 32, 435-445.
- 112.** Nie, S. M.; Emery, S. R. "Probing Single Molecules and Single Nanoparticles by Surface-Enhanced Raman Scattering". *Science* **1997**, 275, 1102-1106.
- 113.** Wang, Z. L. "Transmission Electron Microscopy of Shape-Controlled Nanocrystals and Their Assemblies". *Journal of Physical Chemistry B* **2000**, 104, 1153-1175.
- 114.** Kelly, K. L.; Coronado, E.; Zhao, L. L.; Schatz, G. C. "The Optical Properties of Metal

Nanoparticles: The Influence of Size, Shape, and Dielectric Environment". *Journal of Physical Chemistry B* **2003**, 107, 668-677.

115. Eustis, S.; El-Sayed, M. "Aspect Ratio Dependence of the Enhanced Fluorescence Intensity of Gold Nanorods: Experimental and Simulation Study". *Journal of Physical Chemistry B* **2005**, 109, 16350-16356.

116. Mohamed, M. B.; Volkov, V.; Link, S.; El-Sayed, M. A. "The 'Lightning' Gold Nanorods: Fluorescence Enhancement of over a Million Compared to the Gold Metal". *Chemical Physics Letters* **2000**, 317, 517-523.

117. Osberg, K. D.; Schmucker, A. L.; Senesi, A. J.; Mirkin, C. A. "One-Dimensional Nanorod Arrays: Independent Control of Composition, Length, and Interparticle Spacing with Nanometer Precision". *Nano Letters* **2011**, 11, 820-824.

118. Martin, C. R. "Nanomaterials - a Membrane-Based Synthetic Approach". *Science* **1994**, 266, 1961-1966.

119. Thurn-Albrecht, T.; Schotter, J.; Kastle, C. A.; Emley, N.; Shibauchi, T.; Krusin-Elbaum, L.; Guarini, K.; Black, C. T.; Tuominen, M. T.; Russell, T. P. "Ultra-high-Density Nanowire Arrays Grown in Self-Assembled Diblock Copolymer Templates". *Science* **2000**, 290, 2126-2129.

120. Yu, Y. Y.; Chang, S. S.; Lee, C. L.; Wang, C. R. C. "Gold Nanorods: Electrochemical Synthesis and Optical Properties". *Journal of Physical Chemistry B* **1997**, 101, 6661-6664.

121. Esumi, K.; Matsuhisa, K.; Torigoe, K. "Preparation of Rodlike Gold Particles by UV Irradiation Using Cationic Micelles as a Template". *Langmuir* **1995**, 11, 3285-3287.

122. Jana, N. R.; Gearheart, L.; Murphy, C. J. "Wet Chemical Synthesis of High Aspect Ratio Cylindrical Gold Nanorods". *Journal of Physical Chemistry B* **2001**, 105, 4065-4067.

123. Gao, J. X.; Bender, C. M.; Murphy, C. J. "Dependence of the Gold Nanorod Aspect Ratio on the Nature of the Directing Surfactant in Aqueous Solution". *Langmuir* **2003**, 19, 9065-9070.

124. Johnson, C. J.; Dujardin, E.; Davis, S. A.; Murphy, C. J.; Mann, S. "Growth and Form of Gold Nanorods Prepared by Seed-Mediated, Surfactant-Directed Synthesis". *Journal of Materials Chemistry* **2002**, 12, 1765-1770.

- 125.** Nikoobakht, B.; El-Sayed, M. A. "Evidence for Bilayer Assembly of Cationic Surfactants on the Surface of Gold Nanorods". *Langmuir* **2001**, 17, 6368-6374.
- 126.** Wu, H. Y.; Chu, H. C.; Kuo, T. J.; Kuo, C. L.; Huang, M. H. "Seed-Mediated Synthesis of High Aspect Ratio Gold Nanorods with Nitric Acid". *Chemistry of Materials* **2005**, 17, 6447.
- 127.** Wu, H. Y.; Huang, W. L.; Huang, M. H. "Direct High-Yield Synthesis of High Aspect Ratio Gold Nanorods". *Crystal Growth & Design* **2007**, 7, 831-835.
- 128.** Kim, F.; Sohn, K.; Wu, J. S.; Huang, J. X. "Chemical Synthesis of Gold Nanowires in Acidic Solutions". *Journal of the American Chemical Society* **2008**, 130, 14442.
- 129.** Grzelczak, M.; Perez-Juste, J.; Rodriguez-Gonzalez, B.; Spasova, M.; Barsukov, I.; Farle, M.; Liz-Marzan, L. M. "Pt-Catalyzed Growth of Ni Nanoparticles in Aqueous Ctab Solution". *Chemistry of Materials* **2008**, 20, 5399-5405.
- 130.** Nikoobakht, B.; El-Sayed, M. A. "Preparation and Growth Mechanism of Gold Nanorods (Nrs) Using Seed-Mediated Growth Method". *Chemistry of Materials* **2003**, 15, 1957-1962.
- 131.** Carim, A. H.; Lew, K. K.; Redwing, J. M. "Bicrystalline Silicon Nanowires". *Advanced Materials* **2001**, 13, 1489-1491.
- 132.** Arbiol, J.; Comini, E.; Faglia, G.; Sberveglieri, G.; Morante, J. R. "Orthorhombic Pbcn SnO₂ Nanowires for Gas Sensing Applications". *Journal of Crystal Growth* **2008**, 310, 253-260.
- 133.** Arbiol, J.; Estrade, S.; Prades, J. D.; Cirera, A.; Furtmayr, F.; Stark, C.; Laufer, A.; Stutzmann, M.; Eickhoff, M.; Gass, M. H.; Bleloch, A. L.; Peiro, F.; Morante, J. R. "Triple-Twin Domains in Mg Doped GaN Wurtzite Nanowires: Structural and Electronic Properties of This Zinc-Blende-Like Stacking". *Nanotechnology* **2009**, 20.
- 134.** Arbiol, J.; Kalache, B.; Cabarrocas, P. R. I.; Morante, J. R.; Morral, A. F. I. "Influence of Cu as a Catalyst on the Properties of Silicon Nanowires Synthesized by the Vapour-Solid-Solid Mechanism". *Nanotechnology* **2007**, 18.
- 135.** Arbiol, J.; Morral, A. F. I.; Estrade, S.; Peiro, F.; Kalache, B.; Cabarrocas, P. R. I.; Morante, J. R. "Influence of the (111) Twinning on the Formation of Diamond Cubic/Diamond Hexagonal Heterostructures in Cu-Catalyzed Si Nanowires". *Journal of*

Applied Physics **2008**, 104.

136. Lopez, F. J.; Hemesath, E. R.; Lauhon, L. J. "Ordered Stacking Fault Arrays in Silicon Nanowires". *Nano Letters* **2009**, 9, 2774-2779.

137. Lu, X.; Rycenga, M.; Skrabalak, S. E.; Wiley, B.; Xia, Y. "Chemical Synthesis of Novel Plasmonic Nanoparticles". *Annual Review of Physical Chemistry* **2009**, 60, 167-192.

138. Chockla, A. M.; Harris, J. T.; Korgel, B. A. "Colloidal Synthesis of Germanium Nanorods". *Chemistry of Materials* **2011**, 23, 1964-1970.

Chapter 3

Study of the Self-Assembly Process of Magnetic and Noble Metal Nanoparticles

It is known that under appropriate conditions, colloidal NPs self-assemble into crystalline structures with long-range periodic order as a result of the balance between electrostatic forces, surface tension, entropy, topography, substrate affinity, and evidently, the size, shape, and concentration of the particles.^{1,2} SA process of NPs into ordered structures may be comparable with crystallization, where elements rearrange themselves into a periodic crystal structure.

The spontaneous assembly of monodispersed ligand-capped NPs has been reported by many authors.^{1,3-6} The formation of ordered structures can be promoted by using different techniques such as Langmuir-Blodgett,⁷ magnetic fields⁸ (in the case of magnetic NPs) and electrophoretic deposition.⁹ One well-known methodology used to obtain self-assembled NP structures is the drying-mediated SA,¹⁰ which consists in the controlled evaporation of the solvent from a colloidal particle dispersion on top of the desired substrate allowing the self-organization of the constituent units. Three-dimensional superlattices of different metals such as Ag, Ag₂S and Co have been obtained by slow evaporation of the solvent onto TEM grids and carbon substrates.¹¹ NPs with size distribution less than 5% can then form closed-packed structures, i.e. self-assembled NP superlattices, where the NP acts as individual entities. The NP superlattices do not have strong chemical interactions between particles, but are linked by vdW, hydrogen bonds, and electric/magnetic dipole interactions. This fact allows the NPs to have certain mobility during the evaporation process, what results into a wide number of different structures.

In the SA process, it is important to understand the various interactions between NPs, substrates and solvents, which lead to the formed patterns (see section 1.5). For instance,

evaporation of the solvent affects particle/particle interaction, since the relatively weak attraction between NPs, which is efficiently screened in dilute solution, becomes noticeable as the solvent evaporates, initiating the assembly. In the case of magnetic NPs, the study of the magnetic dipolar interactions, which are not screened or interfered by the medium (solvent, surfactants, by-product, etc.), is fundamental to understand and control such processes.

3.1. Self-assembly of Metal Nanoparticles onto TEM Carbon-Coated Substrates

This section will focus primarily in the different self-assembled structures of both different shape and composition metallic NPs obtained by the drying-mediated method on TEM carbon coated substrates. It will be observed how the particle size, shape (spherical, cubic, rod), composition (Au, Pt, Co) and capping molecules (ionic/organic stabilizers) of the NPs highly affect the SA process to obtain different assemblies.

3.1.1. Spherical Nanoparticles

3.1.1.1 Au Nanoparticles

The controlled organization of Au NPs into desired architectures became a research focus of attention because is relevant for numerous applications, i.e. small metallic features tethered to inorganic surfaces can work as surface Plasmon resonance based chemo- or biosensors with high sensitivity.¹² Colloidal Au NP dispersions synthesized by the well known citrate-reduction method,^{13,14} tend to attach each other forming chain structures when they are drop casted on top of a carbon coated TEM substrate, as can be observed in the Figure 3.1 A. recent study has been published by Zhang *et al.*, where they reported that Au chains of particles can result in chain-like Au nano-assembly by the simple removal of the residual citrate ions acting as the capping agent.¹⁵ On the basis of the HRTEM observations, they believed that the decreased surface energy as well as the dipole-dipole interactions were responsible for the formation of the chain-like structures onto hydrophobic substrates. In the case of well-dispersed and capped NPs, we have observed that the chain-like orientation might be caused by the surface tension owing to the solvent evaporation or by the hydrophilic character of the adsorbed molecules (citrate). By contrast, OAM-capped Au NPs, prepared in organic solvent, self-assemble in hexagonal compact structures (Figure 3.1 B). The protection of the particles by a dense ML of hydrophobic organic molecules, favors their assembly into large arrays with variable degrees of organization. Klabunde *et al.* reported a long-range 2D ordered array of dodecanethiol-

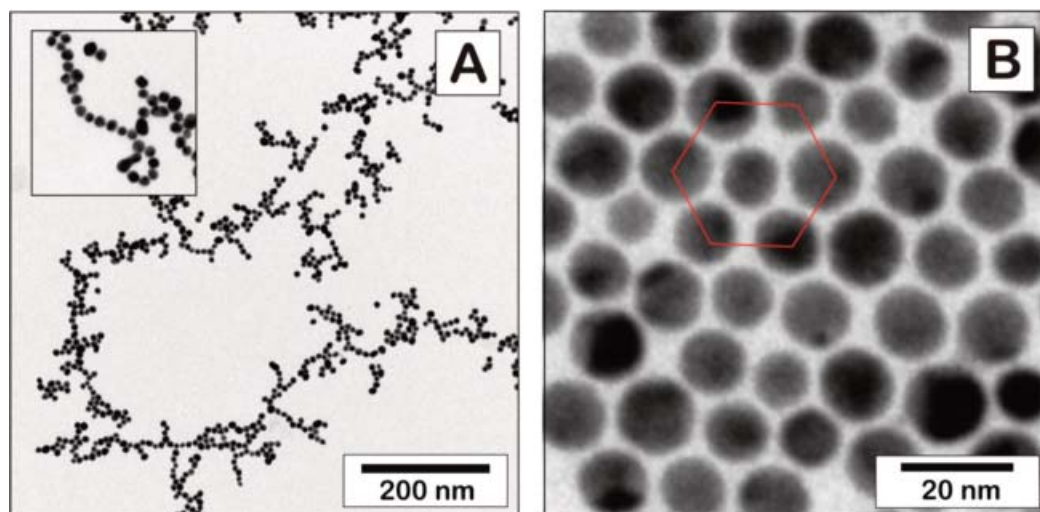


Figure 3.1: TEM images of different self-assembled structures of spherical Au NPs synthesized in A) aqueous citrate solution and B) organic media with OAM as capping agent.

capped Au NPs on SiN substrate.¹⁶ Depending on the organic capping agent and its distribution on the NP surface the inter-particle distance can vary. In addition, the selection of this capping agent has an important influence on the optical properties of these 2D arrays, since it determines the inter-particle distance.¹⁷

3.1.1.2 Co Nanoparticles

In the case of magnetic NPs, different magnetic effects are involved in the SA process such as proximity, long-range interactions, long-range order, domain walls, hysteresis and collective behavior, among others. For nanostructured materials built from magnetic nanometric units, dipolar interactions play an important role in determining the final properties of the material.¹⁸ Dipolar materials arrange themselves into highly non-homogeneous structures as a consequence of the very strong anisotropy of the dipole-dipole interaction. Spherical Co NPs constitute a good example of these materials, and show a wide variety of self-assembled structures (Figure 3.2 A-D).

Co NPs self-assemble from compact to linear structures depending on the particle size, i.e. on their magnetization (see also Chapter 2, Section 2.1). Interestingly enough, when we homogeneously mix different Co NP size populations in solution, they spontaneously segregate when self-assemble onto the TEM substrate. This example illustrates how the self-assembled pattern strongly depends on the size (Figure 3.2 E).

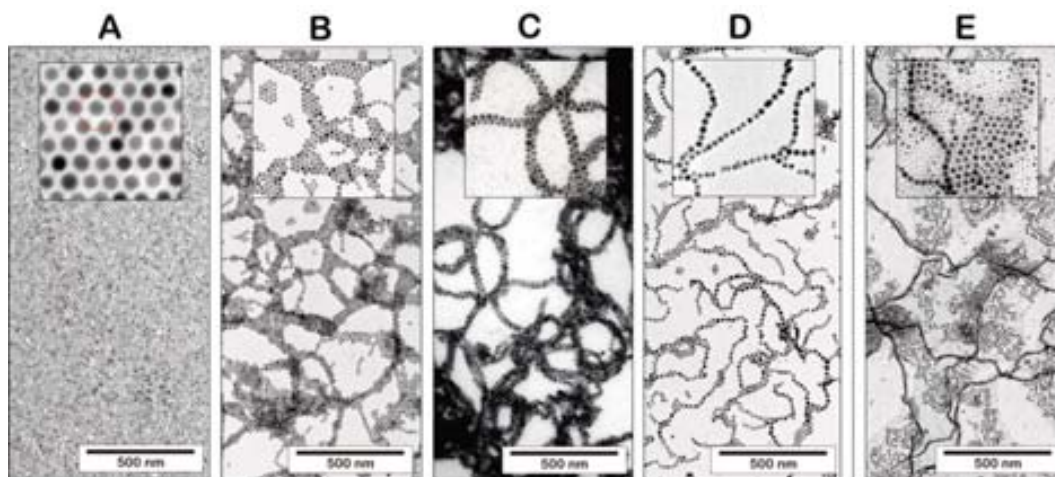


Figure 3.2: TEM image of different self-assembled structures of Co NP of different sizes: (A) 12 nm, (B) 14 nm, (C) 16 nm, (D) 18 nm. E) Mixture of Co NPs of different sizes.

3.1.2 Non-Spherical Nanoparticles

3.1.2.1 Pt Nanoparticles

In the previous chapter we obtained different shapes of Pt NPs by using different reducers (Chapter 2, section 2.2.2). Here we investigate on the self-assembled structures generated by some of these particles depending on their shape. One drop of the original solution was casted on the TEM substrate and left to dry. As can be observed in Figure 3.3 A, the regular cubic particles self-assemble in a highly ordered square arrangement with a well-defined inter-particle spacing, demonstrating their narrow size distribution. The HRTEM image of one NC of the square lattice (Figure 3.3 B) shows that the single Pt cube has preferential orientation with crystallization along the family of $\{111\}$ facets. On the other hand, regular shaped cuboctahedrons (Figure 3.3 C) with faceting also occurring in the $\{111\}$ and $\{002\}$ planes, self-assemble into a compact hexagonal lattice.

Besides the self-organization of the NPs in ordered structures, the oriented attachment has recently been found to be a significant mechanism in the growth of several nanomaterials.^{19,20} This process has been presented as a very promising route for the preparation of complex-shaped nanostructures using NPs as building blocks. It has been reported in several studies the role of oriented attachment in the anisotropic growth of NCs, and also as a mechanism in the synthesis of NPs. We have observed this phenomenon during the synthesis of Pt NCs, where there is a shape transformation via oriented attachment of minor components. This process, that we previously called pasting or *cementation* process (explained in the section 2.3.1.2), is produced during the synthetic process. Figure 3.4 shows a HRTEM image of the cemented Pt particles. It can also be observed that this attachment can produce either poly-crystalline (A)

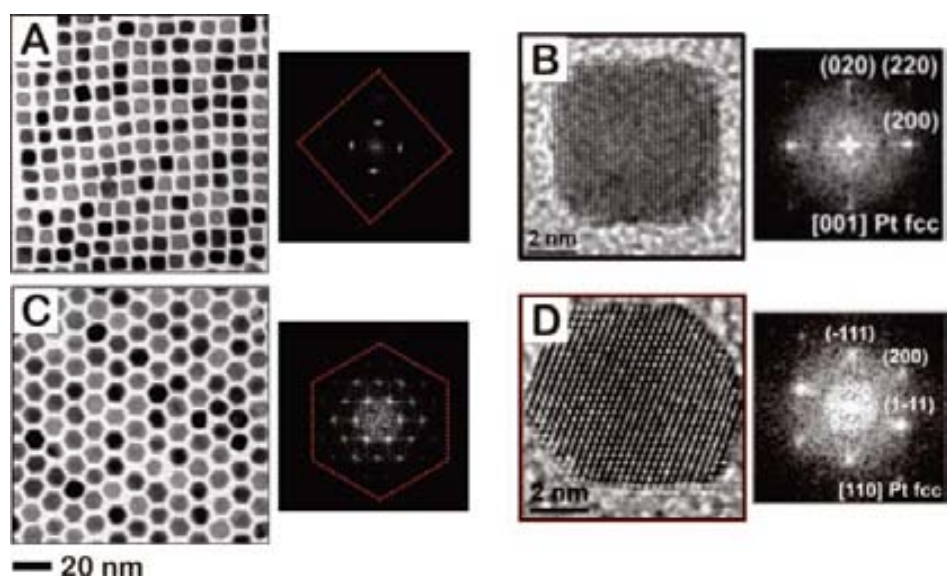


Figure 3.3: TEM images of self-assembled structures formed by cubes (A) and cuboctahedrons (C), and HRTEM images of a single cube (B) and a single cuboctahedron (D). Each image is accompanied by its corresponding FFT pattern.

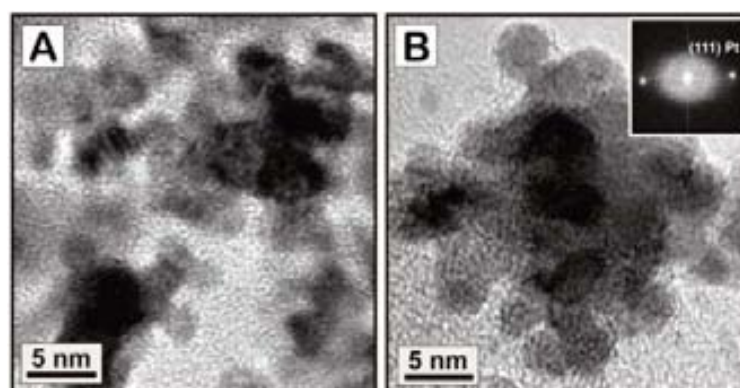


Figure 3.4: HRTEM images of the Pt NPs oriented attached into poly-crystalline (A) and single-crystalline (B) structure. Inset of figure B corresponds to the FFT pattern indicating that the (111) planes are perfectly aligned and have single-crystal structure.

and single-crystalline (B) structures. The FFT pattern in Figure 3.4 B indicates the perfect alienation of the (111) planes, thus confirming the single crystal structure.

3.1.2.2 Rod Shaped Au Nanoparticles

Au NRs with low AR (between 2 to 4) were produced by the methods published by Jana *et al.*²¹ and Nikoobakht and El-Sayed,²² while Au NRs with higher AR were obtained as described in section 2.4. The interaction between NRs in solution consists of both electrostatic repulsive

forces, caused by the overlap of electrical double layers and attractive vdW forces. Au NRs in water are stable up to several months because it is covered by a bilayer of surfactant (CTAB). The governing inter-particle forces in this case are both electrostatic repulsion, due to the electrical double layer, and steric repulsion, caused by the long alkyl chains of the surfactant. Upon repeated centrifugation (usually 3 times), Au NRs tend to aggregate and they are impossible to redisperse again, mediated by vdW attraction. Therefore, we can conclude that a high concentration of surfactant in the solution is critical to avoid agglomeration.

We prepared the solution for SA by centrifuging the initial solution once and redispersing the precipitated NRs in a small volume (from 1 mL to 100 μ L) of water. One drop of the prepared solution was casted onto the TEM substrate and left dry. The self-assembled rod structures were spontaneously aligned side-by-side, preferring this conformation better than end-to-end assembly. This phenomenon can be explained by the capillary force. For rod-like particles, two directional capillary interactions (at transverse and longitudinal directions) should be considered, effect that was studied by Gao *et al.*²³ They found that the transverse capillary force is always stronger than longitudinal capillary force, thus making rod-like particles to align side-by-side preferentially, as expected. Also, the rod transverse capillary force is stronger than spherical particle lateral capillary force, preventing the spheres intermixing at transverse direction when the dispersion contains spheres, prisms and shapeless particles as by-products.

Figure 3.5 shows different self-assembled structures formed by Au rods of variable AR. It can be observed that, independently of the AR, the longer side is the preferred side to self-assemble. Parallel chains of self-assembled rods stack each other by fitting the side of the rods of one of the chains into the spacing of the neighbor chain, minimizing in this way the inter-particle spacing. With the decrease of rod length the transverse capillary force is weakened and the stability of the ordered assembly structures is decreased allowing a greater mixing between

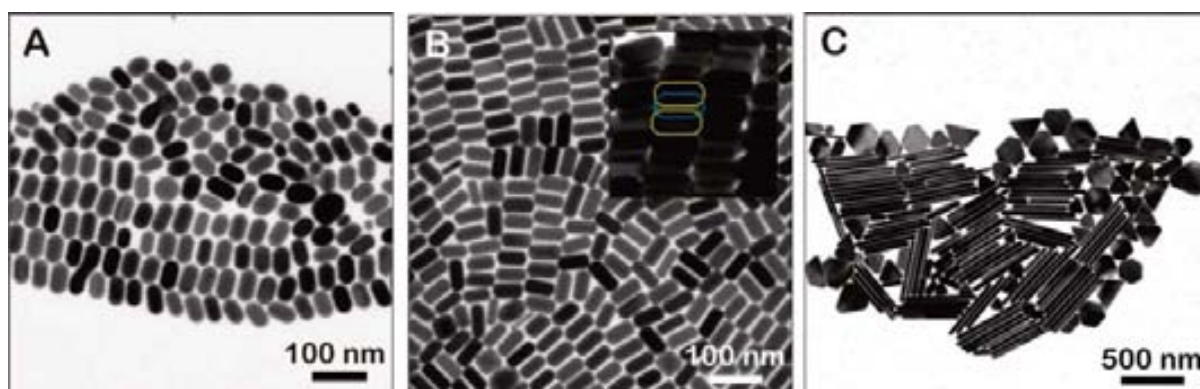


Figure 3.5: TEM image of different self-assembled structures of Au NRs of different AR: (A) 1.84, (B) 2.17 and (C) 15.63.

both rods and spherical particles (Figure 3.5 A). Also, similarly to the case of Co NPs of different sizes, in mixtures of particles with different shapes occurs segregation by morphologies due to the different capillary forces. Figure 3.5 C shows an example of this behavior.

A shape transformation via oriented attachment process has been also observed in Au NRs, similar to the previously observed in Pt NPs. In the case of the synthesis of long rods (section 2.5), we could also observe that some of the NRs suddenly change their direction forming an elbow (Figure 3.6). The analysis of the bending region showed that the shoulder is composed of a grain boundary, which resulted from the merging area between two different NRs that have fused together in some way (growing both along the $[1-10]$ direction). During growth, the reactive surfaces may merge while they are incorporating atoms in the process called *pasting* or *cementation*.²⁴

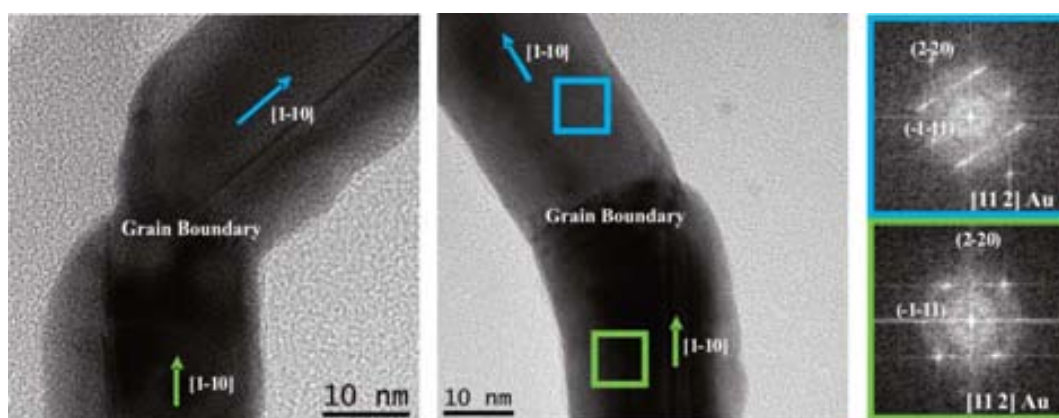


Figure 3.6: Panel of different grain boundaries between long NRs with the corresponding FFT patterns of the selected areas.

3.1.3 Summary

Organic-capped NCs can be organized into close-packed arrays simply by evaporating the solvent from a hydrophobic sterically stabilized dispersion when the size distribution of the particles is sufficiently narrow. NC shape strongly influences the symmetry of superlattices, and small changes in the particle morphology can affect the distribution of the arrangement, as has been observed in the case of the Pt cubes and cuboctahedrons. When prismatic particles with tetragonal geometry were assembled, 2D superlattices with rectangular symmetry were obtained. However, we observed hexagonal pattern in the SA of particles with hexagonal shape. Moreover, the composition of the material, i.e. their inner properties, affects extremely the SA

process. A good example is the case of Co NPs, where the SA depends directly of the magnetization. Finally, oriented attachment-based SA has been also observed in the case of Pt NPs and Au NRs. In this oriented attachment, which is an irreversible process, particles appear fused to form bigger structures.

3.2 Self-Assembly of Co Nanoparticles at Compatible Substrates: Graphite

In particular, magnetic NPs are promising building blocks for high-performance nanodevices for applications such as magnetic data storage and recording media.^{4,25} In magnetic materials, the magnetic behavior is determined by the intrinsic exchange coupling energy and anisotropy energy. Decreasing the single particle size usually reduces the anisotropy energy or modifies the easy magnetization axes increasing the influence of dipolar interactions. If considering a magnetic NP assembly, the particle-particle interaction becomes then an important issue, dominating the collective magnetic behavior.²⁶ Through changing the particle density, inter-distance, or space arrangement, the magnetic properties might be controlled by design.²⁷

Dipolar interactions play an important role in determining cooperative phenomena at the molecular scale and the final properties of the material.²⁸ Dipoles display a fondness for arranging themselves into highly inhomogeneous structures. This is a consequence of the very strong anisotropy of the dipole-dipole interaction, which couples the orientations of the dipole moments with that of the inter-particle vector, what is different from the isotropic vdW interaction.

There have been numerous experimental studies of magnetic NP arrays. FM-like (collective) behavior in magnetization measurements of a 2D self-assembled ML of 9 and 12 nm diameter Co particles has been previously observed.²⁹ Similarly, Georgescu *et al.*³⁰ studied islands of spherical 21 nm size Co-ferrite (CoFe_2O_4) NPs by MFM. They observed that the magnetization pattern of the NPs was determined by the competition between the collective dipole-dipole interactions and the alignment of the dipole moments along the easy axes of magnetization. Russier *et al.*³¹ studied both experimentally and theoretically the dipolar interactions between Co NPs, which they characterized by a random distribution of the easy axes and deposited on graphite.

In this section, we report on the predominant role of the dipolar magnetic interactions on the formation of self-assembled super structures of magnetic NPs in the absence of applied magnetic field. Other factors influencing the formation of those structures, such as the

substrate, the evaporation process, and the interactions NP-substrate are also investigated. The particles used contain a surfactant layer, thus they are at least separated by a couple of nanometers. This means that the possibility of having an exchange interaction between NPs (even in these dense assemblies) is negligible, and their mutual magnetic interactions are, therefore, dominated by long-range dipole-dipole interactions. This study of the SA processes of Co NPs coated with OA onto graphite together with the comparison with the SA on the carbon-coated TEM grids, give the opportunity to study to the minutest detail the balance between NP-NP and NP-substrate interactions, in the particular case where both particles and substrate are highly hydrophobic. Starting with well-defined NPs we can fine-tune the interactions among them by increasing their diameter and therefore the intensity and stability of their magnetic moment.

3.2.1 Experimental

For instrumentation details of this section see Appendix A.6.

Co Nanoparticles. Spherical ϵ -Co NPs coated with OA were synthesized following the procedure detailed in section 2.1. Briefly, a solution containing 0.54 g of $\text{Co}_2(\text{CO})_8$ in 3 mL of anhydrous DCB was injected in a 15 mL of anhydrous DCB refluxing bath containing OA and TOPO as surfactants. The nucleation occurs instantaneously upon injection. The lifetime of the atoms in solution is short leading to the simultaneous formation of many small Co clusters.

Deposition of Co Nanoparticles onto Graphite. The deposition of the NPs onto the substrate was performed by drop casting. We deposited a few drops of the initial Co NPs solution (10^{16} particles per mL) onto a 5x5 mm freshly cleaved HOPG. In some of the

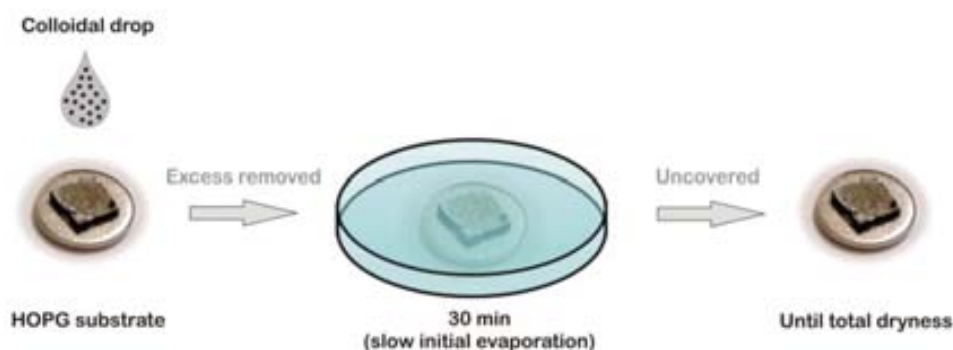


Figure 3.7: Scheme of the deposition process of Co NPs onto HOPG surface. Not drawn to scale.

experiments the excess of solution was removed with the aid of an absorbent paper, leaving the entire surface evenly coated. The substrate was covered with a petri dish for 30 min for facilitate a slow initial evaporation under DCB atmosphere. After 30 min the substrate was uncovered and the evaporation process continued until total dryness of the solvent.

3.2.2 Results and Discussion

Since the majority of studies of SA of magnetic NPs have been developed onto carbon-coated TEM substrates, our objective was to study the SA onto more interesting technological substrates. HOPG presents a set of favorable properties: smooth, flat and clean surface, and hydrophobic character that makes it compatible with the also hydrophobic OA and DCB, what increases the affinity between the NPs and the substrate.

It can be observed different spontaneous self-assembled structures formed by Co NPs depending of the size of the particles, in fact depending on their SPM behavior, onto HOPG. Thus, large ML areas of Co NPs and different micro and macroscopic structures, resulting from the evaporation of colloidal Co NPs solutions, are observed. This process can be modulated by different parameters. In our case we modulated the contribution of dipolar magnetic interactions to the SA process using Co NPs of different sizes (Figure 3.8)

Particularly, in the case of deposition of 6 nm Co NPs, slow evaporation of the DCB (bp = 181 °C) at RT resulted in a spontaneous formation of a random distribution of micrometer sized 3D rice-grain like structures (Figure 3.8 B)

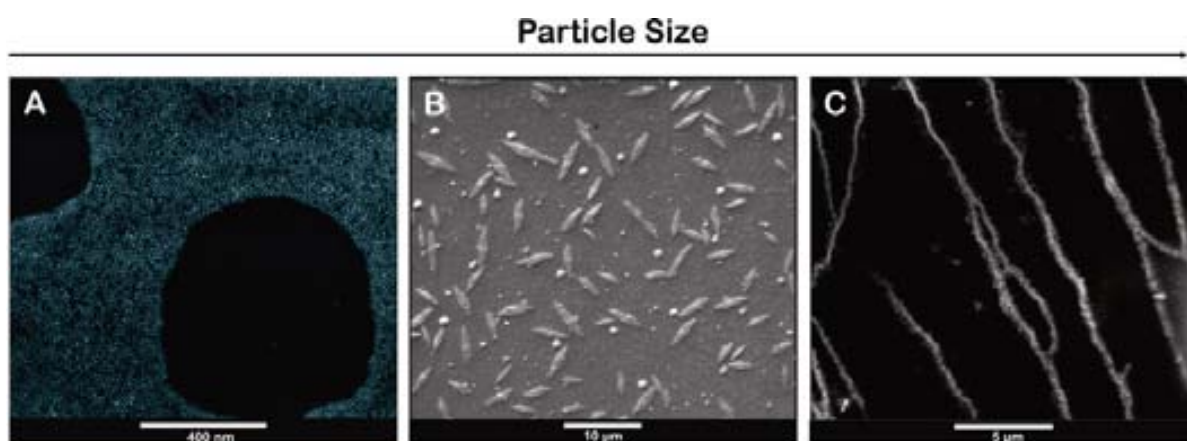


Figure 3.8: SEM images of self-assembled structures formed by Co NPs of different sizes: A) 5 nm , B) 6-7 nm and C) 13 nm onto HOPG.

3.2.2.1 Structural Characterization

The structures were first observed by optical microscope (Figure 3.9 B). The size distribution analysis of the Co rice-grain like structures made up of 6 nm Co NPs reveals a relative narrow size distribution around 1-2 μm in width and a length that varies between 4 and 8 μm (Figure 3.9 C). The observed size distribution (Gaussian and narrow) recalls de LaMer description of homogeneous nucleation and growth of monodisperse NPs in solution known as “brust nucleation” of a supersaturated solution.³² The structures with its truncated flat pyramid shape also remains the Stranski-Krastanov growth, characterized by an intermediary process both 2D layer and 3D island growth.³³

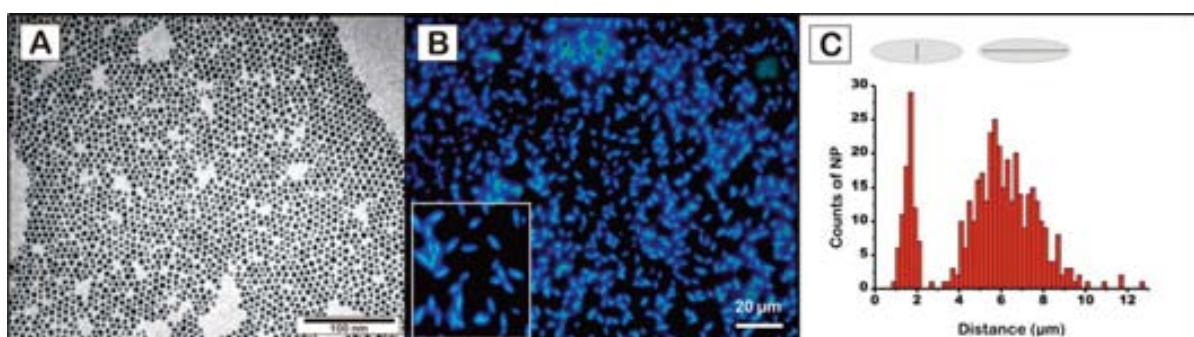


Figure 3.9: A) TEM image of 6 nm Co NPs, B) Optical microscope image of 4-8 μm Co rice-grain like structures and C) short and long diameter of the size distribution analysis of the structures.

SEM images of the structures show in white the Co structures (Figure 3.10 A,B). The corresponding EDX analysis of the structures show that they are formed by Co (Figure 3.10 C). The background of the picture corresponds to the HOPG substrate. The majority of the structures are isolated, fact that suggests that these assemblies did not form first in solution and then sediment. Rather, it indicates that the structures formed on the substrate at the last stages of evaporation.

AFM* measurements (Figure 3.11 A) show that the rice-grain like structures are smooth and therefore support the idea that particles are able to move during structure formation. The observed structures are around 40-60 nm thick indicating that these structures are formed by 10^5 - 10^6 particles and 6-10 NP layers. MFM measurements at RT make evident that the observed Co microstructures exhibit a magnetic response (Figure 3.11 C). Neither magnetic structure inside the microstructures (black corresponds to attraction), nor variation of the contrast changing the orientation of the MFM tip magnetization have been observed, thus corroborating

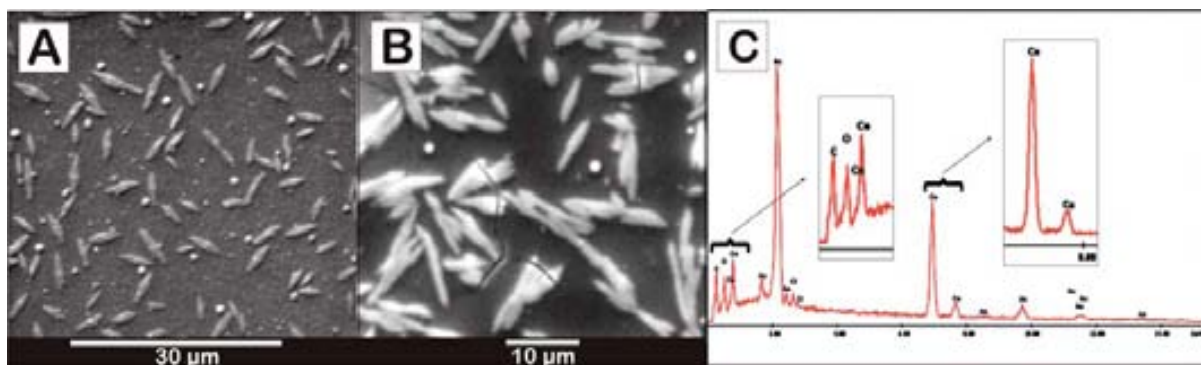


Figure 3.10: A,B) Back Scattered SEM images of 4-8 μm Co rice-grain like structures and C) EDX analysis of the structures indicating that the structures are formed by Co.

the absence of significant remanence and coercivity. One has also to bear in mind that before the MFM scan, where the tip approaches the sample at approximately 50 nm, the tip is scanned at 5 nm to record the surface structure. Thus, the sensing magnet of the tip is first scanned very

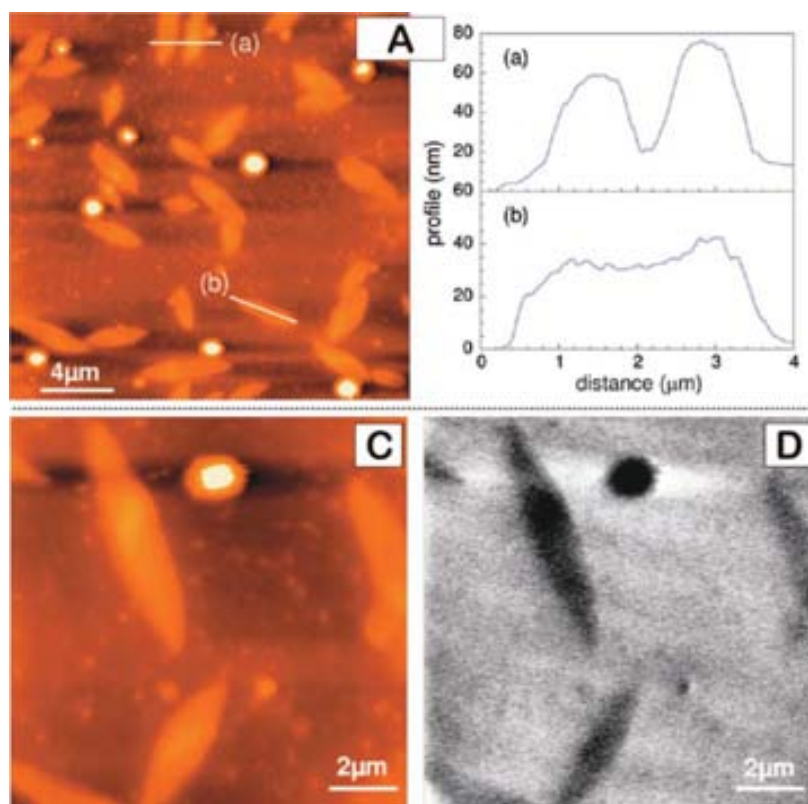


Figure 3.11: A) AFM* image of self-assembled structures integrated by Co NPs with the corresponding scan lines. B) Another AFM* image of self-assembled structures integrated by Co NPs and C) MFM image of some of these structures showing the magnetic character at RT (black corresponds to attraction).

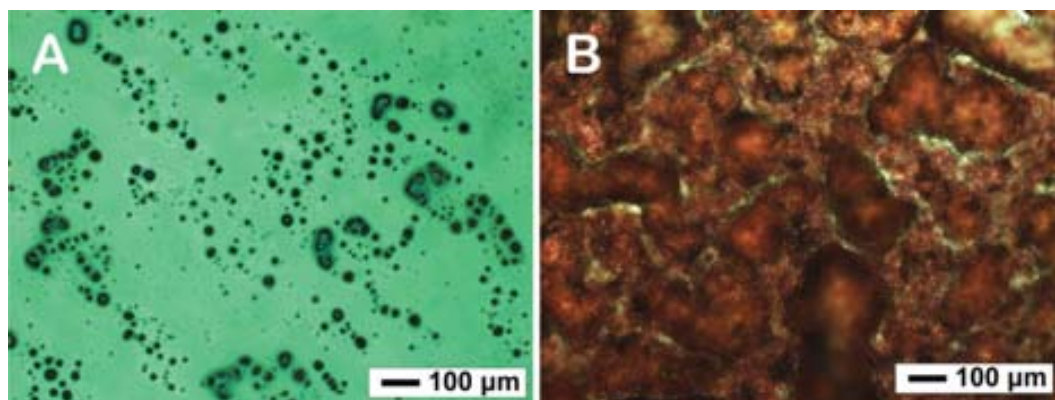


Figure 3.12: Optical image of Co NP deposition onto mica substrate (A) and OAM coated Au NPs onto HOPG substrate (B).

close to the particles in what remains a write (AFM*), read (MFM) process: the AFM* orients the moments in the scanning direction interfering with the following magnetic structure reading if the sample coercivity is smaller than the tip coercivity (ca., 500 Oe) as it is in our case. These results are consistent with a system being constituted by either AFM interacting NPs, disordered moments or weakly FM interacting NPs. The observed anisotropy (the elongated shape) indicates the importance of the AFM interactions.

It should be noticed that the same experiments onto freshly cleaved mica (a clean, flat but hydrophilic substrate) did not yield any particular SA structure due to the poor wettability and repulsion between the hydrophobic solvent, the NPs and the substrate (Figure 3.12 A). As another control experiment, Au NPs of the same size, synthesized in toluene and coated by OAM at similar concentrations, were also deposited onto HOPG. The non-magnetic NPs did not yield any elongated structure, only the expected mono to multi-layered coverage of the substrate (Figure 3.12 B). Thus confirm that the structures observed on Co were obtained due to dipolar magnetic interactions.

3.2.2.2 Magnetic Characterization

Isolated medium size Co NPs (6 nm) are SPM at RT. Figure 3.13 A shows susceptibility curves obtained after a ZFC-FC process in a magnetic field of 100 Oe. A maximum in the ZFC branch is observed around the blocking temperature $T_B \approx 130$ K. The broadness of the peak indicates that NPs present a wide size distribution function.

Figure 3.13 B and C show the $M(H)$ curves of dispersed NPs and self-assembled structure at temperature of 10 K and RT, respectively. For dispersed NPs at RT, $M(H)$ exhibits the typical features of SPM behavior and can be described by using the Langevin PM function

$$M(x) = \coth x - \frac{1}{x} \quad \text{Equation 3.1}$$

being $x = \mu H / (k_B T)$ for a classical Heisenberg spin of moment μ in a magnetic field H . The values obtained for μ were around $10^4 \mu_B$, that assuming the density and moment per Co atom corresponding to bulk fcc Co.³⁴ The particle size estimated from fitting the Langevin function to the RT magnetization curve, gave an estimation of the particle diameter of about 6 nm, being in good agreement with values obtained from the TEM measurements.³⁵ At 10 K, $M(H)$ curve exhibits a well-developed hysteresis loop with a coercive field $H_c \approx 2$ kOe. The remanence to saturation ratio is about 0.5, in agreement with the Stoner-Wohlfarth model for a collection of non interacting particles.³⁶ It is also worth mentioning that after a FC in a high field (10 kOe) the loop is offset from zero along the field axis indicating the existence of exchange anisotropy manifested in an exchange bias field ($H_{ex} \approx 0.5$ kOe). This phenomenon is likely generated by a CoO layer at the surface of the Co NP arising from surface oxidation of NPs because of air exposure or the molecular oxygen of the employed surfactants.³⁷

For SA structures, the $M(H)$ the curve at RT (Figure 3.13 C) is quite similar to that of isolated Co NPs and exhibits no measurable hysteresis. The lack of hysteresis (despite the aggregate state of the NPs) is interpreted in this case as a consequence of a demagnetized “AFM state” of the Co NPs inside the rice-grain like shaped objects. However, at low temperature, the $M(H)$ curve is significantly different from that of isolated Co NPs: the coercive field has been drastically reduced to $H_c \approx 380$ Oe, as well as the exchange bias field $H_{ex} \approx 100$ Oe. Again, these effects are usually attributed to AFM inter-particle interactions: NPs in self-assembled objects are tightly packed and inter-particle interactions strongly affect the magnetic behavior.²⁷

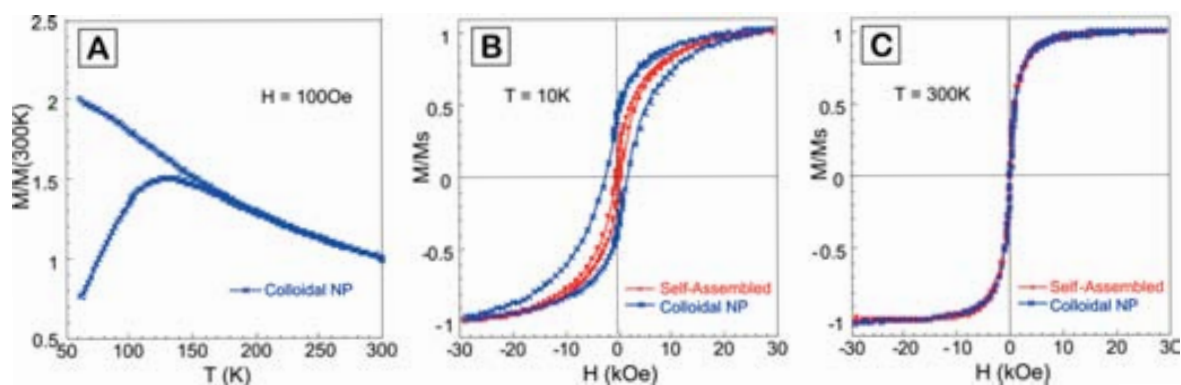


Figure 3.13: (A) ZFC-FC magnetization curves of dispersed Co NPs. Low field zoom of the hysteresis loop for both dispersed Co NPs and self-assembled Co NPs at low temperature (10 K) (B) and RT (C).

In particular, dipolar interactions between NPs can frustrate the orientation along the NP easy axis at low temperature, promoting the appearance of a collective glassy behavior that drastically reduces the coercive field. This state should exhibit a similar behavior to that corresponding to an AFM state. The existence of strong demagnetizing interactions between NPs in the self-assembled structures is also evidenced by the very small measured remanence to saturation ratio.

3.2.2.3 Effect of Increasing Particle Size

When the NPs are larger, as the magnetic moment of the particles increases in stability and intensity, other type of structures have been observed. In the case of 8 nm Co NPs, curled wire structures have been observed, and for NPs around 13 nm, smooth wires are observed (Figure 3.14). The observation of these wire structures are expected since the increase of the dipolar interaction and its unidirectional character.

The deposition of one drop of dense colloidal 13 nm Co NPs solution on graphite through evaporation leads to the formation of NP wires of thickness around 200-300 nm and lengths up to more than hundreds of microns (Figure 3.15 A,B). SEM images with particle resolution show that the wires consist in loose bundles of single-particle chains, where neighboring chains

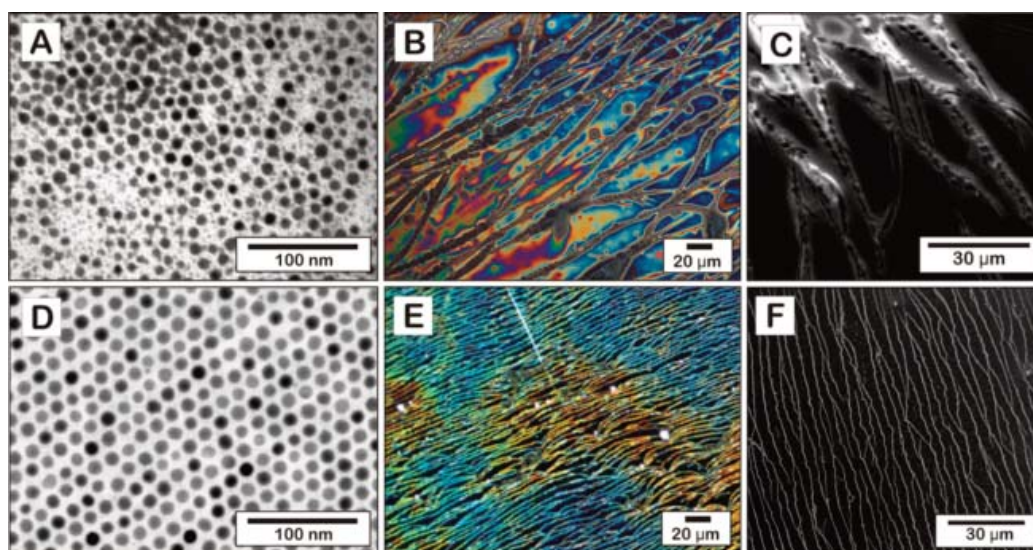


Figure 3.14: A) TEM image of polydisperse Co NPs, B) Optical image and C) SEM image of the self-assembled structures formed by the deposition of the polydisperse Co NPs onto HOPG. D) TEM image of monodisperse Co NPs, E) Optical image and F) SEM image of the self-assembled structures formed by the deposition of the monodisperse Co NPs onto HOPG. Light interference patterns are observed in the optical microscope images, consistent with subwavelength features causing optical interference.

touch each other forming a compact structure (Figure 3.15 C). In the next chapter, complementary studies of the magnetic behavior of these wire structures by Lorentz microscopy and electron holography are described.

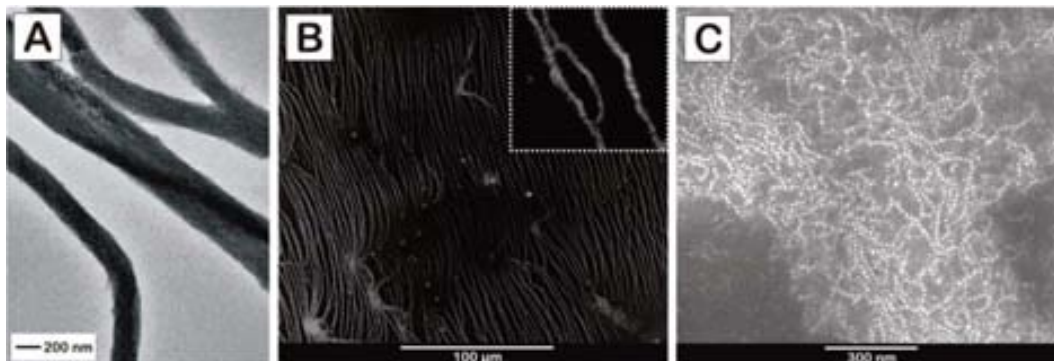


Figure 3.15: TEM (A) and SEM (B,C) images of 13 nm Co NPs wires formed by SA onto HOPG.

Magnetic characterization of smooth wires of Co NPs was previously carried out in a similar sample. Figure 3.16 shows MFM measurements, where it can be observed that a contrast appears on top of the wires consisting of longitudinal domains which respond differently to the oscillating tip. The development of such domains recalls the collective behavior predicted for assemblies of magnetic NPs and the observation of 2D Co NPs arrangements.

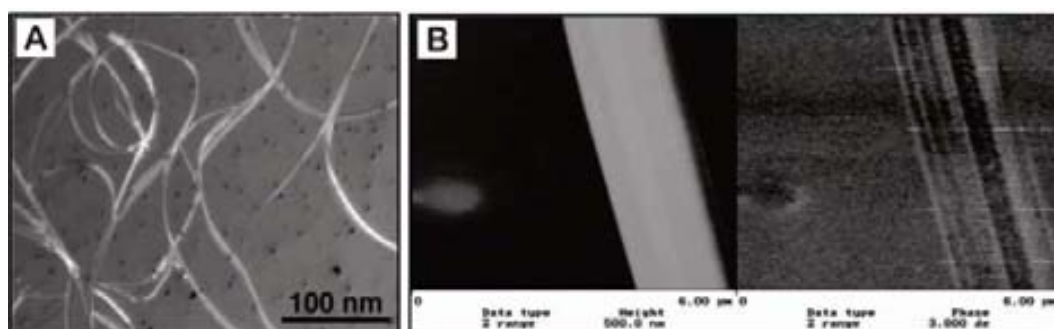


Figure 3.16: AFM* (A) and MFM (B) images of smooth wires integrated by Co NPs.

For larger particles, beyond 15 nm, the strong dipolar interactions lead to the disordered magnetic aggregation and precipitation of the NPs. In these later cases the magnetic interactions are too strong to allow the formation of ordered structures.

3.2.2.4 Effect of Applied Magnetic Fields

The orientation of the Co wires can be manipulated with magnetic fields during the evaporation process. Figure 3.17 shows optical microscope images of three deposition experiments performed under different magnetic fields. We have studied the deposition of 8 nm Co NPs onto HOPG with: i) the substrate on top of a strong magnetic field (NdFeB magnet), ii) the substrate on top of a weak magnetic field (ferrite magnet) and iii) the substrate between two weak magnetic fields (ferrite magnets).

It can be observed three different behaviors depending on the strength of the magnetic field. In the case of strong magnetic field, shorter wires with more density of particles at the ends are observed (Figure 3.17 A). These structures suggest that the strong perpendicular field prevents the particles diffusion on the substrate, and once the solvent was evaporated the structures

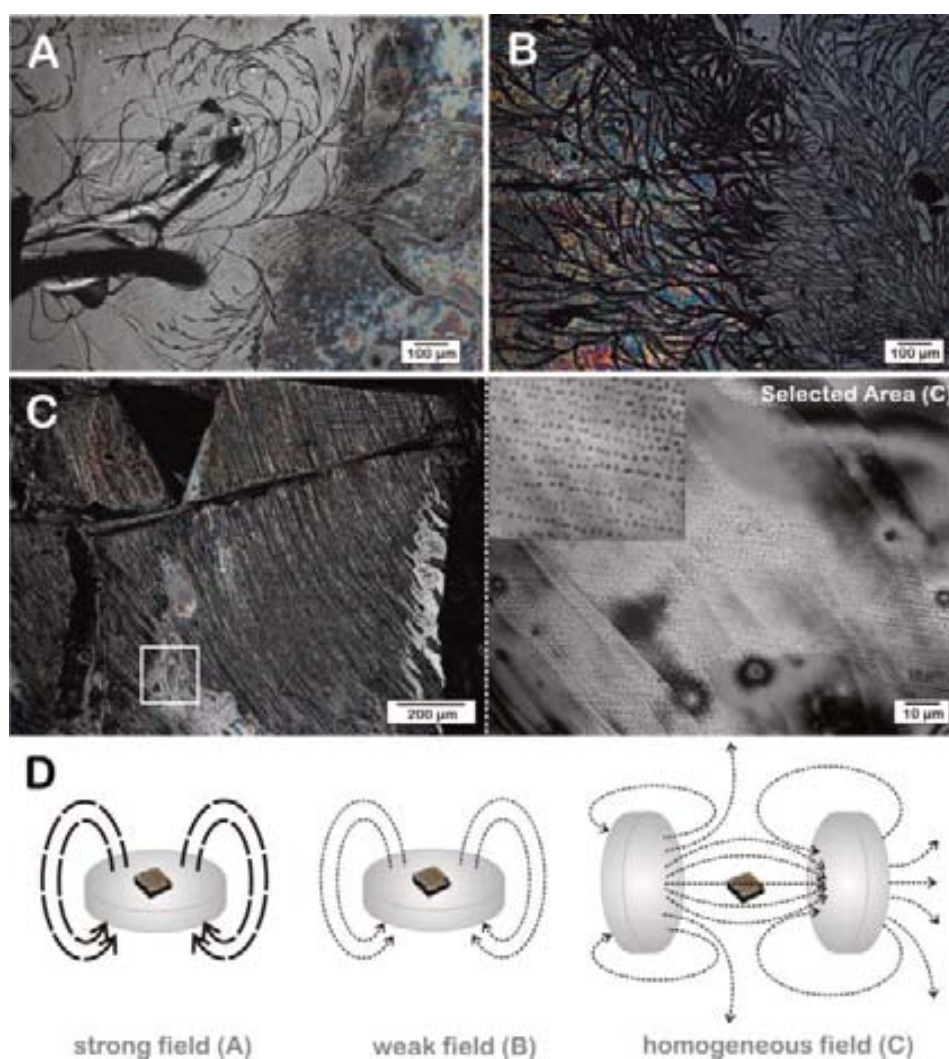


Figure 3.17: Optical images of the assembled structures formed under a strong (A), weak (B) and homogeneous (C) magnetic field. D) Schematic diagram of the influence forces in each case.

collapsed showing this widening at the end. On the other hand, with a weaker perpendicular magnetic field the diffusion process was more favorable, obtaining homogeneous wires well distributed in the substrate (Figure 3.17 B). Finally, in the last case, we observed that the change of the field position clearly affects the orientation of the wires, which changed direction following the field lines (Figure 3.17 C). Zooming in the center of the substrate, well-aligned parallel dot lines formed by Co NPs are observed. These structures suggest the presence of the field parallel aligned to the substrate.

3.2.2.5 Formation Mechanism

Regarding the formation mechanism, it was proposed that the particles self-assembled in solution at very high concentrations, prior to deposition, when the majority of the solvent has been evaporated but NPs are still loosely interacting with the substrate, and then the structure is transferred to the substrate when the evaporation is completed. Or, on the contrary, NPs expelled from the solution reaches the substrate and relocates. These issues can be further corroborated by investigating the effect of NPs mobility reduction by depositing them onto substrates of different affinities (see Chapter 3, section 3.3). Certain mobility is needed once the NP reaches the substrate, or the growing crystal, in order to form ordered structures. The use of high boiling solvents allows slow evaporation at RT. This added thermal energy permits the particles to diffuse to their lowest energy sites during evaporation, producing well-defined superlattice structures. In areas where density of rice-grain like structures is higher, they appear as intersected structures rather than collapsed. All these observations, together with their flat top confirm growth from the substrate. In Puentes *et al.*,²⁹ a similar sample was evaporated onto a (111) single silicon crystal functionalized with an amine self-assembled ML and disordered Co MLs were obtained. Amines are known to bind strongly to Co and therefore reduce particle mobility onto such a substrate. This result confirms that certain mobility is needed once the NP reaches the substrate or the growing crystal in order to form ordered structures. And this also indicates that apart from concentration increase, substrate affinity also plays a crucial role in NPs SA.

Since the colloid solution is stable from months to years, it is clear that SA does not occur either in the dispersed colloid or in the colloid vessel walls (confirmed by DLS in section 2.2.1.2). In fact, the existence of a concentration threshold for the formation of colloidal crystals has been reported.³⁸ Particles also feel an effective attraction by the substrate in addition to their mutual vdW attraction. Therefore, as particles arrive at the substrate, they stick to it for a while before going back to the solution. When the concentration is high enough, the mobility of the particles out of the substrate surface is reduced and then SA starts due to both, a reduction of

available positions for the NPs in solution and an increase in the self-assembled structure stability. In other words, as the particles are packed together, if one of them wants to move, its neighbors will have to cooperate. Therefore, as they are packed even tighter, more particles have to cooperate for anyone to move, what stabilizes the growing structure.

For an isolated Co NP with diameter of ~6 nm and $T_B = 130$ K, the anisotropy constant should be $K_{CoNP} = 2.5 \cdot 10^6$ erg/cm³. Considering the extremely short-range character of exchange interactions and the fact that particles are isolated by at least twice the surfactant layer thickness, the possible coupling of Co through such interactions can be ruled out. However, when such particles are close to each other, inter-particles dipolar interactions develop. The maximum dipolar field created along the axis between two particles in contact being

$$\mu_0 H_{dip} = \frac{\mu_0 N \mu_{at}}{2\pi r^3} = \frac{\mu_0 \mu_{at} R^3}{2\pi a^3 (2R+l)^3} = 7000 \text{ Oe} \quad \text{Equation 3.2}$$

where μ_0 is the permeability of vacuum, N is the number of atoms per particle, μ_{at} is the atomic magnetic moment, R is the particle radius, a is the apparent atomic radius and $l/2$ is the surfactant layer thickness. The energy of ~6 nm Co NP (particle moment $N\mu_{at} \approx 10^4 \mu_B$) in a field of 0.7 T is much higher than RT. Thus, the above oversimplified considerations suggest the possibility of thermally stable magnetic moment interaction during the solvent evaporation, and hence for NP self-assembling coming from the dipolar interactions between SPM NPs.

The intuitive picture of self-organization scenario is as follows (Figure 3.18). Since the dipolar interactions favor formation of chains of particles, “nucleus” of such chains will spontaneously appear during the initial stage of solvent evaporation and they will further grow by attracting particles which are in the vicinity of the chains ends. At the same time, other particles which are positioned far from the end of the chain will not be able to join the chain. Instead they will try to move toward the nearest particle of the chain, orienting their magnetic moments in opposite direction. Thus, chains with progressively shorter lengths will be eventually attached to the original “nucleus” resulting in 3D rice-grain-like objects (Figure 3.18 A). Naturally, the coercivity and the remanence of such rice-grain like objects formed by dipolar forces, being macroscopic “antiferromagnets”, will be close to zero. Of course, the interplay of several parameters (like particle concentration, particle magnetic moment, solvent viscosity, and evaporation conditions) will all play a role in determining whether the particles will self-assemble into rice-grains or chains, confined into layers, or they will not assemble at all. When the NPs are larger, as the magnetic moment of the particles increases in stability and intensity,

two other types of structures have been observed. Curled wires (for NPs around 8 nm) and smooth wires (for NPs around 12 nm) are observed as expected from the increase of the dipolar interaction and its unidirectional character (Figure 3.18 B). The phenomena here observed recalls the description of the magnetic NP chain collapse under the application of an external field as in Martin *et al.*³⁹ Finally, drop evaporation seems to not interfere with the formation of the SA structures.

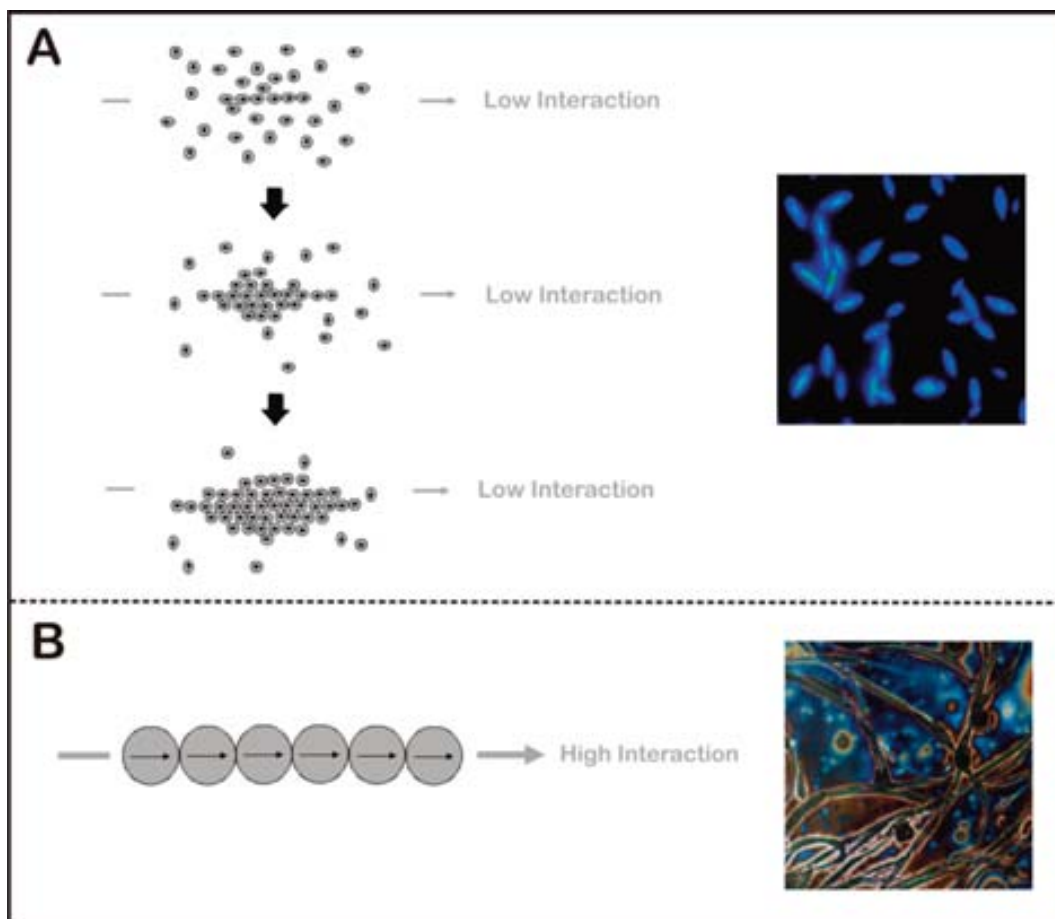


Figure 3.18: Scheme of the self-organization process for <10 nm Co NPs (A) and 10-15 nm Co NPs (B). The field arrows do not mean application of an external field, but indicates the direction of the collective magnetic behavior.

3.2.3 Summary

NPs coated with organic surfactants are able to self-organize into ordered arrays due to the interplay between vdW attractive forces and steric repulsion. When NPs are magnetic, the magnetostatic forces due to dipolar interactions (which are anisotropic) play a relevant role

influencing and even prevailing over isotropic interactions. When magnetic NPs have a stable enough magnetic moment, depending on the relation between magnetostatic forces and dispersive forces, different self-assembled arrays may be generated. It is important to note that the thermally fluctuating SPM moment of an isolated particle could be stabilized when the particle is in the vicinity of other particle and dipole-dipole interactions appear.

For instance, when magnetostatic forces prevail over dispersion forces, the particles form chains. In contrast, when magnetic interactions are weaker than the other isotropic interactions, close-packed structures are formed.^{40,41} Steric forces and vdW interactions can be modulated by using different type of surfactants, whereas dipolar magnetic interactions can be modified by changing the size of the magnetic NPs.

We show that those dipolar interactions may promote SA into elongated superstructures with a narrow size distribution, from micrometric rice-grain like structures to micrometric wire like structures. The properties of the individual particles as well as their mutual interactions determine important features of the NPs systems. A full understanding of the NPs SA will allow the design and construction of complex modular materials with customized properties.

3.3 Self-Assembly of Co Nanoparticles at Non-Compatible Substrates: Silicon Wafers

MLs of magnetic NPs present a great interest because they can be used to functionalize other materials for sensing or spintronics.^{42,43} Self-assembled MLs and multilayers of magnetic NPs can be prepared by using different techniques, apart from deposition and solvent evaporation,¹¹ such as Langmuir-Blodgett⁴⁴ or layer-by-layer deposition,⁴⁵ which are strategies based on transferring dense pre-formed MLs to the desired substrate. It is known that the more developed technique to prepare particle MLs is based on the Langmuir-Blodgett films, where an insoluble particle ML is prepared at the liquid-air interface and later on picked up with a substrate, sometimes vertically or horizontally. However, since such manipulations can be both cost and time consuming, it is interesting to explore the ability of spontaneous SA of NPs, avoiding the introduction and use of additional instrumentation. Thereby, techniques as spin-coating or drop-casting would be preferable.

Periodicity with long-range ordering is hard to achieve experimentally using drying-mediated SA, because of the dewetting of the solvent during the SA process. Dewetting is the process that describes the rupture of a liquid film on the substrate and the formation of rims and drops, and can occur at a solid-liquid or liquid-liquid interface. Moreover, other

parameters such as the type of particles, their surface coating, the solvent and the substrate would also affect the SA formation mechanism (kinetically driven,⁴⁶ late-stage drying-mediated,⁴⁷ or mediated by both the substrate-liquid and liquid-air interfaces⁴⁸).

The study of those SA of OA-protected (hydrophobic) Co NPs onto amorphous carbon (hydrophobic) and smooth graphite (HOPG, also hydrophobic) substrates has been previously studied, and many amazing forms have been observed.⁴⁹ However, the controlled SA of Co NPs onto other type of substrates (hydrophilic) has not been studied. We chose Si wafers as substrates because their technological relevance. Si wafers are thin slices of Si crystal commonly used in the fabrication of integrated circuits and other microdevices. Moreover, their flat surfaces are a key point to ensure the NPs diffusion and to enhance the collective SA of NPs during the drying process.

In this section, drop-casting and spin-coating have been used as deposition techniques for obtaining large ordered MLs of Co NPs (~10 nm in diameter) onto silicon (Si) substrates by drying-mediated SA. The obtained morphologies by both techniques have been studied together with the effect of the substrate temperature. The increase of temperature clearly modifies solvent evaporation rate, which directly affects the SA process.

3.3.1 Experimental

For instrumentation details of this section see Appendix A.7.

3.3.1.1 Substrates

Si wafers with native oxide were used as substrates. These substrates had lateral dimensions of 5 mm x 5 mm and were degassed inside an oven at 120 °C before deposition. AFM* of bare substrates showed a root mean square surface roughness of 0.39 nm (Figure 3.18 H).

3.3.1.2 Deposition of Co Nanoparticles onto Silicon Wafers

A drop of 2 mL of 10 nm Co NPs colloidal solution coated with surfactant molecules (of roughly 1 nm in length) was deposited onto the Si substrates by spin-coating (6000 rpm for 1 min) and drop-casting and then allowed to dry undisturbed for 1 h onto a hot plate at different temperatures. The hot plate was preheated 1 h before the deposition for thermal homogeneity. This NP size was chosen to avoid strong dipolar magnetic interactions, since larger size Co NPs have a strong tendency to form chains. The substrate temperature was increased from RT until 260 °C (being 181 °C the solvent bp on which Co NPs are dispersed).

3.3.2 Results and Discussion

Drop-casting and spin-coating are two deposition techniques commonly used in drying-mediated SA. In the absence of intervention either by spin-coating or drop-casting, at RT, islands and disordered MLs with holes and multilayered areas are observed. During evaporation, the liquid film may become thin enough before the nucleation limit to form the ML is reached, so that dewetting from the substrate occurs before superlattice formation. Dewetting causes holes to open up in the liquid layer, and particles to move outward, away from the holes, as the liquid evaporates, thus forming 3D islands. In addition to the effect of dewetting, which prevents long-range periodicity, a recent AFM* study has suggested that the inter-particle interaction might become strong enough to cause spinodal phase separation during the liquid drying process.⁵⁰ This effect would also cause particles to form percolating domains. In order to obtain the SA of a single ML over extended regions, the substrate temperature was increased from 25 up to 260 °C.

At low magnification, the self-assembled morphologies obtained by both techniques at different temperatures are similar. It has been found that at low substrate temperatures (25 °C), instabilities that destroy the SA homogeneity appear frequently. Anisotropic islands, in the case of spin-coating (Figure 3.19 A), and ribbon-like morphologies, in the case of drop-casting (Figure 3.19 E), have been observed. These patterns suggest that the 2D growth kinetics correspond to the spinodal nucleation and a subsequent coarsening process characteristic of drying-mediated SA. Exist the general idea that extended times would lead to more organized systems; however, it seems that other competitive forces develop when the evaporation time is increased. It can be observed that the presence of instabilities falls when the temperature rises, and in consequence the homogeneity of the ML increases (Figure 3.19). In spin-coating, no irregularities disturb the ML (Figure 3.19 B), and in drop-casting, the instabilities associated with drop shrinking are not present (Figure 3.19 F). It can be also observed, by means of spin-coating, that if we continue increasing the substrate temperature near the solvent bp (181 °C), the evaporation mode changes from liquid-film vaporization to nucleate-boiling and the nucleation phenomena (appearance and arising of gaseous bubbles from the substrate) and strong turbulences destroy the long-range homogeneity of self-assembled MLs (Figure 3.19 C). In addition, at temperatures over the bp the reduction of the time of packing causes cracks to take place at the latest stages of the drying process (Figure 3.19 D). The cracking pattern observed suggests that NPs are somehow bonded to the surface, because freely contracting films do not crack this way.

It can be conclude that a way to suppress growth instabilities appears to be to increase the

substrate temperature to values closer to the solvent bp. In such a way, surface tension as the time-lapse for growth instabilities to disrupt the NP self-assembling process, may be drastically reduced and, in consequence, the homogeneity of the layer improved. The optimal conditions to obtain a homogeneous ML were found to be by drop-casting and a temperature of 150 °C (Figure 3.19 G).

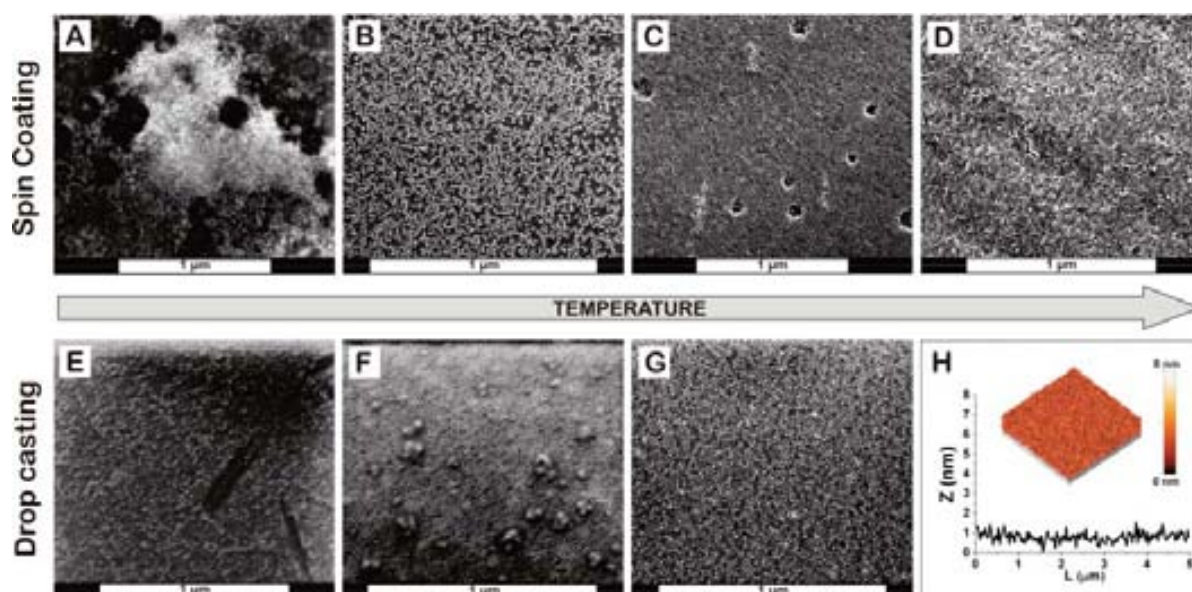


Figure 3.19: SEM images of self-assembled morphologies resulting from spin-coating technique at different substrate temperatures: 25 °C (A), 85 °C (B), 181 °C (C) and 260 °C (D). SEM images of self-assembled morphologies resulting from drop-casting technique at different substrate temperatures: 25 °C (E), 100 °C (F) and 150 °C (G). And AFM* image representative of the Si substrate (5 μm x 5 μm) used for the deposition (the color represents the height that corresponds to the pallet bar), and profile from side to side of the AFM* image (H).

Figure 3.20 shows in detail the SEM image of a NP ML with a remarkable long range homogeneity produced under optimal conditions of temperature and colloidal concentration: a drop of 2 mL of colloidal solution with a particle concentration of $\sim 10^{16}$ NPs/mL deposited by drop-casting technique and evaporated at 150 °C. An ordered ML formed from a colloidal suspension indicates that the NPs have high mobility so they can land and relocate onto the substrates during the solvent evaporation process, as observed over other substrates.⁴⁹

Despite the entropy-driven ordering tendency in the case of high particle concentrations, local disorder and voids were still inevitable in a compacted ML. One explanation would be that defective layers expulse the defects which nucleate into voids leaving a high density of islands

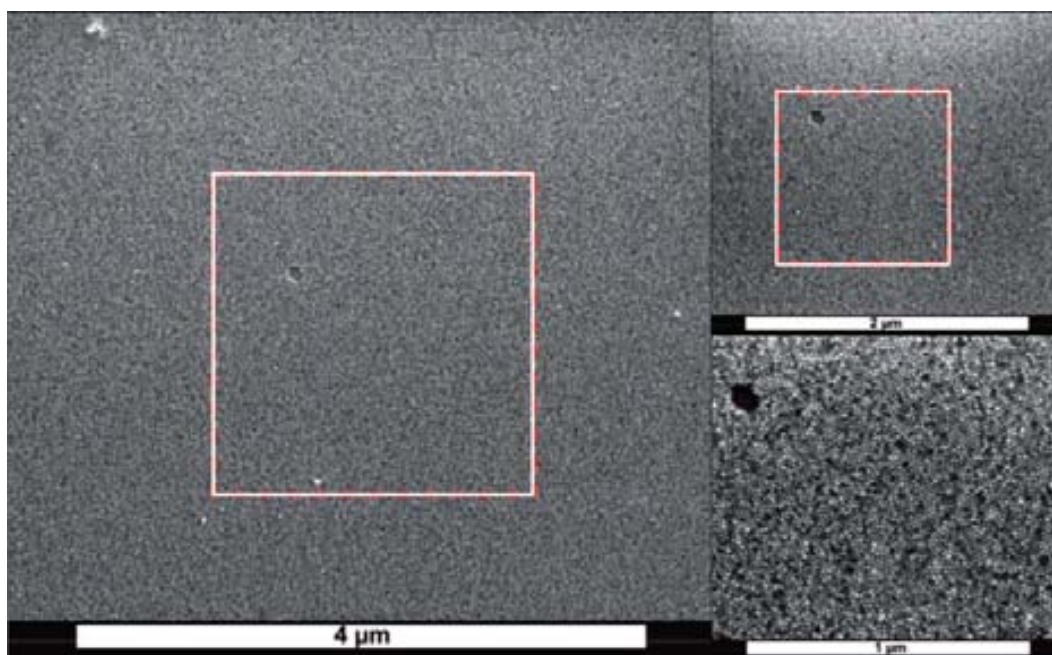


Figure 3.20: SEM images of long-range self-assembled ML of 10 nm Co NPs formed under optimal conditions (drop-casting at 150 °C).

behind. The expulsion of defects to the border of the ordered area, or the occurrence of multiple nucleation events on the substrate, induces the appearance of domain boundaries as a result of a defective percolation process. Both mechanisms support the idea that particles are able to move during the structure formation, i.e., there is still solvent left in contact with the substrate, which is consistent with other observations.⁵⁰ Moreover, depending on the size polydispersity of the employed NPs different degrees of orders are obtained. Zones with narrow size distribution produced long-range ordering. Besides, a sample with broader size distribution shows that the assembly of the same size NPs is broken by the presence of other sized NPs. We have used the 2D height–height correlation function (HHCF) (obtained with the software Mountains) to analyze the degree of ordering in self-assembled MLs. Two zones of the same sample and with different size dispersions (prepared by drop-casting at 150 °C) were analyzed (Figure 3.21). 1D HHCF graph analysis of zone 1 gives a distribution of the center-to-center distance between nearest neighbors (d_h), with a mean value of 7.0 nm and a full width at medium height (FWMH) of 2.5 nm. The same analysis of zone 2 gives a mean value of 7.9 nm with a much narrower FWMH of 1.2 nm. The correlation function for zone 1 shows a low probability even for nearest neighbors. However, zones with narrower size distributions, like zone 2, show hexagonal packing SA MLs with order beyond the eighth nearest neighbor.

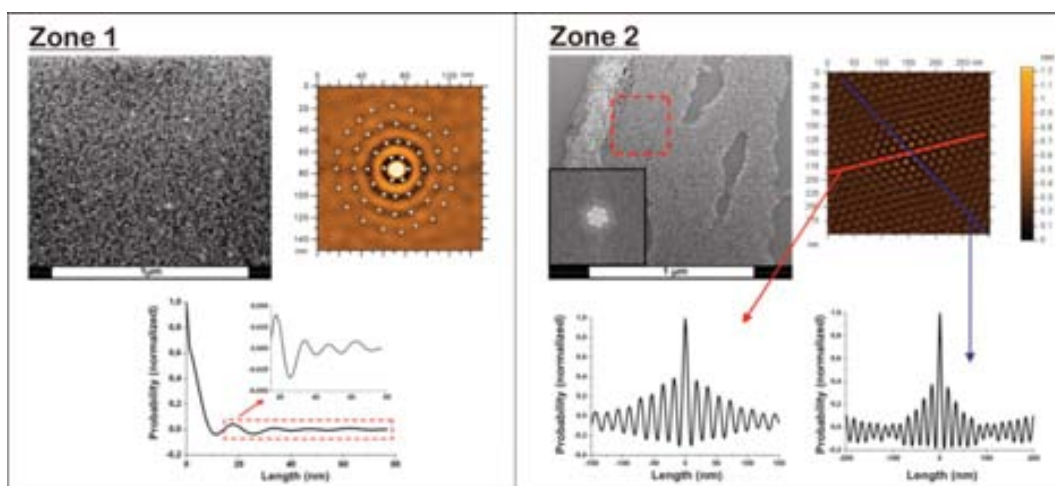


Figure 3.21: SEM images, 2D and 1D height-height correlation function for two different zones of the sample prepared by drop-casting at 150 °C.

This study confirms that the broadness of the particle size distribution is also a critical parameter to achieve long range order. It is also observed a slight increase of the size distribution near the edge of the ML domains, indicating that the size-selection process occurs simultaneously with the assembly process.

3.3.3 Summary

The possibility of obtaining large self-assembled areas of metallic magnetic NPs on top of Si, as a model of technological and hydrophilic substrates, by solvent evaporation (drying-mediated SA) has been studied. The appropriate experimental conditions to obtain self-assembled MLs of magnetic Co NPs onto Si by spin-coating and drop-casting techniques have also been determined. The influence of the evaporation temperature on the deposition morphology, determining the optimal temperature for obtaining extended and highly ordered self-assembled MLs, has been studied. And the analysis of 2D height–height correlation function of the assemblies confirms the existence of long range ordering at the micrometric scale and makes evident the major role played by the broadness of NPs size distribution.

3.4 Conclusions

NP Self-assembled structures onto amorphous carbon and smooth graphite have been studied and many amazing forms have been observed as a result of the balance between different parameteres such as electrostatic interactions, capillary forces, surface tension, volume

exclusion, substrate topography and affinity, as well as other parameters such as particle size, shape and concentration. It is especially at the nanoscale that forces such as the vdW and the directional dipolar interactions compete with comparable strength.

In a colloidal suspension, individual NCs may be viewed as analogous to dissolved molecules. As the solvent evaporates from a droplet of such a colloid on a substrate, the solubility limit will be exceeded and a superlattice of NCs can nucleate on the surface because of both particle-particle and particle-substrate interactions. Due to the increasing of particle concentration, the pinning effect becomes stronger because of the increased frequency of particle-particle interactions. There is a reduction of the available positions for the NPs and an increase of the self-assembled structure stability (once self-assembled, to move a NP require moving its neighbors). When the structure is formed, it may be strong enough to avoid perturbation when dewetting finally occurs. Beyond the substrate affinity and monodispersity of the particles, it is also important to maintain a wetting layer on the surface to allow mobility of the NCs and form large structures. Thus, the use of solvents with bp greater than RT allows the control of the evaporation rate by the choice of substrate temperature. This added thermal energy, permits the particles to diffuse to their lowest energy sites during evaporation, producing well-defined large periodical structures of Co NPs. It could be argued that the particles self-assemble in solution at very high concentrations (prior to deposition), when the majority of the solvent has been evaporated but they are still independent from the substrate, and then that the structure is transferred to the substrate when the evaporation is completed. However, we would like to note that DLS measurements showed no aggregation of the NPs before deposition (section 2.2.1.2). In addition, for the same particles, different structural patterns and dynamics were obtained with different substrates, indicating that substrate affinity plays a crucial role in the SA process.¹¹

3.5 References

1. Murray, C. B.; Kagan, C. R.; Bawendi, M. G. "Synthesis and Characterization of Monodisperse Nanocrystals and Close-Packed Nanocrystal Assemblies". *Annual Review of Materials Science* **2000**, 30, 545-610.
2. Puentes, V. F.; Bastus, N. G.; Pagonabarraga, I.; Iglesias, O.; Labarta, A.; Batlle, X. "Nucleation Phenomenon in Nanoparticle Self-Assemblies". *International Journal of Nanotechnology* **2005**, 2, 62-70.

- 3.** Sun, S. H.; Murray, C. B. "Synthesis of Monodisperse Cobalt Nanocrystals and Their Assembly into Magnetic Superlattices (Invited)". *Journal of Applied Physics* **1999**, 85, 4325-4330.
- 4.** Sun, S.; Murray, C. B.; Weller, D.; Folks, L.; Moser, A. "Monodisperse FePt Nanoparticles and Ferromagnetic FePt Nanocrystal Superlattices". *Science* **2000**, 287, 1989-1992.
- 5.** Puntès, V. F.; Krishnan, K. M.; Alivisatos, A. P. "Colloidal Nanocrystal Shape and Size Control: The Case of Cobalt". *Science* **2001**, 291, 2115-2117.
- 6.** Korgel, B. A.; Fitzmaurice, D. "Self-Assembly of Silver Nanocrystals into Two-Dimensional Nanowire Arrays". *Advanced Materials* **1998**, 10, 661-665.
- 7.** Dabbousi, B. O.; Murray, C. B.; Rubner, M. F.; Bawendi, M. G. "Langmuir-Blodgett Manipulation of Size-Selected CdSe Nanocrystallites". *Chemistry of Materials* **1994**, 6, 216-219.
- 8.** Legrand, J.; Petit, C.; Pileni, M. P. "Domain Shapes and Superlattices Made of 8 Nm Cobalt Nanocrystals: Fabrication and Magnetic Properties". *Journal of Physical Chemistry B* **2001**, 105, 5643-5646.
- 9.** Giersig, M.; Mulvaney, P. "Preparation of Ordered Colloid Monolayers by Electrophoretic Deposition". *Langmuir* **1993**, 9, 3408-3413.
- 10.** Rabani, E.; Reichman, D. R.; Geissler, P. L.; Brus, L. E. "Drying-Mediated Self-Assembly of Nanoparticles". *Nature* **2003**, 426, 271-274.
- 11.** Pileni, M. P. "Nanocrystal Self-Assemblies: Fabrication and Collective Properties". *Journal of Physical Chemistry B* **2001**, 105, 3358-3371.
- 12.** Nath, N.; Chilkoti, A. "Label-Free Biosensing by Surface Plasmon Resonance of Nanoparticles on Glass: Optimization of Nanoparticle Size". *Analytical Chemistry* **2004**, 76, 5370-5378.
- 13.** Turkevich, J.; Stevenson, P. C.; Hillier, J. "A Study of the Nucleation and Growth Processes in the Synthesis of Colloidal Gold". *Discussions of the Faraday Society* **1951**, 55.
- 14.** Frens, G. "Controlled Nucleation for Regulation of Particle-Size in Monodisperse Gold Suspensions". *Nature-Physical Science* **1973**, 241, 20-22.

15. Zhang, D.-F.; Zhang, Q.; Niu, L.-Y.; Jiang, L.; Yin, P.-G.; Guo, L. "Self-Assembly of Gold Nanoparticles into Chain-Like Structures and Their Optical Properties". *Journal of Nanoparticle Research* **2011**, 13, 3923-3928.
16. Lin, X. M.; Jaeger, H. M.; Sorensen, C. M.; Klabunde, K. J. "Formation of Long-Range-Ordered Nanocrystal Superlattices on Silicon Nitride Substrates". *Journal of Physical Chemistry B* **2001**, 105, 3353-3357.
17. Kim, B.; Tripp, S. L.; Wei, A. "Self-Organization of Large Gold Nanoparticle Arrays". *Journal of the American Chemical Society* **2001**, 123, 7955-7956.
18. Poddar, P.; Telem-Shafir, T.; Fried, T.; Markovich, G. "Dipolar Interactions in Two- and Three-Dimensional Magnetic Nanoparticle Arrays". *Physical Review B* **2002**, 66, 060403.
19. Penn, R. L.; Oskam, G.; Strathmann, T. J.; Searson, P. C.; Stone, A. T.; Veblen, D. R. "Epitaxial Assembly in Aged Colloids". *The Journal of Physical Chemistry B* **2001**, 105, 2177-2182.
20. Lee, E. J. H.; Ribeiro, C.; Longo, E.; Leite, E. R. "Oriented Attachment: An Effective Mechanism in the Formation of Anisotropic Nanocrystals". *The Journal of Physical Chemistry B* **2005**, 109, 20842-20846.
21. Jana, N. R.; Gearheart, L.; Murphy, C. J. "Wet Chemical Synthesis of Silver Nanorods and Nanowires of Controllable Aspect Ratio". *Chemical Communications* **2001**, 617-618.
22. Nikoobakht, B.; El-Sayed, M. A. "Preparation and Growth Mechanism of Gold Nanorods (Nrs) Using Seed-Mediated Growth Method". *Chemistry of Materials* **2003**, 15, 1957-1962.
23. Xu, Z.-C.; Shen, C.-M.; Xiao, C.-W.; Yang, T.-Z.; Chen, S.-T.; Li, H.-L.; Gao, H.-J. "Fabrication of Gold Nanorod Self-Assemblies from Rod and Sphere Mixtures Via Shape Self-Selective Behavior". *Chemical Physics Letters* **2006**, 432, 222-225.
24. Lim, S. I.; Ojea-Jimenez, I.; Varon, M.; Casals, E.; Arbiol, J.; Puntes, V. "Synthesis of Platinum Cubes, Polypods, Cuboctahedrons, and Raspberries Assisted by Cobalt Nanocrystals". *Nano Letters* **2010**, 10, 964-973.
25. Moser, A.; Takano, K.; Margulies, D. T.; Albrecht, M.; Sonobe, Y.; Ikeda, Y.; Sun, S. H.; Fullerton, E. E. "Magnetic Recording: Advancing into the Future". *Journal of Physics D-Applied Physics* **2002**, 35, R157-R167.

- 26.** Yamamoto, K.; Majetich, S. A.; McCartney, M. R.; Sachan, M.; Yamamuro, S.; Hirayama, T. "Direct Visualization of Dipolar Ferromagnetic Domain Structures in Co Nanoparticle Monolayers by Electron Holography". *Applied Physics Letters* **2008**, 93.
- 27.** Zeng, H.; Li, J.; Liu, J. P.; Wang, Z. L.; Sun, S. H. "Exchange-Coupled Nanocomposite Magnets by Nanoparticle Self-Assembly". *Nature* **2002**, 420, 395-398.
- 28.** Zeng, H.; Li, J.; Liu, J. P.; Wang, Z. L.; Sun, S. "Exchange-Coupled Nanocomposite Magnets by Nanoparticle Self-Assembly". *Nature* **2002**, 420, 395-398.
- 29.** Puentes, V. F.; Gorostiza, P.; Aruguete, D. M.; Bastus, N. G.; Alivisatos, A. P. "Collective Behaviour in Two-Dimensional Cobalt Nanoparticle Assemblies Observed by Magnetic Force Microscopy". *Nature Materials* **2004**, 3, 263-268.
- 30.** Georgescu, M.; Viota, J. L.; Klokkenburg, M.; Erne, B. H.; Vanmaekelbergh, D.; van Emmichoven, P. A. Z. "Short-Range Magnetic Order in Two-Dimensional Cobalt-Ferrite Nanoparticle Assemblies". *Physical Review B* **2008**, 77.
- 31.** Russier, V.; Petit, C.; Legrand, J.; Pileni, M. P. "Collective Magnetic Properties of Cobalt Nanocrystals Self-Assembled in a Hexagonal Network: Theoretical Model Supported by Experiments". *Physical Review B* **2000**, 62, 3910-3916.
- 32.** LaMer, V. K.; Dinegar, R. H. "Theory, Production and Mechanism of Formation of Monodispersed Hydrosols". *Journal of the American Chemical Society* **1950**, 72, 4847-4854.
- 33.** Stranski, I. N.; Krastanow, L. "Abhandlungen der Mathematisch-Naturwissenschaftlichen Klasse IIB". *Akademie der Wissenschaften Wien* **1938**, 146, 797-810.
- 34.** Suzuki, T.; Weller, D.; Chang, C. A.; Savoy, R.; Huang, T.; Gurney, B. A.; Speriosu, V. "Magnetic and Magneto-optic Properties of Thick Face-Centered-Cubic Co Single-Crystal Films". *Applied Physics Letters* **1994**, 64, 2736-2738.
- 35.** Chantrell, R. W.; Popplewell, J.; Charles, S. W. "Measurements of Particle-Size Distribution Parameters in Ferrofluids". *IEEE Transactions on Magnetics* **1978**, 14, 975-977.
- 36.** Stoner, E. C.; Wohlfarth, E. P. "A Mechanism of Magnetic Hysteresis in Heterogeneous Alloys". *Philosophical Transactions of the Royal Society of London. Series A, Mathematical*

and *Physical Sciences* **1948**, 240, 44.

37. Skumryev, V.; Stoyanov, S.; Zhang, Y.; Hadjipanayis, G.; Givord, D.; Nogues, J. "Beating the Superparamagnetic Limit with Exchange Bias". *Nature* **2003**, 423, 850-853.

38. Alder, B. J.; Wainwright, T. E. "Phase Transition for a Hard Sphere System". *Journal of Chemical Physics* **1957**, 27, 1208-1209.

39. Martin, J. E.; Anderson, R. A.; Tigges, C. P. "Thermal Coarsening of Uniaxial and Biaxial Field-Structured Composites". *Journal of Chemical Physics* **1999**, 110, 4854-4866.

40. Korgel, B. A.; Fitzmaurice, D. "Small-Angle X-Ray-Scattering Study of Silver-Nanocrystal Disorder-Order Phase Transitions". *Physical Review B* **1999**, 59, 14191-14201.

41. Yamamuro, S.; Farrell, D. F.; Majetich, S. A. "Direct Imaging of Self-Assembled Magnetic Nanoparticle Arrays: Phase Stability and Magnetic Effects on Morphology". *Physical Review B* **2002**, 65.

42. Sun, S. "Recent Advances in Chemical Synthesis, Self-Assembly, and Applications of Fept Nanoparticles". *Advanced Materials* **2006**, 18, 393-403.

43. Yakushiji, K.; Ernult, F.; Imamura, H.; Yamane, K.; Mitani, S.; Takanashi, K.; Takahashi, S.; Maekawa, S.; Fujimori, H. "Enhanced Spin Accumulation and Novel Magnetotransport in Nanoparticles". *Nat Mater* **2005**, 4, 57-61.

44. Kotov, N. A.; Meldrum, F. C.; Wu, C.; Fendler, J. H. "Monoparticulate Layer and Langmuir-Blodgett-Type Multiparticulate Layers of Size-Quantized Cadmium-Sulfide Clusters - a Colloid-Chemical Approach to Superlattice Construction". *Journal of Physical Chemistry* **1994**, 98, 2735-2738.

45. Kotov, N. A., *Multilayer Thin Films*, eds. G. Decher and J. B. Schlenoff, Wiley-VCH Verlag GmbH & Co., Weinheim, **2002**, Chapter 8. .

46. Bigioni, T. P.; Lin, X. M.; Nguyen, T. T.; Corwin, E. I.; Witten, T. A.; Jaeger, H. M. "Kinetically Driven Self Assembly of Highly Ordered Nanoparticle Monolayers". *Nature Materials* **2006**, 5, 265-270.

47. Tang, J.; Ge, G. L.; Brus, L. E. "Gas-Liquid-Solid Phase Transition Model for Two-Dimensional Nanocrystal Self-Assembly on Graphite". *Journal of Physical Chemistry B* **2002**, 106, 5653-5658.

48. Korgel, B. A.; Fitzmaurice, D. "Condensation of Ordered Nanocrystal Thin Films". *Physical Review Letters* **1998**, 80, 3531-3534.

49. Varon, M.; Pena, L.; Balcells, L.; Skumryev, V.; Martinez, B.; Puntès, V. "Dipolar Driven Spontaneous Self Assembly of Superparamagnetic Co Nanoparticles into Micrometric Rice-Grain Like Structures". *Langmuir* **2010**, 26, 109-116.

50. Ge, G. L.; Brus, L. "Evidence for Spinodal Phase Separation in Two-Dimensional Nanocrystal Self-Assembly". *Journal of Physical Chemistry B* **2000**, 104, 9573-9575.

Chapter 4

Electron Holography and Lorentz Microscopy of Self-Assembled Cobalt Nanoparticles Structures

In recent years, the dynamics of the assemblies of interacting magnetic NPs has been subject of extensive research as much as tailoring the properties of solids made up of magnetic NPs assemblies. This approach is being explored for a variety of applications such as logic gates,¹ thermally stable magnetic memories² or strong magnets for high-end electronics,³ among others. Ordering on the NP scale produces changes in the energy band gaps of the crystalline materials, which determine their chemical and physical properties.⁴ On the other hand, the lack of symmetry can lead to distinctly different properties that are unique to non-crystalline materials.⁵ This is especially true for magnetic NPs, where materials may achieve new magnetic properties by mixing NPs of different hardness and saturation intensity.² Thus, when considering the magnetic NP assembly, the particle-particle interactions becomes a determining issue, dominating the macroscopic magnetic behavior.⁶ Therefore, through changing the particle density, inter-distance, or space arrangement, the magnetic properties might be controlled by design.^{7,8}

An assembly of NPs can be considered as a meta-material where the atoms are replaced by NPs, and where dipolar interactions between single-domain ferro- or ferrimagnetic NPs may be strong and lead to magnetic ordering.^{7,9-11} Dipolar ferromagnetism (or superferromagnetism) is a collective FM state of single domain FM particles.¹² As a consequence, superferromagnetic domains are expected to be similar to FM domains with the difference that *atomic spins* are replaced by the *super-spins* of the single-domain NPs. Since the particles contain a surfactant layer (they are generally separated a few nanometers) the exchange interactions between NP, even in the dense assemblies, is negligible, and their mutual interactions are therefore

dominated by long-range dipole-dipole interactions. In addition, the magneto-crystalline anisotropy energy of the magnetic NPs is known to be low, meaning that the magnetization pattern of an assembly of spherical magnetic NPs is mainly determined by collective dipole-dipole interactions. Georgescu *et al.* showed recently a MFM study, supported by numerical simulations, which showed a strong tendency of the moments to arrange themselves in flux-closure structures within 2D islands formed by spherical NPs.¹³ Furthermore, spin-glass like behavior has been also demonstrated for these 2D systems of NPs.^{6,9}

Studies based on microscopic imaging are usually difficult to carry out. Scanning probe techniques such as spin-polarized scanning tunnelling microscopy (SP-STM)^{14,15} and MFM,^{11,13,16,17} while being powerful for magnetic domain imaging, are generally difficult to be used for imaging NP assemblies due to the significant interference of the morphological corrugations. In contrast, electron probes are little affected by morphology and give vector signals that are directly proportional to magnetization. Electron microscopy has revolutionized the understanding of materials by completing the processing-structure-properties links down to atomistic levels. In particular, TEM is a powerful and widely used tool for characterizing the microstructure and chemistry of materials.¹⁸ But, an important limitation of most of the TEM imaging modes is that only spatial distribution of image intensity is recorded. All information about phase shift of the high-energy electron wave that passes through the specimen is lost. However, in electron microscopy the objects are especially phase shifted according to the Aharonov-Bohm effect.¹⁹ In TEM, there are two primary techniques for achieving useful micromagnetic image contrast: **Lorentz microscopy** and **electron holography**. Both techniques take advantage of the so-called Lorentz force, which occurs whenever an electron beam passes through a region with transverse magnetic fields. Electron holography has the ability to yield quantitative and local information about the nanoscale magnetic properties. Studies of the magnetic fields in different materials such as NCs,^{20,21} nanostructures,²² thin films²³ or devices²⁴ have been carried out. Recently, dipolar ferromagnetism has been observed in array of different magnetic NPs. Majetich and co workers observed long-range dipolar ferromagnetism in MLs of Co particles²⁵ and, later on, the dipolar FM phase transition in a ML of F_3O_4 NPs.²⁶

In this chapter we report on different studies of magnetic self-assembled structures formed by Co NPs by using Lorentz microscopy and electron holography. We mapped the in-plane induced magnetic field in 2D self-assembled structures formed by ϵ -Co NPs and demonstrated the formation of magnetically ordered regions and vortex states. A number of previous simulations have predicted vortex structures due to magnetostatic interactions,²⁷⁻²⁹ perhaps due to the finite sample size or the treatment of boundary conditions. Here we performed the

direct observation of the magnetic flux distribution of the SA structures, showing the FM ordering of the dipole neighboring particles.

4.1 Basis of Lorentz Microscopy and Electron Holography

Lorentz microscopy and electron holography has been used for several years to investigate the magnetic structure of thin FM films. These special imaging techniques make use of the deflection of charged particles in electric and magnetic domains caused by the Lorentz force. The Lorentz force for an electron passing through a specimen with the magnetic flux density B , is given by

$$F = -|e|(v \times B) \quad \text{Equation 4.1}$$

where v is the velocity and e the elementary electric charge. The direction of the force expressed by the vector product is given by Fleming's left hand rule.

And the electrons passing experience Lorentz deflection given by

$$\theta = \frac{eB\lambda t}{h} \quad \text{Equation 4.2}$$

where λ is the electron wavelength, t is the thickness of the domain and h is Plank's constant.

The deflection of the electron can be use to image magnetic domains.

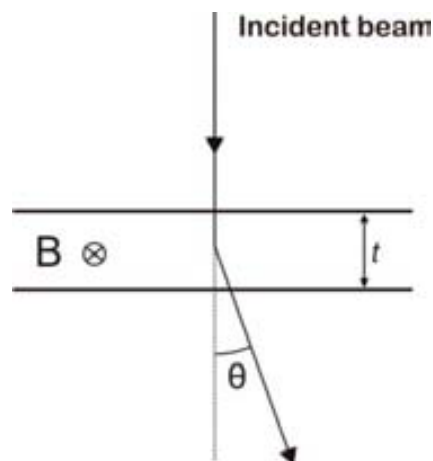


Figure 3.2: Schematic overview of the deflection of an electron by the Lorentz force.

There are different techniques which fall in the category of **Lorentz microscopy**. In the present work we considered the Fresnel mode.³⁰ The principle involved in Fresnel imaging is that electrons are deflected uniformly in each domain, resulting in the beam converging/diverging below the walls in the sample. And by taking the image out of focus, i.e. in a plane not coincident by the sample plane, contrast is generated at the boundary regions which are delineated by bright and dark bands. Figure 4.2 shows how the image plane is shifted below the specimen plane. An important advantage of Lorentz microscopy is the possibility to take multiple image sequences because no reconstruction process is required. Nevertheless, the main problem is the limited resolution of the defocused images, which can be a drawback in the interpretation of the results.

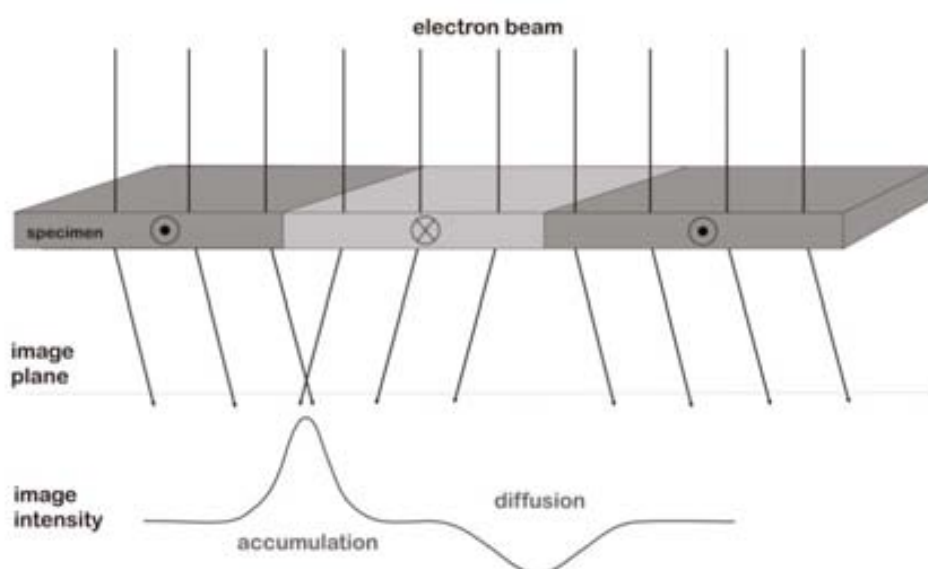


Figure 4.2: Scheme showing the Fresnel imaging mode of Lorentz microscopy. The Lorentz force deflects electrons (velocity v) passing through a magnetic domain (flux B) of the specimen, what leads to regions of accumulation and diffusion at the border of the magnetic domain. The suggested intensity distribution corresponds to the case of over focus.

Denis Gabor developed the **electron holography** technique in 1948, based on the formation of an interference pattern or “hologram” in the TEM.^{31,32} In contrast of most conventional TEM techniques, which only records spatial distributions of image intensity, electron holography allows recording the entire object information in an interference pattern. Thus, also allows the phase shift of the high-energy electron wave that has passed through the specimen to be measured directly. Phase shift is sensitive to local variations in both the in-plane

magnetic induction and electrostatic potential in the sample, allowing the extraction of quantitative information about magnetic and electric fields in materials. The particular advantage of the electron holography is that unwanted contributions to the contrast such as variations of sample composition and thickness can be removed from the holographic phase more easily than from images recorded by other techniques such as Lorentz microscopy. Furthermore, Ruijter and Weiss studied the detection limits of the magnetic signals that can be measured using electron holography, suggesting that a practical phase precision of $\pi/100$ radians may be achieved for a special resolution of 1-3 nm.³³

4.1.1. Off-Axis Electron Holography

The off-axis (or “sideband”) mode of electron holography involves the examination of an electron-transparent specimen using defocused illumination from a highly coherent field-emission gun (FEG) electron source.³⁴ The general setup used for the acquisition of off-axis electron holograms can be observed in Figure 4.3. To acquire a hologram, the region of interest on the specimen should be positioned covering approximately half the field of view. One characteristic feature (together with the FEG) is the presence of an electron biprism located below the sample,³⁵ which takes the form of a fine wire made from either Pt- or Au-coated quartz and two grounded metal electrodes.

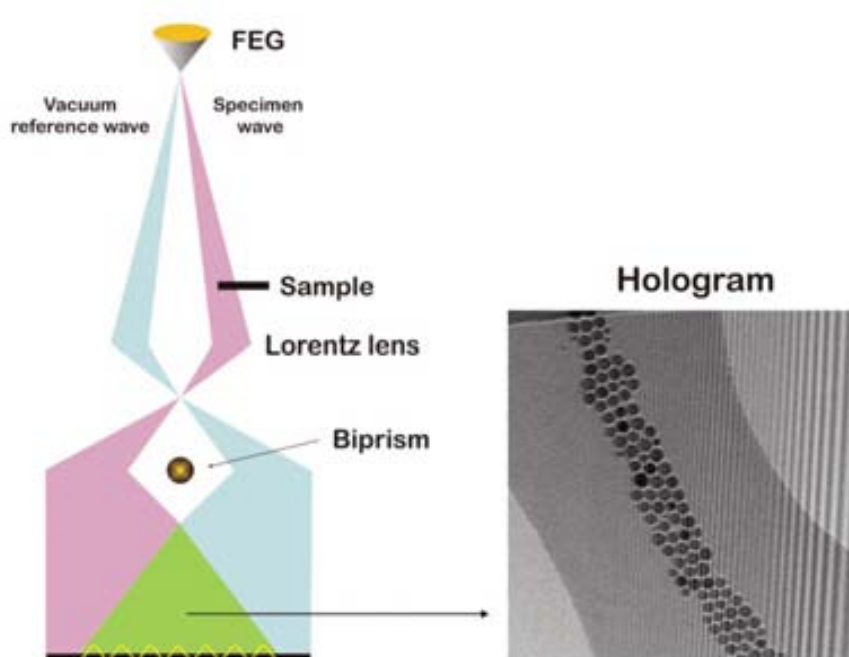


Figure 4.3: Scheme illustration of the setup used for generating off-axis electron holograms.

The application of a voltage to the biprism results in an overlap of a reference electron wave that has passed through vacuum (or a thin region of support film) with the electron wave that had passed through the specimen. If the illumination is sufficiently coherent, then the holographic interference fringes are formed in the overlap region, with a spacing that is inversely proportional to the biprism voltage (typically between 50 and 200 V). The amplitude and the phase shift of the electron wave from the specimen are recorded in the intensity and the position of the holographic fringes, respectively. Hence, the hologram contains information about complete wavefunction transmitted by the specimen (amplitude and phase information).

4.1.1.1 Imaging Theory

A fraction of the electron wave that is transmitted through the object, changes its amplitude (A) and phase (φ). For coherent TEM imaging, the electron wavefunction at the exit surface of the sample can be written in form

$$\psi_s(\mathbf{r}) = A_s(\mathbf{r})e^{i\varphi_s(\mathbf{r})} \quad \text{Equation 4.3}$$

where \mathbf{r} is a 2D vector in the plane of the sample with components x,y . And the electron wavefunction in the image plane, which contains all the desired information, can be written in the form

$$\psi_i(\mathbf{r}) = A_i(\mathbf{r})e^{i\varphi_i(\mathbf{r})} \quad \text{Equation 4.4}$$

where \mathbf{r} is a 2D vector in the plane of the sample and the subscript i refers to the image plane.

In a standard bright field TEM image, the recorded intensity distribution is then given by the expression

$$I(\mathbf{r}) = |A_i(\mathbf{r})|^2 \quad \text{Equation 4.5}$$

A reference wave Ψ_r , (where the electron has not been affected by the object) is additionally required to record the off-axis electron hologram. The intensity can be obtained by adding a

plane wave with a tilt corresponding to $\mathbf{q}=\mathbf{q}_c$ to the electron wave, where \mathbf{q}_c is a 2D vector in the reciprocal space.

$$\psi_r(\mathbf{r}) = e^{i2\pi\mathbf{q}_c\cdot\mathbf{r}} \quad \text{Equation 4.6}$$

Thus the image intensity can be described as the modulus squared of an electron wavefunction that has been modified by the specimen and the objective lens. After passing the biprism, the two beams interfere at the image plane giving the electron hologram with the following intensity distribution

$$I_{hol}(\mathbf{r}) = |\psi_i(\mathbf{r}) + \psi_r(\mathbf{r})|^2 = |\psi_s(\mathbf{r}) \otimes t(\mathbf{r}) + e^{i2\pi\mathbf{q}_c\cdot\mathbf{r}}|^2 \quad \text{Equation 4.7}$$

$$= 1 + A_i^2(\mathbf{r}) + 2A_i(\mathbf{r}) \cos[2\pi\mathbf{q}_c \cdot \mathbf{r} + \varphi_i(\mathbf{r})] \quad \text{Equation 4.8}$$

where the tilt of the reference wave is specified by the 2D reciprocal space vector $\mathbf{q}=\mathbf{q}_c$. There are three separated contributions to the intensity distribution in a hologram: the reference wave, the image wave, and an additional set of cosinusoidal fringes with local phase shifts and amplitudes that are exactly equivalent to the phase and amplitude of the electron wavefunction in the image plane, φ_i and A_i , respectively.

4.1.1.2 Hologram Reconstruction

To obtain amplitude and phase information, the off-axis electron hologram is first Fourier transformed. From Equation 4.8, the complex Fourier transform of the hologram is given by

$$FT[I_{hol}(\mathbf{r})] = \delta(\mathbf{q}) + FT[A_i^2(\mathbf{r})] \quad (\text{autocorrelation})$$

$$+ \delta(\mathbf{q} + \mathbf{q}_c) \otimes [A_i(\mathbf{r})e^{i\varphi_i(\mathbf{r})}] \quad (\text{sideband } +1)$$

$$+ \delta(\mathbf{q} - \mathbf{q}_c) \otimes [A_i(\mathbf{r})e^{-i\varphi_i(\mathbf{r})}] \quad (\text{sideband } -1)$$

$$\text{Equation 4.9}$$

The four terms of Equation 4.9 can be described as follows: A first peak at the reciprocal space origin corresponding to the Fourier transform of the reference image (contribution of electrons that propagate through the system without being affected by the sample), a second peak centered on the origin corresponding to the Fourier transform of a bright-field TEM image of the sample (yields the intensity), a third peak centered at $\mathbf{q}=-\mathbf{q}_c$ corresponding to the Fourier transform of the desired image wavefunction, and a last peak centered at $\mathbf{q}=\mathbf{q}_c$ corresponding to Fourier transform of the complex conjugate of the wavefunction. These contributions are visible as a central “autocorrelation” peak and two “sidebands” (containing identical information) as can be observed in the Figure 4.4 b).

Both the amplitude and the phase can be numerically reconstructed following the procedure described in Figure 4.4. After the Fourier transform of the holographic phase is made, two sidebands can be detected. If one of the two sidebands are selected digitally with a circular aperture and inverse Fourier transformed, the amplitude and phase of this complex wavefunction can be then easily calculated (Figure 4.4 c,d).

An inverse Fourier transform will provide the complex image wave $\psi_i=Ae^{i\varphi(r)}$ or its complex conjugated $\psi_i^*=Ae^{-i\varphi(r)}$ depending on the choice of the sideband. We can now determine the amplitude and phase φ of the image wave, whereby a negative sign of the phase can be reversed by a contrast inversion. When the phase image is calculated digitally, some 2π phase discontinuities that are not related with the specimen feature can appear. This is because the reconstruction process is unable to determine between a phase change of π and $\pi+2\pi$. In this case a phase unwrapping is able to handle this problem by applying suitable algorithms before the interpretation of the results.

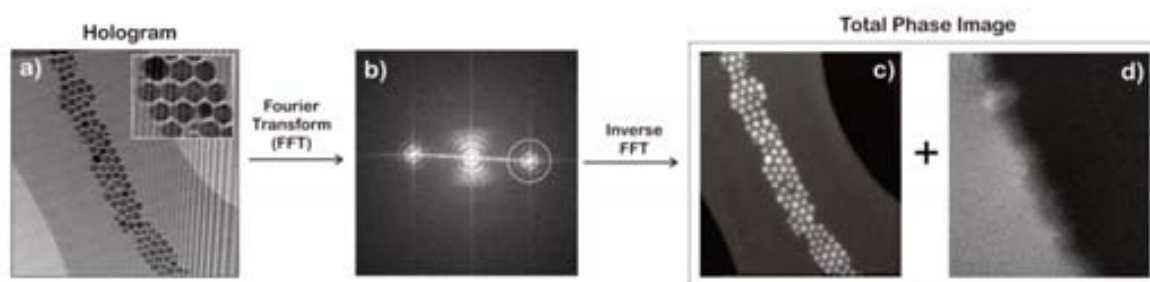


Figure 4.4: Step-by-step procedure to reconstruct the phase from an electron hologram of a self-assembled structure of Co NPs. a) Representative off-axis electron hologram of a self-assembled Co NPs structure (inset: enlargement of the image showing interference fringes within the sample). b) Fourier transform of the electron hologram. c+d) Phase image obtained after inverse Fourier transformation of one of the side bands, formed by the electrostatic (c) and the magnetic (d) component.

4.1.2. Magnetic and Mean Inner Potential Contributions to the Phase

The total phase image contains both the electric and the magnetic contribution to the phase shift. Neglecting dynamical diffraction (i.e., assuming that the specimen is thin and weakly diffracting), the phase shift can be expressed in the form

$$\varphi(x) = \varphi_E + \varphi_M = C_E \int V(x, z) dz - \left(\frac{e}{h}\right) \int A_z(x, z) dz \quad \text{Equation 4.10}$$

$$= C_E \int V(x, z) dz - \left(\frac{e}{h}\right) \iint B_{\perp}(x, z) \quad \text{Equation 4.11}$$

where φ_E is the electrostatic component of the phase shift, φ_M is the magnetic component of the phase shift, and C_E is the energy dependent constant

$$C_E = \left(\frac{2\pi}{\lambda}\right) \left(\frac{E+E_0}{E(E+2E_0)}\right) \quad \text{Equation 4.12}$$

z is the incident electron beam direction, x is a direction in the plane of the specimen, A_z is the component of the magnetic vector potential A in the beam direction, B_{\perp} is the component of the magnetic induction within and outside the specimen perpendicular to both x and z , V is the electrostatic potential, λ is the (relativistic) electron wavelength, and E and E_0 are, respectively, the kinetic and rest mass energies of the incident electron.³⁶ And C_E has values of 7.29×10^6 , 6.53×10^6 , and $5.39 \times 10^6 \text{ rad V}^{-1} \text{ m}^{-1}$ at 200 kV, 300 kV and 1 MV, respectively.

The dominant contribution to the electrostatic potential is from the **mean inner potential**, which depends on the local composition and density of the sample. If neither V nor B_{\perp} varies along the electron beam direction within a sample of thickness t , then

$$\varphi(x) = C_E V(x)t(x) - \left(\frac{e}{h}\right) \int B_{\perp}(x)t(x) dx \quad \text{Equation 4.12}$$

Determination of the phase gradient is particularly useful for a magnetic material because of the following relationship (differentiating Equation 4.13):

$$\frac{d\varphi(x)}{dx} = C_E \frac{d}{dx} \{V(x)t(x)\} - \left(\frac{e}{h}\right) B_{\perp}(x)t(x) \quad \text{Equation 4.14}$$

In a sample with uniform thickness and composition, the first term (electrostatic potential contribution) disappears and the phase gradient is directly proportional to the in-plane component of the magnetic induction in the specimen:

$$\frac{d\varphi(x)}{dx} = \left(\frac{e}{h}\right) B_{\perp}(x)t(x) \quad \text{Equation 4.15}$$

4.1.3 Measurement of Magnetic Fields

4.1.3.1 Separation of the Phase Information

As explained above, when characterizing magnetic fields inside nanostructured materials, the mean inner potential (MIP) contribution to the measured phase shift must, in general, be removed to interpret the magnetic contribution. Experimentally, there are two different ways to calculate the MIP:

I) Acquisition of two holograms of the same area but at two different acceleration voltages (A and B). The magnetic signal is independent of the accelerating voltage used, and subtraction of the two phase images (A-B) can be used to provide us the MIP.

II) Acquisition of two holograms of the same nanostructure but with opposite direction of the magnetic contribution (C and D). This method involves performing magnetization reversal *in situ* of the in the electron microscope. From here, it is easy to calculate the MIP contribution to the phase from $\frac{1}{2}(C+D)$ because the inverse magnetic parts will cancel out entirely.

Subtracting the MIP from the total phase image of the original nanostructure provides access to its magnetic information. The magnetic information can also be calculated directly from the second way (II) by calculating $\frac{1}{2}(C-D)$, serving as an additional proof to make sure that the magnetization reversed completely and that the particles are properly saturated in the additional holograms.

4.1.3.2 Visualization of the Magnetic Contribution to the Phase

Once the magnetic contribution is obtained, a direct representation of the magnetic induction can therefore be obtained by adding contours to a magnetic phase image. The contours provide a semi-quantitative map of the strength of the local magnetic field in the sample, corresponding to magnetic lines of force, along which $\int B \cdot dS = 0$. The fact that phase differences of 2π between adjacent contours correspond to $\int B \cdot dS = (h/e) = 4 \cdot 10^{-15}$ Wb provides the basis for the measurement of magnetic fields. Subject to limitations of signal-to-noise ratio, smaller phase differences can be measured by decreasing the spacing of the contours obtained from the phase image.

Figure 4.5 show the two possible representations of the magnetic contribution (b): by contour lines (c), showing the strength of the local magnetic flux; and by a color code (d), indicating the direction of the magnetization. It is possible combine both signal representations in one image, and also apply a position mask of the interest region for a better visualization (e).

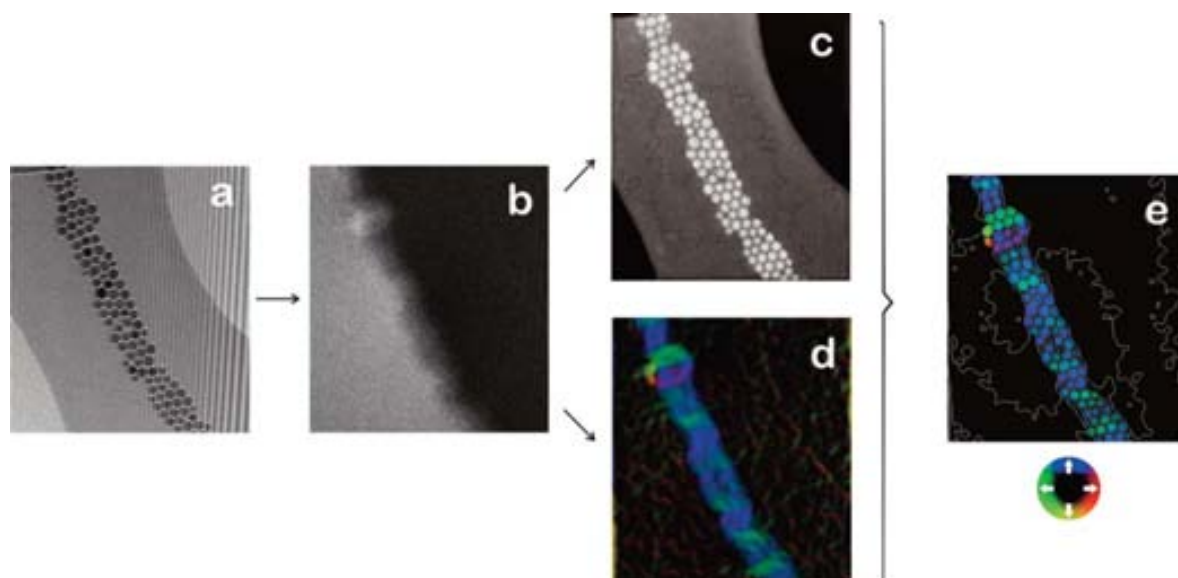


Figure 4.5: a) Off-axis electron hologram, b) Magnetic component image, c) Magnetic signal represented by contour lines and overlaid onto a MIP image, d) Magnetic signal represented by color map and e) Combination of c and b images (after applying a position mask for visualize only the NPs).

4.2. Electron Holography of Chain-like Self-Assembled Structures

4.2.1. Experimental

4.2.1.1 Sample Preparation

On drop of ~15 nm Co NPs solution was deposited onto a holey carbon-coated copper TEM grid and left to dry inside a globe box. These dispersion conditions produced a variety of self-assembled chain nanostructures as imaged by TEM (Figure 4.6). The magnetic induction of different Co self-assembled structures forming chains while increasing the chain width has been studied. Also, the grid was mounted in the TEM holder inside the globe box for avoid oxidation of the Co particles.

4.2.1.2 Data Acquisition

Two sets of experiments were performed. Off-axis electron holograms were acquired in Lorentz mode in a Titan Analytical 80-300ST TEM with a charge-coupled device (CCD) camera and biprism voltages of 180 and 200 V for each set of experiments, respectively. The experiments were performed at RT, and the acquisition time was of 6 s and 12 s. The direction of magnetization in each chain was *in situ* reversed by tilting the sample by ± 60 degrees and turning on the conventional microscope objective lens to apply a magnetic field (2 T) to the sample parallel to the direction of the electron beam. Then, the objective lens was turned off and the sample tilted back to 0 degrees for hologram acquisition in field-free conditions with the particles at remanence. Following this procedure, the different holograms were recorded with the chains magnetized in opposite directions and analyzed using Semper.⁴¹

4.2.2 Results and Discussion

Off-axis electron holography has been used to reveal the magnetic induction associated to different distributions of self-assembled Co NPs. The first observations of the magnetic induction in 2D self-assembled NPs structures with unprecedented resolution of ~5 nm, a resolution smaller than the particle size, are shown. Long spontaneously formed chains are commonly observed for individual magnetic NPs provided by the fact that the interacting forces between the particles are suitably balanced. If the NP magnetic moments are too weak, or the surfactants too long and bulky, the particles would not magnetically attract each other, which would result in a hexagonal lattice. And if the magnetic moments of the particles are too strong,

or the surfactants too short), the particles would quickly agglomerate into 3D structures. Formation of such 2D chain structures of single or few NPs in wide is very interesting and requires a delicate balance of the interaction on two different scales: on one hand, the magnetic interaction between the particles must be weaker than the vdW forces for the particles to assemble in a hexagonal pattern in the assembly; however, the magnetic interaction between the particles must be strong enough to give the assembly a magnetic dipole that results in the formation of the elongated structures. It could be a vdW that when place few NPs together those develop the magnetic interaction and elongated growth. The balance between the 2D self-assembled MLs and the single particle magnetic chain can be easily tuned by the size of the NP.³⁷ In particular, as the mean dipolar energy increases with the particle volume, the thermal energy at RT becomes comparable to the dipolar energy of two stacking Co particles at about 12 nm.^{37,38}

In this experiment, eleven different regions of a TEM grid corresponding to different self-assembled Co NP structures have been analyzed by electron holography. The Figure 4.6 shows the bright field images of all the analyzed zones. The structures consist of MLs of Co particles packed in a hexagonal lattice with different thicknesses, and also two different rounded structures forming a ring and a patch of Co particles. The particles are separated ~ 2 nm wide corresponding to the length of the surfactant. The different contrast of the particles indicates a random crystalline orientation (verified by dark field studies). Also HRTEM has often revealed that the outer ~ 0.5 nm layer of the particles is oxidized Co.

For 2D systems, at vanishing temperatures, calculations have shown that the microstructure of the assembly determines the type of order. Thus, it has been proposed that a 2D hexagonal lattice results in a FM order and a square lattice in AFM order.¹⁰ Especially interesting is the

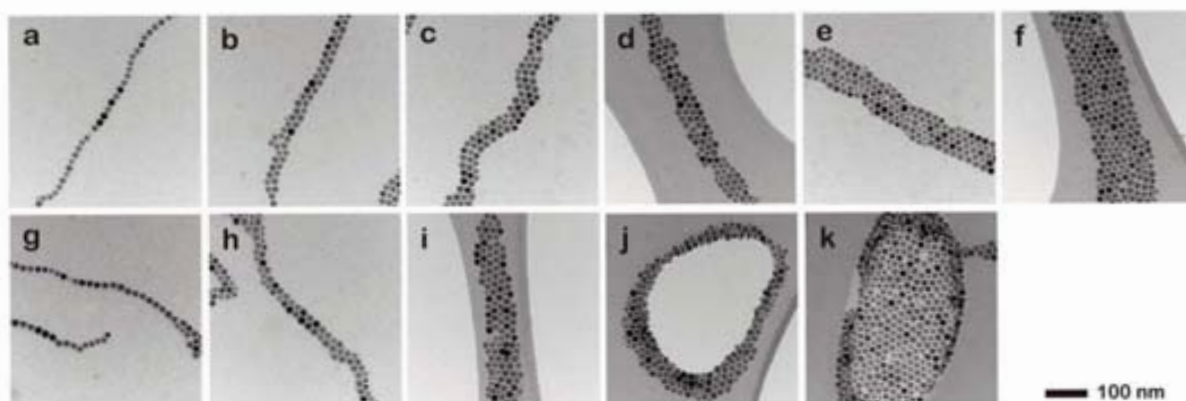


Figure 4.6: a - k) TEM bright field images of the different regions of self-assembled structures studied by electron holography.

case of self-assembled structures since the final magnetic structure is conformed while the NPs are assembling competing to other forces as vdW and capillarity. All these contributions faded as the magnetic moment of the particle dipole in the self-assembled structures increases in stability and intensity taking over the control of the SA process driving the system towards elongated structures satisfying north-to-south dipolar interactions.

Figure 4.7 shows the in-plane magnetic field signal of each structure obtained by off-axis electron holography and after their subsequent image processing. It can be observed long-range magnetic order along the chains, even the hexagonal lattice defects, and that is stable over time, thus corresponding to the magnetic phase of a dipolar ferromagnet. Modifications of the local order has an important impact in the dipole distribution, increasing the degree of FM order as the regularity of the array (which is correlated with the degree of particle monodispersity) resulting on in-plane parallel magnetic dipole organization. Besides, depending on the local symmetry of the array a vortex formation is observed, as shows Figure 4.7 d). Also, a “wiggling” of the magnetization is generally observed in all the NP chain structures (from *a* to *i*), mainly at frontiers.

Other interesting features can be observed, as an onion state in the image *j*) of the Figure 4.7. The structure corresponds to a collection of particles which are self-assembled around a hole of the amorphous carbon film with a symmetric magnetic behavior in both sides of the applied magnetic field direction. On the other hand, the image *k*) of the Figure 4.7, which corresponds to a patch of NPs, present different magnetic domains forming vortex structures. Also different vortex states are observed due to the closed structure and probably favoured by the rounded shape of the patch. Lastly, in Figure 4.7 *g*) and *h*), it can be observed magnetic interaction between neighbouring chains. In the first case (Figure 4.7 *g*), one of the single-particle chains present an inversion of the magnetization, clearly observed by the colour change from red to blue. This phenomenon can be explained if the direction of the applied magnetic field is perpendicular respect to the chain direction. Moreover, the neighbour chain may also have an influence in this reversal of the magnetization, because it can be appreciated an interaction between chains by following the contour lines. In the second case (Figure 4.7 *h*), both double chains have the same in-plane magnetic field direction (same colour), indicating the same direction of the magnetization, and the inter-chain interaction can also be observed by looking the contour lines.

Among all the images, seven regions formed by Co NP chains with increasing width have been selected (Figure 4.8) and the magnetic phase shift has been measured. The phase shift can be estimated by multiplying the number of contour spacing located inside the structure by its value in radians (in our case: 0.082 radians x n° contour lines). More precisely, the phase

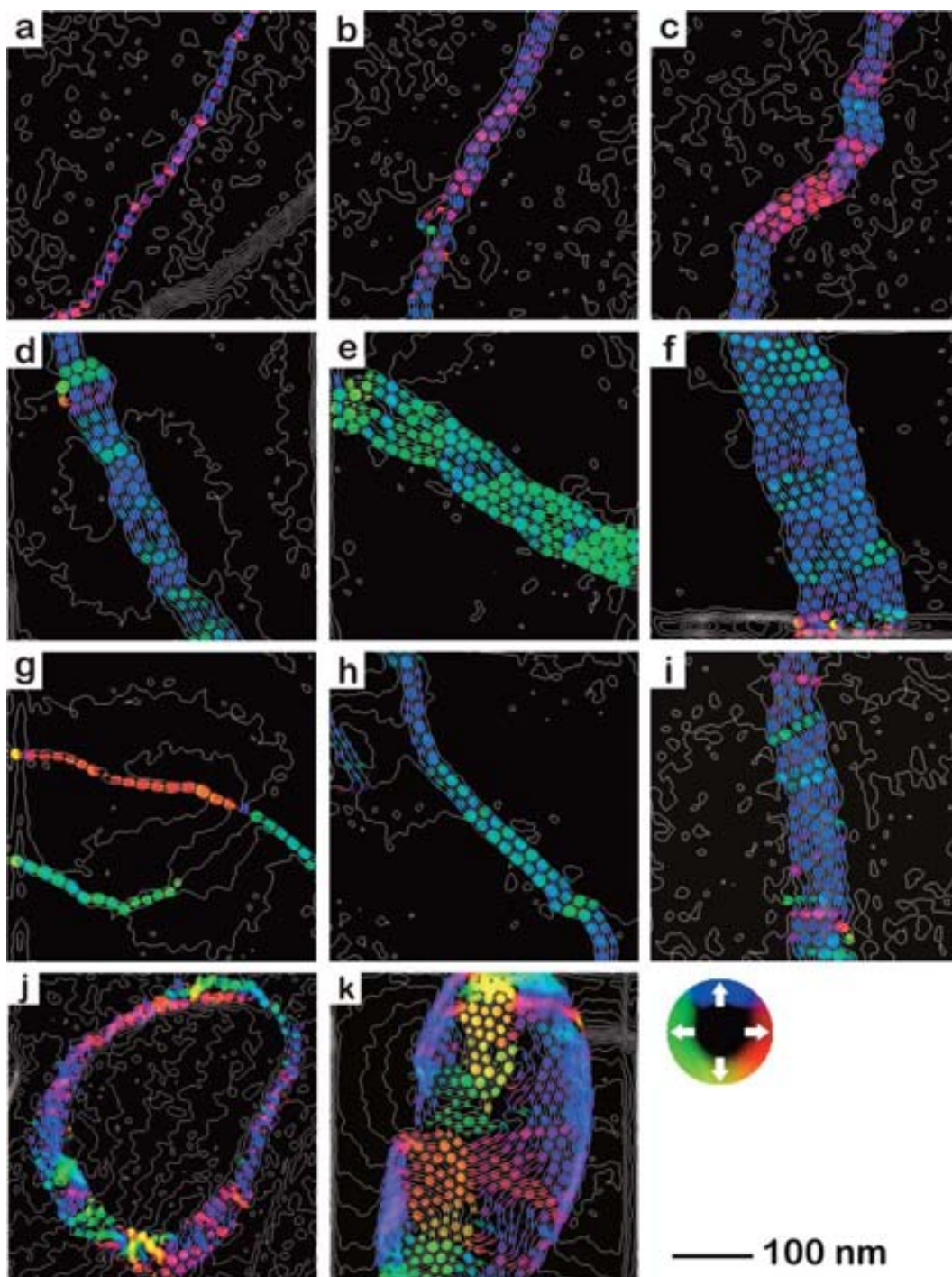


Figure 4.7: a - k) Electron holograms of the magnetic contribution to the phase of the selected areas. 0.082 radian contours generated from the image processing and overlaid onto the colour map of the masked images of each region.

shift can be calculated by making a line profile in the magnetic contribution to the phase image, and measuring the phase “step” (after a previous flattening process of the phase image). It has been found that the phase shift continuously increases from 0.29 radians in the 1-particle chain

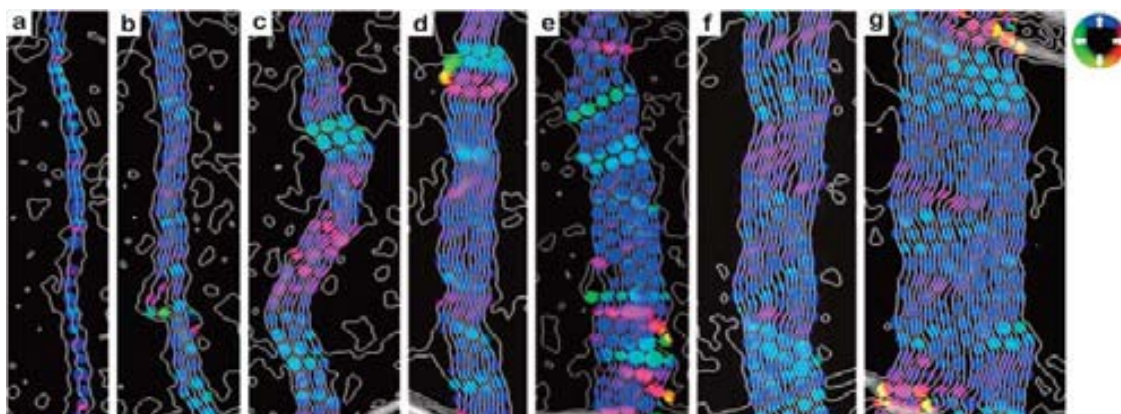


Figure 4.8: a - g) Selected self-assembled structures formed by Co NP chains and with increasing width.








	Region a (1 chain)	Region b (2 chain)	Region c (3 chain)	Region d (3 chain with vortex)	Region e (4 chain)	Region f (5 chain)	Region g (7 chain)
Phase Shift (radians)	0.29	0.64	0.92	1.03	1.36	1.38	2.29
Phase Shift/ number chains	0.29	0.32	0.31	0.34	0.34	0.28	0.33
Magnetic Induction (T)	2.07	1.99	1.91	1.85	1.88	1.86	1.89
Phase Image (Magnetic Contribution)							

Table 4.1: Comparison of the phase shift and magnetic induction values obtained as increasing chain width in the selected self-assembled structures. Also, the images of the magnetic contribution to the phase of each region are showed.

to 2.29 radians in the 7-particle chain, as can be observed in the Table 4.1. Dividing the phase values by the number of chains gives an almost constant value of 0.31 ± 0.02 indicating the robustness of the measurements.

One of the most relevant parameters that can be obtained from the magnetic contribution to the phase is the quantitative measurement of the magnetic induction of the structure.³⁹ Using the experimental magnetic phase shift of each region, the magnetic induction along y (in-plane, B_{\perp}) on the sample has been calculated using the next expression (obtained from Equation 4.13):

$$\Delta\varphi_{MAG} = \left(\frac{e}{h}\right) \cdot B_{\perp} \cdot A \quad \text{Equation 4.16}$$

where $\Delta\varphi_{MAG}$ is the change in the magnetic contribution to the phase across the chain (radians), and A is the area of the chain structure crossed by the in-plane magnetic field. A has been calculated dividing the sum of the volume of all the particles forming the chain by the length of the chain.

The mean magnetic induction determined from the experiments (in which a field of 2 T has been used to magnetize the sample) has been found to be similar to the theoretical bulk value for Co (1.8 T). The mean experimental magnetic induction of all the structures, 1.92 ± 0.08 T, indicates an increase of a 7% with respect to the bulk material. It is important to note that these results are subject to an experimental error in the calculations since the calculation of the area crossed by the magnetic field at this nanometre scale is difficult to achieve. The measurements of surface area are made from the TEM images, and a change of even one nanometer will affect the magnetic induction value. Therefore, complementary studies, such as some simulations, will be needed to confirm the results. It is also worthy to mention that has been previously reported on an enhancement of the magnetization in the case of ultrafine Co particles. This phenomena is associated to the influence of the surface atoms and that is more significant with decreasing size.⁴⁰

Moreover, the direction of the magnetic moment of each individual particle within the structure has been calculated, thus confirming that self-assembled dipolar ferromagnetism forms as a ground state of the structures with a hexagonal lattice. Figure 4.9 (a-f) represents these individual magnetic moment directions by color code and by arrows. Also, in this image is easier

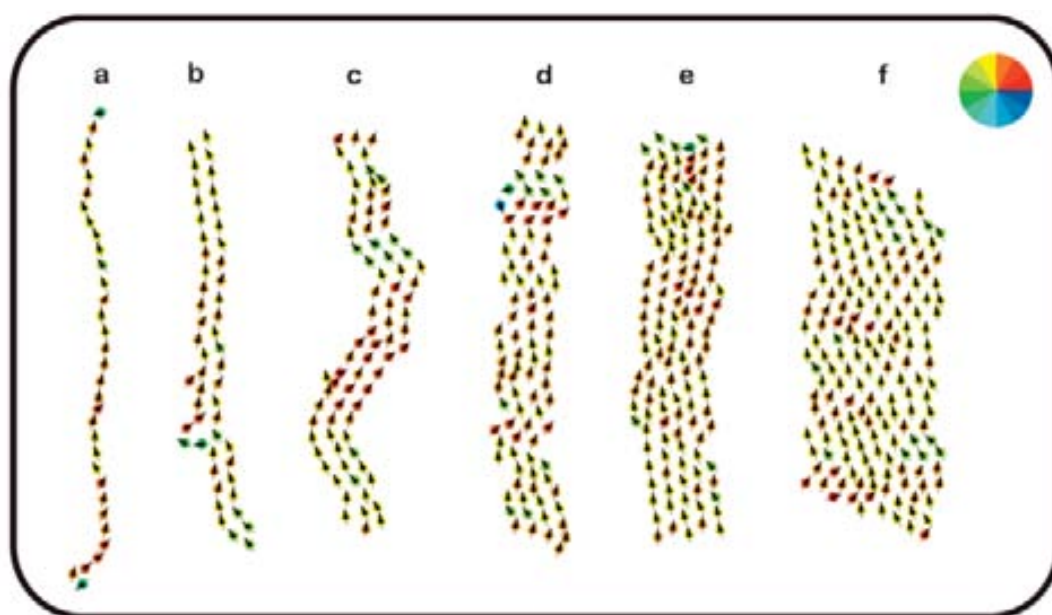


Figure 4.9: a - f) Representation of the direction of the in-plane contribution of the magnetic moment of each individual particle forming the chains by colour and by arrows.

to observe the previously mentioned “wiggling” of the magnetization along the chains. And can be clearly appreciated a relationship between the magnetic order and the geometric order.

Measurements of the central position of the particles (x,y), and the distances between particle centres (r), together with changes in the magnetic moment direction ($\Delta\theta_m$) between all particles, are still in progress in order to correlate the geometric order with the magnetic order with the help of simulations.

4.2.3 Summary

Off-axis electron holography has been used to map with a few nanometers resolution the in-plane magnetic field in self-assembled structures formed by Co NPs of ~ 15 nm. It has been demonstrated that self-assembled dipolar ferromagnetism forms as a ground state of the structures with hexagonal particle lattices, even when they have some geometric disorder.

4.3. Electron Holography of Self-Assembled Co Structures with Increasing Temperature

4.3.1 Experimental

4.3.1.1 Sample Preparation

One drop of diluted solution of ~ 11 nm Co NPs was deposited onto a holey carbon-coated copper TEM grid and left to dry inside a globe box. Also, the grid was mounted in the TEM holder fast to prevent the oxidation of the particles, being in contact with the air atmosphere only for a few seconds. These dispersion conditions produced patches of 2D self-assembled nanostructures as imaged by TEM (Figure 4.10). The magnetic induction of two different self-assembled structures has been studied while increasing temperature.

4.3.1.2 Data Acquisition

Off-axis electron holograms were acquired in Lorentz mode in a Titan Analytical 80-300ST TEM with a Gif CCD camera using biprism voltages of 180 V for the experiment. A heating holder was used for increase the temperature of the sample from RT until 455 °C. The direction of magnetization was reversed *in situ* by tilting the sample ± 25 degrees, and turning on the

conventional microscope objective lens to apply a magnetic field (2 T) to the sample parallel to the direction of the electron beam. Then, the hologram acquisition was carried out in field-free conditions (objective lens off and at 0 degrees). Following this procedure, holograms were recorded with the 2D areas of crystals magnetized in opposite directions and also at different temperatures: 28, 50, 65, 75, 85, 100, 130, 180, 245, 300 and 455 °C.

For all experiments, MIP contribution must be removed to interpret the magnetic contribution (as described in section 4.1.3). The magnetic and MIP to the phase can be calculated by taking half the difference and half the sum of the phases, respectively, of each pair of holograms. The holograms were analyzed using the Semper image-processing package.⁴¹

4.3.2 Results and Discussion

Two different regions of self-assembled 2D Co structures have been analyzed by electron holography as a function of the temperature. The balance between the 2D self-assembled ML and the 2D chain structure, can be easily tuned by the size of the NPs.⁴² Thus, by choosing ~ 11 nm SPM Co NPs it was possible to obtain closed packed structures. And by the dilution of the original sample, it was favoured the formation of isolated “islands” of particles.

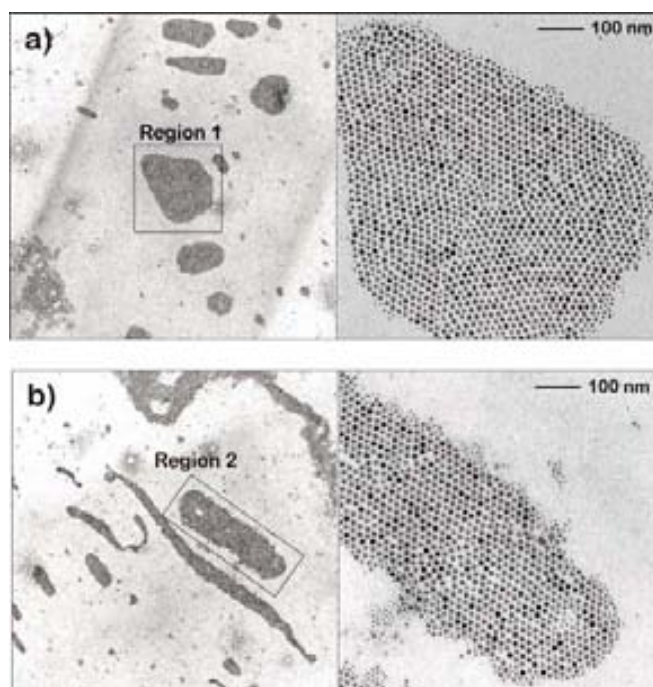


Figure 4.10: TEM bright field images of the two different regions of self-assembled structures studied by electron holography as a function of the temperature: a) Region 1 and b) Region 2.

Figure 4.10 shows bright field TEM images of the two analyzed zones. The self-assembled structures consist of a ML of Co NPs forming: i) a polygonal structure of size around 700 nm (Region 1) and ii) a larger structure of Co NPs with elongated shape (Region 2). The arrays of particles have hexagonal ordering with some packing defects due to the little polydispersity of the sample.

These experiments do not have the nanometer resolution because they have been performed at lower magnification but it has been possible to obtain the magnetic behavior of the whole structure. The holograms were taken at different temperatures (from 25 to 455 °C) recording the evolution of the internal magnetic structure. The acquisition of the pair of holograms with reversed magnetization direction, for the calculation of the MIP (see Experimental for details), was carried out before increasing the temperature (at 25 °C).

4.3.2.1 Region 1

The corresponding magnetic contributions to the phase, acquired at all the temperatures, are shown in Figure 4.11. As can be observed, structures c) and d) correspond to an interval of temperatures, meaning that all the holograms acquired at intermediate temperatures present similar magnetic structure. The white lines in the structure corresponds to magnetic flux lines with a spacing of 0.07 radians between a pair of lines, and the colour is used to show the in-plane magnetization direction. The different colours indicate different domains forming a spiral or vortex structure.

Figures 4.11 a) and b), show the two holograms acquired at RT (25 °C) with reversal magnetization. It can be observed that they are not the same magnetic structure with different sign of magnetization, i.e. identical domain distribution but with different colour. Instead, Figure 4.11 c) which corresponds to the magnetic structure measured after reversal magnetization and at temperatures comprised between 50 and 130 °C, shows the same magnetic structure than Figure 4.11 a) but with opposite sign. Thus, in this particular case, the MIP has to be calculated from images a) and c). It can be determined that the magnetic structure recorded in hologram b) may correspond to an intermediate magnetic state that then evolved to a more stable magnetic structure (c). It is particularly interesting that, in Figures 4.11 a) and c), there is a 180° switch from one line of particles to the next between some different domains. In this simply abrupt switch from one orientation to the other the exchange energy cost would be very high. One way to get around this is to spread the change over a gradual switch, as can be observed with increasing temperature, in where the wider the wall the less the exchange energy. As the sample temperature increased until reach temperatures between 130 and 180 °C, the smaller domain disappeared to form a structure with less, larger and closed domains

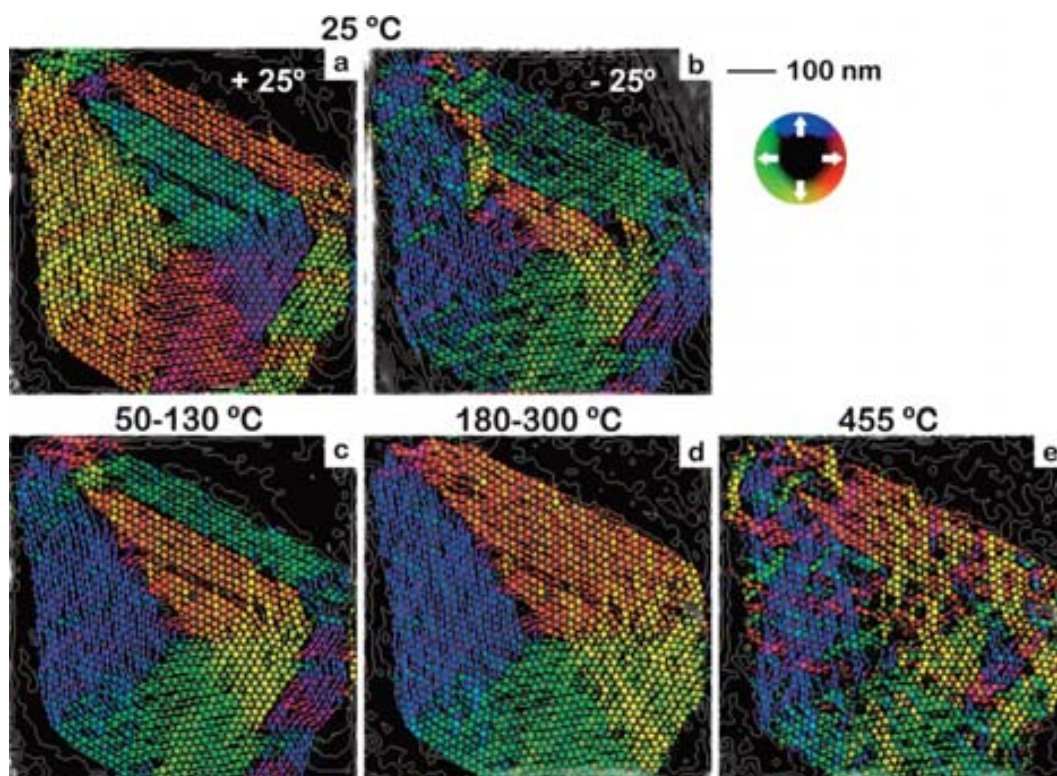


Figure 4.11: a-e) Electron holograms of the magnetic contribution to the phase of the Region 1 and acquired while increasing temperature. 0.07 radian contours generated from the image processing and overlaid onto the colour map of the masked images of each region.

(Figure 4.11 d). And, therefore, a more gradual switch from one direction to the other was obtained. Finally, another change occurs as the temperature increases even more. At 455 °C, it can be observed the increase of the magnetic disorder within the domains. Another clear proof of the weaker in-plane field is the spread in the contour lines. As previously mentioned, the coloured area only represents the in-plane magnetic component. Thus, the colourless areas observed in Figure 4.11 e) do not mean the absence of magnetic field, but also its perpendicular component.

Since the Curie temperature of bulk Co is 1115 °C, this phenomena cannot be assigned to a magnetic phase transition. Observing the ordering of the clusters as a function of the temperature, one can observe how from a quite disordered state at RT the NP spins evolve towards more ordered domains where the NPs are parallel oriented and then, with a further increase of the temperature, the domain structure and the spin correlation are lost. This recalls the ZFC process in a collection of SPM NPs. In this case, when a random collection of single domain SPM NPs is frozen in the absence of magnetic fields, the net magnetization of the

sample is zero. Then a small magnetic field (able to orient but not to reverse the spins, so they can easily compete thermally with the applied field) is applied and, as temperature increases, frozen moments are able to progressively move towards the direction of the applied field up to a maximum, from where thermal agitation disorders the spins and the magnetization, and the degree of order decreases again. In both systems, despite that the physical principles involved are different (dipolar interactions in the NP assembly and thermal vs anisotropy energy in the NP collection), one can observe how raising temperature on evolves from a disordered state to another disordered state though a more ordered one.

Although it is clear that the SPM state it is not reached, this abrupt change on the magnetic structure suggest the start of a more disordered phase. We tentatively assign this change to a magnetic transition to a superferromagnetic state, i.e. spin-glass behavior, with short-range magnetic order. Besides order, spin-glass like behavior, with the corresponding low susceptibility and memory effects, has also been demonstrated for these types of 2D systems of magnetic NPs.^{6,43,44} The term spin-glass implies that the spin orientation has similarity to this type of location of atoms in glasses: spins are randomly frozen in glasses. We consider that depending on the size of the self-assembled area the temperature transition to a disordered state will be different. Thus, in smaller areas the change will occur at lower temperatures, similarly like the T_B varies in ZFC-FC processes. As an example, Figure 4.12 shows the ZFC-FC of different size Co NPs, where it can be observed how the T_B decreases with particle size.

Moreover, it is known that ϵ -Co phase is stable at RT for several months, but phase transition of ϵ -Co to the hcp or fcc structures can be easily done by annealing at the proper temperature. Heating the sample at 300 °C quantitatively converts ϵ -Co to hcp-Co, while heating to 500 °C completely transforms it to the fcc structure. In addition, subsequent cooling of the heated samples does not revert them back to the original ϵ -Co structure.⁴⁵ The magnetic moment per

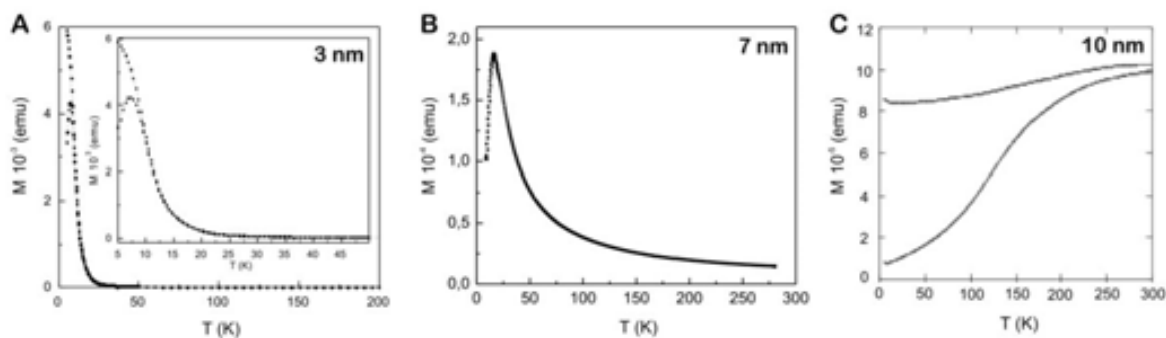


Figure 4.12: ZFC-FC magnetization curves of different size Co NP: A) 3 nm ($T_B \approx 8$ K), B) 7 nm ($T_B \approx 30$ K) and C) 10 nm ($T_B \approx RT$).

Crystal Structure	Magnetic Moment per Atom (μ_B)	Magnetocrystalline Anisotropy (10^6 erg/cm ³)
hcp	1.72	4.2
fcc	1.75	2.7
ϵ	1.70	1.5

μ_B = Bohr Magneton = 0.927×10^{-21} erg/Oe

Table 4.2: Magnetic moment per atom and magnetocrystalline anisotropy for hcp-Co, fcc-Co, and ϵ -Co.^{46,47}

atom and magnetocrystalline anisotropy of ϵ -Co are compared to the values for bulk hcp-Co and fcc-Co in the table of Table 4.2.

Figure 4.13 shows the phase shift plot of the selected area as function of the distance, and for all temperatures. By this plot, it can be observed that the phase shift at 455 °C is slightly smaller than the phase at 180-300 °C, corroborating the decrease of the in-plane magnetization.

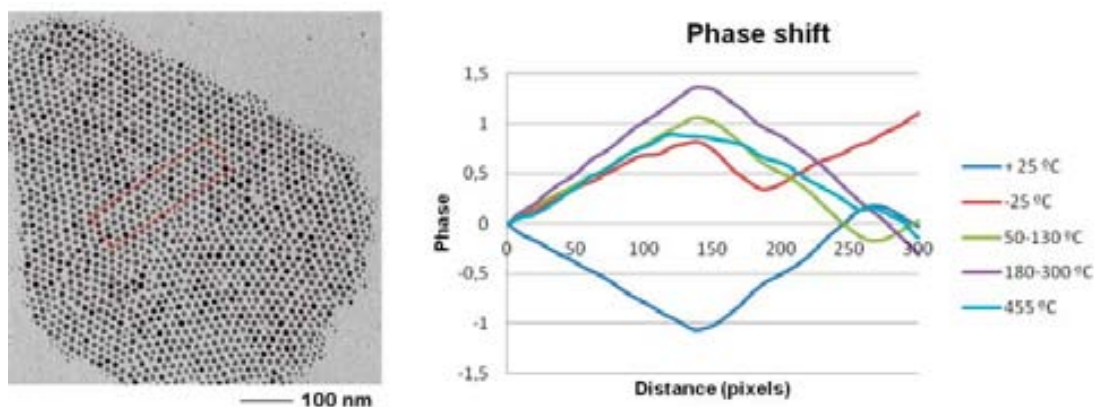


Figure 4.13: Bright field TEM image of the Region 1 and phase profiles plotted as a function of the distance, obtained for the selected area showed by a red square and measured at different temperatures.

Since the used experimental conditions do not allow perform the experiment at higher temperatures, the same experiment but of a smaller area will be needed to further explore this phenomenon. Recently, similar changes in the magnetic structure of Co single crystal areas, up to 500 °C, have been observed by a different technique (spin-polarized scanning electron microscopy). Significant changes occurred in the magnetic domain structure between 200 and 300 °C, reducing the number of domains. And then, sub-micron-order magnetic domains were formed within the larger magnetic domain previously formed between 400 and 500 °C.⁴⁸

4.3.2.2 Region 2

Similarly to the previous region, the corresponding magnetic contributions to the phase, acquired at different temperatures are shown in Figure 4.14. Images c) and d) correspond to an interval of temperatures and different holograms that present identical magnetic structure, as in the previous region. The white lines in the structure correspond to magnetic flux lines with a spacing of 0.06 radians between a pair of lines, and the colour is used to show the in-plane magnetization direction. In this experiment, only a part of the structure is recorded and we cannot observe the magnetic structure of the whole region. Images a) and b), show the two holograms with reversal magnetization acquired at RT (25 °C). They present the same magnetic structure with different sign of magnetization, i.e. identical domain distribution but with different colour. Thus, this pair can be used to determine the MIP. The formation of a small 2-chain domain with opposite direction of the magnetization in the middle of the structure can be observed at temperatures between 50 and 130 °C (Figure 4.14 c).

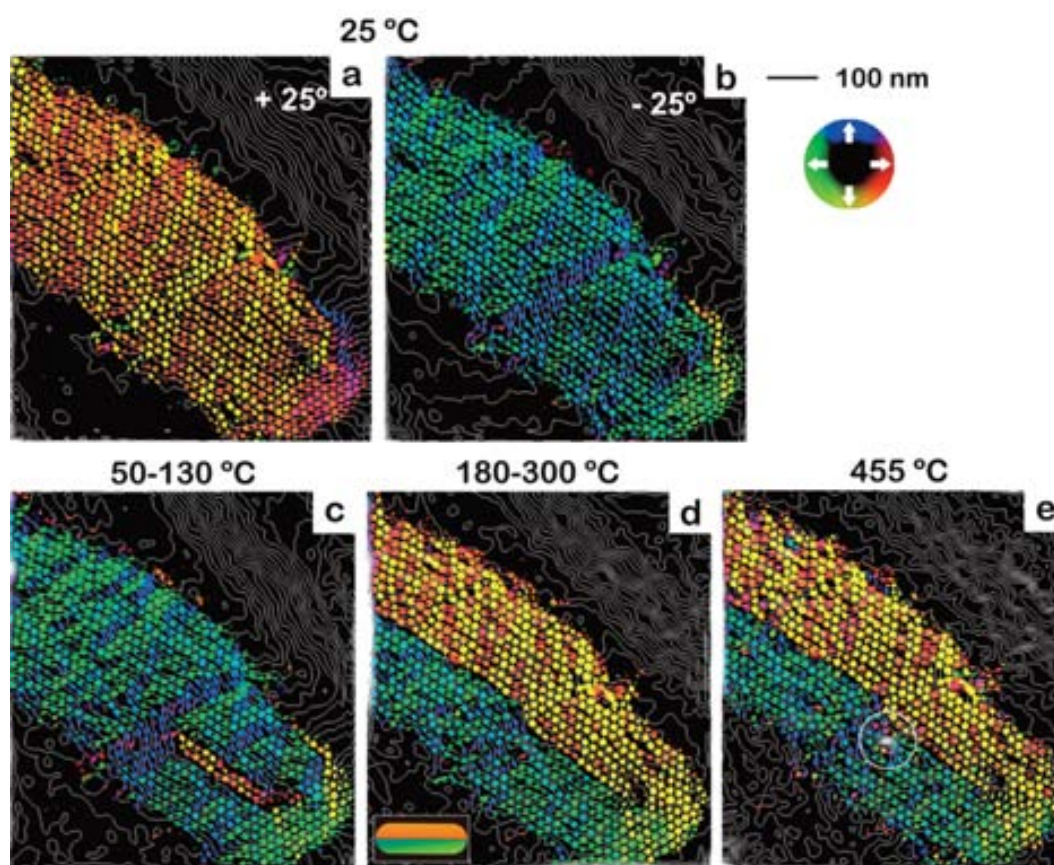


Figure 4.15: a - e) Electron holograms of the magnetic contribution to the phase of the Region 2 and acquired while increasing temperature. 0.06 radian contours generated from the image processing and overlaid onto the colour map of the masked images of each region.

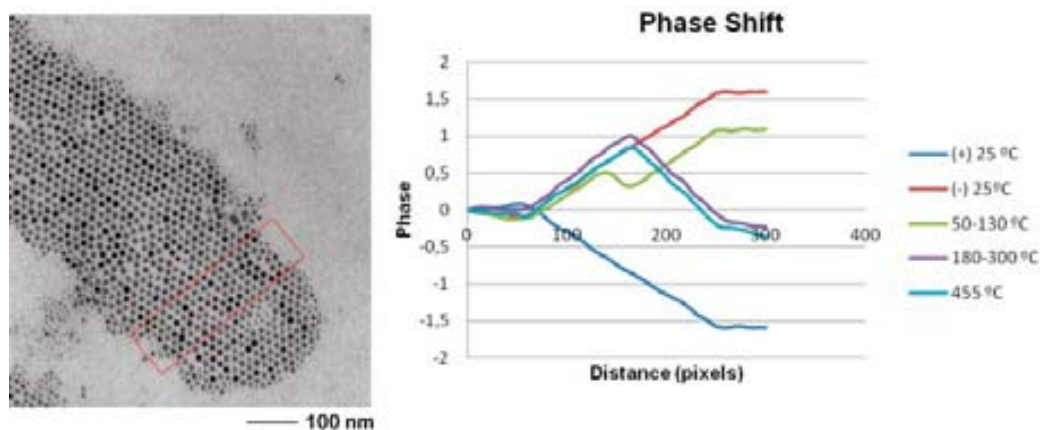


Figure 4.15: Bright field TEM image of the Region 2 and phase profiles plotted as a function of the distance, obtained for the selected area showed by a red square and measured at different temperatures.

As the temperature continues increasing, the magnetic structure evolves towards a 2-domain-vortex structure (Figure 4.14 d). The magnetostatic energy can be approximately halved if the magnetization splits into two domains magnetized in opposite directions. This subdivision into more and more domains cannot continue indefinitely because the domain wall requires energy to be produced and maintained. Also, an equilibrium number of domains will be reached for a given structure. Similarly than in Region 1, at temperatures between 180 and 300 °C, the most favourable state in the structure is the vortex, and the number of domains depends on the structure shape anisotropy. On the other hand, unlike Region 1, significant changes in the magnetization cannot be observed when the temperature increases up to 455 °C. The only evidence of change is an increase of the wiggling in the contour lines and a small vortex formation in the middle part of the structure, visually appreciated by the increasing of the contour lines density (inside the white circle in Figure 4.14 d).

The phase shift plot of the selected area as function of the distance, and of all temperatures, is showed in Figure 4.15. In this region it can be observed that there are not significantly difference between the phase at 180-300 °C and at 455 °C, being slightly smaller.

We can conclude that the Region 2 has a more stable magnetic structure, probably due to the shape anisotropy of the whole structure; and, in consequence, higher temperature will be needed to observe the decrease of the in-plane magnetization. Region 2 is a more robust system, and indicates how geometry determines the magnetic behavior.

4.3.3 Summary

In this section, the magnetic domain changes under high temperature conditions have been observed by off-axis electron holography. During the heating process of Co NPs self-assembled structures, previously magnetic induced, drastic changes were observed in the magnetic domains between RT and 300 °C,. And at 455 °C some decreasing of the magnetism is also observed. These changes in the magnetic structure occur with temperature-related changes in Co phase, which may have an effect in the process.

4.4 Lorentz Microscopy and Electron Holography of Wire-Like Co Self-Assembled Structures

4.4.1 Experimental

4.4.1.1 Sample Preparation

One drop of the initial solution of 13 nm Co NPs was drop casted onto a TEM carbon-coated substrate. The preparation was carried out inside the globe box for avoiding oxidation. This dispersion produced wire-like Co NP self-assembled structures, which have been characterized by TEM and SEM in section 3.2.2.3 (Figure 3.15). Both Lorentz microscopy and electron holography images were acquired in Lorentz mode in a Titan Analytical 80-300ST TEM working at 120 kV. The acquisition process is detailed as follows.

4.4.1.2 Data Acquisition Lorentz Microscopy

The selected region was magnetized in one direction by applying a magnetic field higher than 5000 Oe using the objective lens. Then, the objective lens was also used for change the magnetization to the opposite direction. Starting from zero field conditions, the value of the objective lens was varied until reach a field value of 400 Oe, where the complete reversal of the magnetization could be observed. Different images were acquired out of focus at field intervals of ~ 20 Oe.

4.4.1.3 Data Acquisition Electron Holograph

The direction of magnetization of the sample was reversed in situ by tilting the sample by ± 30 degrees, and then turning on the conventional microscope objective lens to apply a magnetic field (>2 T) to the sample parallel to the direction of the electron beam. Then, the hologram

acquisition was carried out with a CCD camera, in field-free conditions and at 0 degrees. Following this procedure, holograms were recorded in different wire-like Co NPs structures magnetized in opposite directions. In these experiments the MIP contribution could not be removed because the complexity of the magnetic structures (the samples magnetized in opposite directions presented different magnetic structures). Nevertheless, both magnetic signals were high enough for be observed without the MIP removal.

4.4.2 Results and Discussion

Lorentz and electron holography experiments have been performed in the sample showed in Figure 4.16. In the bright field image, it can be distinguished MLs and multilayers of Co NPs, indicated by arrows. The Lorentz experiment has been performed in the whole span of the image, while electron holography experiments have been done in five smaller regions of the sample formed by both monolayer and multilayer.

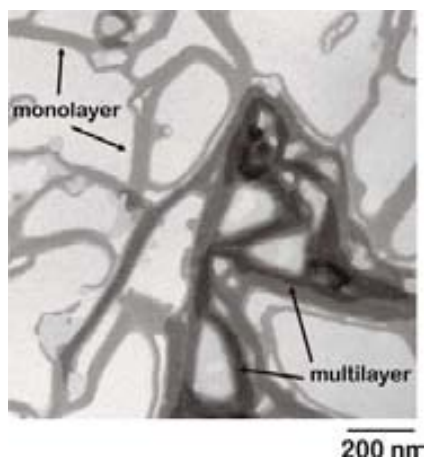


Figure 4.16: Low magnification image of the sample used for the Lorentz microscopy and electron holography experiments. MLs and multilayer regions are indicated by arrows.

4.4.2.1 Electron Holography

Bright field images of the five selected regions are observed in Figure 4.17 (a-e). Four of the regions correspond to structures formed by a ML of Co NPs (from a to d) and one of the regions corresponds to a multilayer structure of Co NPs (e). The acquired holograms were processed following a standard methodology: first, executing a Fourier transform, and then applying an inverse Fourier transform to one of the sidebands. From the resulting total phase images, the

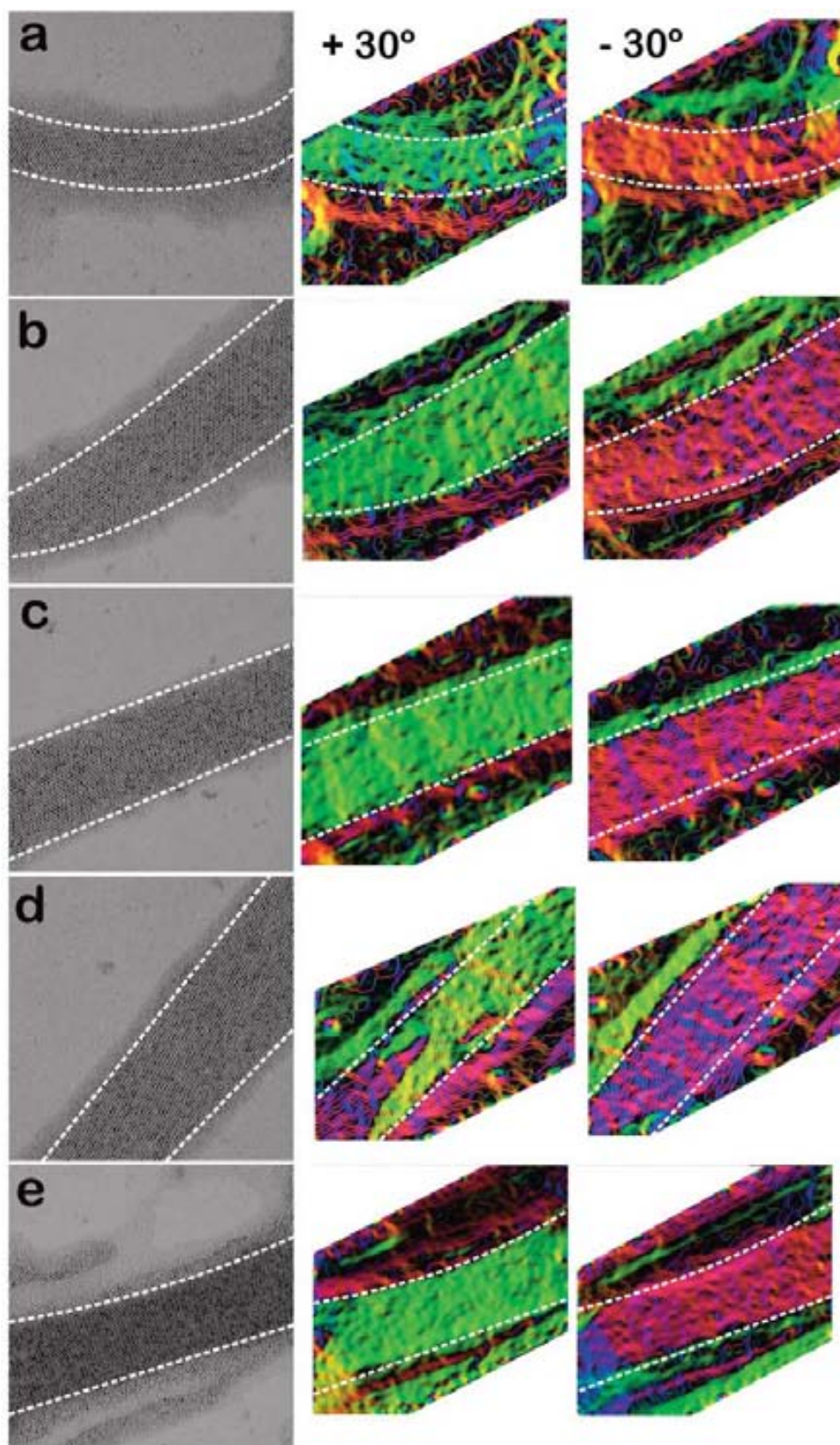


Figure 4.17: a-e) TEM bright field images of the five wire-like Co NPs structures studied by electron holography. They are formed by a ML (a-d) and multilayer (e) of self-assembled Co NPs.

signal was represented by contour lines and color map and then superimposed. Figure 4.17 shows the superimposition of both representations (lines + color) observed in the acquired holograms (magnetized at ± 30 degrees) for each region. It is generally observed in all the regions that opposite magnetic structures are obtained after the reversal of the magnetization, even in the simplest case of the MLs (a-d). These domains present more or less complexity depending on the region and are parallel oriented along the chains. In the case of the Region d (Figure 4.17 d), is more evident the two different magnetic contributions. This behavior can be explained by the complexity of the whole Co NP structure. It has to be in account that the magnetic structure of the selected regions can be affected by the magnetic behavior of the whole structure, which continues longer in both sides.

With the aim of better understand the magnetic behavior of these structures, Lorentz microscopy was carried out and the results are shown below.

4.4.2.2 Lorentz Microscopy

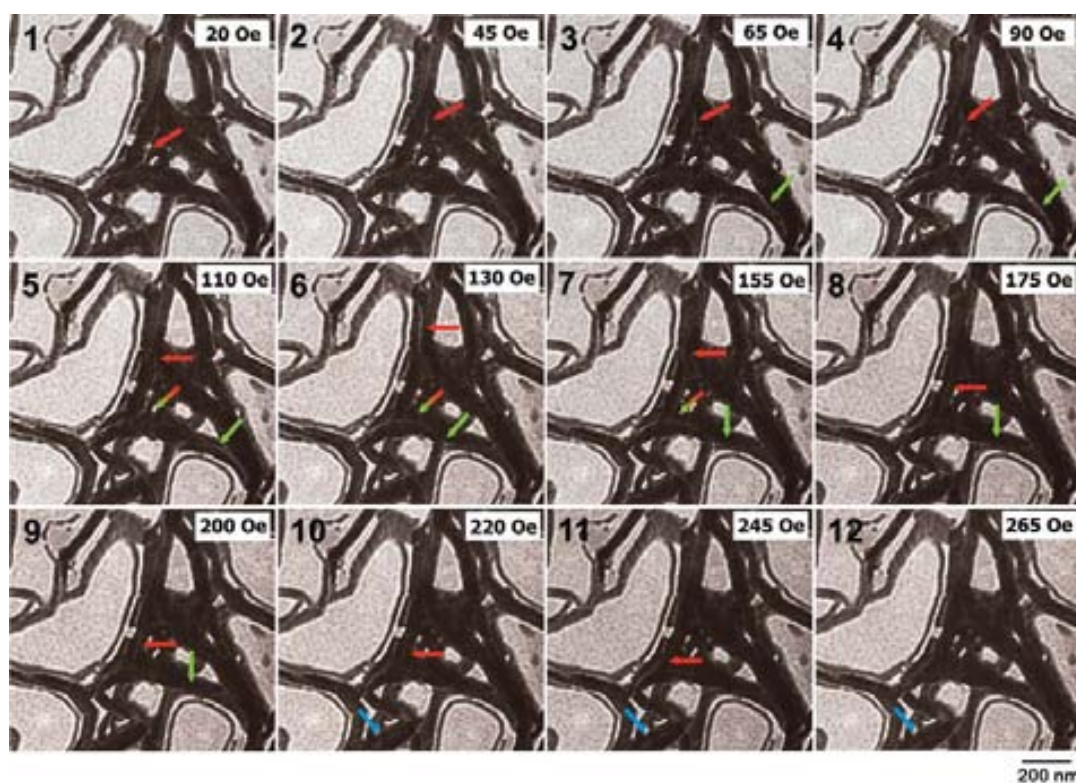


Figure 4.18: Lorentz microscopy experiment. From image 1 to image 12 it can be observed the reversal of the magnetization, producing the movement of the domain walls along the structure. The movement can be observed looking at the colored arrows. Each color indicates the movement of one domain wall. The arrows composed of two colors correspond to the coalescence of two domain walls.

Defocused Fresnel images acquired during the reversal of the magnetization are shown in Figure 4.18. The bright lines (marked with arrows) correspond to domain wall boundaries of the magnetic structure. It can be followed the movement of the domain walls along the wires when the direction of the applied magnetic field is reversed *in situ*, by changing the value of the objective lens (each image correspond to a change of the magnetic field around 20 Oe). Following one colored arrow it can be observed the movement of one particular magnetic wall, while the arrows composed of two colors correspond to the coalescence of two different domain walls. It is also confirmed by Lorentz microscopy that the dipole magnetization and domain walls are preferentially oriented along the length of the wires as observed in Figure 3.16. These observations, together with the electron holography measurements, indicate that the magnetic behavior of the NPs on the wire-like structures is FM (dipolar ferromagnetism).

4.4.3 Summary

The magnetic behavior of wire-like self-assembled Co NPs structures has been analyzed either by electron holography and Lorentz microscopy. The complexity of the magnetic structure made impossible to obtain exclusively the magnetic signal of the sample, but the signal was high enough for be observed without the removal of the MIP. It has been possible to obtain an idea of the magnetic behavior, confirmed afterwards by Lorentz microscopy, demonstrating the existence of dipolar FM domains in the Co NPs structures. The existence of domain walls is a signature of superferromagnetism.

4.5 Conclusions

The off-axis mode of electron holography is ideally suited to characterize the magnetic behavior of Co NPs assemblies because unwanted contributions to the contrast from local variations in composition and specimen thickness can usually be removed from a phase image more easily than from images recorded using other TEM phase contrast techniques. For example, the Fresnel and Foucault modes of Lorentz microscopy and differential phase contrast (DPC) imaging provide signals that are approximately proportional to either the first or the second differential of the phase shift. These techniques inherently enhance contributions to the contrast from rapid variations in specimen thickness and composition, as compared with the weak and slowly varying magnetic signal. Nevertheless, the main disadvantage of the electron

holography is that dynamic events cannot be followed in real time because the holograms are usually processed off-line. Moreover the field of view is limited to about 5 μm .

Summarizing, our results demonstrate the existence of dipolar ferromagnetism in different 2D self-assembled Co NPs structures. Dipolar interactions have been studied in a set of chain-like Co NP structures with different widths, founding that the magnetization is distributed along the chain. It has been also observed a direct relationship between the structure order and the magnetic order. Complementary studies based in computer simulations are in progress for determine the mentioned relationship. Moreover, changes in the magnetic structure in 2D self-assembled “closed” structures have been studied as a function of the temperature. It is observed that, in the dipole-interacting structures, the domain size and shapes varies over time from RT until 300 °C. Furthermore, at 455 °C it can be observed a decreasing of the magnetic order, more evident in Region 1 than in Region 2. This phenomenon is tentatively assigned to a first observation of a magnetic phase transition to a short-order magnetic structure (spin-glass structure) due to the thermal agitation of the NP dipoles within the structure. Further experiments will be needed to confirm this hypothesis. Finally, dipolar ferromagnetism has been demonstrated by Lorentz microscopy, observing domain wall movement as reversal of the magnetization in wire-like structures formed by Co NPs.

Electron holography and Lorentz microscopy can play a valuable and complementary role in characterizing the magnetic structure of nanostructured magnetic materials. And the combination of both techniques allows conducting in situ studies as a function of temperature and/or the strength of any external applied magnetic field.

4.6 References

1. Cowburn, R. P.; Welland, M. E. "Room Temperature Magnetic Quantum Cellular Automata". *Science* **2000**, 287, 1466-1468.
2. Zeng, H.; Li, J.; Liu, J. P.; Wang, Z. L.; Sun, S. "Exchange-Coupled Nanocomposite Magnets by Nanoparticle Self-Assembly". *Nature* **2002**, 420, 395-398.
3. Jones, N. "The Pull of Stronger Magnets". *Nature* **2011**, 472, 22-23.
4. Altmann, S. L. *Band Theory of Solids: An Introduction from the Point of View of Symmetry*; Oxford University Press, **1994**.

- 5.** L. Pye, D.; La Course, W. C.; Stevens, H. J. *The Physics of Non-Crystalline Solids*; Taylor & Francis Ltd **1992**.
- 6.** Majetich, S. A.; Sachan, M. "Magnetostatic Interactions in Magnetic Nanoparticle Assemblies: Energy, Time and Length Scales". *Journal of Physics D-Applied Physics* **2006**, 39, R407-R422.
- 7.** Scheinfein, M. R.; Schmidt, K. E.; Heim, K. R.; Hembree, G. G. "Magnetic Order in Two-Dimensional Arrays of Nanometer-Sized Superparamagnets". *Physical Review Letters* **1996**, 76, 1541-1544.
- 8.** Tomita, S.; Akamatsu, K.; Shinkai, H.; Ikeda, S.; Nawafune, H.; Mitsumata, C.; Kashiwagi, T.; Hagiwara, M. "Tuning Magnetic Interactions in Ferromagnetic-Metal Nanoparticle Systems". *Physical Review B* **2005**, 71.
- 9.** Mørup, S.; Christiansen, G. "Influence of Magnetic Anisotropy on the Superferromagnetic Ordering in Nanocomposites". *Journal of Applied Physics* **1993**, 73, 6955-6957.
- 10.** Russier, V. "Calculated Magnetic Properties of Two-Dimensional Arrays of Nanoparticles at Vanishing Temperature". *Journal of Applied Physics* **2001**, 89, 1287-1294.
- 11.** Puentes, V. F.; Gorostiza, P.; Aruguete, D. M.; Bastus, N. G.; Alivisatos, A. P. "Collective Behaviour in Two-Dimensional Cobalt Nanoparticle Assemblies Observed by Magnetic Force Microscopy". *Nature Materials* **2004**, 3, 263-268.
- 12.** Mørup, S.; Bo Madsen, M.; Franck, J.; Villadsen, J.; Koch, C. J. W. "A New Interpretation of Mössbauer Spectra of Microcrystalline Goethite: "Super-Ferromagnetism" or "Super-Spin-Glass" Behaviour". *Journal of Magnetism and Magnetic Materials* **1983**, 40, 163-174.
- 13.** Georgescu, M.; Klokkenburg, M.; Erne, B. H.; Liljeroth, P.; Vanmaekelbergh, D.; van Emmichoven, P. A. Z. "Flux Closure in Two-Dimensional Magnetite Nanoparticle Assemblies". *Physical Review B* **2006**, 73.
- 14.** Kubetzka, A.; Pietzsch, O.; Bode, M.; Wiesendanger, R. "Magnetism of Nanoscale Fe Islands Studied by Spin-Polarized Scanning Tunneling Spectroscopy". *Physical Review B* **2001**, 63.
- 15.** Schlickum, U.; Wulfhekel, W.; Kirschner, J. "Spin-Polarized Scanning Tunneling

- Microscope for Imaging the in-Plane Magnetization". *Applied Physics Letters* **2003**, 83, 2016-2018.
- 16.** Georgescu, M.; Viota, J. L.; Klokkenburg, M.; Erne, B. H.; Vanmaekelbergh, D.; van Emmichoven, P. A. Z. "Short-Range Magnetic Order in Two-Dimensional Cobalt-Ferrite Nanoparticle Assemblies". *Physical Review B* **2008**, 77.
- 17.** Koch, S. A.; Velde, R. H. T.; Palasantzas, G.; De Hosson, J. T. M. "Magnetic Versus Structural Properties of Co Nanocluster Thin Films: A Magnetic Force Microscopy Study". *Applied Physics Letters* **2004**, 84, 556-558.
- 18.** Dunin-Borkowski, R. E.; McCartney, M. R.; Smith, D. J. Electron Holography of Nanostructured Materials. In *Encyclopaedia of Nanoscience and Nanotechnology*; Nalwa, H. S., Ed., **2004**; Vol. 3; pp 41-100.
- 19.** Aharonov, Y.; Bohm, D. "Significance of Electromagnetic Potentials in the Quantum Theory". *Physical Review* **1959**, 115, 485-491.
- 20.** Thomas, J. M.; Simpson, E. T.; Kasama, T.; Dunin-Borkowski, R. E. "Electron Holography for the Study of Magnetic Nanomaterials". *Accounts of Chemical Research* **2008**, 41, 665-674.
- 21.** Gao, Y.; Shindo, D.; Bao, Y.; Krishnan, K. "Electron Holography of Core-Shell Co/CoO Spherical Nanocrystals". *Applied Physics Letters* **2007**, 90.
- 22.** Snoeck, E.; Dunin-Borkowski, R. E.; Dumestre, F.; Renaud, P.; Amiens, C.; Chaudret, B.; Zurcher, P. "Quantitative Magnetization Measurements on Nanometer Ferromagnetic Cobalt Wires Using Electron Holography". *Applied Physics Letters* **2003**, 82, 88-90.
- 23.** Dunin-Borkowski, R. E.; McCartney, M. R.; Smith, D. J.; Parkin, S. S. P. "Towards Quantitative Electron Holography of Magnetic Thin Films Using in Situ Magnetization Reversal". *Ultramicroscopy* **1998**, 74, 61-73.
- 24.** Twitchett, A. C.; Dunin-Borkowski, R. E.; Midgley, P. A. "Quantitative Electron Holography of Biased Semiconductor Devices". *Physical Review Letters* **2002**, 88, 238302.
- 25.** Yamamoto, K.; Majetich, S. A.; McCartney, M. R.; Sachan, M.; Yamamuro, S.; Hirayama, T. "Direct Visualization of Dipolar Ferromagnetic Domain Structures in Co Nanoparticle Monolayers by Electron Holography". *Applied Physics Letters* **2008**, 93.

- 26.** Yamamoto, K.; Hogg, C. R.; Yamamuro, S.; Hirayama, T.; Majetich, S. A. "Dipolar Ferromagnetic Phase Transition in Fe₃O₄ Nanoparticle Arrays Observed by Lorentz Microscopy and Electron Holography". *Applied Physics Letters* **2011**, 98.
- 27.** Ghazali, A.; Levy, J. C. "Two-Dimensional Arrangements of Magnetic Nanoparticles". *Physical Review B* **2003**, 67.
- 28.** Bennett, A. J.; Xu, J. M. "Simulating Collective Magnetic Dynamics in Nanodisk Arrays". *Applied Physics Letters* **2003**, 82, 2503-2505.
- 29.** Kotzler, J.; Gorlitz, D.; Kurfiss, M.; von Sawilski, L.; Vedmedenko, E. Y. "Vortex Fluctuations and Freezing of Dipolar-Coupled Granular Moments in Thin Ferromagnetic Films". *Physical Review B* **2006**, 73.
- 30.** Chapman, J. N. "The Investigation of Magnetic Domain-Structures in Thin Foils by Electron-Microscopy". *Journal of Physics D-Applied Physics* **1984**, 17, 623.
- 31.** Gabor, D. "Microscopy by Reconstructed Wave-Fronts". *Proceedings of the Royal Society of London. Series A. Mathematical and Physical Sciences* **1949**, 197, 454-487.
- 32.** Gabor, D. "Microscopy by Reconstructed Wave Fronts: II". *Proceedings of the Physical Society. Section B* **1951**, 64, 449.
- 33.** de Ruijter, W. J.; Weiss, J. K. "Detection Limits in Quantitative Off-Axis Electron Holography". *Ultramicroscopy* **1993**, 50, 269-283.
- 34.** Tonomura Akira, M. T., Endo Junji. "High Resolution Electron Holography with Field Emission Electron Microscope". *Japanese Journal of Applied Physics* **1979**, 18, 9-14.
- 35.** Hannes, L. "Electron Holography: Optimum Position of the Biprism in the Electron Microscope". *Ultramicroscopy* **1996**, 64, 79-86.
- 36.** Reimer, L. *Transmission Electron Microscopy*; Springer-Verlag: Berlin, **1989**.
- 37.** Varon, M.; Pena, L.; Balcells, L.; Skumryev, V.; Martinez, B.; Puentes, V. "Dipolar Driven Spontaneous Self Assembly of Superparamagnetic Co Nanoparticles into Micrometric Rice-Grain Like Structures". *Langmuir* **2010**, 26, 109-116.
- 38.** Puentes, V. F.; Krishnan, K. M.; Alivisatos, P. "Synthesis, Self-Assembly, and Magnetic Behavior of a Two-Dimensional Superlattice of Single-Crystal Epsilon-Co Nanoparticles". *Applied Physics Letters* **2001**, 78, 2187-2189.

- 39.** Beleggia, M.; Kasama, T.; Dunin-Borkowski, R. E. "The Quantitative Measurement of Magnetic Moments from Phase Images of Nanoparticles and Nanostructures I. Fundamentals". *Ultramicroscopy* **2010**, 110, 425-432.
- 40.** Respaud, M.; Broto, J. M.; Rakoto, H.; Fert, A. R.; Thomas, L.; Barbara, B.; Verelst, M.; Snoeck, E.; Lecante, P.; Mosset, A.; Osuna, J.; Ely, T. O.; Amiens, C.; Chaudret, B. "Surface Effects on the Magnetic Properties of Ultrafine Cobalt Particles". *Physical Review B* **1998**, 57, 2925-2935.
- 41.** <http://www.microscopy.cen.dtu.dk/computing/semper/index.html>.
- 42.** Poddar, P.; Telem-Shafir, T.; Fried, T.; Markovich, G. "Dipolar Interactions in Two- and Three-Dimensional Magnetic Nanoparticle Arrays". *Physical Review B* **2002**, 66, 060403.
- 43.** Farrell, D.; Cheng, Y.; McCallum, R. W.; Sachan, M.; Majetich, S. A. "Magnetic Interactions of Iron Nanoparticles in Arrays and Dilute Dispersions". *The Journal of Physical Chemistry B* **2005**, 109, 13409-13419.
- 44.** Petit, C.; Wang, Z. L.; Pileni, M. P. "Ferromagnetic Cobalt Nanocrystals Achieved by Soft Annealing Approach—from Individual Behavior to Mesoscopic Organized Properties". *Journal of Magnetism and Magnetic Materials* **2007**, 312, 390-399.
- 45.** Shukla, N.; Svedberg, E. B.; Ell, J.; Roy, A. J. "Surfactant Effects on the Shapes of Cobalt Nanoparticles". *Materials Letters* **2006**, 60, 1950-1955.
- 46.** Cullity, B. D.; Graham, C. D. *Introduction to Magnetic Materials* Wiley-IEEE Press, **1972**.
- 47.** <http://www.hitachi.com/New/cnews/100921c.pdf>.

Chapter 5

General Conclusions

The two main objectives of this thesis have been the development of synthetic processes of metallic and bimetallic NPs and the study of their SA processes.

Concerning the first objective, syntheses of different types of metal NPs, with controlled size and shape, have been developed. The synthesis of different metallic and bimetallic NPs composed by Co and some of its oxides, Au, Pt and some alloys has been achieved.

- Co NPs of different sizes have been synthesized, and different parameters affecting the variation of their magnetic properties such as the particle size and the oxidation state have been studied. It has been observed how Co NPs self-assemble into hexagonal lattice or linear structures depending on their magnetization.

- The syntheses of Pt NPs with different size and shape have also been successfully achieved by controlling different parameters during the synthetic process such as the temperature, the used surfactants, the addition of metal “traces” and the reaction time. In particular, it has been determined how the incorporation of a small amount of Co NPs in the synthesis has an effect as shape directing agent.

- The synthesis of single crystal Au rods (bars) has been developed by using a one-step seed-mediated method, under smooth conditions, and by using Pt seed NPs as a reaction catalyst. The effect of different parameters such as the role of Pt in the process and its

influence in the rods' length has been also explored, concluding that Pt is involved in the rod formation in the form of metallic NP and not as an ion. Moreover, working at RT favors a slow growth that at the same time favors the extremely length of the rods.

- Finally, the formation process of Au/Pt heterodimers has been developed at RT, and the different factors that affect the final heterostructure (concentrations, reaction time and amount of Pt NCs) have been studied. It has been concluded that the presence of Pt particles accelerates again the synthetic process, acting both as nucleation platforms and initial catalytic reducer.

Concerning the second objective, it has been studied the different interactions that drive the SA of NPs into different structures. In particular, the SA process of magnetic Co NPs onto different substrates has been studied.

- A close correlation between the shape and composition of the NPs and type of SA has been determined, which cannot be changed but manipulated by changing external parameters.

- Self-assembled NP structures have been prepared on different types of surfaces (carbon, graphite, silicon wafers) by controlled evaporation. Different parameters such as the solvent nature, the temperature, the atmosphere conditions and the substrate have been varied for the formation of different self-assembled structures as a result of the balance between different forces.

- In the particular case of magnetic Co NPs, dipolar interactions play an important role in the SA process. Different self-assembled structures are obtained by modulating the strength of magnetic interactions by controlling the Co NP size. It has been also observed how different parameters such the particle size distribution and the nature of the substrates, which will change the interactions substrate-NP, can be used to modulate the SA process, and different patterns like MLs of NPs or wire-like structures can be obtained.

Understand the nature and intensity of the forces present in this type of nanostructured magnetic materials is crucial for their future applications. Thanks to the electron holography and Lorentz microscopy, it has been possible to the record the magnetic signal of different Co self-assembled structures at NP resolution and also follow the changes in the magnetic structure

with increasing temperature.

- Lorentz microscopy and the electron holography have confirmed the existence of dipolar ferromagnetism in the observed self-assembled structures. The spontaneous appearance of dipolar ferromagnetism suggests that dipolar coupling is as strong and influential for the present arrangement of NPs as exchange coupling in conventional magnetic materials. Interestingly, these results show that dipolar FM order is extremely persistent even at a high degree of lattice disorder.

Chapter 6

Appendix: Instrumentation

A.1 Synthesis of Co Nanoparticles

TEM analysis was performed on a JEOL 1010 with an accelerating voltage of 80 kV and a digitalization image system Bioscan (Gatan). HRTEM, z-contrast and color maps analysis, were performed on a Titan Analytical 80-300ST TEM with an accelerating voltage of 300 kV. The magnetic characterization has been done using a SQUID magnetometer (MPMS, Quantum Design) was used to record the magnetic signal of a Co NPs between 5 and 50 K and fields up to 5 T. Diluted NPs were dispersed in paraffin to have a solid dispersion of noninteracting NPs. X-ray diffraction (XRD) data were collected on a PANalytical X'Pert diffractometer using a Co K α radiation source ($\lambda=1.179 \text{ \AA}$). In a typical experiment, the 2θ diffraction (Bragg) angles were measured by scanning the goniometer from 10° to 100° . The samples were prepared by precipitating the Co NPs in the presence of methanol or ethanol followed by brief centrifugation. The supernatant was discarded and the samples were dried under nitrogen before smearing onto (510) silicon wafers (3° off axis) for XRD analysis.

A.2 Formation of Core/Shell Co/CoO and Hollow CoO Nanoparticles

TEM analysis was performed on a JEOL 1010 with an accelerating voltage of 80 kV and a digitalization image system Bioscan (Gatan). HRTEM, BFSTEM, and HAADF or Z-contrast STEM images analyses were performed on a JEOL 2100 with an accelerating voltage of 200

kV equipped with an energy-dispersive X-ray spectroscopy (EDX) detector. HRTEM was performed on a JEOL JEM 2010F field emission gun microscope with an accelerating voltage of 200 kV. For the Z-contrast imaging we used a HAADF detector coupled to the same microscope, which allows working in STEM mode. In order to model the Z-contrast profiles obtained for the nanostructures, we followed the methodology published elsewhere.¹ The DLS and z-potential measurements has been done using a Zetasizer Nano from Malvern and the Dip cell kid for non aqueous measurements, and diluting the sample 100 times. A superconducting quantum interference device (SQUID) magnetometer (MPMS Quantum Design) was used to record the magnetic signal of the samples. The temperature was varied between 5 and 300 K according to a classical ZFC/FC procedure in the presence of an applied magnetic field (50 kOe), and the hysteresis cycles were obtained at different temperatures in a magnetic field varying from +50 to -50 kOe. The samples were prepared in gelatine capsules under air.

A.3 Synthesis of Pt and PtCo Nanoparticles

A.3.1 Synthesis of Pt and PtCo Nanoparticles Assisted by Metal Traces

TEM analysis was performed on a JEOL 1010 with an accelerating voltage of 80 kV. HRTEM analysis was performed on a JEOL 2100 with an accelerating voltage of 200 kV equipped with an EDX detector. The Pt NCs were drop-cast onto a carbon coated grid and allowed to air dry under ambient conditions. XRD data were collected on a PANalytical X'Pert diffractometer using a Cu K α radiation source ($\lambda=1.541$ Å). In a typical experiment, the 2θ diffraction (Bragg) angles were measured by scanning the goniometer from 25° to 100° at a speed of 0.021° s⁻¹. The samples were prepared by precipitating the Pt NCs in the presence of methanol or ethanol followed by brief centrifugation to ensure that all the NCs precipitated. The supernatant was discarded and the samples were dried under nitrogen before smearing onto (510) silicon wafers (3° off axis) for XRD analysis. Estimates of nanocrystal size were obtained using the Scherrer equation ($d = K\lambda / \beta \cos\theta$) where d is the mean crystallite dimension, K is the shape factor (0.9), λ is the X-ray wavelength, β is the line broadening at full width half maximum (FWHM) (radians) and θ is the Bragg angle. The peak positions were determined using the X'Pert HighScore program and compared before and after baseline correction. Vegard's law of alloy nanocrystals was considered for a slight shift in the 2θ Bragg peaks when compared to those for bulk Pt. ICP-MS was performed using an ICP-MS Agilent instrument (Model: 7500cx) with a detection limit of 0.02386 ppb. For each sample, the as-synthesized NCs, the purified NCs and the supernatant from the purification were all subjected to ICP-MS analysis. Aliquots of

the Pt NC samples were dissolved in concentrated aqua regia, which was then heated to ensure complete dissolution of all the metals, and diluted to an optimal concentration for ICP-MS analysis. Ga was used as the internal standard and the integration time/point and time/mass were 0.1 sec and 0.3 sec, respectively with a 3x repetition.

A.3.2 Synthesis of Pt and PtCo Nanoparticles by Using Competing Reducers

TEM analysis was performed on a JEOL 1010 with an accelerating voltage of 80 kV. HRTEM analysis was performed on a JEOL 2010F field emission gun microscope. The 3D supercell atomic models were designed by using the Rhodius software package available online at the University of Cadiz.^{2,3} In general, the supercell atomic models created are composed of 6000 to 25000 Pt atoms, and correspond to the same diameters as the experimental crystals found. EDX analysis was performed on a JEOL 2100 with an accelerating voltage of 200 kV equipped with an EDX detector. The NCs were drop-cast onto a carbon-coated grid and allowed to air-dry under ambient conditions. XRD data were collected on a PANalytical X'Pert diffractometer using a Cu K α radiation source ($\lambda=1.541$ Å). In a typical experiment, the 2θ diffraction (Bragg) angles were measured by scanning the goniometer from 25° to 100° at a speed of 0.021° s $^{-1}$. The samples were prepared by precipitating the NCs in the presence of methanol followed by brief centrifugation to ensure that all the NCs precipitated. The supernatant was discarded, and the samples were dried under nitrogen before smearing onto (510) silicon wafers (3° off axis) for XRD analysis. Estimates of NC size were obtained using the Scherrer equation and the peak positions were determined using the X'Pert HighScore program and compared before and after baseline correction. Calculations using Vegard's law support the observed shifts in the 2θ Bragg peaks when compared to those for pure Pt and Co NCs. ICP-MS was performed using an ICP-MS Agilent instrument (Model: 7500cx) with a detection limit of 0.02386 ppb. Aliquots of the purified NC samples were dissolved in concentrated aqua regia, which was heated to ensure complete dissolution of all metals, and diluted to an optimal concentration for ICP-MS analysis. Ga was used as the internal standard, and the integration time/point and time/mass were 0.1 and 0.3 s, respectively, with a 3x repetition.

A.4 Synthesis of Bimetallic Au/Pt Heterostructures

TEM analysis was performed on a JEOL 1010 with an accelerating voltage of 80 kV. HRTEM analysis was performed on a JEOL 2100 with an accelerating voltage of 200 kV. XRD data were

collected on a PANalytical X'Pert diffractometer using a Cu K α radiation source ($\lambda = 1.541 \text{ \AA}$). In a typical experiment, the 2θ diffraction (Bragg) angles were measured by scanning the goniometer from 25° to 100° at a speed of 0.021° per s. The samples were prepared by precipitating the NCs in the presence of methanol, and dried under nitrogen before smearing onto (510) silicon wafers (3° off axis) for XRD analysis. The peak positions were determined using the X'Pert High Score program and compared before and after baseline correction. UV-Vis spectra were obtained with a Shimadzu UV-2401PC spectrophotometer, over the range of 200–800 nm with a 1 cm path length quartz cuvette. Baseline correction was performed and the spectra were stacked in order to compare the changes in the absorption peak. Pt analyses were performed using an ICP-MS Agilent instrument (Model: 7500cx) with a detection limit of 0.02386 ppb. Aliquots of the samples were diluted to an optimal concentration for ICP-MS analysis. Gallium was used as the internal standard and the integration time/point and time/mass were 0.1 s and 0.3 s, respectively, with a 3x repetition.

A.5 Synthesis of Extremely Long Rod Shaped Au Nanocrystals

TEM analysis was performed on a JEOL 1010 with an accelerating voltage of 80 kV and a digitalization image system Bioscan (Gatan). HRTEM was performed on a JEOL JEM 2010F field emission gun microscope with an accelerating voltage of 200 kV. For the Z-contrast imaging we used a HAADF detector coupled to the same microscope, which allows working in STEM mode. In both cases, the NRs solution was concentrated and separated from the small nanospheres and surfactant by centrifugation. A volume of 1 mL of solution was centrifuged at 1500 rpm for 20 min. The supernatant was drawn off with a syringe and the precipitate was redispersed in 20 μL of distilled water. Finally, the concentrated solution was dropped onto a carbon-coated copper grid. SEM analysis was performed on a MERLIN Field Emission SEM (Fe-SEM) from Zeiss with an operating voltage of 1.2 kV. The Au NR solution was dropped on a HOPG substrate, and after 5 min the excess was removed tilting the substrate onto an absorbent paper. Then was rinsed with methanol and distilled water to remove CTAB. For optical images, Axio Observer z1m from Zeiss was used. The sample deposition onto a MICA substrate was prepared by means the same procedure explained above. UV-Vis spectra were obtained with a Shimadzu UV-2401PC spectrophotometer, over the range of 200–1000 nm with a 1 cm path length quartz cuvette.

A.6 Self-Assembly of Co Nanoparticles at Compatible Substrates: Graphite

TEM analysis was performed on a JEOL 1010 with an accelerating voltage of 80 kV. HRTEM analysis was performed on a JEOL 2010F field emission gun microscope. An ESEM Quanta 200FEI XTE325/D8395 was used to obtain resolution images of the NP layers. The instrument can be used in high vacuum (HV) mode, low vacuum (LV) mode and the so-called ESEM mode. The images were taken at low vacuum conditions (up to 1 Torr) with a large field detector (LFD) and at high vacuum with a conventional Everhart-Thornley secondary electron detector (ETD). The chemical analysis of the structures was performed with an EDX system with an energy-dispersive spectrometer (EDS) detector for the spectra acquisition. And a SEM Helios EBS3 was used to obtain NP resolution. For the acquisition of optical images, Axio Observer z1m optical microscope from Zeiss was used. The magnetic characterization has been done using a SQUID magnetometer (MPMS, Quantum Design) was used to record the magnetic signal of a Co NPs between 5 and 50 K and fields up to 5 T. NPs assemblies were introduced together with the substrate (which was previously measured to ensure non magnetic signal) into the sample holder.

A.7 Self-Assembly of Co Nanoparticles at Non-Compatible Substrates: Silicon Wafers

TEM analysis was performed on a JEOL 1010 with an accelerating voltage of 80 kV. An ESEM Quanta 200FEI XTE325/D8395 was used to obtain resolution images of the NP layers.

Image processing. The most direct method to quantitatively obtain insight into the structural arrangement of NPs is to analyze the height–height correlation of the surface using real-space imaging techniques (here SEM). Image processing was done using the software Mountains (Digital Surface 5.1.1.5541).

A.8 References

1. Lima, E., Jr.; Vargas, J. M.; Zysler, R. D.; Rechenberg, H. R.; Cohen, R.; Arbiol, J.; Goya, G. F.; Ibarra, A.; Ibarra, M. R. "Single-Step Chemical Synthesis of Ferrite Hollow Nanospheres". *Nanotechnology* **2009**, 20.

- 2.** Bernal, S.; Botana, F. J.; Calvino, J. J.; Lopez-Cartes, C.; Perez-Omil, J. A.; Rodriguez-Izquierdo, J. M. "The Interpretation of Hrem Images of Supported Metal Catalysts Using Image Simulation: Profile View Images". *Ultramicroscopy* **1998**, 72, 135-164.

- 3.** Pérez-Omil, J. A. D. T., University of Cádiz, Spain, **1994**.

List of Abbreviations

α : Lattice parameter	FEG : Field-emission gun
A : Amplitude	FFT : Fast Fourier transform
AA : Ascorbic Acid	FM : Ferromagnetic
AFM : Antiferromagnetic	FWHM : Full Width at Half Maximum
AFM* : Atomic Force Microscopy	GPA : Geometrical phase analysis
AR : Aspect ratio	h : Planck constant
B : Magnetic flux	\hbar : Reduced Planck constant
BF-STEM : Bright Field Scanning Transmission Electron Microscopy	H : Magnetic field
bp : Boiling point	H_c : Coercivity field
CCD : Charge-coupled device	H_e : Exchange field
cmc : Critical micelle concentration	HAADF : High Angle Annular Dark Field
CTAB : Cetyl trimethylammonium bromide	hcp : Hexagonal close-packed
DCB : Dichlorobenzene	HDD : Hexadecanediol
DLS : Dynamic Light Scattering	HHCF : Height-height correlation function
DM : Diamagnetic	HOPG : Highly oriented pyrolytic graphite
e : Elementary electric charge	HRTEM : High Resolution Transmission Electron Microscopy
E° : Standard electrode potential	ICP-MS : Inductively coupled plasma mass spectrometry
EDX : Energy-Dispersive X-ray Spectroscopy	IR : Infrared
EELS : Electron-Energy-Loss Spectroscopy	K : Anisotropy:
FC : Field cool	K_BT : Thermal energy
fcc : Face-centered cubic	LBL : Layer-by-layer
	m : Magnetic moment

M: Magnetization	XRD: X-ray powder diffraction
MFM: Magnetic Force Microscopy	ZFC: Zero field cool
MIP: Mean inner potential	SPR: Surface Plasmon resonance
ML: Monolayer	β: Beta
mp: Melting point	ϵ : Epsilon
NC: Nanocrystal	ρ : Density
ND: Nanodisk	φ: Phase
NP: Nanoparticle	ψ: Electron wavefunction
NR: Nanorod	μ: Spin moment
NW: Nanowire	μ_0: Permeability of the free space
OA: Oleic acid	μ_{at}: Atomic magnetic moment
OAM: Oleylamine	μ_B : Bohr magneton
PM: Paramagnetic	τ_0: Moment relaxation time
PSA: Particle size analyzer	τ_m: Measuring time
PVP: Poly vinyl pyrrolidone	χ: Susceptibility
QD: Quantum dot	1D: One-dimensional
RT: Room temperature	2D: Two-dimensional
SA: Self-assembly	3D: Three-dimensional
SEM: Scanning Electron Microscopy	
SLS: Solution-liquid solid	
SP-STM: Spin-Polarized Scanning Tunnelling Microscopy	
SPM: Superparamagnetic	
T: Temperature	
T_B: Blocking temperature	
T_C: Curie temperature	
T_N: Néel temperature	
TEM: Transmission electron microscopy	
THF: Tetrahydrofuran	
TOPO: Trioctylphosphine oxide	
UD: Undecanol	
UV-vis: Ultraviolet-visible	
V: Volume	
v: Velocity	
vdW: Van der Waals	

List of Publications

Peer-reviewed papers

1. Peña L., Varón M., Konstantinovic Z., Balcells Ll., Martínez B. and Puentes V. “Large 2D self-assembled domains of cobalt nanoparticles onto silicon wafers” *J. Mater. Chem.* **2011**, 21, 16973-16977.
2. Lim S.I., Varon M., Ojea-Jiménez I., Arbiol J. and Puentes V. “Pt nanocrystal evolution in the presence of Au(III)-salts at room temperature: spontaneous formation of AuPt heterodimers” *J. Mater. Chem.* **2011**, 21, 11518-11523.
3. Amigo J.M., Bastús N.G., Hoen R., Vázquez-Campos S., Varón M., Royo M. and Puentes V. “Analysis of time-dependent conjugation of gold nanoparticles with an antiparkinsonian molecule by using curve resolution methods” *Analytica Chimica Acta* **2011**, Volume 683, Issue 2, 170-177.
4. Lim S.I. , Varon M., Ojea-Jimenez I., Arbiol J., Puentes V. “Exploring the Limitations of the Use of Competing Reducers to Control the Morphology and Composition of Pt and PtCo Nanocrystals” *Chemistry of Materials* **2010**, 22, 4495-4504.
5. Lim S.I., Ojea-Jimenez I., Varon M., Casals E., Arbiol J., Puentes V. “Synthesis of Platinum Cubes, Polypods, Cuboctahedrons, and Raspberries Assisted by Cobalt Nanocrystals” *Nano Letters* **2010**, 10, 964-973.
6. Varon M., Peña L., Balcells Ll., Skumryev V., Martínez B., and Puentes V. F. “Dipolar Driven Spontaneous Self Assembly of Superparamagnetic Co Nanoparticles into Micrometric Rice-Grain like Structures” *Langmuir* **2010**, 26, 109-116.

7. Casals E., Bastús N.G., Vazquez-Campos S., Varon M., Comenge J. and Puentes V.. “Inorganic Nanoparticles and Biology”, *Contributions to Science* **2007**, 3(3).

In preparation

8. Varón M., Beleggia M., Kasama T., Harrison R.J., Dunin-Borkowski R.E., Puentes V.F., and Frandsen C. “Dipolar Ferromagnetism in Low-dimensional Nanoparticle Structures”.
9. Varón M., Ojea-Jiménez I., Arbiol J., Puentes V.F. “Spontaneous Formation of Hollow Cobalt Oxide Nanoparticles at Room Temperature at the Water/Air Interface Shows Enhanced Solid-Solid Diffusion at the Nanoscale”.
10. Varón M., Ojea-Jiménez I., Arbiol J., Puentes V.F. “Sustained Growth Synthesis of Extremely Long Gold Nanorods at Room Temperature”.
11. Varón M., Kasama T., Beleggia M., Mateiu R.V., Fuller A., Puentes V.F., and Frandsen C. “Dipolar ferromagnetism and domain structure in wire-like structures of self-assembled cobalt nanoparticles”.

Book Chapters

1. Bastús N. G., Casals E., I. Ojea, Varon M. and Puentes V. “The Reactivity of Colloidal Inorganic Nanoparticles”. Published by In Tech, Accepted. Edited by Abbass Hashim.

